

Modeling and simulation of electrically driven quantum dot based single-photon sources

— From classical device physics to open quantum systems —

vorgelegt von

Markus Kantner, M. Sc.

geb. in Zerbst/ Anhalt

Von der Fakultät II – Mathematik und Naturwissenschaften
der Technischen Universität Berlin

zur Erlangung des akademischen Grades

Doktor der Naturwissenschaften

— Dr. rer. nat. —

genehmigte Dissertation

Promotionsausschuss

Vorsitzender: Prof. Dr. rer. nat. Stephan Reitzenstein

Gutachter: Prof. Dr. rer. nat. Andreas Knorr

Gutachter: Prof. Dr. sc. techn. Bernd Witzigmann

Gutachter: Priv.-Doz. Dr. rer. nat. Uwe Bandelow

Tag der wissenschaftlichen Aussprache: 4. September 2018

Berlin 2018

Abstract

Semiconductor quantum optics is on the leap from the lab to real world applications. The currently unfolding “second quantum revolution” aims at the development of novel quantum technologies that exploit inherent quantum mechanical phenomena like entanglement and quantum superposition for communication and information processing tasks. Many applications, such as eavesdropping-secure encryption methods and optical quantum computers, rely on efficient quantum light sources that can emit single photons or entangled photon pairs on demand. Semiconductor quantum dots have been identified as an ideal optically active element for such devices as they can be directly integrated into complex semiconductor structures and photonic resonators. On the step from basic research to new technologies, device engineers will need simulation tools that combine classical device physics with cavity quantum electrodynamics, to support the development and optimization of novel quantum light sources. This thesis is focused on the device scale modeling and numerical simulation of electrically driven single-photon emitters based on semiconductor quantum dots.

The main result of this thesis is the introduction of a new *hybrid quantum-classical* modeling approach, that self-consistently describes the macroscopic carrier transport in semiconductor devices along with the dynamics of open quantum systems. This is achieved by coupling van Roosbroeck’s semi-classical drift-diffusion equations with a Markovian quantum master equation in Lindblad form. The approach allows for a comprehensive description of quantum dot based devices on multiple scales: It enables the calculation of the quantum optical figures of merit along with the simulation of the spatially resolved current flow in realistic, multi-dimensional semiconductor device geometries out of one box. The approach goes beyond existing multi-scale approaches in semiconductor device simulation and closes a gap between microscopic and macroscopic simulation tools, that could be useful to support the development of future devices. The hybrid model system is shown to be consistent with fundamental principles of (non-)equilibrium thermodynamics – in particular it obeys the second law of thermodynamics.

Single-photon sources based on semiconductor quantum dots are typically operated at extremely low temperatures, which poses a significant challenge for the simulation of such devices already at the semi-classical level. First, the strong degeneration of the electron-hole plasma requires a modification of the standard discretization method towards the accurate inclusion of Fermi–Dirac statistics. Second, the van Roosbroeck system is ill-conditioned at cryogenic temperatures, which leads to serious convergence issues. In this thesis, several recent discretization approaches are reviewed and assessed with respect to their accuracy and structure preserving properties. Moreover, a new temperature-embedding scheme is introduced that enables the carrier transport simulation at cryogenic temperatures. These methods are employed to theoretically investigate the current injection into electrically driven single-photon emitting diodes. A central result of the analysis is an electrical device design that enables the highly selective electrical excitation of single quantum dots for single-photon emission.

Zusammenfassung

Die Halbleiter-Quantenoptik befindet sich auf dem Sprung von der Grundlagenforschung zu realen Anwendungen. Die „Zweite Quantenrevolution“ zielt auf die Nutzung quantenmechanischer Phänomene wie Superposition und Verschränkung zur Entwicklung neuartiger Technologien für Quantenkommunikation und Quanteninformationsverarbeitung. Viele Anwendungen, wie beispielsweise abhörsichere Verschlüsselungsverfahren und optische Quantencomputer, erfordern die Verfügbarkeit effizienter Quantenlichtquellen, welche einzelne Photonen oder verschränkte Photonenpaare „auf Knopfdruck“ erzeugen können. Halbleiter-Quantenpunkte stellen ein ideales optisch aktives Element für solche Quantenlichtquellen dar, da sie sich direkt in komplexe Halbleiterstrukturen und photonische Resonatoren integrieren lassen. Für den Schritt von der Grundlagenforschung zu neuen Technologien werden neue Simulationsmethoden benötigt, welche sowohl die Physik klassischer Halbleiterbauelemente als auch die Resonator-Quantenelektrodynamik beschreiben, um die Entwicklung und Optimierung neuer Quantenlichtquellen voranzutreiben. Die vorliegende Dissertation beschäftigt sich mit der Modellierung und numerischen Simulation elektrisch gepumpter Einzelphotonenquellen auf der Basis von Halbleiter-Quantenpunkten.

Das zentrale Ergebnis dieser Arbeit ist die Einführung eines neuen *hybrid quantenklassischen* Modellierungsansatzes, der den makroskopischen Ladungsträgertransport in Halbleiterstrukturen selbstkonsistent mit der Dynamik offener Quantensysteme beschreibt. Dies wird durch die Kopplung des van Roosbroeck-Systems (Drift-Diffusions-Gleichungen) mit einer Markov’schen Quanten-Master-Gleichung in Lindblad-Form erreicht. Der Ansatz ermöglicht eine umfassende Beschreibung quantenpunktbasierter Bauelemente auf mehreren Skalen – so lassen sich insbesondere die mikroskopischen, quantenoptischen Eigenschaften des Bauelements gemeinsam mit dem räumlich aufgelösten Ladungsträgertransport in realistischen, mehrdimensionalen Halbleiterstrukturen aus einem Modell berechnen. Der Ansatz geht über bisherige Multi-Skalen-Methoden zur Simulation von Halbleiterbauelementen hinaus und schließt eine Lücke zwischen mikroskopischen und makroskopischen Simulationsansätzen. Das Modell kann zur Entwicklung neuartiger Bauelemente beitragen und steht im Einklang mit fundamentalen Prinzipien der (Nicht-)Gleichgewichts-Thermodynamik – insbesondere befolgt es den zweiten Hauptsatz der Thermodynamik.

Auf Halbleiter-Quantenpunkten basierende Einzelphotonenquellen werden typischerweise bei extrem tiefen Temperaturen betrieben. Daraus ergeben sich neue Herausforderungen für die numerische Simulation des Ladungsträgertransports. Die starke Entartung des Elektron-Loch-Plasmas bei kryogenischen Temperaturen macht die Berücksichtigung der Fermi-Dirac Statistik und damit eine Verallgemeinerung des Standard-Diskretisierungsverfahrens erforderlich. Weiterhin ist das van Roosbroeck-System bei extrem tiefen Temperaturen schlecht konditioniert, was zu schwerwiegenden Konvergenzproblemen führt. In dieser Arbeit werden mehrere aktuelle Diskretisierungsmethoden hinsichtlich ihrer strukturerhaltenden Eigenschaften und Genauigkeit verglichen. Darüber hinaus wird eine neue Pfadverfolgungsmethode eingeführt, welche die Simulation des Ladungsträgertransports bei kryogenischen Temperaturen ermöglicht. Die numerischen Methoden werden zur Untersuchung der Strominjektion in elektrisch betriebenen Einzelphotonen-LEDs verwendet. Ein wichtiges Resultat dieser Arbeit ist ein elektrisches Bauelement-Design, das die selektive elektrische Anregung einzelner Quantenpunkte für die Emission einzelner Photonen ermöglicht.

Acknowledgements

At this point, I would like to thank the people who made this thesis possible. First and foremost, I would like to thank Priv.-Doz. Dr. Uwe Bandelow for giving me the opportunity to work with a great freedom on the exciting and challenging field of optoelectronic device simulation and related topics in the last few years. Moreover, I would like to thank Prof. Dr. Andreas Knorr and Prof. Dr. Bernd Witzigmann for making themselves available as reviewers and co-examiners of this thesis. I'm grateful to Prof. Dr. Stephan Reitzenstein for chairing the board of referees.

My deepest gratitude I would like to express to Dr. Hans-Jürgen "Ede" Wünsche and Dr. Thomas Koprucki, who constantly supported and encouraged me in my work. I'm grateful to Ede for sharing his unlimited knowledge on virtually all fields of physics, his scientific intuition and his great experience with me. To Thomas I'm deeply in debt for his literally tireless commitment on working out new ideas, improving manuscripts and advising me in countless scientific and non-scientific problems.

A special thanks goes to my office mate Dr. Shalva Amiranashvili for uncountable (and sometimes also never-ending) discussions on physics, math, history, language and various other fascinating topics that always broadened my horizon.

Moreover, I'd like to thank many other colleagues from the Weierstrass Institute for the welcoming working atmosphere over the last few years. I can not mention everybody here, but I'm particularly grateful for inspiring discussions and collaborations with Markus Mittnenzweig, Dr. Jürgen Fuhrmann, Dr. Matthias Liero, Dr. Dirk Peschka, Prof. Dr. Alexander Mielke, Dr. Alexander Linke, the *ddfemi* team and the members of the research group *Laser Dynamics*.

The work leading to the results in this thesis has received funding from the Deutsche Forschungsgemeinschaft within the Collaborative Research Center CRC 787 *Semiconductor Nanophotonics* under project B4. I'm grateful to the *School of Nanophotonics* runned by the CRC 787 for providing a unique possibility to get in touch with many bright minds in a nice atmosphere and – of course – for the considerable financial support that allowed me to attend several international conferences.

List of publications

Journal articles

- M. Kantner, M. Mittnenzweig and T. Koprucki: “Hybrid quantum-classical modeling of quantum dot devices,” *Phys. Rev. B* **96**, 205301/1–17 (2017)
- M. Kantner and T. Koprucki: “Numerical simulation of carrier transport in semiconductor devices at cryogenic temperatures,” *Opt. Quant. Electron.* **48**, 543/1–7 (2016)
- M. Kantner, U. Bandelow, T. Koprucki, J.-H. Schulze, A. Strittmatter and H.-J. Wünsche: “Efficient current injection into single quantum dots through oxide-confined pn-diodes,” *IEEE Trans. Electron Dev.* **63**, 2036–2042 (2016)

Book chapters

- M. Kantner, A. Mielke, M. Mittnenzweig and N. Rotundo: “Mathematical modeling of semiconductors: From quantum mechanics to devices,” submitted (2018)
- P. Farrell, N. Rotundo, D. H. Doan, M. Kantner, J. Fuhrmann and T. Koprucki: “Mathematical methods: Drift-diffusion models,” in *Handbook of Optoelectronic Device Modeling and Simulation – Vol. 2*, edited by J. Piprek (CRC Press, 2017), Chap. 50, pp. 731–771

Conference proceedings

- M. Kantner, M. Mittnenzweig and T. Koprucki: “A hybrid quantum-classical modeling approach for electrically driven quantum light sources,” *Proc. SPIE 10526, Physics and Simulation of Optoelectronic Devices XXVI*, 1052603, edited by B. Witzigmann, M. Osiński, Y. Arakawa
- M. Kantner, U. Bandelow, T. Koprucki and H.-J. Wünsche: “Simulation of quantum dot devices by coupling of quantum master equations and semi-classical transport theory,” *Proc. Int. Conf. Numerical Simulation of Optoelectronic Devices (NUSOD)*, edited by J. Piprek, M. Willatzen, pp. 217–218 (2017)
- M. Kantner, U. Bandelow, T. Koprucki and H.-J. Wünsche: “Multi-scale modelling and simulation of single-photon sources on a device level,” *Proc. of Euro-TMCS II: Theory, Modelling and Computational Methods for Semiconductors*, edited by E. O’Reilly, S. Schulz, S. Tomic, p. 65 (2016)
- M. Kantner, U. Bandelow, T. Koprucki and H.-J. Wünsche: “Modeling and simulation of injection dynamics for quantum dot based single-photon sources,” *Proc. Int. Conf. Numerical Simulation of Optoelectronic Devices (NUSOD)*, edited by J. Piprek, C. Poulton, M. Steel, M. de Sterke, pp. 219–220 (2016)
- M. Kantner, U. Bandelow, T. Koprucki, J.-H. Schulze, A. Strittmatter and H.-J. Wünsche: “On current injection into single quantum dots through oxide-confined pn-diodes,” *Proc. Int. Conf. Numerical Simulation of Optoelectronic Devices (NUSOD)*, edited by J. Piprek, C. Poulton, M. Steel, M. de Sterke, pp. 215–216 (2016)

- M. Kantner, U. Bandelow, T. Koprucki and H.-J. Wünsche: “Modeling and numerical simulation of electrically pumped single-photon emitters,” Proc. Int. Conf. Numerical Simulation of Optoelectronic Devices (NUSOD), edited by J. Piprek, Y.-R. Wu, pp. 151–152 (2015)
- M. Kantner, U. Bandelow and T. Koprucki: “Multi-scale Modeling and Simulation of Single-Photon Sources,” Proc. Int. Nano-Optoelectronics Workshop (iNOW), edited by Y. Arakawa, F. Koyama, C. Chang-Hasnain, D. Bimberg, pp. 129–130 (2015)
- T. Koprucki, M. Kantner, J. Fuhrmann and K. Gärtner: “On modifications of the Scharfetter–Gummel scheme for drift-diffusion equations with Fermi-like statistical distribution functions,” Proc. Int. Conf. Numerical Simulation of Optoelectronic Devices (NUSOD), edited by J. Piprek, J. Javaloyes, pp. 155–156 (2014)

Further publications

Publications which are not part of this thesis.

- M. Kantner, E. Schöll and S. Yanchuk: “Delay-induced patterns in a two-dimensional lattice of coupled oscillators,” Sci. Rep. **5**, 8522 (2015)
- M. Kantner, T. Koprucki and H.-J. Wünsche: “Numerical simulation and optimization of electrical resistance in distributed Bragg reflectors,” Proc. Int. Nano-Optoelectronics Workshop (iNOW), edited by C. Chang-Hasnain, Z. I. Alferov and V. G. Dubrovskii, pp. 89–90 (2014)
- M. Kantner and S. Yanchuk: “Bifurcation analysis of delay-induced patterns in a ring of Hodgkin–Huxley neurons,” Phil. Trans. Roy. Soc. A **371**, 20120470 (2013)

Table of contents

Abstract	III
Zusammenfassung	V
Acknowledgements	VII
List of publications	IX
1 Introduction	1
1.1 Semiconductor quantum dots	3
1.2 Single-photon sources and applications	4
1.2.1 Requirements	5
1.2.2 Applications	6
1.3 Device scale simulation of single-photon sources	7
1.4 Outline	8
2 Semi-classical charge transport in semiconductor devices	9
2.1 The van Roosbroeck system	9
2.1.1 Poisson’s equation	10
2.1.2 Charge carrier density	10
2.1.3 Current density	14
2.1.4 Carrier recombination and generation	15
2.1.5 Boundary conditions	18
2.2 Derivation from the semi-classical Boltzmann transport equation	19
2.3 Thermodynamics of the van Roosbroeck system	23
2.3.1 Thermodynamic potentials	24
2.3.2 Consistency with (non-)equilibrium thermodynamics	27
3 Numerical simulation of carrier transport at cryogenic temperatures	31
3.1 Finite volume method	31
3.1.1 Delaunay triangulation and Voronoï boxes	32
3.1.2 Discretization of balance equations	33
3.2 Discrete van Roosbroeck system	35
3.3 Scharfetter–Gummel schemes for Fermi–Dirac statistics	36
3.3.1 Classical Scharfetter–Gummel scheme	37
3.3.2 Generalized schemes for Fermi–Dirac statistics	38
3.4 Structure preserving properties of the discretization	43
3.5 Nonlinear iteration method	44
3.6 Annealing method for simulation at cryogenic temperatures	46
3.7 Simulation of wide band gap semiconductors using the annealing method	48
3.8 Conclusions	49
4 Current injection into oxide-confined single-photon emitting diodes	51
4.1 Introduction	51
4.2 Device design and site-controlled quantum dot nucleation	52
4.3 Electroluminescence of parasitic quantum dots and current spreading	53
	XI

4.4	Numerical simulation of the carrier injection	53
4.4.1	Stationary injection in the pin-design	54
4.4.2	Impact of QDs on free carrier densities	56
4.4.3	Current confinement in the ppn-design	58
4.5	Conclusions	60
5	Hybrid modeling of electrically driven quantum light sources	61
5.1	Motivation	61
5.2	Lindblad equation for grand canonical reservoirs	62
5.2.1	Open quantum systems	62
5.2.2	Derivation of the Lindblad equation in the weak-coupling limit with charge conservation constraint	63
5.2.3	Thermodynamic properties	69
5.3	Hybrid quantum-classical model for electrically driven quantum light sources	71
5.3.1	Modeling of the quantum system	73
5.3.2	Confined charge density and charge conservation	74
5.3.3	Energy, charge and entropy balance	75
5.3.4	Thermodynamic equilibrium	76
5.3.5	Macroscopic scattering rates	78
5.3.6	Microscopic transition rates	80
5.3.7	Entropy production and the second law of thermodynamics	83
5.4	Relation of the hybrid quantum-classical model to the GENERIC formalism	85
5.5	Conclusions	86
6	Hybrid simulation of an electrically driven single-photon source	89
6.1	Device structure	89
6.2	Model specification	90
6.2.1	Hamiltonian	90
6.2.2	Dissipation superoperators	91
6.2.3	Transition rate models	94
6.3	Numerical method	96
6.4	Stationary operation	98
6.5	Pulsed electrical excitation	101
6.6	Discussion and outlook	104
6.7	Conclusions	107
7	Summary and outlook	109
Appendix		113
A.1	Dopant ionization at cryogenic temperatures	113
A.2	Recombination rate models	116
A.3	Numerical evaluation of Fermi–Dirac integrals	119
A.4	Two-time correlation functions and the quantum regression theorem	120
A.5	Alternative approach for the macroscopic scattering rates	121
A.6	Wave functions and energy levels of lens shape InGaAs quantum dots	123
Bibliography		i

Chapter 1

Introduction

The quantum theory of light started more than a century ago when Max Planck explained the black body radiation spectrum by assuming that light is emitted in discrete, fundamental units of energy that we denote today as *photons*. Based on the same hypothesis, which involves a particle-like conception of the electromagnetic field that was formerly understood as an entirely wave-like phenomenon, Albert Einstein gave an explanation of the photoelectric effect for which he was awarded with the Nobel Prize in 1921. Subsequently also wave-like properties of matter have been discovered that finally lead to the advent of quantum mechanics – a scientific revolution persisting until the present day. By the mid of the 20th century, the classical theory of electromagnetism was superseded by quantum electrodynamics, which forms the basis of our modern understanding of light, matter and their interaction on a fundamental level. Soon it was discovered that light can exist in different states with distinct statistical properties. These states of the radiation field include coherent states (lasers), thermal states (black body radiation), number states (non-classical light) and even more exotic squeezed states. But it was not until 1977 when H. J. Kimble, M. Dagenais and L. Mandel first demonstrated the emission of a single photon from a single atom at one time [164]. This observation finally gave a convincing evidence that light consists of photons [315]. Such a single-photon state of the electromagnetic field is a truly non-classical state of light, which shows phenomena like “anti-bunching” that can only be understood in terms of a quantized electromagnetic field [234].

Today, quantum optics has become a thriving field with promising real world applications and ever broadening horizons [76, 276]. Among others, the research in quantum optics on single photons and entangled photon pairs stimulated progress in quantum information theory, which aims at using photons as qubits – units of quantum information – for optical quantum computing and information processing tasks [163]. Some of the most celebrated applications in that field are the various approaches to eavesdropping-secure encryption methods for secure data transmission based on quantum key distribution [99]. The security of quantum key distribution relies on well approved quantum mechanical effects rather than on mathematical hardness and assumptions on the available computational power as in classical methods.

The experimental generation of quantum states of light using single atoms requires a large technical effort due to bulky and complex experimental setups. However, with the advent of semiconductor quantum dots – nano-crystalline structures with many atom-like

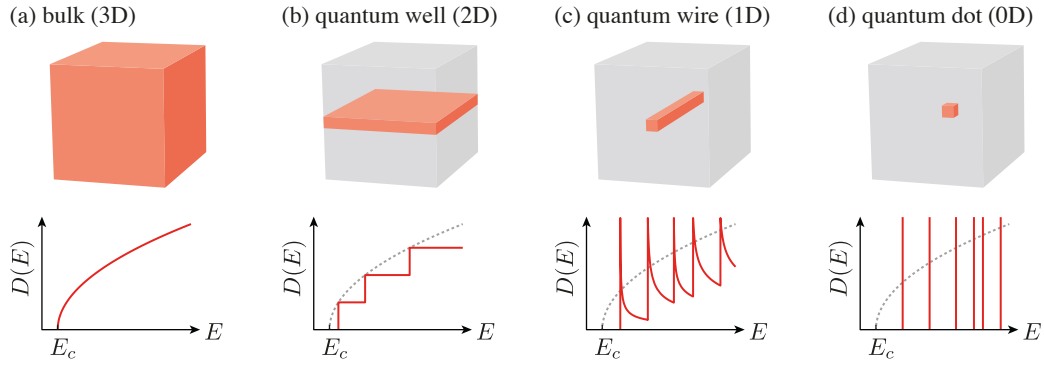


Fig. 1.1 Density of states (DOS) of different quantum confined structures (semiconductor with a smaller band gap than the cladding semiconductor) in comparison to bulk material. The progression of quantum confinement modifies the density of electronic states from (a) square root-like continuous DOS for 3D bulk semiconductors to a (b) staircase-like DOS in 2D quantum wells and a (c) discontinuous DOS of 1D quantum wires exhibiting typical singularities. The full confinement in all three spatial dimensions finally leads to the (d) discrete energy spectrum of quantum dots. The conduction band edge is denoted by E_c .

properties that can confine electrons within solid state structures (see Fig. 1.1) – the fundamental research in quantum optics merged with the well-developed semiconductor technology. Semiconductor quantum dots are a solid-state analogue of single atoms, whose electro-optical properties can be tailored on purpose by the growth process. Moreover, semiconductor quantum dots can be directly integrated into semiconductor devices and micro-resonators by standard manufacturing techniques. This has led to many novel concepts for opto-electronic and photonic devices including solid state quantum light sources and ultimately downsized nanolasers [41, 48, 49, 179, 212, 263, 295].

Today, semiconductor quantum optics is on the leap from basic research to commercial applications [298]. The currently unfolding “second quantum revolution” aims at the development of quantum technologies that address individual quantum states (instead of ensembles) and exploit inherent quantum mechanical phenomena like entanglement and quantum superposition [60]. This development is driven by highly-specialized start-up enterprises, large global companies (e.g., Google, IBM, Intel, Microsoft, Toshiba [251]) and large national funding programs comprising UKNQT¹ (United Kingdom), QuTech² (Netherlands), QUTEGA³ (Germany), CQT⁴ (Singapore) and QUESS (China). Moreover, the European Commission supports the development of quantum technologies within the research program *Horizon 2020* and has launched a new flagship program on quantum technologies in 2018 that is currently in an operational ramp-up phase [251].

For the development of novel electrically driven quantum optical devices, which are desirable for practical applications, efficient mathematical models and simulation tools are needed to support the advancement of the technology. Numerical simulations can help to optimize particular designs and decrease the development costs by reducing the demand for the expensive and time-consuming growth and processing of a large number of prototypes. For instance, the spectacular progress in miniaturization and performance of microelectronics and transistor technology following Moore’s law over the last decades was

¹ <http://uknqt.epsrc.ac.uk>

² <https://qutech.nl>

³ <http://www.qutega.de/>

⁴ <https://www.quantumlah.org>

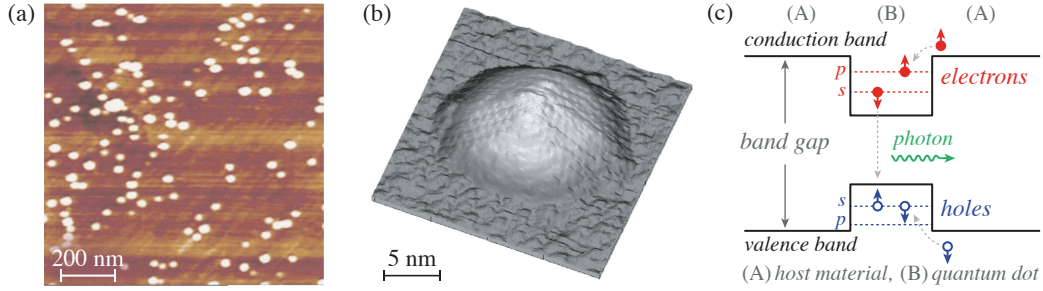


Fig. 1.2 (a) Atomic force microscopy image of a layer of InGaAs-QDs grown by molecular beam epitaxy. Reprinted from Ref. [187]. © 2017 The Korean Vacuum Society. (b) Scanning tunneling microscope image of an uncovered InAs-QD grown on GaAs. Reprinted with permission from Ref. [205]. © 2001 American Institute of Physics. (c) Schematic representation of a type I semiconductor QD heterostructure with confined states for both electrons and holes.

strongly supported by TCAD (Technology Computer Aided Design) simulation tools [299, 311]. For the description of electrically driven quantum light sources on a comprehensive level, a combination of models from classical device physics (i.e., TCAD) and cavity quantum electrodynamics is required. In particular, one has to connect the semi-classical semiconductor transport theory (describing the flow of electrons and holes within the device) with quantum optical models for the light-matter interaction in semiconductor quantum dots. The comprehensive and thermodynamically consistent modeling and simulation of quantum optical devices based on semiconductor quantum dots is a central scope of this thesis.

1.1 Semiconductor quantum dots

Semiconductor quantum dots (QDs) are nanoscopic crystalline structures embedded within a host semiconductor crystal,⁵ where the carrier wave functions (conduction band electrons and valence band holes) are tightly confined in all three spatial dimensions such that there is no possibility of free propagation in any direction [29]. The three dimensional confinement of carriers on a nanometer scale represents the ultimate limit of carrier confinement and leads to a fully discrete energy spectrum, see Fig. 1.1. The energy spectrum and the localized wave functions strongly resemble the properties of atoms which is reflected in the often used denotation of QDs as “artificial atoms”. However, unlike in atoms, the energy quantization in QDs occurs in a solid state structure containing typically around $10^4 - 10^5$ atoms [194], see Fig. 1.2. The number of confined states provided by the QD and their energetic position depends strongly on the size and geometry of the dot, its chemical composition, strain and piezoelectric fields in its vicinity etc. and are tunable by altering the parameters of the growth process [29, 131, 273, 292]. In opto-electronics, self-assembled (Stranski–Krastanov growth mode) InGaAs-QDs are of particular importance [29, 30].

QDs can be directly integrated within photonic crystals [64, 195] and micro-resonators [243, 245], which allows to tailor their electro-optical properties by exploiting effects from cavity quantum electrodynamics (QED) such as, e.g., the Purcell enhancement [240] of the spontaneous emission and the strong coupling regime of light-matter interaction [165, 194, 241, 243]. Based on these exceptional physical properties, QDs are an interesting platform for basic research in (semiconductor) quantum optics [144, 165, 208, 211, 332]

⁵ Semiconductor QDs can also be embedded in other environments [254], but this is not considered here.

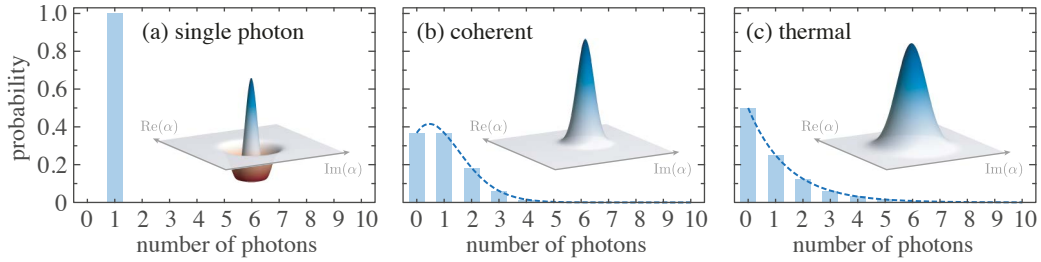


Fig. 1.3 Comparison of the photon number distributions of the (a) single-photon Fock state, (b) coherent light (Poissonian distribution) and (c) thermal light (Bose–Einstein distribution) with mean photon number $\langle n \rangle = 1$. The insets show a phase space representation of the photon states using the Wigner quasi-probability function [276], where negative values (color-coded in red) indicate non-classical states.

and promising candidates for many applications in semiconductor nano-photonics and novel photonic devices such as ultimately downsized nanolasers [30, 48, 49, 93, 179, 244, 295], sources of single photons and entangled photon pairs [31, 37, 41, 242, 262, 263, 272, 282, 283, 305, 330], intermediate band solar cells [98, 327] and optical amplifiers [28, 328].

1.2 Single-photon sources and applications

Single-photon sources ideally emit a single photon with a probability of one in response to an external excitation. Hence, in the ideal case, the probability to emit fewer or more than one photon is zero, see Fig. 1.3 (a). This requirement can neither be fulfilled by a laser nor a thermal light source, which both emit radiation with each a characteristic photon number distribution: The coherent light emitted by a laser has a Poissonian photon number distribution shown in Fig. 1.3 (b) and the thermal light emitted, e.g., by a light bulb, shows a Bose–Einstein distribution (see Fig. 1.3 (c)). Even though strongly attenuated lasers can emit single photons, there is always a non-zero probability of generating zero or multiple photons. Hence, an ideal single-photon source must emit light in a non-classical number state which is called a Fock state [41, 276]. Currently, there are two main types of single-photon sources which are either based on atoms or atom-like emitters, or rely on nonlinear optical processes such as spontaneous parametric down-conversion [41, 76]. Here, the focus is on the atom-like systems and in particular on semiconductor QDs.

The central advantage of atom-like emitters is that the emission process can be triggered by an external electrical or optical excitation. In the case of optical excitation, the emitter converts an incoming laser pulse into a stream of single photons: The laser pulse drives the emitter into an excited state, which subsequently relaxes back to the ground state via spontaneous emission of a single photon [41, 263]. As long as the emitter is not excited again, the emission of further photons is not possible. Hence, the photons emitted by the source have the tendency to be well separated in time, which is called “photon anti-bunching”. The photon anti-bunching phenomenon was first observed in resonance fluorescence experiments on sodium atoms in 1977 [164] and is deemed to be the first clear experimental evidence for the existence of photons and a quantized electromagnetic field.⁶ Its detection stimulated the formation of quantum optics as a specific field of research

⁶ Previously known phenomena like, e.g., the photoelectric effect can be explained by a semi-classical conception that requires only the quantization of matter. The electromagnetic field can be treated classically according to Maxwell’s equations [76, 313].

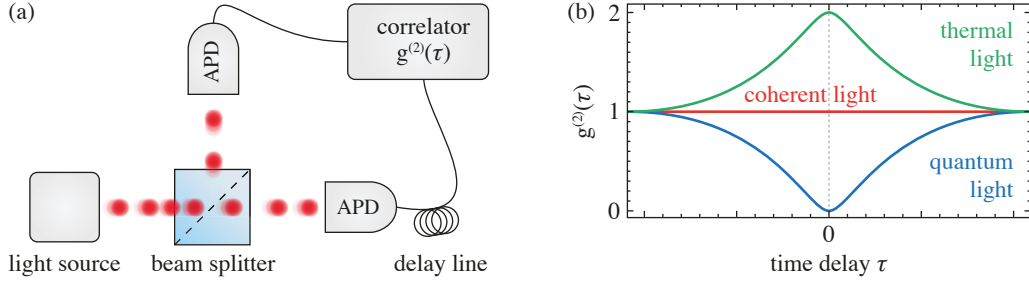


Fig. 1.4 (a) Hanbury Brown–Twiss experiment using two avalanche photodiodes (APDs) for the measurement of the second-order correlation function $g^{(2)}(\tau)$. (b) Characteristic behavior of the time-resolved second-order correlation function $g^{(2)}(\tau)$ for different states of light. The second-order correlation function reveals characteristic intensity fluctuations of the light source.

[313]. In the following, single photon emission has been observed from various solid state systems such as nitrogen vacancy centers in diamonds [182], single dye molecules [18] and semiconductor QDs [209]. In the last two decades, semiconductor QDs moved into the focus of the research on single-photon sources [41, 48, 91, 165, 210, 263, 282, 332], mainly because they can be easily integrated into optical micro-cavities [41, 194, 243]. See Refs. [25, 41, 210, 263, 283] for a review on QD-based single-photon sources.

1.2.1 Requirements

There are numerous applications which differ in their requirements on the quality of the photon source. This section gives an overview of some central requirements for practical single-photon emitters, see Refs. [41, 263] for details.

Single-photon purity. The statistical and coherence properties of the different states of the quantized electromagnetic field are described by correlation functions [276]. The most central requirement on a single-photon source is a low value of the second-order correlation function $g^{(2)}(0)$ that describes the intensity autocorrelation and ensures that the source indeed emits only single photons at one time (anti-bunching). A plot of the characteristic behavior of the second-order correlation function for different states of light is shown in Fig. 1.4 (b): A perfectly coherent laser light source shows randomly (Poissonian) distributed intensity fluctuations that are uncorrelated at all times $g^{(2)}(\tau) \equiv 1$. In contrast, thermal light sources have a tendency to emit photons in bunches $g^{(2)}(0) > 1$, while an ideal single-photon source shows the aforementioned anti-bunching phenomena reflected by $g^{(2)}(0) < 1$ (and $g^{(2)}(0) = 0$ in the ideal case). A measurement of the second-order correlation function can be carried out by photon counting experiments using a Hanbury Brown–Twiss setup [124] shown in Fig. 1.4 (a), where the radiation emitted by the source is separated by a 50/50 beam splitter and then collected by two photodetectors. This allows to reconstruct the second-order correlation function by recording a histogram of waiting times between two subsequent detection events [76]. In practice, a value of $g^{(2)}(0) < 0.5$ indicates the presence of the $n = 1$ single-photon Fock state [209].

Indistinguishability. Many applications require single-photon sources that emit indistinguishable photons, i.e., photons in exactly the same mode, having the same wavelength and polarization. Even though the spontaneous emission from an ideal, Fourier-transform limited and resonantly excited emitter yields perfectly indistinguishable photons, this indistinguishability can be lost as a consequence of dephasing and spectral diffusion [41,

263]. Both processes lead to a broadening of the line width due to fluctuations of the optical transition frequency and impact the properties of the photon wave packets. Dephasing arises due to collision events with a carrier or heat bath and leads to a gradual loss of coherence. For solid state systems at elevated temperature, the dephasing time is typically short in comparison to the radiative life time such that the line width is usually much broader than the Fourier limit. Wavelength fluctuations due to spectral diffusion is typically a slow process that arises in solid state systems due to Coulomb interaction of the emitter with charges trapped in nearby defects. The indistinguishability of two photons can be examined by a Hong–Ou–Mandel experiment, where two incoming, indistinguishable photons show a fully destructive interference at a beam splitter [76, 106, 303].

Efficiency. The efficiency quantifies the ratio of the emitted single-photons to the number of applied excitation triggers. The efficiency of a source is mainly determined by the spontaneous emission factor β_{sp} that describes the fraction of generated light coupled into a optical mode of interest. Moreover, non-radiative recombination processes (in particular in solid-state systems) can degrade the efficiency of the source. Finally, the photon extraction efficiency, i.e., the fraction of light transmitted from the device into the collection lens or an optical fiber, is an important figure of merit for efficient devices [16, 106, 155, 332].

Emission rate/brightness. The emission rate of a single-photon source is limited by the radiative life time of the emitter. By embedding the emitter into an optical resonator, the local density of photonic states in the vicinity of the emitter can be increased. This leads to an enhancement of the spontaneous emission rate which is known as Purcell effect. If off-resonant excitation schemes (in particular in electrically driven solid state systems) are employed, additional carrier relaxation times slow down the emission rate.

1.2.2 Applications

This section briefly describes some of the most important applications of single-photon sources. See Refs. [41, 263] for a detailed overview.

Quantum key distribution (QKD) denotes several methods (e.g., BB84, E91 protocol) which aim to provide common random numbers secretly to two remote parties by exploiting quantum mechanical effects [99]. These random numbers can be used as a secret key for classical cryptographic methods (e.g., a *one-time pad*), where encrypted messages are exchanged secretly via a public channel. The security of QKD is based on the quantum-mechanical observer effect and the no-cloning theorem. Any potential eavesdropper leaves a statistical imprint in the communication between the actual sender and receiver, which leads to the detection of the attack. Then the key is discarded and the QKD is restarted.

Quantum computers and **quantum simulators** employ quantum-mechanical phenomena, such as quantum superposition and entanglement, for information processing tasks [184]. The unit of quantum information manipulated in quantum computers is a *qubit*, which can be in a superposition of states. For certain problems, such as integer factorization [220] or the simulation of quantum many-body problems [7], large-scale quantum computers have the potential to outperform classical computers. Single photons are ideal candidates for qubits due to their ability to propagate over long distances, their low decoherence and the flexibility offered in information encoding (e.g., polarization or time bin) [41]. Universal logic gates (in particular the C-NOT gate) can be implemented using linear optics and photon counting [170]. The realization of optical quantum computers has high demands on the indistinguishability and the brightness of the photon source.

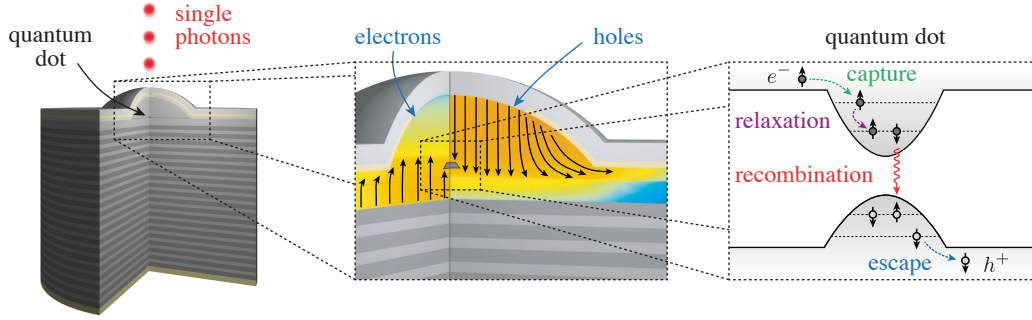


Fig. 1.5 Illustration of the multi-scale simulation approach subject to this thesis. The *hybrid quantum-classical modeling approach* combines charge transport theory in semiconductor devices with microscopic models from cavity quantum electrodynamics for the QD-photon system.

Quantum metrology aims at the development of highly sensitive measurement techniques by exploiting quantum mechanical effects. In conventional laser metrology based on coherent states, the relative uncertainty in phase and amplitude are roughly equal. By using single photons instead, which are squeezed states of light with a fixed photon number but indeterminate phase [276], the quantum mechanical uncertainties can be redistributed allowing, e.g., for a suppression of shot noise [41]. Moreover, squeezed state measurements can potentially be employed in gravitational wave detectors [276]. Furthermore, single-photon pump-probe measurements can be used for molecule spectroscopy [178, 247].

1.3 Device scale simulation of single-photon sources

The central element in the theoretical description of QD-based quantum light sources is the accurate modeling of the coupled emitter-photon system. This requires a fully quantized description of light, matter and their interaction which is given by cavity quantum electrodynamics. There is an extensive literature on model systems for QD-based light sources [48, 49, 54, 92, 95, 137, 181, 249] that deals with a microscopic description of quantum light sources and nanolasers. The fully quantum mechanical modeling approach enables a characterization of the quantum optical properties of the system (see figures of merit listed in Sec. 1.2.1) and thereby facilitates the exploration of interesting parameter and operation regimes.

In the microscopic modeling approach the influence of the environment of the quantum emitter is usually described by effective parameters, that drive certain excitation, decay and decoherence processes. For the investigation of the system's dynamics and the exploration of essential effects this is fully adequate and sufficient, however, the step towards quantum device technology for real-world applications requires a comprehensive consideration of the emitter's electrical and photonic environment. Hence, the theoretical description must be extended, on the one hand, towards the optical Maxwell equations that describe the optical resonator modes, Purcell enhancement and photon extraction efficiency, in order to optimize the geometrical shape and refractive index profile of the optical cavity [16, 106, 112]. On the other hand, for the development and optimization of electrically driven devices, the doping profile and the heterostructure design must be tailored to achieve an efficient carrier injection into the QD [156]. This can be investigated on the basis of modeling approaches from semi-classical semiconductor device physics, namely the van Roosbroeck system [255, 278]. Eventually, this leads to the question, how these different levels of description can

be combined to attain a comprehensive mathematical model for the physics of quantum optical devices on a broad range of technological relevant scales. Moreover, it raises the question how such a multi-scale model can be constructed without violating fundamental physical principles and conservation laws. The self-consistent coupling of microscopic, quantum-mechanical models for the QD-photon system with the van Roosbroeck system (see Fig. 1.5) is one of the central goals of this thesis.

In the last decades, the van Roosbroeck system has been applied successfully to the (multi-dimensional) simulation of a wide range of opto-electronic devices [237, 238] including light-emitting diodes (LEDs) and semiconductor lasers. The application of the van Roosbroeck system to QD-based quantum light sources, however, raises several new research issues – already without the consideration of the microscopic physics of the emitter-photon system. This fact arises from the “unconventional” operation conditions of current state-of-the-art quantum light emitters based on InGaAs-QDs, that are typically operated at cryogenic temperatures and very low injection currents. This regime is rarely explored in semi-classical carrier transport simulation and leads to novel design principles, that are different from those for LEDs and lasers. Finally, the extremely low operation temperature poses an enormous challenge for the realization of numerical carrier transport simulations that can no longer be performed using the standard routine.

1.4 Outline

This thesis is organized as follows:

Chapter 2 provides an introduction to the modeling of charge transport in semiconductor devices based on the van Roosbroeck system. Next to a brief survey on the underlying assumptions from basic solid state physics and semi-classical kinetics, it provides also a review on the essential thermodynamic properties of the van Roosbroeck system.

Chapter 3 gives an introduction to the finite volume Scharfetter–Gummel method for the multi-dimensional numerical simulation of the van Roosbroeck system. Several recent generalizations of the Scharfetter–Gummel method for the inclusion of Fermi–Dirac statistics are compared and assessed. Finally, it contains a description of a novel parameter-embedding approach for the numerical simulation at cryogenic temperatures.

In Chapter 4 the van Roosbroeck system is applied to investigate the experimentally observed excitation of parasitic QDs in a single-photon emitting diode. By means of simulations of the current flow, the phenomenon is traced back to inherent properties of the device design. Finally, a revised design with superior performance is suggested.

Chapter 5 deals with the coupling of the van Roosbroeck system to microscopic models for the QD-photon system. Based on the Lindblad master equation, a hybrid quantum-classical model system is introduced, that allows for the self-consistent description of carrier transport and quantum dynamics out of one box. The model equations are investigated in detail and are shown to obey fundamental principles of non-equilibrium thermodynamics.

Chapter 6 provides a *proof-of-principle* application of the hybrid modeling approach introduced in the preceding chapter. The model equations are applied to the numerical simulation of an electrically driven single-photon source, that is investigated in the stationary and pulsed excitation regime.

Chapter 7 summarizes the central results of this thesis and provides an outlook on future research directions.

Chapter 2

Semi-classical charge transport in semiconductor devices

This chapter gives an introduction to the semi-classical modeling of charge transport in semiconductor devices based on the van Roosbroeck system. The model equations are explained in detail in Sec. 2.1, including a survey on boundary conditions, recombination rate models, carrier and current density expressions. The focus of this thesis is on the modeling of charge transport in quantum optical devices, that are typically operated at extremely low temperatures. Therefore, a particular focus is put on the thorough inclusion of degeneration effects due to Fermi–Dirac statistics in all relevant parts of the model system – ranging from nonlinear diffusion to boundary conditions and a generalized structure of the standard recombination rate models, that goes beyond the usual textbook presentations. Sec. 2.2 reviews the underlying approximations of the van Roosbroeck system by outlining its derivation from the semi-classical Boltzmann transport equation. Sec. 2.3 provides a detailed discussion of the van Roosbroeck system from the viewpoint of non-equilibrium thermodynamics. The consistency with fundamental laws of non-equilibrium thermodynamics is regarded as a major principle for the construction of a hybrid quantum-classical model system in a later chapter.

2.1 The van Roosbroeck system

In 1950 W. W. van Roosbroeck introduced a system of coupled, nonlinear partial differential equations that describes the charge transport in semiconductor devices on a macroscopic level [255]. Since then, the *van Roosbroeck system* has become the standard model for multi-dimensional semiconductor device simulation and has been applied to a vast range of devices – from solar cells [9, 222], photodetectors [85, 138], transistors [125, 311], organic semiconductor devices [169] and light-emitting diodes [161] to semiconductor lasers [13, 111, 236] and single-photon sources [156].

The van Roosbroeck system represents the simplest model system in a hierarchy of semi-classical transport models, which can be derived from the semi-classical Poisson–Boltzmann system [104, 135, 143, 152, 299]. In the last decades, it has been studied by electrical engineers, physicists and mathematicians and became subject to several textbooks [204, 278]. The striking feature of the van Roosbroeck system is its relative simplicity (in

comparison to kinetic and higher order hydrodynamic models), which allows for a rigorous mathematical analysis [78, 82, 145, 218] and for the development of specialized, robust and efficient numerical methods [115, 268]. This enables the simulation of stationary and transient charge transport processes in fairly complex, multi-dimensional device geometries, which is hardly achieved by other transport models. Today, the van Roosbroeck system is well-established and used in many semiconductor device simulation packages [8, 59, 83, 90, 286, 301, 329].

The van Roosbroeck system reads

$$-\nabla \cdot \varepsilon \nabla \phi = q(p - n + C), \quad (2.1a)$$

$$\partial_t n - \frac{1}{q} \nabla \cdot \mathbf{j}_n = -R, \quad (2.1b)$$

$$\partial_t p + \frac{1}{q} \nabla \cdot \mathbf{j}_p = -R, \quad (2.1c)$$

where Poisson's Eq. (2.1a) describes the electrostatic field generated by a spatio-temporally varying (net-)charge density and the continuity Eqs. (2.1b)–(2.1c) model the transport and recombination dynamics of electrons and holes.

2.1.1 Poisson's equation

The net-charge density $\varrho = q(p - n + C)$ on the right hand side of Poisson's Eq. (2.1a) comprises the volume densities of (conduction band) electrons n , (valence band) holes p and the doping density profile

$$C = N_D^+ - N_A^-. \quad (2.2)$$

Here, N_D^+ and N_A^- are the density of singly ionized donors and acceptors, respectively. The elementary charge is denoted by q . The absolute dielectric permittivity is given as $\varepsilon = \varepsilon_0 \varepsilon_r$, where ε_0 is the vacuum permittivity and ε_r is the relative permittivity of the semiconductor material in the low-frequency limit. In the *quasi-static approximation*¹ the electric field $\mathbf{E} = -\nabla \phi$ is given as the gradient of the scalar electrostatic potential ϕ (transverse field components are neglected). The electric displacement field reads $\mathbf{D} = \varepsilon \mathbf{E}$.

2.1.2 Charge carrier density

The volume charge carrier densities are computed from

$$n = \int_{\mathbb{R}} dE D_c(E) f\left(\frac{E - q\phi - \mu_c}{k_B T}\right), \quad (2.3a)$$

$$p = \int_{\mathbb{R}} dE D_v(E) \left(1 - f\left(\frac{E - q\phi - \mu_v}{k_B T}\right)\right), \quad (2.3b)$$

where $D_c(E)$ and $D_v(E)$ is the density of electronic states in the conduction and valence band, respectively. The (bare) single-carrier energy levels E in Eq. (2.3) are shifted by the potential energy $-q\phi$ to account for the self-consistent electrostatic interaction of the charges. The single-particle distribution function $f \in [0, 1]$ describes the occupation

¹ The *quasi-static approximation* simplifies the expression for the electric field $\mathbf{E} = -\nabla \phi - \partial_t \mathbf{A} \approx -\nabla \phi$, which is typically amply fulfilled under the assumption of slowly (in comparison to the internal time scales) changing external fields (e.g., voltage pulses). This becomes even better as the length scale of the device decreases [259, 323]. In linear dielectric media Poisson's equation (2.1a) for the scalar potential ϕ can be decoupled from the vector potential \mathbf{A} via the *generalized* Coulomb gauge $\nabla \cdot (\varepsilon \mathbf{A}) = 0$ [313].

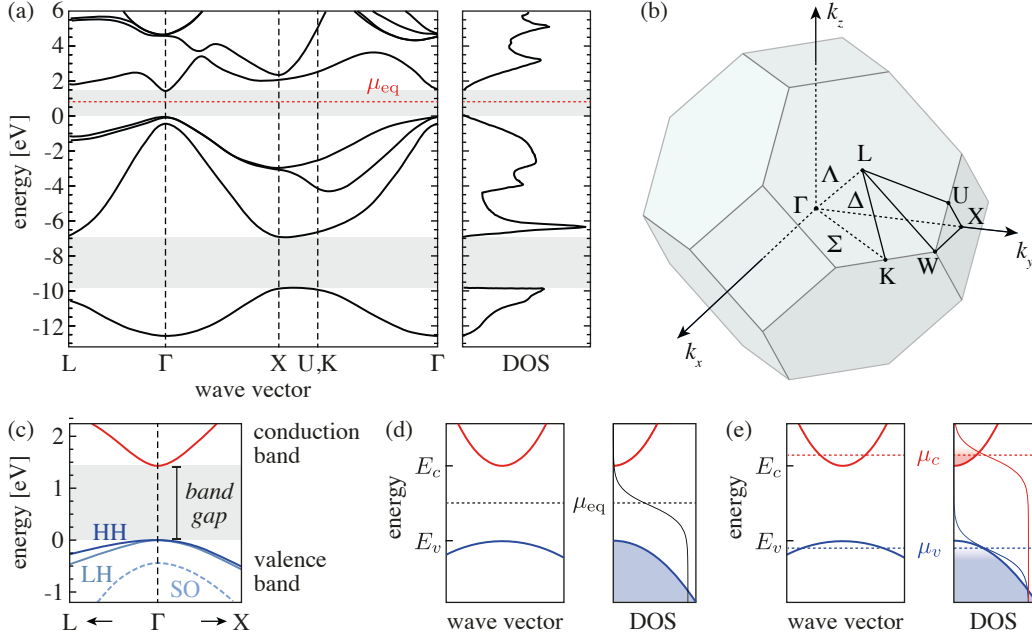


Fig. 2.1 (a) Energy band structure (reduced zone scheme) and electronic density of states (DOS) of zinc blende GaAs at 300 K (data taken from Ref. [47]). The high-symmetry points of the Brillouin zone are labeled by L , Γ , X , U and K . (b) Brillouin zone and high-symmetry points of a face-centered cubic crystal, e.g., zinc blende GaAs (based on [320]). (c) Zoom on the band structure of GaAs in the vicinity of the Γ -point, where the energy bands are approximately parabolic. The valence band is degenerate at the Γ -point, where the heavy hole (HH) and the light hole (LH) bands have the same energy level. The split-off bands (SO) are energetically close to the band edge. (d) Simplified two-band scheme with a conduction band and a single, effective valence band. If the equilibrium chemical potential μ_{eq} (Fermi level) is located within the band gap, the valence band is almost fully occupied and nearly no electron exists in the conduction band. (e) Non-equilibrium configuration with separated quasi-Fermi levels $\mu_c \gg \mu_v$, that leads to the excitation of electrons to the conduction band, leaving holes in the valence band behind.

probability of the electronic states at a certain energy. Since holes are missing electrons in the valence band, the corresponding occupation probability in Eq. (2.3b) is stated as $(1 - f)$. Under *quasi-equilibrium conditions* [50, 264], the occupation probability can be approximated by the Fermi function

$$f(x) = \frac{1}{e^x + 1}, \quad (2.4)$$

which describes the occupation probability of electronic states in an ideal Fermi gas as a function of the quasi-Fermi energies (or *chemical potentials*) μ_c and μ_v of the carrier ensembles in the two bands. The quasi-equilibrium approximation assumes an infinitely fast thermalization of the carrier ensembles due to various scattering processes (carrier-carrier scattering, carrier-phonon scattering etc.) and describes the time evolution on a coarse grained time-scale. In the thermodynamic equilibrium, the chemical potentials of both bands approach a common, globally constant equilibrium value μ_{eq} .

The energy band structure of GaAs, which is one of the most important materials in semiconductor opto-electronics, is shown in Fig. 2.1 (a). The transport and recombination

properties of semiconductors are essentially determined by scattering processes of carriers close to the band edge. Therefore, the description is reduced to the vicinity of the band minima (conduction band) or maxima (valence band²), respectively, where the energy dispersion curves are approximately parabolic

$$\varepsilon_c(\mathbf{k}) = E_c + \frac{\hbar^2 \|\mathbf{k}\|^2}{2m_c^*}, \quad \varepsilon_v(\mathbf{k}) = E_v + \frac{\hbar^2 \|\mathbf{k}\|^2}{2m_v^*}. \quad (2.5)$$

In GaAs, this reduces the description to the vicinity of the Γ -point, see Fig. 2.1 (a, c–e). In Eq. (2.5), E_c is the conduction band edge, E_v is the valence band edge and

$$\left(\frac{1}{m_\lambda^*} \right)_{i,j} = \frac{1}{\hbar^2} \left. \frac{\partial^2 \varepsilon_\lambda(\mathbf{k})}{\partial k_i \partial k_j} \right|_{\mathbf{k}_0}, \quad \lambda \in \{c, v\},$$

is the *effective mass tensor* [166] that describes the curvature of the energy band at a high-symmetry point \mathbf{k}_0 (e.g., the Γ -point $\mathbf{k}_0 = (0, 0, 0)^T$). If the tensor is diagonal and isotropic, it can be reduced to a scalar effective mass such that the energy dispersion relation close to the band edges formally matches the dispersion relation of free electrons in vacuum. This allows for a very simple interpretation, as the motion of near band edge electrons in solids is virtually identical to the motion of free electrons with a modified mass $m_{c/v}^*$, that reflects the influence of the crystal ions and core electrons.³ Within the effective mass approximation [166], the density of electronic states in isotropic bulk semiconductors with parabolic energy dispersion is obtained as [166]

$$D_c(E) = \frac{1}{2\pi^2} \left(\frac{2m_e^*}{\hbar^2} \right)^{3/2} \sqrt{E - E_c} \Theta(E - E_c),$$

$$D_v(E) = \frac{1}{2\pi^2} \left(\frac{2m_h^*}{\hbar^2} \right)^{3/2} \sqrt{E_v - E} \Theta(E_v - E),$$

where Θ is the Heaviside step function and $m_e^* = m_c^*$ and $m_h^* = -m_v^*$ are the effective electron and hole masses, respectively. Hence, the carrier densities are expressed as

$$n = N_c F_{1/2} \left(\frac{\mu_c - E_c + q\phi}{k_B T} \right), \quad (2.6a)$$

$$p = N_v F_{1/2} \left(\frac{E_v - q\phi - \mu_v}{k_B T} \right), \quad (2.6b)$$

with the *effective density of states* (cubed inverse thermal wavelength of the carriers)

$$N_c = 2 \left(\frac{m_e^* k_B T}{2\pi \hbar^2} \right)^{3/2}, \quad N_v = 2 \left(\frac{m_h^* k_B T}{2\pi \hbar^2} \right)^{3/2}, \quad (2.7)$$

and the Fermi–Dirac integral [32]

$$F_\nu(\eta) = \frac{1}{\Gamma(\nu + 1)} \int_0^\infty d\xi \frac{\xi^\nu}{e^{\xi - \eta} + 1}. \quad (2.8)$$

² The valence band throughout this section is an *effective valence band* that summarizes – depending on the material system – heavy holes, light holes and split-off holes in a suitable fashion. See Ref. [166] for a detailed introduction to the energy band structures of semiconductors.

³ Note that the effective mass of valence band electrons is typically negative.

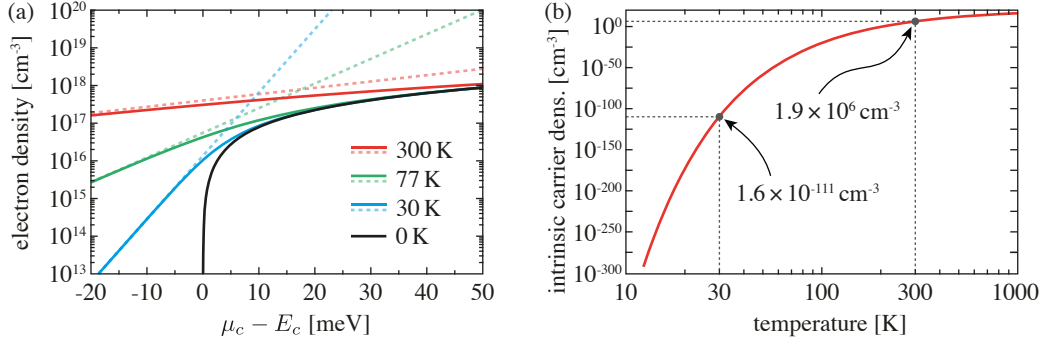


Fig. 2.2 (a) Electron density in GaAs vs. quasi-Fermi energy at different temperatures. The solid lines for Fermi–Dirac statistics are obtained from Eq. (2.6a), the dashed lines show the Maxwell–Boltzmann approximation $F_{1/2}(\eta) \approx \exp(\eta)$. (b) Temperature-dependence of the intrinsic carrier density (2.9) in GaAs. The temperature dependent parameters are taken from Ref. [232]. © 2016 Springer Science+Business Media. Reprinted, with permission, from Ref. [158].

If the chemical potential is far below the conduction band edge energy $\mu_c \ll E_c - q\phi$ (or vice versa $\mu_v \gg E_v - q\phi$ in the case of holes), the carrier density is low and degeneration effects due to Pauli blocking are negligible. In this case, the Fermi–Dirac integral is well approximated by an exponential $F_\nu(\eta) \xrightarrow{\eta \rightarrow -\infty} \exp(\eta)$, such that the carrier density expressions (2.6) recover the result of the classical ideal gas theory involving the Maxwell–Boltzmann velocity distribution [189]. In the following, this limit will be denoted as the *non-degenerate limit*. Fig. 2.2 (a) shows the electron density in GaAs as a function of the chemical potential for different temperatures according to Eq. (2.6a). Moreover, the electron density obtained using Maxwell–Boltzmann statistics is shown for comparison as a dashed line. At room temperature ($T = 300$ K) the impact of Fermi–Dirac statistics becomes significant only at high carrier densities. However, in the low temperature regime the Maxwell–Boltzmann approximation leads to a drastic overestimation of carrier densities as soon as the Fermi energy exceeds the band edge energy. This overestimation of the carrier density is critical, as it affects all density-dependent quantities such as the current densities (see Sec. 2.1.3) and recombination rates (see Sec. 2.1.4). Moreover, Fig. 2.2 (a) shows that the carrier density becomes highly sensitive to small changes of the Fermi level at low temperatures. The fully degenerate limit is reached at $T = 0$ K, where the Fermi distribution function (2.4) approaches a step function such that the exponential low density tail vanishes to identical zero. This leads to full depletion wherever the Fermi energy drops below the band edge and gives rise to extremely sharp internal layers between doped and intrinsic layers. In the $T = 0$ K case, the carrier density is given by Sommerfeld’s expansion [166] and the bijective relation between carrier density and chemical potential is lost. The mathematical analysis of the van Roosbroeck system with fully degenerate carrier statistics has been carried out in Refs. [150, 151]. The Maxwell–Boltzmann limit can be used to obtain a simple approximation of the intrinsic carrier density

$$n_{\text{intr}}(T) \approx \sqrt{N_c(T) N_v(T)} e^{-\frac{E_g(T)}{2k_B T}}, \quad (2.9)$$

which follows from the charge neutrality condition $n_{\text{intr}} = n_{\text{eq}} = p_{\text{eq}}$ (in the absence of ionized impurities). The intrinsic carrier density is a measure of the intrinsic conductivity of semiconductors and strongly depends on the temperature and the band gap. Fig. 2.2 (b) shows the freeze out of the intrinsic carrier density in GaAs at cryogenic temperatures.

2.1.3 Current density

Following the theory of linear irreversible thermodynamics [108, 228], the charge current densities are driven by the gradients of the chemical potentials of the respective bands

$$\mathbf{j}_n = \frac{1}{q} \sigma_n \nabla \mu_c, \quad (2.10a)$$

$$\mathbf{j}_p = \frac{1}{q} \sigma_p \nabla \mu_v, \quad (2.10b)$$

where the electrical conductivities $\sigma_n = qM_n n$ and $\sigma_p = qM_p p$ are elements of the Onsager matrix [228]. In the thermodynamic equilibrium the chemical potentials approach a global constant such that the vanishing gradients in Eq. (2.10) lead to zero currents. This reflects the detailed balance principle due to the microscopic reversibility in the thermodynamic equilibrium [189], where the number of carriers traveling in opposite directions is the same such that the net current flow is zero.

The carrier mobilities $M_{n/p}$ relate the drift velocity of the carriers with the applied electric field and are material specific functions that depend in general strongly on the temperature and the ionized impurity density. As a rule of thumb, at room temperature and low doping concentrations the mobilities are almost constant and primarily limited by phonon scattering processes, whereas at higher doping concentrations the scattering at ionized impurities (in particular dopants) leads to a significant decrease of the mobility [311]. For a more detailed consideration also intraband scattering at interfaces, deformation potential interaction, piezoelectric interaction, scattering at alloy imperfections and velocity saturation at high electric fields must be taken into account [135, 143]. The total mobility results from the combination of all intraband scattering effects and is obtained by *Matthiessen's rule* [143]. For quantitative charge transport simulations in the framework of the van Roosbroeck system one resorts to empirical material-specific mobility models, which can be obtained either from kinetic Monte Carlo simulations of the semi-classical Boltzmann transport equation [135, 143] or from experimental measurements [188, 217, 232, 278]. The mobility of conduction band electrons in GaAs according to the empirical model given in Ref. [217] is shown in Fig. 2.3 (a).

By inverting the state equations (2.6), the current densities (2.10) can be written in the drift-diffusion form

$$\mathbf{j}_n = -qM_n n \nabla \phi + qD_n(n) \nabla n, \quad (2.11a)$$

$$\mathbf{j}_p = -qM_p p \nabla \phi - qD_p(p) \nabla p, \quad (2.11b)$$

where the diffusion coefficients $D_{n/p}$ are connected with the mobilities $M_{n/p}$ via the *generalized Einstein relation* for degenerate Fermi gases [185]

$$D_n(n) = \frac{M_n k_B T}{q} g\left(\frac{n}{N_c}\right), \quad D_p(p) = \frac{M_p k_B T}{q} g\left(\frac{p}{N_v}\right). \quad (2.12)$$

The Einstein relation is a manifestation of the fluctuation-dissipation theorem from linear response theory in statistical physics [180]. As a consequence of the Pauli exclusion principle in Fermi gases, the usual Einstein relation obtained from classical ideal gas theory is modified by the density dependent *degeneration factor* (see Fig. 2.3 (c))

$$g(x) = x(F_{1/2}^{-1})'(x) = \frac{x}{F_{-1/2}(F_{1/2}^{-1}(x))}, \quad (2.13)$$

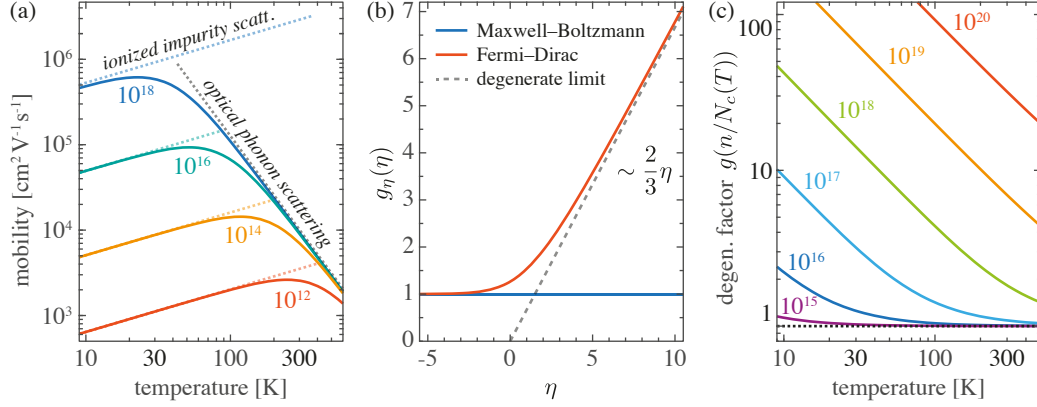


Fig. 2.3 (a) Electron mobility in GaAs vs. temperature for different ionized impurity densities (in cm^{-3}) according to the empirical model given in Ref. [217]. At low temperatures the carrier mobility is limited by the scattering of electrons with ionized impurities whereas at high temperatures the polar optical phonon scattering (Fröhlich coupling [264]) is the limiting factor [143]. (b) Plot of the degeneration factor $g_\eta(\eta)$ given in Eq. (2.14) vs. the argument η of the Fermi-Dirac integral (dimensionless relative chemical potential). In the non-degenerate limit $\eta \rightarrow -\infty$ the degeneration factor approaches the Maxwell-Boltzmann limit $g_\eta^{\text{MB}} \equiv 1$ while in the degenerate limit $\eta \gg 1$ the degeneration factor grows linearly with η . (c) Plot of the degeneration factor (2.13) of conduction band electrons in GaAs vs. temperature for different electron densities (in cm^{-3}). At cryogenic temperatures the degeneration is already significant at comparably low electron densities.

where the property $F'_\nu(x) = F_{\nu-1}(x)$ [32] of the derivatives of the Fermi-Dirac integral has been used. Since $g(x) > 1$, this implies an *enhancement* of the diffusion current density with respect to the non-degenerate case [206]. This can be understood from the higher energy per particle in the case of Fermi-Dirac statistics in comparison to the classical ideal gas (with the same number of particles) that leads to an increased thermal velocity. In the non-degenerate limit, where the Fermi-Dirac integral reduces to an exponential, one recovers the usual Einstein relation for linear diffusion (i.e., the degeneration factor reduces to exactly $g \equiv 1$). A particularly useful representation of the degeneration factor, which is plotted in Fig. 2.3 (b), is obtained by substituting $x = F_{1/2}(\eta)$

$$g_\eta(\eta) = g(F_{1/2}(\eta)) = \frac{F_{1/2}(\eta)}{F_{-1/2}(\eta)}. \quad (2.14)$$

2.1.4 Carrier recombination and generation

Interband scattering processes that lead to the relaxation of a conduction band electron to the valence band, where it neutralizes a hole, are called *recombination* processes. The opposite event, where an electron-hole pair is created by the excitation of a valence band electron to the conduction band is a *generation* process. The continuity Eqs. (2.1b)–(2.1c) account for the generation and recombination of carriers via the volume net-recombination rate R , which is the difference of the recombination and generation rate per volume. The modeling of the generation-recombination dynamics plays a crucial role in semiconductor transport simulation, as the recombination rate imposes a significant contribution to the electrical resistivity and contributes to current guiding. In opto-electronic devices, the radiative recombination rate and the quantum efficiency are of central interest.

In the framework of the van Roosbroeck system, where the carriers are described by thermalized quasi-equilibrium distribution functions in a two-band semiconductor, the volume net-recombination rate R can be written in the form [69]

$$R = r(\mu_c, \mu_v, \phi) (1 - e^{-\beta(\mu_c - \mu_v)}), \quad r(\mu_c, \mu_v, \phi) \geq 0, \quad (2.15)$$

where $r(\mu_c, \mu_v, \phi) = \sum_{\alpha} r_{\alpha}(\mu_c, \mu_v, \phi)$ is the total recombination rate that results from a variety of radiative and non-radiative scattering processes labeled by α . Some of the most important recombination processes will be described below. The corresponding generation rate $r(\mu_c, \mu_v, \phi) e^{-\beta(\mu_c - \mu_v)}$ is either suppressed ($V_F > 0$, forward bias) or enhanced ($V_F < 0$, reverse bias) by the Fermi voltage $V_F = (\mu_c - \mu_v)/q$. In the thermodynamic equilibrium the net-recombination rate vanishes exactly due to $(\mu_c - \mu_v)|_{\text{eq}} \equiv 0$. It shall be noted that Eq. (2.15) deviates from the formula

$$R_{\text{MB}} = \tilde{r}(n, p) (np - n_{\text{intr}}^2) \quad (2.16)$$

given in the standard literature on the topic [51, 204, 278], where the recombination rate is driven by the difference between the product np and the squared intrinsic carrier density (2.9). It is easy to see that R_{MB} is only accurate in the case of Maxwell–Boltzmann statistics, which is the only case where the product of the equilibrium carrier densities equals n_{intr}^2 in the sense of Eq. (2.9). For Fermi–Dirac statistics (regardless of the density of states), the form (2.16) violates the detailed balance principle and results in non-zero recombination rates in the thermodynamic equilibrium. Even though the usage of Eq. (2.16) instead of Eq. (2.15) imposes typically only a small error in the numerical evaluation, the form (2.15) guarantees important structural properties such as the non-negativity of the entropy production rate and the consistency with the thermodynamic equilibrium (see Sec. 2.3). A detailed motivation of the form (2.15) is given in Appx. A.2.

Shockley–Read–Hall recombination

Trap-assisted recombination, where a conduction band electron relaxes first to a deep trap state within the band gap before recombining with a valence band hole (see Fig. 2.4 (a)), was studied first in Refs. [121, 284]. Deep traps are localized states that result from impurities and structural defect centers in the crystal lattice. The carrier relaxation happens via phonon emission, which leads to heating of the material. Shockley–Read–Hall (SRH) processes are the dominant recombination channel in indirect band gap materials (e.g., silicon) and can be of leading order in direct band gap semiconductors at low carrier densities. Based on kinetic models for the occupation of trap states [103], one obtains under stationary conditions the Shockley–Read–Hall recombination rate

$$R_{\text{SRH}} = \frac{np}{\tau_p(n + n_d) + \tau_n(p + p_d)} (1 - e^{-\beta(\mu_c - \mu_v)}), \quad (2.17)$$

with $n_d = N_c e^{\beta(E_T - q\phi - \mu_c)}$ and $p_d = N_v e^{-\beta(E_T - q\phi - \mu_v)}$. The carrier life times $\tau_{n/p}$ strongly depend on the material quality (density of impurities and defects) and the position of the trap level E_T . The dependency of the carrier life times on the impurity density can be modeled by the so-called Scharfetter relation [63, 232], the field and temperature dependence can be included according to Ref. [269]. For similar carrier life times, SRH recombination is most efficient for trap states located in the center of the band gap.

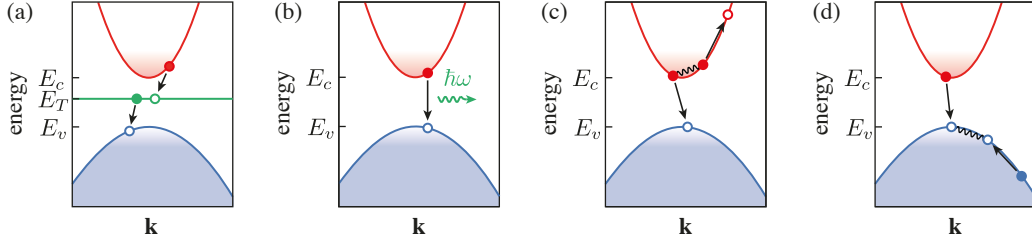


Fig. 2.4 Recombination processes considered in the van Roosbroeck system: (a) Shockley–Read–Hall recombination via phonon assisted scattering to an intermediate trap state at energy E_T within the band gap, (b) direct band-to-band transition via spontaneous emission of a photon and (c) Auger recombination assisted by electron–electron scattering or (d) hole–hole scattering. Electrons are illustrated as filled dots, whereas holes are shown as empty dots.

Direct recombination

In direct band gap semiconductors, the direct band-to-band transition is typically a radiative recombination process that leads to the spontaneous emission of a photon (see Fig. 2.4 (b)). In indirect band gap materials it can, however, be phonon-assisted. The radiative recombination rate is of particular importance in opto-electronic devices such as light-emitting diodes. The opposite process – electron-hole pair generation via photon absorption – is the key process in solar cells and photodetectors. Because of the small momentum of the photon in comparison to the carrier’s momentum, the transition is a vertical transition in the energy-momentum diagram, cf. Fig. 2.4 (b), such that it is favored in direct band gap semiconductors. In a simple approximation, the direct band-to-band recombination rate is proportional to the electron and hole carrier density

$$R_{\text{dir}} = Bnp(1 - e^{-\beta(\mu_c - \mu_v)}). \quad (2.18)$$

The *bimolecular recombination coefficient* B depends on the interband joint density of states, the refractive index of the material, the absorption coefficient and the temperature. For simple parabolic two-band models it can be estimated either from the van Roosbroeck–Shockley model [256], Hall’s method [122] or from advanced luminescence calculations involving the microscopically computed energy band structure [51, 289].

Auger recombination

Scattering processes, in which a conduction band electron recombines with a valence band hole while transferring the transition energy to another electron or hole, are denoted as Auger recombination. Since Auger recombination relies on the interaction between three particles, it becomes increasingly important at high non-equilibrium carrier densities. In the framework of the van Roosbroeck system, the recombination rate is written as

$$R_{\text{Au}} = (C_{\text{Au}}^n n + C_{\text{Au}}^p p) np(1 - e^{-\beta(\mu_c - \mu_v)}), \quad (2.19)$$

where the material specific coefficients $C_{\text{Au}}^{n/p}$ describe the efficiency of electron or hole assisted recombination events, respectively. The coefficients show a weak temperature dependence and decrease with increasing band gap [232, 279]. An accurate treatment of Auger recombination requires a detailed consideration of the energy band structure (in particular the valence band structure) and can be found, e.g., in Refs. [20, 128, 250].

Further recombination processes

The van Roosbroeck system can be extended by further recombination-generation processes, depending on the device of interest. This includes, e.g., stimulated emission [13, 111, 175], impact ionization [138], surface recombination [232, 278] and interband tunneling [139, 261, 270]. As these processes are beyond the scope of this thesis, a detailed description is omitted here. The form (2.15) is sometimes used for the modeling of capture and escape processes of bulk carriers to quantum wells [62], where the quantum well carriers are described as thermalized ensembles with Fermi-like distribution functions.

2.1.5 Boundary conditions

The van Roosbroeck system (2.1) must be supplemented with boundary conditions that model the electric contacts (semiconductor-metal interfaces) attached to the device, semiconductor-insulator interfaces or artificial boundary conditions. Throughout this thesis only Dirichlet and Neumann boundary conditions are considered, such that the boundary of the computational domain $\Omega \subset \mathbb{R}^d$, $d \in \{1, 2, 3\}$, takes the form

$$\partial\Omega = \Gamma_D \cup \Gamma_N.$$

Here, $\Gamma_D = \bigcup_i \Gamma_{D,i}$ denotes the boundary segments on which Dirichlet boundary conditions are enforced and Γ_N labels the segments with Neumann conditions. Boundary conditions for Schottky, gate and current-controlled contacts or semiconductor-insulator junctions are beyond the scope of this thesis and can be found in Refs. [224, 232, 275, 278].

2.1.5.1 (Ideal) ohmic contacts

Ideal ohmic contacts are semiconductor-metal interfaces with a vanishing space charge region at the junction, such that there is no contact resistance. This requires a vanishing Schottky barrier at the interface, which is approximately achieved in many technologically relevant semiconductors (except, e.g., wide band gap materials) at high doping concentrations close to the contact [110, 302]. The boundary conditions for the ideal ohmic contact posed on $\Gamma_{D,i}$ neglect the microscopic details of material fluctuations, thermionic emission and tunneling processes and simply enforce the local charge neutrality at the junction via

$$(p - n + C)|_{\Gamma_{D,i}} = 0. \quad (2.20)$$

In the thermodynamic equilibrium, this gives rise to a *built-in potential* ϕ_{eq} that solves

$$N_v F_{1/2} \left(\frac{E_v - q\phi_{\text{eq}} - \mu_{\text{eq}}}{k_B T} \right) - N_c F_{1/2} \left(\frac{\mu_{\text{eq}} - E_c + q\phi_{\text{eq}}}{k_B T} \right) + C = 0$$

on the corresponding boundary segments $\Gamma_{D,i}$. In the case of Maxwell–Boltzmann statistics an analytical solution of Eq. (2.20) is found as

$$\phi_{\text{eq}}^{\text{MB}} = -\frac{\mu_{\text{eq}}}{q} + \frac{E_v + E_c}{2q} + \frac{k_B T}{2q} \log \left(\frac{N_v}{N_c} \right) + \frac{k_B T}{q} \operatorname{arsinh} \left(\frac{C}{2n_{\text{intr}}} \right),$$

whereas in the Fermi–Dirac case it must be obtained numerically. Due to the strict monotonicity of the Fermi–Dirac integral, the solution always exists and is unique.

By applying an external voltage to the electric contacts, the semiconductor device is driven out of equilibrium. For the ohmic boundary conditions, this is modeled by enforcing

(non-equilibrium) Dirichlet boundary values on $\Gamma_{D,i}$

$$\phi = \phi_{\text{eq}} + U_i^{\text{appl}}, \quad (2.21\text{a})$$

$$\mu_c = \mu_{\text{eq}} - qU_i^{\text{appl}}, \quad (2.21\text{b})$$

$$\mu_v = \mu_{\text{eq}} - qU_i^{\text{appl}}, \quad (2.21\text{c})$$

where U_i^{appl} is the electric potential applied to the i -th ohmic contact. Note that the Dirichlet boundary conditions (2.21) preserve the local charge neutrality condition (2.20) at the contact. The chemical potentials of the conduction and the valence band are both in equilibrium with the chemical potential of the adjacent metal $\mu_{\text{Metal}} = \mu_{\text{eq}} - qU_i^{\text{appl}}$, which guarantees by Eq. (2.15) a vanishing net-recombination rate at the ohmic contacts.

2.1.5.2 Artificial boundaries

Due to limited computational resources, the computational domain in semiconductor device simulation must be restricted to a small subdomain of the real device structure, which must however be large enough to describe the essential effects of the particular problem at hand [204, 275, 278]. This leads to the specification of so-called *artificial boundaries*, which are no physical boundaries, but are intended to guarantee that the domain under consideration is self contained. Artificial boundaries prohibit any flux across the boundary and are modeled by homogeneous Neumann conditions on Γ_N

$$\mathbf{n} \cdot \nabla \phi = 0, \quad (2.22\text{a})$$

$$\mathbf{n} \cdot \mathbf{j}_n = 0, \quad (2.22\text{b})$$

$$\mathbf{n} \cdot \mathbf{j}_p = 0, \quad (2.22\text{c})$$

where \mathbf{n} is the outward-oriented normal vector on the boundary.

2.2 Derivation from the semi-classical Boltzmann transport equation

The continuity equations (2.1b)–(2.1c) and the current density expressions (2.10) of the van Roosbroeck system can be derived from the semi-classical Boltzmann transport equation by the *method of moments* [135, 143]. The Boltzmann transport equation

$$\left(\frac{\partial}{\partial t} + \frac{d\mathbf{r}}{dt} \cdot \nabla_{\mathbf{r}} + \frac{d\mathbf{k}}{dt} \cdot \nabla_{\mathbf{k}} \right) f(\mathbf{r}, \mathbf{k}, t) = \mathcal{C}[f], \quad (2.23)$$

describes the evolution of a classical single-particle probability distribution function $f(\mathbf{r}, \mathbf{k}, t)$ in a 6-dimensional phase space. The Liouvillian on the left hand side models the evolution according to a Poisson bracket involving Hamilton's equations of motion

$$\frac{d\mathbf{r}}{dt} = +\frac{1}{\hbar} \nabla_{\mathbf{k}} H, \quad \frac{d\mathbf{k}}{dt} = -\frac{1}{\hbar} \nabla_{\mathbf{r}} H.$$

The Boltzmann equation can be obtained from the Liouville equation for a classical many-body problem by truncating the BBGKY hierarchy⁴ at the single-particle level

⁴ The Bogolyubov–Born–Green–Kirkwood–Yvon (BBGKY) hierarchy is a coupled chain of equations equivalent to the Liouville equation of classical statistical mechanics.

[189]. The collision operator $\mathcal{C}[f]$ involves two-particle distribution functions, which need to be approximated in an appropriate way by single-particle functions. Based on the *molecular chaos hypothesis* [189], the collision integral can be approximated as a nonlinear functional of single-particle functions such that a closed equation for f is obtained. The collision integral leads to a dissipative evolution of f and allows, according to Boltzmann's H-theorem [189], to recover the second law of thermodynamics on a microscopic level.

The drift-diffusion system can be derived from the Boltzmann transport equation for a two-band semiconductor with parabolic energy dispersion. With the Hamilton function of the conduction band electrons $H(\mathbf{r}, \mathbf{k}) = E_c + \frac{\hbar^2 \mathbf{k}^2}{2m_e^*} - q\phi(\mathbf{r}, t)$ and the Lorentz force (in the quasi-static limit) $\mathbf{F} = -\nabla_{\mathbf{r}} H = q\nabla_{\mathbf{r}} \phi(\mathbf{r}, t) = -q\mathbf{E}(\mathbf{r}, t)$, the evolution of the conduction band electron distribution function $f_c(\mathbf{r}, \mathbf{k}, t)$ is given by

$$\left(\frac{\partial}{\partial t} + \frac{\hbar \mathbf{k}}{m_e^*} \cdot \nabla_{\mathbf{r}} + \frac{1}{\hbar} \mathbf{F} \cdot \nabla_{\mathbf{k}} \right) f_c(\mathbf{r}, \mathbf{k}, t) = \mathcal{C}_c[f_c, f_v]. \quad (2.24)$$

The collision integral accounts for intra- ($\lambda = c$) and interband ($\lambda = v$) scattering processes

$$\begin{aligned} \mathcal{C}_c[f_c, f_v] = \sum_{\lambda=\{c,v\}} \frac{V}{(2\pi)^3} \int d^3k' (S_{\lambda \rightarrow c}(\mathbf{k}', \mathbf{k}) f_{\lambda}(\mathbf{r}, \mathbf{k}', t) (1 - f_c(\mathbf{r}, \mathbf{k}, t)) - \\ - S_{c \rightarrow \lambda}(\mathbf{k}, \mathbf{k}') f_c(\mathbf{r}, \mathbf{k}, t) (1 - f_{\lambda}(\mathbf{r}, \mathbf{k}', t))), \end{aligned} \quad (2.25)$$

where in the semi-classical framework the scattering rates $S_{\lambda \rightarrow \lambda'}(\mathbf{k}, \mathbf{k}')$ are typically obtained from *Fermi's golden rule* [135, 143]. The transport equation for the distribution function of the valence band holes $f_h(\mathbf{r}, \mathbf{k}, t) = 1 - f_v(\mathbf{r}, \mathbf{k}, t)$ is analogous.

In the thermodynamic equilibrium, all scattering processes are balanced according to the principle of detailed balance [189], such that there is no net-transfer of energy or momentum. As a consequence, the collision integral vanishes and the evolution is given by the time reversible dynamics on the left hand side of Eq. (2.24). From the theory of ideal quantum gases, the equilibrium distribution function of quasi-free electrons is known as

$$f_c^{\text{eq}}(\mathbf{r}, \mathbf{k}) = \left[e^{\beta \left(E_c + \frac{\hbar^2 \mathbf{k}^2}{2m_e^*} - q\phi(\mathbf{r}) - \mu_{\text{eq}} \right)} + 1 \right]^{-1},$$

which is an even function in \mathbf{k} : $f_c^{\text{eq}}(\mathbf{r}, \mathbf{k}) = f_c^{\text{eq}}(\mathbf{r}, -\mathbf{k})$. The equilibrium chemical potential is μ_{eq} and $\beta = (k_B T)^{-1}$ is the inverse temperature.

Following Stratton's approach [294], a solution of Eq. (2.24) is approximated by

$$f_{\lambda}(\mathbf{r}, \mathbf{k}, t) \approx f_{\lambda}^0(\mathbf{r}, \mathbf{k}, t) + f_{\lambda}^1(\mathbf{r}, \mathbf{k}, t), \quad \lambda \in \{c, v\},$$

where $f_{\lambda}^0(\mathbf{r}, \mathbf{k}, t) = f_{\lambda}^0(\mathbf{r}, -\mathbf{k}, t)$ is even and $f_{\lambda}^1(\mathbf{r}, \mathbf{k}, t) = -f_{\lambda}^1(\mathbf{r}, -\mathbf{k}, t)$ is odd in all components of \mathbf{k} . In the thermodynamic equilibrium the even part approaches the Fermi function $f_{\lambda}^0(\mathbf{r}, \mathbf{k}, t) \xrightarrow{\text{relax}} f_{\lambda}^{\text{eq}}(\mathbf{r}, \mathbf{k})$, whereas $f_{\lambda}^1(\mathbf{r}, \mathbf{k}, t)$ must vanish to zero. For a small perturbation $0 < f^1 \ll 1$ of a state close to the equilibrium, the collision integral can be written in the *relaxation time approximation* to first order in f^1 as

$$\mathcal{C}_c[f_c, f_v] \approx \left. \frac{\partial f_c^0}{\partial t} \right|_{\text{coll}} - \frac{f_c^1(\mathbf{r}, \mathbf{k}, t)}{\tau_c(\mathbf{k})}. \quad (2.26)$$

This is based on the assumption of fast intraband relaxation processes in comparison to the interband relaxation time scale. The inter- and intraband collisions depend only on

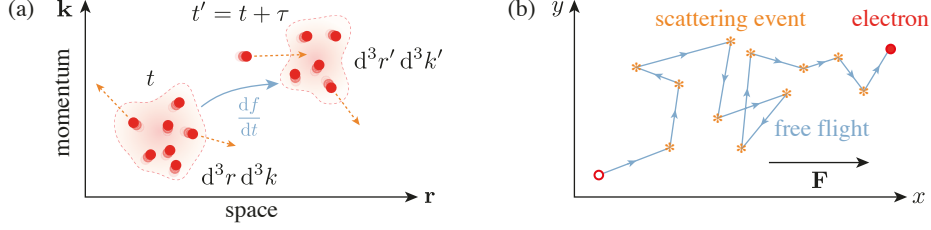


Fig. 2.5 (a) Illustration of the evolution in phase space: An electron ensemble is propagated by the Boltzmann transport equation from an infinitesimal phase space volume element $d^3r d^3k$ at time t to the volume element $d^3r' d^3k'$ at a later time t' . In and out scattering of electrons is shown by dashed lines, free streaming of the ensemble is indicated by the blue arrow. (b) Propagation of an electron on a 2D-projection of the space under the impact of an external force field \mathbf{F} and scattering. In the Boltzmann transport equation the free flight (blue lines) is described classically, whereas the scattering events (orange) follow from quantum mechanical perturbation theory.

the even functions f_λ^0 :

$$\begin{aligned} \left. \frac{\partial f_c^0}{\partial t} \right|_{\text{coll}} &= \sum_{\lambda=\{c,v\}} \frac{V}{(2\pi)^3} \int d^3k' (S_{\lambda \rightarrow c}(\mathbf{k}', \mathbf{k}) f_\lambda^0(\mathbf{r}, \mathbf{k}', t) (1 - f_c^0(\mathbf{r}, \mathbf{k}, t)) - \\ &\quad - S_{c \rightarrow \lambda}(\mathbf{k}, \mathbf{k}') f_c^0(\mathbf{r}, \mathbf{k}, t) (1 - f_\lambda^0(\mathbf{r}, \mathbf{k}', t))), \\ &= \left. \frac{\partial f_c^0}{\partial t} \right|_{\text{coll}}^{\text{inter}} + \left. \frac{\partial f_c^0}{\partial t} \right|_{\text{coll}}^{\text{intra}}. \end{aligned} \quad (2.27)$$

The relaxation rate of the conduction band electrons is given as

$$\frac{1}{\tau_c(\mathbf{k})} = \sum_{\lambda=\{c,v\}} \frac{V}{(2\pi)^3} \int d^3k' (S_{c \rightarrow \lambda}(\mathbf{k}, \mathbf{k}') [1 - f_\lambda^0(\mathbf{r}, \mathbf{k}', t)] + S_{\lambda \rightarrow c}(\mathbf{k}', \mathbf{k}) f_\lambda^0(\mathbf{r}, \mathbf{k}', t)).$$

Here and below the scattering rates S are assumed to be even in all components of \mathbf{k} .

Since the Boltzmann transport equation is a nonlinear integro-differential equation on a high-dimensional phase space, its mathematical analysis is very challenging and the numerical solution is computationally demanding. Therefore, simplified approaches are necessary. In the following, the continuity Eq. (2.1b) and the drift-diffusion current density (2.11a) will be derived from the zeroth and first moment of Eq. (2.24)

Continuity equations

By integrating out the \mathbf{k} -dependency and employing the symmetry properties introduced above, the zeroth moment (i.e., the *mean*) of the Boltzmann equation (2.24) is given from

$$\begin{aligned} \frac{\partial}{\partial t} \int d^3k f_c^0(\mathbf{r}, \mathbf{k}, t) + \nabla_{\mathbf{r}} \cdot \int d^3k \frac{\hbar \mathbf{k}}{m_e^*} f_c^1(\mathbf{r}, \mathbf{k}, t) + \frac{1}{\hbar} \int d^3k \nabla_{\mathbf{k}} \cdot (\mathbf{F} f_c^1(\mathbf{r}, \mathbf{k}, t)) &= \\ &= \int d^3k \mathcal{C}_c[f_c, f_v]. \end{aligned}$$

The force term yields a vanishing surface integral (assume $\lim_{\mathbf{k} \rightarrow \pm\infty} f_\lambda(\mathbf{r}, \mathbf{k}, t) = 0$) and, by symmetry arguments, the collision integral (2.27) is reduced to interband scattering

processes only. These constitute the net-recombination rate R in Eqs. (2.1b)–(2.1c)

$$\frac{1}{4\pi^3} \int d^3k \mathcal{C}_c [f_c, f_v] = \frac{1}{4\pi^3} \int d^3k \left. \frac{\partial f_c^0}{\partial t} \right|_{\text{coll}}^{\text{inter}} = -R. \quad (2.28)$$

With the definitions of the electron density and electron current density

$$n(\mathbf{r}, t) = \frac{1}{4\pi^3} \int d^3k f_e^0(\mathbf{r}, \mathbf{k}, t), \quad \mathbf{j}_n(\mathbf{r}, t) = -\frac{q}{4\pi^3} \int d^3k \frac{\hbar \mathbf{k}}{m_e^*} f_e^1(\mathbf{r}, \mathbf{k}, t),$$

one arrives at the continuity equation (2.1b) for the electron density (holes analogously)

$$\frac{\partial}{\partial t} n(\mathbf{r}, t) - \frac{1}{q} \nabla_{\mathbf{r}} \cdot \mathbf{j}_n(\mathbf{r}, t) = -R.$$

Drift-diffusion equations

The drift-diffusion equation is obtained from Eq. (2.24) by evaluating the average electron velocity $\mathbf{v} = \hbar \mathbf{k} / m_e^*$. The collision integral in relaxation time approximation (2.26) yields

$$\frac{1}{4\pi^3} \int d^3k \frac{\hbar \mathbf{k}}{m_e^*} \mathcal{C}_c [f_c, f_v] = -\frac{1}{4\pi^3} \int d^3k \frac{\hbar \mathbf{k}}{m_e^*} \frac{f_c^1(\mathbf{r}, \mathbf{k}, t)}{\tau_c(\mathbf{k})} = \frac{1}{q\bar{\tau}_c} \mathbf{j}_n(\mathbf{r}, t),$$

where $\bar{\tau}_c$ is the average electron relaxation time. An expression for the current density \mathbf{j}_n in terms of the external force \mathbf{F} and the electron density n is obtained from evaluating the corresponding left hand side of Eq. (2.24). First, the time derivative term yields

$$\frac{\partial}{\partial t} \frac{1}{4\pi^3} \int d^3k \frac{\hbar \mathbf{k}}{m_e^*} f_c(\mathbf{r}, \mathbf{k}, t) = \frac{1}{q} \frac{\partial}{\partial t} \mathbf{j}_n(\mathbf{r}, t).$$

With the tensor divergence identity $\text{div}(\mathbf{A} \otimes \mathbf{B}) = \mathbf{B}(\nabla \cdot \mathbf{A}) + (\mathbf{A} \cdot \nabla) \mathbf{B}$, the second term in Eq. (2.24) leads to

$$\frac{1}{4\pi^3} \int d^3k \frac{\hbar \mathbf{k}}{m_e^*} \left(\frac{\hbar \mathbf{k}}{m_e^*} \cdot \nabla_{\mathbf{r}} f_c(\mathbf{r}, \mathbf{k}, t) \right) = \frac{1}{4\pi^3} \left(\frac{\hbar}{m_e^*} \right)^2 \text{div}_{\mathbf{r}} \left(\int d^3k \mathbf{k} \otimes \mathbf{k} f_c(\mathbf{r}, \mathbf{k}, t) \right),$$

which will turn out to be the diffusion current below. Similarly, the force term yields

$$\begin{aligned} \int d^3k \frac{\hbar \mathbf{k}}{m_e^*} \frac{1}{\hbar} (\mathbf{F} \cdot \nabla_{\mathbf{k}} f(\mathbf{r}, \mathbf{k}, t)) &= \frac{1}{m_e^*} \int d^3k (\text{div}_{\mathbf{k}}(f(\mathbf{r}, \mathbf{k}, t) \mathbf{F} \otimes \mathbf{k}) - (f(\mathbf{r}, \mathbf{k}, t) \mathbf{F} \cdot \nabla_{\mathbf{k}}) \mathbf{k}) \\ &= -\frac{1}{m_e^*} \mathbf{F} \int d^3k f^0(\mathbf{r}, \mathbf{k}, t) = -\frac{4\pi^3}{m_e^*} \mathbf{F} n(\mathbf{r}, t). \end{aligned}$$

Combining the individual terms, one obtains with the electron mobility $M_n = q\bar{\tau}_c/m_e^*$ and for a quasi-static electric field $\mathbf{F} = -q\mathbf{E} \approx q\nabla_{\mathbf{r}}\phi$

$$\mathbf{j}_n(\mathbf{r}, t) = \bar{\tau}_c \partial_t \mathbf{j}_n(\mathbf{r}, t) - qM_n n(\mathbf{r}, t) \nabla \phi(\mathbf{r}, t) + M_n \frac{1}{2\pi^3} \text{div}_{\mathbf{r}} \left(\int d^3k \frac{\hbar^2 \mathbf{k} \otimes \mathbf{k}}{2m_e^*} f_c(\mathbf{r}, \mathbf{k}, t) \right).$$

The last term involves the average of the energy tensor of the conduction band electrons, which is a second-order moment of the distribution. This term must be modeled by a *closure relation* to truncate the hierarchy of moments at first order. By assuming a diagonal

and isotropic energy tensor $\mathbf{k} \otimes \mathbf{k} \approx \frac{1}{3}k^2 I_{3 \times 3}$, the diffusion current reduces to a gradient

$$\frac{1}{2\pi^3} \operatorname{div}_{\mathbf{r}} \left(\int d^3k \frac{\hbar^2 \mathbf{k} \otimes \mathbf{k}}{2m_e^*} f_c(\mathbf{r}, \mathbf{k}, t) \right) \approx \nabla_{\mathbf{r}} \left(\frac{2}{3} \frac{1}{4\pi^3} \int d^3k \frac{\hbar^2 k^2}{2m_e^*} f_c^0(\mathbf{r}, \mathbf{k}, t) \right).$$

The integral is evaluated by assuming that the even part of the distribution function can be written as a quasi-equilibrium Fermi function (see Sec. 2.1.2) such that energy density of the quasi-free electron gas is obtained as (cf. Sec. 2.3.1.1)

$$\frac{2}{3} \frac{1}{4\pi^3} \int d^3k \frac{\hbar^2 k^2}{2m_e^*} f_c^0(\mathbf{r}, \mathbf{k}, t) = k_B T N_c F_{3/2} \left(F_{1/2}^{-1} \left(\frac{n(\mathbf{r}, t)}{N_c} \right) \right)$$

with the effective density of states N_c as defined in Eq. (2.7) and the Fermi–Dirac integral (2.8). By evaluating the gradient, one finally arrives at

$$\nabla_{\mathbf{r}} N_c F_{3/2} \left(F_{1/2}^{-1} \left(\frac{n(\mathbf{r}, t)}{N_c} \right) \right) = g \left(\frac{n(\mathbf{r}, t)}{N_c} \right) \nabla_{\mathbf{r}} n(\mathbf{r}, t)$$

with the degeneration factor g as defined in Eq. (2.13). Using the generalized Einstein relation (2.12), the current density expression follows as

$$\mathbf{j}_n(\mathbf{r}, t) = \bar{\tau}_c \partial_t \mathbf{j}_n(\mathbf{r}, t) - q M_n n(\mathbf{r}, t) \nabla \phi(\mathbf{r}, t) + q D_n (n(\mathbf{r}, t)) \nabla_{\mathbf{r}} n(\mathbf{r}, t).$$

The time derivative $\bar{\tau}_c \partial_t \mathbf{j}_n(\mathbf{r}, t)$ can be ignored if the mean free path is small in comparison to the characteristic length scale of the device [152], which is typically well justified. This finally yields the drift-diffusion form stated in Eq. (2.11a).

2.3 Thermodynamics of the van Roosbroeck system

Consistency with (non-)equilibrium thermodynamics is crucial in semiconductor device simulation, as frequently complicated multi-physics problems need to be solved where, e.g., the charge transport problem is solved along with the heat equation [4, 13, 193, 233, 314]. This gives rise to thermoelectric cross-effects (Seebeck effect, Thomson-Peltier heating, recombination heating, Joule heating etc.), that need to be modeled in a consistent way without violating fundamental laws of (non-)equilibrium thermodynamics – namely the Onsager relations [228], the second law of thermodynamics and the microscopic reversibility in thermodynamic equilibrium. In opto-electronic device simulation the situation is even more complicated, since the electro-thermal problem is additionally coupled to the optical Maxwell equations to model, e.g., the thermal rollover of the optical gain, absorption heating and hot cavity effects such as thermal lensing [13, 111]. A consistent multi-physics model relies on carefully constructed building blocks that guarantee the consistency with thermodynamics on their own. This section gives an overview on the thermodynamic properties of the van Roosbroeck system, which have been studied before in Ref. [4]. The results are reviewed here in order to provide a basis for the discussion of the thermodynamic properties of a hybrid quantum-classical model system introduced later on in Chap. 5.

First, the thermodynamic potentials of the non-interacting electron-hole gas are derived from the model of the quasi-free Fermi gas in Sec. 2.3.1. In a second step, the thermodynamic potentials of the van Roosbroeck system are completed by including the (classical) electrostatic interaction energy. In Sec. 2.3.2, the entropy production rate is derived from entropy balance considerations and shown to obey the second law of thermodynamics.

2.3.1 Thermodynamic potentials

2.3.1.1 Quasi-free electron-hole gas

The quasi-free Fermi gas is a simple model for the physical properties of an electron ensemble in a solid. The model neglects the electron-phonon and electron-electron interactions, such that – within the scalar effective mass approximation – the Hamiltonian of a single electron in a solid is formally equivalent to a free electron in vacuum.⁵ The quasi-free Fermi gas model is an inherent part of the van Roosbroeck system, where it describes the electron-hole plasma in a two-band semiconductor. In second quantization, the Hamiltonian reads

$$H = \sum_{\mathbf{k},\sigma} \varepsilon_c(\mathbf{k}) e_{\mathbf{k},\sigma}^\dagger e_{\mathbf{k},\sigma} - \sum_{\mathbf{k},\sigma} \varepsilon_v(\mathbf{k}) h_{\mathbf{k},\sigma}^\dagger h_{\mathbf{k},\sigma},$$

where the creation and annihilation operators $e_{\mathbf{k},\sigma}$ and $e_{\mathbf{k},\sigma}^\dagger$ obey the fermionic anti-commutator relations $\{e_{\mathbf{k},\sigma}, e_{\mathbf{k}',\sigma'}^\dagger\} = \delta_{\sigma,\sigma'} \delta_{\mathbf{k},\mathbf{k}'}$ and $\{e_{\mathbf{k},\sigma}, e_{\mathbf{k}',\sigma'}\} = 0 = \{e_{\mathbf{k},\sigma}^\dagger, e_{\mathbf{k}',\sigma'}^\dagger\}$ (analogous for holes). The energy dispersion relations are assumed to be parabolic as given in Eq. (2.5). With the separate quasi-Fermi energies μ_c and μ_v for the conduction and the valence band electron ensembles and the electron and hole number operators $n_e = \sum_{\mathbf{k},\sigma} e_{\mathbf{k},\sigma}^\dagger e_{\mathbf{k},\sigma}$ and $n_h = \sum_{\mathbf{k},\sigma} h_{\mathbf{k},\sigma}^\dagger h_{\mathbf{k},\sigma}$, a quasi-equilibrium state of the electron-hole gas is described by the grand canonical ensemble density matrix

$$\rho = \frac{1}{Z} e^{-\beta(H - \mu_c n_e + \mu_v n_h)}. \quad (2.29)$$

The partition function Z enforces the normalization of the density matrix $\text{tr}(\rho) = 1$ and provides the starting point to derive the thermodynamic potentials of the system. The partition function is obtained as

$$Z(\mu_c, \mu_v, T) = \text{tr}(e^{-\beta(H - \mu_c n_e + \mu_v n_h)}) = \prod_{\mathbf{k},\sigma} (1 + e^{-\beta(\varepsilon_{c,\mathbf{k}} - \mu_c)}) \prod_{\mathbf{k}',\sigma'} (1 + e^{\beta(\varepsilon_{v,\mathbf{k}'} - \mu_v)}).$$

The grand potential of the non-interacting, spatially homogeneous system (indicated by the superscript zero) follows immediately as

$$\begin{aligned} \Phi^0 &= -k_B T \log Z = -k_B T \sum_{\mathbf{k},\sigma} \log(1 + e^{-\beta(\varepsilon_{c,\mathbf{k}} - \mu_c)}) - k_B T \sum_{\mathbf{k},\sigma} \log(1 + e^{+\beta(\varepsilon_{v,\mathbf{k}} - \mu_v)}) \\ &= -k_B T V \left(N_c(T) F_{3/2} \left(\frac{\mu_c - E_c}{k_B T} \right) + N_v(T) F_{3/2} \left(\frac{E_v - \mu_v}{k_B T} \right) \right), \end{aligned}$$

where the sums have been evaluated in the continuum limit [166]. The effective density of state functions $N_{c/v}(T)$ are given in Eq. (2.7). According to *Gibbs' fundamental relation* [108], the carrier densities are obtained as derivatives with respect to the chemical potentials

$$n^0(\mu_c, T) = -\frac{1}{V} \frac{\partial \Phi^0}{\partial \mu_c} = N_c(T) F_{1/2} \left(\frac{\mu_c - E_c}{k_B T} \right), \quad (2.30a)$$

$$p^0(\mu_v, T) = +\frac{1}{V} \frac{\partial \Phi^0}{\partial \mu_v} = N_v(T) F_{1/2} \left(\frac{E_v - \mu_v}{k_B T} \right). \quad (2.30b)$$

⁵ The conduction band electrons and valence band holes are fermionic *quasi-particles* of the system [166].

Finally, the free energy $\mathcal{F}^0 = \Phi^0 + V (n^0 \mu_c - p^0 \mu_v)$ of the non-interacting and spatially homogeneous Fermi gas is obtained by the Legendre transformation of Φ^0 with respect to the chemical potentials and the (non-interacting) carrier densities as

$$\begin{aligned} \mathcal{F}^0(n^0, p^0, T) = & V \left(k_B T \left[n^0 F_{1/2}^{-1} \left(\frac{n^0}{N_c(T)} \right) - N_c(T) F_{3/2} \left(F_{1/2}^{-1} \left(\frac{n^0}{N_c(T)} \right) \right) \right] + E_c n^0 + \right. \\ & \left. + k_B T \left[p^0 F_{1/2}^{-1} \left(\frac{p^0}{N_v(T)} \right) - N_v(T) F_{3/2} \left(F_{1/2}^{-1} \left(\frac{p^0}{N_v(T)} \right) \right) \right] - E_v p^0 \right). \end{aligned} \quad (2.31)$$

2.3.1.2 Electrostatic field energy

The considerations of the previous section need to be supplemented by the (classical) electrostatic interaction between the carriers. The (self-consistent) electrostatic field energy contributes to the total energy of the van Roosbroeck system and will be important for the definition of the chemical potentials in the full system.

Following Ref. [4], the electrostatic potential ϕ can be split into two contributions $\phi = \phi_{\text{int}} + \phi_{\text{ext}}$, where the *internal* part ϕ_{int} is generated by the free charge densities n and p of the system and *external* part ϕ_{ext} results from the built-in doping profile C and Dirichlet boundary conditions (applied voltage, cf. Sec. 2.1.5). This yields a separation of Poisson's equation (2.1a) into the homogeneous boundary value problem

$$-\nabla \cdot \varepsilon \nabla \phi_{\text{int}} = \varrho_{\text{int}} \quad \text{on } \Omega, \quad (2.32a)$$

$$\mathbf{n} \cdot \nabla \phi_{\text{int}} = 0 \quad \text{on } \Gamma_N, \quad (2.32b)$$

$$\phi_{\text{int}} = 0 \quad \text{on } \Gamma_D, \quad (2.32c)$$

where $\varrho_{\text{int}} = q(p - n)$ is the mobile (net-)charge density of the system and, secondly, the inhomogeneous boundary value problem

$$-\nabla \cdot \varepsilon \nabla \phi_{\text{ext}} = qC \quad \text{on } \Omega, \quad (2.33a)$$

$$\mathbf{n} \cdot \nabla \phi_{\text{ext}} = 0 \quad \text{on } \Gamma_N, \quad (2.33b)$$

$$\phi_{\text{ext}} = \phi_{\text{eq}} + U^{\text{appl}} \quad \text{on } \Gamma_D. \quad (2.33c)$$

The electrostatic energy of a charge cloud in vacuum is equal to the work that is required to assemble it by moving its elementary constituents successively from infinity into the system against the electrostatic field generated by the charges already present in the system [142]. In dielectric media, also the work required to build up polarization charges must be considered. The field energy of a charge cloud in a dielectric medium is known as [142]

$$\mathcal{E}_\phi^{\text{int}} = \frac{1}{2} \int_\Omega d^3r \mathbf{E}_{\text{int}} \cdot \mathbf{D}_{\text{int}} = \frac{1}{2} \int_\Omega d^3r \varepsilon \|\nabla \phi_{\text{int}}\|^2,$$

where $\mathbf{D}_{\text{int}} = \varepsilon \mathbf{E}_{\text{int}}$ with $\mathbf{E}_{\text{int}} = -\nabla \phi_{\text{int}}$ and ϕ_{int} solves the boundary value problem (2.32). The symbol $\|\cdot\|$ denotes the vector norm.

A second contribution to the electrostatic field energy arises from the interaction of the charge density ϱ_{int} with the external potential ϕ_{ext} that solves the boundary value problem (2.33). This energy contribution reads [142]

$$\mathcal{E}_\phi^{\text{ext}} = \int_\Omega d^3r \varrho_{\text{int}} \phi_{\text{ext}}.$$

Combining both contributions, one obtains the total electrostatic field energy [3, 4]

$$\mathcal{E}_\phi = \mathcal{E}_\phi(\varrho_{\text{int}}) = \frac{1}{2} \int_{\Omega} d^3r \varepsilon \|\nabla \phi_{\text{int}}(\varrho_{\text{int}})\|^2 + \int_{\Omega} d^3r \varrho_{\text{int}} \phi_{\text{ext}}, \quad (2.34)$$

where $\phi_{\text{int}} = \phi_{\text{int}}(\varrho_{\text{int}})$ is a functional of the free charge density ϱ_{int} . Alternatively, using the Green's function of Poisson's equation, the functional from of Eq. (2.34) can be stated more explicitly.⁶ The essential property of $\mathcal{E}_\phi(\varrho_{\text{int}})$ is the functional derivative [3, 4]

$$\langle D\mathcal{E}_\phi, \delta\varrho_{\text{int}} \rangle = \int_{\Omega} d^3r \phi \delta\varrho_{\text{int}}. \quad (2.37)$$

This is obtained from the variation of the charge density $\varrho_{\text{int}} \rightarrow \varrho_{\text{int}} + a\delta\varrho_{\text{int}}$ in Eq. (2.34)

$$\begin{aligned} \mathcal{E}_\phi(\varrho_{\text{int}} + a\delta\varrho_{\text{int}}) &= \\ &= \mathcal{E}_\phi(\varrho_{\text{int}}) + a \int_{\Omega} d^3r \varepsilon \nabla \phi_{\text{int}}(\varrho_{\text{int}}) \cdot \nabla \delta\phi_{\text{int}}(\delta\varrho_{\text{int}}) + a \int_{\Omega} d^3r \phi_{\text{ext}} \delta\varrho_{\text{int}} + \mathcal{O}(a^2), \end{aligned}$$

where $0 < a \ll 1$ is a small parameter, $\phi_{\text{int}}(\varrho_{\text{int}} + a\delta\varrho_{\text{int}}) \approx \phi_{\text{int}}(\varrho_{\text{int}}) + a\delta\phi_{\text{int}}(\delta\varrho_{\text{int}})$ and $\delta\phi_{\text{int}}$ obeys the boundary value problem (2.32) for the right hand side $\delta\varrho_{\text{int}}$. Therefore, it holds $\int_{\Omega} d^3r \varepsilon \nabla \phi_{\text{int}} \cdot \nabla \delta\phi_{\text{int}} = \int_{\Omega} d^3r \phi_{\text{int}} \delta\varrho_{\text{int}}$ such that one obtains

$$\mathcal{E}_\phi(\varrho_{\text{int}} + a\delta\varrho_{\text{int}}) = \mathcal{E}_\phi(\varrho_{\text{int}}) + a \int_{\Omega} d^3r (\phi_{\text{int}} + \phi_{\text{ext}}) \delta\varrho_{\text{int}} + \mathcal{O}(a^2).$$

Thus, the function derivative (2.37) holds in the sense of the Gâteaux derivative

$$\langle D\mathcal{E}_\phi, \delta\varrho_{\text{int}} \rangle = \lim_{a \rightarrow 0} \frac{\mathcal{E}_\phi(\varrho_{\text{int}} + a\delta\varrho_{\text{int}}) - \mathcal{E}_\phi(\varrho_{\text{int}})}{a} = \int_{\Omega} d^3r \phi \delta\varrho_{\text{int}}.$$

2.3.1.3 Thermodynamic potentials of the van Roosbroeck system

By combining the energy contributions of the two previous sections, one obtains the free energy functional of the interacting electron-hole gas subject to the van Roosbroeck system

$$\begin{aligned} \mathcal{F}(n, p, T) &= \int_{\Omega} d^3r \left(k_B T \left[n F_{1/2}^{-1} \left(\frac{n}{N_c(T)} \right) - N_c(T) F_{3/2} \left(F_{1/2}^{-1} \left(\frac{n}{N_c(T)} \right) \right) \right] + E_c n + \right. \\ &\quad \left. + k_B T \left[p F_{1/2}^{-1} \left(\frac{p}{N_v(T)} \right) - N_v(T) F_{3/2} \left(F_{1/2}^{-1} \left(\frac{p}{N_v(T)} \right) \right) \right] - E_v p \right) \\ &\quad + \mathcal{E}_\phi[q(p - n)], \end{aligned} \quad (2.38)$$

where n and p are now the spatially varying carrier densities. Note that the electrostatic interaction does not contribute to the entropy (only the energy \mathcal{E}_ϕ is added to the total free energy). The (local) chemical potentials follow again via Gibbs' fundamental relation

⁶ The (total) electrostatic field energy can be written as

$$\begin{aligned} \mathcal{E}_\phi(\varrho_{\text{int}}) &= \frac{1}{2} \int_{\Omega} d^3r \int_{\Omega} d^3r' G(\mathbf{r}, \mathbf{r}') \varrho_{\text{int}}(\mathbf{r}) \varrho_{\text{int}}(\mathbf{r}') + q \int_{\Omega} d^3r \int_{\Omega} d^3r' G(\mathbf{r}, \mathbf{r}') \varrho_{\text{int}}(\mathbf{r}) C(\mathbf{r}') - \\ &\quad - \int_{\Omega} d^3r \int_{\Gamma_D} dA' \varrho_{\text{int}}(\mathbf{r}) \varepsilon(\mathbf{r}') (\phi_{\text{eq}}(\mathbf{r}') + U_{\text{appl}}(\mathbf{r}')) \mathbf{n} \cdot \nabla_{\mathbf{r}'} G(\mathbf{r}, \mathbf{r}'), \end{aligned} \quad (2.35)$$

where $G(\mathbf{r}, \mathbf{r}')$ is the Green's functions of Poisson's Eq. (2.1a) satisfying $-\nabla_{\mathbf{r}'} \cdot \varepsilon(\mathbf{r}') \nabla_{\mathbf{r}'} G(\mathbf{r}, \mathbf{r}') = \delta(\mathbf{r} - \mathbf{r}')$

as functional derivatives with respect to the carrier density. Using Eq. (2.37), one obtains⁷

$$D_n \mathcal{F} = \mu_c = +k_B T F_{1/2}^{-1} \left(\frac{n}{N_c(T)} \right) + E_c - q\phi, \quad (2.39a)$$

$$-D_p \mathcal{F} = \mu_v = -k_B T F_{1/2}^{-1} \left(\frac{p}{N_v(T)} \right) + E_v - q\phi, \quad (2.39b)$$

which in turn yields the local carrier density relations (2.6)

$$n = N_c(T) F_{1/2} \left(\frac{\mu_c - E_c + q\phi}{k_B T} \right), \quad p = N_v(T) F_{1/2} \left(\frac{E_v - q\phi - \mu_v}{k_B T} \right).$$

Finally, the entropy functional is obtained as the negative partial derivative of the free energy functional with respect to the temperature

$$\begin{aligned} \mathcal{S}(n, p, T) &= -\frac{\partial \mathcal{F}(n, p, T)}{\partial T} = \\ &= k_B \int_{\Omega} d^3 r \left[\frac{5}{2} N_c(T) F_{3/2} \left(F_{1/2}^{-1} \left(\frac{n}{N_c(T)} \right) \right) - n F_{1/2}^{-1} \left(\frac{n}{N_c(T)} \right) + \right. \\ &\quad \left. + \frac{5}{2} N_v(T) F_{3/2} \left(F_{1/2}^{-1} \left(\frac{p}{N_v(T)} \right) \right) - p F_{1/2}^{-1} \left(\frac{p}{N_v(T)} \right) \right] \end{aligned} \quad (2.40)$$

and the total energy reads

$$\begin{aligned} \mathcal{E}(n, p, T) &= \mathcal{F}(n, p, T) + T \mathcal{S}(n, p, T) = \\ &= \mathcal{E}_{\phi}[q(p - n)] + \int_{\Omega} d^3 r \left[\frac{3}{2} k_B T N_c(T) F_{3/2} \left(F_{1/2}^{-1} \left(\frac{n}{N_c(T)} \right) \right) + E_c n + \right. \\ &\quad \left. + \frac{3}{2} k_B T N_v(T) F_{3/2} \left(F_{1/2}^{-1} \left(\frac{p}{N_v(T)} \right) \right) - E_v p \right]. \end{aligned} \quad (2.41)$$

2.3.2 Consistency with (non-)equilibrium thermodynamics

The interacting electron-hole gas subject to the van Roosbroeck system (2.1) is an open thermodynamic system S , which can exchange energy and charge with the reservoir R in its environment. The balance laws for the conservation of energy (first law of thermodynamics) and charge read

$$\Delta \mathcal{S}_S + \Delta \mathcal{S}_R = 0, \quad (2.42)$$

$$\Delta \mathcal{N}_S + \Delta \mathcal{N}_R = 0, \quad (2.43)$$

on $\mathbf{r}' \in \Omega$, $G(\mathbf{r}, \mathbf{r}') = 0$ on $\mathbf{r}' \in \Gamma_D$ and $\mathbf{n} \cdot \nabla_{\mathbf{r}'} G(\mathbf{r}, \mathbf{r}') = 0$ on $\mathbf{r}' \in \Gamma_N$ for $\mathbf{r} \in \Omega$. Using Green's theorem

$$\begin{aligned} \int_{\Omega} d^3 r' \left(G(\mathbf{r}, \mathbf{r}') \nabla_{\mathbf{r}'} \cdot \varepsilon(\mathbf{r}') \nabla_{\mathbf{r}'} \phi(\mathbf{r}') - \phi(\mathbf{r}') \nabla_{\mathbf{r}'} \cdot \varepsilon(\mathbf{r}') \nabla_{\mathbf{r}'} G(\mathbf{r}, \mathbf{r}') \right) = \\ = \oint_{\partial \Omega} dA' \varepsilon(\mathbf{r}') \left(G(\mathbf{r}, \mathbf{r}') \mathbf{n} \cdot \nabla_{\mathbf{r}'} \phi(\mathbf{r}') - \phi(\mathbf{r}') \mathbf{n} \cdot \nabla_{\mathbf{r}'} G(\mathbf{r}, \mathbf{r}') \right), \end{aligned} \quad (2.36)$$

the formal solutions of the Poisson problems (2.32)–(2.33) read $\phi_{\text{int}}(\mathbf{r}) = \int_{\Omega} d^3 r' G(\mathbf{r}, \mathbf{r}') \varrho_{\text{int}}(\mathbf{r}')$ and $\phi_{\text{ext}}(\mathbf{r}) = q \int_{\Omega} d^3 r' G(\mathbf{r}, \mathbf{r}') C(\mathbf{r}') - \int_{\Gamma_D} dA' \varepsilon(\mathbf{r}') \left(\phi_{\text{eq}}(\mathbf{r}') + U_{\text{appl}}(\mathbf{r}') \right) \mathbf{n} \cdot \nabla_{\mathbf{r}'} G(\mathbf{r}, \mathbf{r}')$. Eq. (2.36) ensures the symmetry of the Green's function in its arguments $G(\mathbf{r}, \mathbf{r}') = G(\mathbf{r}', \mathbf{r})$, which finally yields Eq. (2.35) from Eq. (2.34). The central result (2.37) is obtained by straightforward differentiation of Eq. (2.35).

⁷ The functional derivative $D_n \mathcal{F}$ is defined via $\langle D_n \mathcal{F}, \delta n \rangle = \lim_{a \rightarrow 0} \frac{1}{a} (\mathcal{F}(n + a \delta n, p, T) - \mathcal{F}(n, p, T))$.

where the change of the charge in the different ohmic contact reservoirs is given by $\Delta\mathcal{N}_R = \sum_i \Delta\mathcal{N}_{R_i}$ (cf. Sec. 2.1.5). The change of the total entropy of the combined system $S + R$ is given by the entropy changes of the subsystems

$$\Delta\mathcal{S}_{\text{tot}} = \Delta\mathcal{S}_S + \Delta\mathcal{S}_R \geq 0, \quad (2.44)$$

which must be non-negative according to the second law of thermodynamics [108]. For systems in *local thermodynamic equilibrium* [108], the change of the entropy in the reservoir is given by Gibbs' fundamental relation

$$\Delta\mathcal{S}_R = \frac{1}{T}\Delta\mathcal{E}_R - \sum_i \frac{\mu_i}{T}\Delta\mathcal{N}_{R_i},$$

where μ_i is the chemical potential of the electron gas in the i -th ohmic contact. The temperature T is considered as a globally constant parameter throughout this work. Hence, with Eq. (2.42) the entropy production rate reads

$$\lim_{\Delta t \rightarrow 0} \frac{\Delta\mathcal{S}_{\text{tot}}}{\Delta t} = \frac{d\mathcal{S}_{\text{tot}}}{dt} = -\frac{1}{T} \frac{d\mathcal{F}_S}{dt} + \sum_i \frac{\mu_i}{qT} \int_{\Gamma_{D,i}} d\mathbf{A} \cdot (\mathbf{j}_n + \mathbf{j}_p), \quad (2.45)$$

where

$$\lim_{\Delta t \rightarrow 0} \frac{\Delta\mathcal{N}_{R_i}}{\Delta t} = \frac{d\mathcal{N}_{R_i}}{dt} = -\frac{1}{q} \int_{\Gamma_{D,i}} d\mathbf{A} \cdot (\mathbf{j}_n + \mathbf{j}_p), \quad (2.46)$$

is the charge flux across the i -th ohmic contact and $\mathcal{F}_S = \mathcal{E}_S - T\mathcal{S}_S$ is the free energy of the system S . In the thermodynamic equilibrium ($\mu_i \equiv \mu_{\text{eq}}$), Eq. (2.45) reduces to

$$\left. \frac{d\mathcal{S}_{\text{tot}}}{dt} \right|_{\text{eq}} = -\frac{1}{T} \frac{d}{dt} (\mathcal{F}_S - \mu_{\text{eq}}\mathcal{N}_S) = -\frac{1}{T} \frac{d\Phi_S^{\text{eq}}}{dt} = 0, \quad (2.47)$$

where Eq. (2.43) has been used. Moreover,

$$q\mathcal{N}_S [n, p] = q \int_{\Omega} d^3r (n - p) \quad (2.48)$$

is the (negative) total charge and $\Phi_S^{\text{eq}} = \mathcal{F}_S - \mu_{\text{eq}}\mathcal{N}_S$ is the equilibrium grand potential of the system S . As the grand potential approaches its (global) minimum in the thermodynamic equilibrium, the corresponding entropy production rate is zero.

2.3.2.1 Charge conservation

The van Roosbroeck system preserves the total charge $Q_{\text{tot}} = q \int_{\Omega} d^3r (p - n + C)$. This is easily seen by taking the total time derivative $\frac{dQ_{\text{tot}}}{dt}$, assuming a stationary doping profile $\partial_t C = 0$ and substituting the continuity Eqs. (2.1b)–(2.1c), which yields the (local) continuity equation for the charge density $\varrho_{\text{int}} = q(p - n)$

$$\partial_t \varrho_{\text{int}} + \nabla \cdot (\mathbf{j}_n + \mathbf{j}_p) = 0. \quad (2.49a)$$

Alternatively, by taking the time-derivative of Poisson's Eq. (2.1a), one arrives at

$$\nabla \cdot (\mathbf{j}_n + \mathbf{j}_p + \partial_t \mathbf{D}) = 0, \quad (2.49b)$$

which states that the total current density $\mathbf{j}_{\text{tot}} = \mathbf{j}_n + \mathbf{j}_p + \partial_t \mathbf{D}$ is divergence free. Here, $\partial_t \mathbf{D} = -\varepsilon \partial_t \nabla \phi$ is the dielectric displacement current density. Both formulations (2.49a) and (2.49b) are equivalent and connected by Gauss' law $\nabla \cdot \mathbf{D} = \varrho_{\text{int}} + qC$ (or rather Poisson's Eq. (2.1a)).

2.3.2.2 Thermodynamic equilibrium

Following Eq. (2.47), the thermodynamic equilibrium solution is obtained by finding the stationary state that minimizes the equilibrium grand potential

$$\Phi_S [n, p] |_{\text{eq}} = \mathcal{F}_S [n, p] - \mu_{\text{eq}} \mathcal{N}_S [n, p] \rightarrow \min.$$

This involves the free energy functional (2.38) of the van Roosbroeck system and the net-charge functional (2.48). By variation of the carrier densities $n \rightarrow n + a\delta n$, $p \rightarrow p + a\delta p$ (with a small parameter $0 < a \ll 1$) one obtains

$$\begin{aligned} 0 &\stackrel{!}{=} \lim_{a \rightarrow 0} \frac{\Phi_S [n + a\delta n, p + a\delta p] - \Phi_S [n, p] |_{\text{eq}}}{a} = \\ &= \int_{\Omega} d^3r \left(k_B T F_{1/2}^{-1} \left(\frac{n}{N_c} \right) + E_c - \mu_{\text{eq}} - q\phi_{\text{eq}} \right) \delta n \\ &\quad + \int_{\Omega} d^3r \left(k_B T F_{1/2}^{-1} \left(\frac{p}{N_v} \right) - E_v + \mu_{\text{eq}} + q\phi_{\text{eq}} \right) \delta p. \end{aligned}$$

Since the variations δn , δp are arbitrary on the computational domain Ω , this yields the (expected) equilibrium carrier densities

$$\begin{aligned} n_{\text{eq}} &= n(\mu_{\text{eq}}, \phi_{\text{eq}}) = N_c F_{1/2} \left(\frac{\mu_{\text{eq}} - E_c + q\phi_{\text{eq}}}{k_B T} \right), \\ p_{\text{eq}} &= p(\mu_{\text{eq}}, \phi_{\text{eq}}) = N_v F_{1/2} \left(\frac{E_v - q\phi_{\text{eq}} - \mu_{\text{eq}}}{k_B T} \right). \end{aligned}$$

The equilibrium potential ϕ_{eq} solves the nonlinear Poisson problem (cf. Sec. 2.1.5)

$$\begin{aligned} -\nabla \cdot \varepsilon \nabla \phi_{\text{eq}} &= q(p(\mu_{\text{eq}}, \phi_{\text{eq}}) - n(\mu_{\text{eq}}, \phi_{\text{eq}}) + C) && \text{on } \Omega, \\ \mathbf{n} \cdot \nabla \phi_{\text{eq}} &= 0 && \text{on } \Gamma_N, \\ p(\mu_{\text{eq}}, \phi_{\text{eq}}) - n(\mu_{\text{eq}}, \phi_{\text{eq}}) + C &= 0 && \text{on } \Gamma_D. \end{aligned}$$

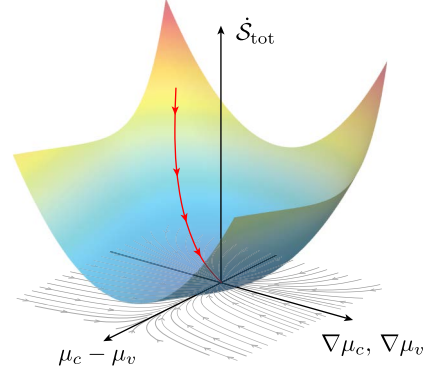
Consequently, the naively expected equilibrium state coincides with the state of vanishing entropy production and is therefore consistent with the second law of thermodynamics.

2.3.2.3 Entropy production rate and second law of thermodynamics

The entropy production rate of the van Roosbroeck system is obtained from Eq. (2.45) using the free energy functional (2.38) and its functional derivatives (2.39) as

$$\frac{d\mathcal{S}_{\text{tot}}}{dt} = -\frac{1}{T} \int_{\Omega} d^3r \left(\mu_c \frac{\partial n}{\partial t} - \mu_v \frac{\partial p}{\partial t} \right) + \sum_i \frac{\mu_i}{qT} \int_{\Gamma_{D,i}} d\mathbf{A} \cdot (\mathbf{j}_n + \mathbf{j}_p).$$

Fig. 2.6 Schematic illustration on the thermodynamic consistency of the van Roosbroeck system. The colored manifold shows the integrand of the non-negative entropy production rate (2.50), which represents a Lyapunov function for the relaxation of the system (red line) to the globally stable thermodynamic equilibrium.



By substituting the continuity Eqs. (2.1b)–(2.1c) and partial integration one obtains

$$\begin{aligned} \frac{dS_{\text{tot}}}{dt} &= \frac{1}{T} \int_{\Omega} d^3r (\mu_c - \mu_v) R - \frac{1}{qT} \oint_{\partial\Omega} d\mathbf{A} \cdot (\mu_c \mathbf{j}_n + \mu_v \mathbf{j}_p) + \\ &+ \frac{1}{qT} \int_{\Omega} d^3r (\mathbf{j}_n \cdot \nabla \mu_c + \mathbf{j}_p \cdot \nabla \mu_v) + \sum_i \frac{\mu_i}{qT} \int_{\Gamma_{D,i}} d\mathbf{A} \cdot (\mathbf{j}_n + \mathbf{j}_p). \end{aligned}$$

Using the (ideal) ohmic boundary conditions detailed in Sec. 2.1.5, the surface integral in the first line reduces to

$$\oint_{\partial\Omega} d\mathbf{A} \cdot (\mu_c \mathbf{j}_n + \mu_v \mathbf{j}_p) = \sum_i \mu_i \int_{\Gamma_{D,i}} d\mathbf{A} \cdot (\mathbf{j}_n + \mathbf{j}_p)$$

and cancels with the charge exchange term (last term in the second line). Finally, with the current densities (2.10), the total entropy production rate is obtained as (cf. [13, 81])

$$\frac{dS_{\text{tot}}}{dt} = \frac{1}{T} \int_{\Omega} d^3r (\mu_c - \mu_v) R + \frac{1}{q^2 T} \int_{\Omega} d^3r (\sigma_n \|\nabla \mu_c\|^2 + \sigma_p \|\nabla \mu_v\|^2) \geq 0, \quad (2.50)$$

which is evidently non-negative. The integrand of the first integral, which corresponds to recombination heating, is non-negative due to the pseudo-convex form $x(1 - e^{-x}) \geq 0$ ($\forall x \in \mathbb{R}$) generated by the structure of the recombination rate (2.15)

$$(\mu_c - \mu_v) R = r(\mu_c, \mu_v, \phi) (\mu_c - \mu_v) (1 - e^{-\beta(\mu_c - \mu_v)}) \geq 0.$$

Note that the recombination rate kernel $r(\mu_c, \mu_v, \phi) \geq 0$ is non-negative by construction (cf. Sec. 2.1.4 and Appx. A.2). The non-negativity of the second integral, which corresponds to dissipation via Joule heating, results from the quadratic form in the integrand and the positivity of the electrical conductivities $\sigma_{n,p} \geq 0$. The equality in Eq. (2.50) holds if and only if $\mu_c, \mu_v \rightarrow \mu_{\text{eq}} = \text{const.}$, i.e., in the thermodynamic equilibrium. Consequently, the van Roosbroeck system is consistent with the second law of thermodynamics.⁸

The entropy production rate (2.50) represents a Lyapunov function for the relaxation of the van Roosbroeck system to its equilibrium state (see Fig. 2.6) and proves the global stability of the thermodynamic equilibrium.

⁸ Note that stationary boundary conditions (DC bias) have been assumed here. For time-dependent applied voltages, the non-negativity of Eq. (2.50) can not be expected.

Chapter 3

Numerical simulation of carrier transport at cryogenic temperatures

This chapter provides an introduction to the finite volume Scharfetter–Gummel method for the multi-dimensional numerical simulation of the van Roosbroeck system. The scope of this thesis is the numerical simulation of charge transport in quantum light sources based on InGaAs-QDs, which are typically operated at cryogenic temperatures. This requires an extension of the standard discretization scheme towards an accurate consideration of Fermi–Dirac statistics, to properly describe the strong degeneration effects that arise in the electron-hole gas at extremely low temperatures. In the recent years, several generalizations of the classical Scharfetter–Gummel discretization scheme for Fermi–Dirac statistics have been proposed, which are compared and assessed in Sec. 3.3. The comparison presented here goes beyond the reviews in the literature. Moreover, at cryogenic temperatures, the discrete van Roosbroeck system is subject to serious convergence issues and numerical underflow using the standard continuation scheme. The problem is investigated in Sec. 3.6 and traced back to an ill-conditioned Jacobian matrix. This observation leads to the revision of the standard continuation routine towards a new *annealing method*. In Sec. 3.7 the advantage of the proposed annealing method for the simulation of wide band gap semiconductors is discussed. The results on the annealing method are published in Ref. [158] and are reprinted with permission. © 2016 Springer Science+Business Media.

3.1 Finite volume method

The finite volume method is a numerical technique for the discretization of balance equations (i.e. partial differential equations describing conservation laws) that allows to strictly preserve the conserved quantities of a continuous problem on the discrete level [66, 186, 190]. The finite volume method is independent of the domain geometry and dimensionality and is easily formulated on unstructured, anisotropic meshes built on arbitrary polygonal or polyhedral cells. This allows for an efficient simulation of problems on complicated spatial domains. The finite volume method is well suited to handle problems with jumping coefficients and stiff solutions exhibiting extreme internal layers, boundary layers or shocks [190, 204]. Due to these properties, the method is widely used in computational fluid dynamics [190], electro-chemistry [77] and electronics [15, 69, 81, 278].

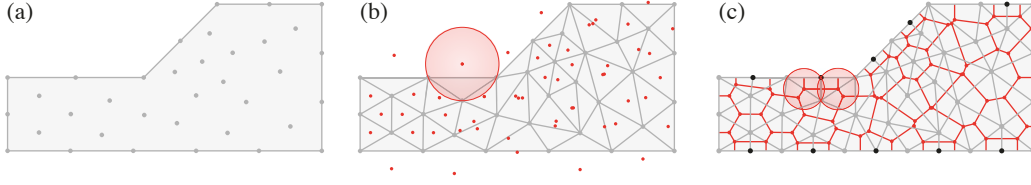


Fig. 3.1 (a) Piecewise linear description of the computational domain (planar straight line graph) and given point set (grey dots). (b) Delaunay triangulation of the point set and triangle circumcenters (small red dots). For several boundary triangles the angles opposite to the boundary exceed 90° such that their circumcenters are outside of the computational domain. (c) Boundary conforming Delaunay triangulation of the point set with ten additionally inserted Steiner points on the domain boundary (large black dots). The boundaries of the (restricted) Voronoï cells are shown in red. The Delaunay triangulation was created using *Triangle* [281].

3.1.1 Delaunay triangulation and Voronoï boxes

The finite volume method is based on the partition of the computational domain Ω into small elements called *control volumes*. The control volumes constitute a disjoint tessellation of Ω and can be given by arbitrary polyhedral or polygonal geometrical objects, depending on the dimensionality d of the problem. The canonical method for the construction of meshes for space-discretized numerical simulation methods (e.g., finite volume method, finite element method) is based on Delaunay triangulations. The Delaunay triangulation provides a triangulation of a given coordinate set $X = \{\mathbf{r}_K \in \Omega \subset \mathbb{R}^d\}_{K=1 \dots N_{\text{nodes}}}$ in the d -dimensional Euclidian space, such that no point of X is located within the circumsphere of any d -simplex of the triangulation (i.e., in $d = 2$ no point of X is located within any circumcircle of any triangle belonging to the Delaunay triangulation of X). Delaunay triangulation has several beneficial properties, in particular it tends to avoid triangles with very acute angles by maximizing the minimum angle in the triangulation. Moreover, many fast algorithms for the construction of Delaunay triangulations have been developed, e.g., the *divide and conquer algorithm* with runtime $\sim N_{\text{nodes}} \log(N_{\text{nodes}})$ [114]. The Delaunay triangulation of a point set obtained with *Triangle* [281] is shown in Fig. 3.1.

The actual control volumes of the finite volume method considered throughout this work are the Voronoï boxes, that can be obtained from the Delaunay triangulation by joining the circumcenters of adjacent triangles. As shown in Fig. 3.1 (b), the standard Delaunay triangulation of a point set may yield boundary triangles with obtuse angles opposite to the boundary, such that the corresponding triangle circumcenter is located outside of the computational domain. In this case the Voronoï box tessellation is not congruent to the domain such that the Voronoï boxes are no admissible control cells. This limitation is overcome by *boundary conforming Delaunay triangulations* that have additional restrictions on the angles of boundary simplices [285]. By extending the original coordinate set by additional so-called Steiner points and enforcing the boundary conforming Delaunay property, the corresponding *restricted* Voronoï box tessellation yields an admissible partition of the computational domain $\Omega = \bigcup_{K=1}^{N_{\text{nodes}}} \Omega_K$ [69]. An example is shown in Fig. 3.1 (c). For any vertex $\mathbf{r}_K \in X$, the corresponding Voronoï box is given by

$$\Omega_K = \{\mathbf{r} \in \Omega \mid \|\mathbf{r} - \mathbf{r}_K\| \leq \|\mathbf{r} - \mathbf{r}_L\| \forall \mathbf{r}_L \neq K \in X\}.$$

The Voronoï tessellation is said to be *dual* to the Delaunay triangulation as for any edge $\mathbf{r}_{K,L} = s\mathbf{r}_L + (1-s)\mathbf{r}_K$, $s \in [0, 1]$, it holds $\partial\Omega_K \cap \partial\Omega_L \neq \emptyset$. Finally, it shall be noted that there is no need for an explicit construction of the control volumes as geometrical objects

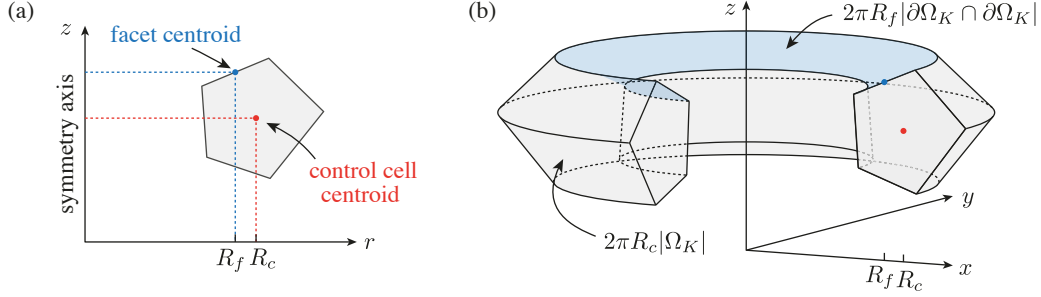


Fig. 3.2 Construction of geometry factors for problems with rotational symmetry. The modified cell volumes and edge factors are obtained from the planar geometry factors by using the Pappus–Guldinus centroid theorem. (a) The centroids of all Voronoi cells and of each intersection between adjacent Voronoi cells must be computed. (b) Illustration of a rotated Voronoi cell.

for the implementation in numerical software. For the finite volume method it is sufficient to incrementally precompute the cell volumes $|\Omega_K|$ and the so-called edge factors

$$s_{K,L} = \frac{|\partial\Omega_K \cap \partial\Omega_L|}{\|\mathbf{r}_L - \mathbf{r}_K\|} \quad (3.1)$$

in a simplex based assembly loop over all elements of the triangulation [69, 81].

The semiconductor devices investigated in Chap. 4 and 6 have a rotational symmetry. In this case the computational problem can be effectively reduced to a two-dimensional calculation with modified geometry factors. By using the Pappus–Guldinus centroid theorem [127], the rotated cell volumes and edge factors are obtained from the planar geometry factors. This requires the calculation of the cell and facet centroids (i.e., the geometric barycenters), which can – just as the planar geometry factors – be obtained incrementally in a simplex based sweep over the triangulation. An illustration of the modified geometry factors in axisymmetric problems is shown in Fig. 3.2.

3.1.2 Discretization of balance equations

A balance equation is a partial differential equation of the form

$$\partial_t u + \nabla \cdot \mathbf{j}(u, \nabla u) = S(u), \quad (3.2)$$

on a polygonal open domain $\Omega \subset \mathbb{R}^d$, $d \in \{1, 2, 3\}$, where $u = u(\mathbf{r}, t)$ is a scalar field describing density of some quantity that changes due to the flux \mathbf{j} and a source term S . The domain boundary $\partial\Omega = \Gamma_D \cup \Gamma_N$ is split into segments with Dirichlet boundary conditions on Γ_D and boundary conditions of third kind on Γ_N such that

$$\begin{aligned} \mathbf{n} \cdot \mathbf{j}(u(\mathbf{r}, t), \nabla u(\mathbf{r}, t)) &= g(u(\mathbf{r}, t)) && \text{on } \Gamma_N, \\ u(\mathbf{r}, t) &= u_D(\mathbf{r}, t) && \text{on } \Gamma_D, \\ u(\mathbf{r}, 0) &= u_I(\mathbf{r}) && \text{on } \Omega, \end{aligned}$$

where \mathbf{n} is the outer normal unit vector on $\partial\Omega$ and the last line denotes the initial values. The boundary condition of third kind is reduced to a homogeneous Neumann boundary condition if the function g is identical zero. The partial differential equation is cast into

the weak formulation by integration over the control volumes

$$\frac{d}{dt} \int_{\Omega_K} d^d r u + \oint_{\partial\Omega_K} d\mathbf{A} \cdot \mathbf{j} = \int_{\Omega_K} d^d r S,$$

where the divergence theorem was employed. Following Ref. [66], the weak form of Eq. (3.2) is discretized with respect to a set of discrete unknowns u_K as

$$0 = |\Omega_K| \frac{d}{dt} u_K + \sum_{L \in \mathcal{N}(K)} |\partial\Omega_K \cap \partial\Omega_L| \mathbf{n}_{K,L} \cdot \mathbf{j} - |\Omega_K| S_K \\ + |\partial\Omega_K \cap \Gamma_N| \mathbf{n}_K^{(N)} \cdot \mathbf{j} + |\partial\Omega_K \cap \Gamma_D| \mathbf{n}_K^{(D)} \cdot \mathbf{j},$$

for $K \in \{1 \dots N_{\text{nodes}}\}$. Here, u_K is the average value of u on the K -th control volume

$$u_K(t) = \frac{1}{|\Omega_K|} \int_{\Omega_K} d^d r u(\mathbf{r}, t),$$

$S_K = S(u_K)$, $|\Omega_K|$ is the cell volume, $|\partial\Omega_K \cap \partial\Omega_L|$ is the interface volume of adjacent cells and $\mathcal{N}(K)$ is the list of cells adjacent to the K -th control volume. The boundary surface volumes $|\partial\Omega_K \cap \Gamma_N|$, $|\partial\Omega_K \cap \Gamma_D|$ vanish for interior cells that do not touch the boundary. With $\mathbf{n}_{K,L} = (\mathbf{r}_L - \mathbf{r}_K) / \|\mathbf{r}_L - \mathbf{r}_K\|$ and the boundary conditions, one obtains

$$0 = |\Omega_K| \frac{d}{dt} u_K + \sum_{L \in \mathcal{N}(K)} s_{K,L} j_{K,L} - |\Omega_K| S_K \\ + |\partial\Omega_K \cap \Gamma_N| g(u_K) + P |\partial\Omega_K \cap \Gamma_D| (u_K - u_D)$$

where $j_{K,L} = (\mathbf{r}_L - \mathbf{r}_K) \cdot \mathbf{j}$ is the flux projection on the edge $\mathbf{r}_{K,L} = s\mathbf{r}_L + (1-s)\mathbf{r}_K$ (with $s \in [0, 1]$), and $s_{K,L}$ is the edge factor defined in Eq. (3.1). For practical reasons, the Dirichlet boundary condition has been replaced by a boundary condition of third kind $\mathbf{n} \cdot \mathbf{j} = P(u(\mathbf{r}, t) - u_D(\mathbf{r}, t))$ on Γ_D , which recovers the original condition in the limit $P \rightarrow \infty$ (P is called a *penalty value*). In finite precision arithmetics, an accurate result is obtained for very large values of P due to numerical cancellation. The time derivative is discretized by an implicit Euler method with time step $\Delta t^{(i)} = t^{(i)} - t^{(i-1)}$ yielding

$$F_{u_K^{(i)}} = |\Omega_K| (u_K^{(i)} - u_K^{(i-1)}) + \Delta t^{(i)} \sum_{L \in \mathcal{N}(K)} s_{K,L} j_{K,L}^{(i)} - \Delta t^{(i)} |\Omega_K| S_K^{(i)} + \\ + \Delta t^{(i)} |\partial\Omega_K \cap \Gamma_N| g(u_K^{(i)}) + \Delta t^{(i)} P |\partial\Omega_K \cap \Gamma_D| (u_K^{(i)} - u_D(t_i)). \quad (3.3)$$

The stationary limit is recovered for $\Delta t^{(i)} \rightarrow \infty$.

The discrete fluxes $j_{K,L}$ are required to obey the symmetry property

$$j_{K,L} = -j_{L,K},$$

which ensures that flux entering the volume Ω_K from an adjacent cell Ω_L is equal to the flux leaving the cell Ω_L towards Ω_K (cf. Fig. 3.3).

In problems with spatially varying or jumping parameters (e.g., semiconductor het-

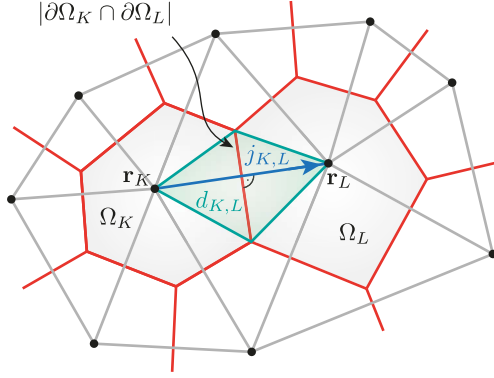


Fig. 3.3 Flux between two Voronoi boxes. The flux projection $j_{K,L} = (\mathbf{r}_K - \mathbf{r}_L) \cdot \mathbf{j}$ along the edge $\mathbf{r}_{K,L}$ is weighted by the edge factor $s_{K,L}$ that is related to the diamond volume $d_{K,L} = \frac{1}{d} s_{K,L} \|\mathbf{r}_L - \mathbf{r}_K\|^2$.

erostructures), Eq. (3.3) generalizes to

$$F_{u_K^{(i)}} = \sum_r \left(|\Omega_K \cap \Omega_r| (u_{K,r}^{(i)} - u_{K,r}^{(i-1)}) + \Delta t^{(i)} \sum_{L \in \mathcal{N}(K)} s_{K,L,r} j_{K,L,r}^{(i)} - \Delta t^{(i)} |\Omega_K \cap \Omega_r| S_{K,r}^{(i)} + \Delta t^{(i)} |\partial \Omega_K \cap \partial \Omega_r \cap \Gamma_N| g_r(u_{K,r}^{(i)}) + \Delta t^{(i)} P |\partial \Omega_K \cap \partial \Omega_r \cap \Gamma_D| (u_{K,r}^{(i)} - u_{D,r}(t_i)) \right),$$

with $s_{K,L,r} = |\partial \Omega_K \cap \partial \Omega_L \cap \partial \Omega_r| / \|\mathbf{r}_L - \mathbf{r}_K\|$, where $\Omega = \sum_{r=1}^{N_{\text{regions}}} \Omega_r$ is a partition of the computation domain into regions with common parameter sets (e.g., material coefficients).

3.2 Discrete van Roosbroeck system

Following the steps outlined above, the Voronoi box-based finite volume discretization of the van Roosbroeck system (2.1) introduced in Sec. 2.1 is obtained as

$$F_{\phi_K^{(i)}} = \sum_r \left(\sum_{L \in \mathcal{N}(K)} s_{K,L,r} D_{K,L,r}^{(i)} - q |\Omega_K \cap \Omega_r| (p_{K,r}^{(i)} - n_{K,r}^{(i)} + C_{K,r}) + P \sum_{\alpha} |\partial \Omega_K \cap \partial \Omega_r \cap \partial \Gamma_{D,\alpha}| (\phi_K^{(i)} - U_{\alpha}(t^{(i)})) \right), \quad (3.4a)$$

$$F_{\phi_{n,K}^{(i)}} = \sum_r \left(|\Omega_K \cap \Omega_r| (n_{K,r}^{(i)} - n_{K,r}^{(i-1)}) - \frac{1}{q} \Delta t^{(i)} \sum_{L \in \mathcal{N}(K)} s_{K,L,r} j_{n,K,L,r}^{(i)} - \Delta t^{(i)} P \sum_{\alpha} |\partial \Omega_K \cap \partial \Omega_r \cap \partial \Gamma_{D,\alpha}| (U_{\alpha}(t^{(i)}) - \phi_{n,K}^{(i)}) + \Delta t^{(i)} |\Omega_K \cap \Omega_r| \sum_r R_{K,r}^{(i)} \right), \quad (3.4b)$$

$$\begin{aligned}
 F_{\phi_{p,K}^{(i)}} = & \sum_r \left(|\Omega_K \cap \Omega_r| (p_{K,r}^{(i)} - p_{K,r}^{(i-1)}) + \frac{1}{q} \Delta t^{(i)} \sum_{L \in \mathcal{N}(K)} s_{K,L,r} j_{p,K,L,r}^{(i)} + \right. \\
 & + \Delta t^{(i)} P \sum_{\alpha} |\partial\Omega_K \cap \partial\Omega_r \cap \partial\Gamma_{D,\alpha}| (\phi_{p,K}^{(i)} - U_{\alpha}(t^{(i)})) + \\
 & \left. + \Delta t^{(i)} |\Omega_K \cap \Omega_r| \sum_r R_{K,r}^{(i)} \right). \quad (3.4c)
 \end{aligned}$$

The carrier densities on the K -th Voronoi cell are given as

$$n_K^{(i)} = \frac{1}{|\Omega_K|} \sum_r |\Omega_K \cap \Omega_r| n_{K,r}^{(i)}, \quad p_K^{(i)} = \frac{1}{|\Omega_K|} \sum_r |\Omega_K \cap \Omega_r| p_{K,r}^{(i)},$$

with the carrier densities on partitions of the restricted Voronoi cells

$$\begin{aligned}
 n_{K,r}^{(i)} &= N_{c,r} F_{1/2}(\eta_{n,K,r}^{(i)}), & \eta_{n,K,r}^{(i)} &= (-E_{c,r} + q\phi_K^{(i)} - q\phi_{n,K}^{(i)})/(k_B T), \\
 p_{K,r}^{(i)} &= N_{v,r} F_{1/2}(\eta_{p,K,r}^{(i)}), & \eta_{p,K,r}^{(i)} &= (+E_{v,r} - q\phi_K^{(i)} + q\phi_{p,K}^{(i)})/(k_B T).
 \end{aligned}$$

Because of possible jumps in the material parameters $E_{c,v}$ and $N_{c,v}$, the carrier densities may exhibit discontinuities at the material interfaces. Therefore, carrier densities do not represent suitable basic variables in the case of heterostructure devices. Throughout this thesis, the quasi-Fermi potentials $\phi_n = -q\mu_c$ and $\phi_p = -q\mu_v$, which are closely related to the quasi-Fermi energies, are used as basic variables in the numerical method. The doping profile C can be prescribed either in a domain-based, a vertex-based or in a hybrid fashion as $C_{K,r} = C_r + C_K$. The discrete displacement flux in Poisson's Eq. (3.4a) reads

$$D_{K,L,r}^{(i)} = (\mathbf{r}_L - \mathbf{r}_K) \cdot \mathbf{D}_{K,L,r}^{(i)} = -\varepsilon_r (\phi_L^{(i)} - \phi_K^{(i)}),$$

where the subscript r labels the region. The discrete recombination rate is (cf. Eq. (2.15))

$$R_{K,r}^{(i)} = R_r(\phi_K^{(i)}, \phi_{n,K}^{(i)}, \phi_{p,K}^{(i)}) = (1 - e^{\frac{q}{k_B T}(\phi_{n,K}^{(i)} - \phi_{p,K}^{(i)})}) \sum_{\alpha} r_{\alpha,r}(\phi_K^{(i)}, \phi_{n,K}^{(i)}, \phi_{p,K}^{(i)}). \quad (3.5)$$

Dirichlet boundary values are enforced via the penalty value method described above. Following Sec. 2.1.5, on Γ_N only homogeneous Neumann boundary conditions are considered, which do not occur in the discretization (3.4) (natural boundary conditions). A note on the numerical evaluation of Fermi–Dirac integrals is given in Appx. A.3.

3.3 Scharfetter–Gummel schemes for Fermi–Dirac statistics

This section deals with the Scharfetter–Gummel method for the robust discretization of the current densities in numerical semiconductor device simulation. After a brief introduction to the classical approach suggested by D. L. Scharfetter and H. K. Gummel in Ref. [268], several recent generalizations of the method towards Fermi–Dirac statistics are reviewed and assessed with respect to their structural properties and accuracy. The presentation given here goes beyond the recent review given in Ref. [69], as it extends the comparison to a larger number of approaches and provides a systematic analysis of their asymptotic features in important limiting cases.

3.3.1 Classical Scharfetter–Gummel scheme

The discrete van Roosbroeck system (3.4) must be supplemented by an expression for the edge current densities $j_{n,K,L,r}$ and $j_{p,K,L,r}$. The typically exponentially increasing or decreasing doping profiles (and therefore of electrons and holes) in semiconductor devices lead to numerical instabilities when using the standard finite difference discretization. In particular, the naive discretization approach results in spurious oscillations and may cause unphysical results such as negative carrier densities [40, 69]. A robust discretization scheme for the drift-diffusion current was given by D. L. Scharfetter and H. K. Gummel in 1969 [268], who explicitly solved the current density expression as a separate differential equation along the edge between two nodes of the mesh. This yields a discrete current formula with exponential terms, that reflects the characteristics of the doping profile and allows for numerically stable calculations. The so-called Scharfetter–Gummel scheme is an *exponential fitting method* [40], that smoothly interpolates between the central difference approximation for diffusive currents and the upwind scheme for convection currents. With the advent of the Scharfetter–Gummel discretization it became possible to accurately deal with the stiff solutions of the van Roosbroeck system on coarse grids such that practically relevant devices could be studied with reasonable computational effort [204].

The Scharfetter–Gummel scheme is obtained from the drift-diffusion form of the current density (2.11), projected on the edge $\mathbf{r}_{K,L} = s\mathbf{r}_L + (1-s)\mathbf{r}_K$ ($s \in [0, 1]$)

$$j_{n,K,L} = (\mathbf{r}_L - \mathbf{r}_K) \cdot \mathbf{j}_n = -qM_n n (\phi_L - \phi_K) + M_n k_B T g(n/N_c) (\mathbf{r}_L - \mathbf{r}_K) \cdot \nabla n.$$

Here, $j_{n,K,L}$ is the current density projection, $(\mathbf{r}_L - \mathbf{r}_K) \cdot \mathbf{E} = -(\phi_L - \phi_K)$ is the projected electric field and M_n is the mobility along the edge. The time-step index (i) and the region index r are omitted throughout this section ($j_{n,K,L,r}^{(i)} \equiv j_{n,K,L}$) as all quantities are evaluated at equal instances of time in a homogeneous material domain.¹ Integration along the edge \overline{KL} with $\int_0^1 ds (\mathbf{r}_L - \mathbf{r}_K) = \int_{\mathbf{r}_K}^{\mathbf{r}_L} d\mathbf{r}$ yields the two-point boundary value problem

$$\frac{q(\phi_L - \phi_K)}{k_B T} = \int_{\mathbf{r}_K}^{\mathbf{r}_L} d\mathbf{r} \cdot \frac{g(n/N_c)}{\frac{j_{n,K,L}}{qM_n(\phi_L - \phi_K)} + n} \nabla n, \quad (3.6a)$$

$$n(\mathbf{r}_K) = n_K, \quad (3.6b)$$

$$n(\mathbf{r}_L) = n_L, \quad (3.6c)$$

which is an integral equation for the edge current $j_{n,KL}$.

In the case of linear diffusion $g(n/N_c) \equiv 1$, the integral can be solved analytically

$$\frac{q(\phi_L - \phi_K)}{k_B T} = \int_{n_K}^{n_L} dn \frac{1}{\frac{j_{n,KL}}{qM_n(\phi_L - \phi_K)} + n} = \log \left(\frac{j_{n,KL}}{qM_n N_c (\phi_L - \phi_K)} + \frac{n}{N_c} \right) \Big|_{n_K}^{n_L},$$

yielding the classical Scharfetter–Gummel expression for the discrete current density [268]

$$j_{n,KL}^{\text{SG}} = M_n k_B T \left(n_L B \left(\frac{q(\phi_L - \phi_K)}{k_B T} \right) - n_K B \left(-\frac{q(\phi_L - \phi_K)}{k_B T} \right) \right) \quad (3.7)$$

¹ Using restricted Voronoï cells based on a boundary conforming Delaunay triangulation, the discrete current expression is required only *along* and never *across* material interfaces. At heterointerfaces, the discrete fluxes along the segment are weighted by the edge factors $s_{KL,r}$ of the adjacent domains.

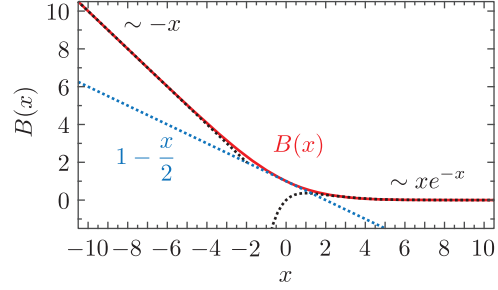


Fig. 3.4 Plot of the Bernoulli function $B(x)$. The asymptotics for small and large arguments, which are crucial for the asymptotic correctness of the Scharfetter–Gummel scheme (3.7) in the diffusion- and drift-dominated limits, are shown as dashed lines.

with the so-called *Bernoulli function*

$$B(x) = \frac{x}{e^x - 1} \quad (3.8)$$

that is depicted in Fig. 3.4. An analogous expression is obtained for the discrete hole current density. The formula (3.7) has several remarkable properties: First, in case of vanishing electric fields, it reduces to the central difference scheme

$$j_{n,KL}^{\text{cd}} = \lim_{\phi_L \rightarrow \phi_K} j_{n,KL}^{\text{SG}} = M_n k_B T (n_L - n_K) = q D_n (n_L - n_K) \quad (3.9)$$

(with the linear diffusion constant $D_n = M_n k_B T / q$), that is an appropriate discretization for diffusion currents in the absence of drift [69]. Second, in the limit of high field strength (which is important, e.g., at p-n junctions and heterointerfaces), Eq. (3.7) recovers by virtue of the asymptotics of the Bernoulli function (cf. Fig. 3.4) the upwind scheme

$$j_{n,KL}^{\text{upw}} = \lim_{\phi_L - \phi_K \rightarrow \pm\infty} j_{n,KL}^{\text{SG}} = -q M_n (\phi_L - \phi_K) \times (n_K \Theta(\phi_L - \phi_K) + n_L \Theta(-[\phi_L - \phi_K])), \quad (3.10)$$

that is suitable for the discretization of drift-dominated currents [69]. Finally, in the thermodynamic equilibrium the Scharfetter–Gummel formula (3.7) obeys the detailed balance condition, as the flux vanishes exactly under equilibrium conditions

$$\lim_{\substack{n \rightarrow n^{\text{eq}} \\ \phi \rightarrow \phi^{\text{eq}}}} j_{n,KL}^{\text{SG}} = M_n k_B T \left(n_L^{\text{eq}} - n_K^{\text{eq}} e^{\frac{q}{k_B T} (\phi_L^{\text{eq}} - \phi_K^{\text{eq}})} \right) B \left(\frac{q (\phi_L^{\text{eq}} - \phi_K^{\text{eq}})}{k_B T} \right) = 0.$$

This follows from $B(-x) = e^x B(x)$ and the identity $n_L^{\text{eq}} \exp\left(-\frac{q\phi_L^{\text{eq}}}{k_B T}\right) \equiv n_K^{\text{eq}} \exp\left(-\frac{q\phi_K^{\text{eq}}}{k_B T}\right)$ holding in the case of Maxwell–Boltzmann statistics, that was implicitly assumed above by restricting the considerations to linear diffusion (cf. Sec. 2.1.3).

3.3.2 Generalized schemes for Fermi–Dirac statistics

As pointed out in Secs. 2.1.2 and 2.1.3, the classical Maxwell–Boltzmann approximation for the carrier density breaks down at cryogenic temperatures and degeneration effects due to the Pauli exclusion principle need to be taken into account. For the discretization of the current density, this requires a generalization of the Scharfetter–Gummel scheme towards Fermi–Dirac statistics. The classical Scharfetter–Gummel scheme (3.7) inherently assumes Maxwell–Boltzmann statistics and is not applicable anymore in the presence of strong nonlinear diffusion (see below). However, there is no closed form solution of the

integral problem (3.6) in the case of Fermi–Dirac statistics, such that one has to resort to approximations. At the same time, it is highly desirable to keep the structural properties of the Scharfetter–Gummel scheme (see Sec. 3.3.1) in any generalization of the method.

In the recent years, several generalizations of the Scharfetter–Gummel scheme for Fermi–Dirac statistics have been proposed. This section is restricted to generalized schemes that are consistent with the thermodynamic equilibrium, which is considered a high priority [67, 68, 77, 172, 174]. These approaches will be reviewed and compared in the following with respect to their structural properties. Finally, an assessment of the different discretizations will be given by comparison with a numerically exact solution in Sec. 3.3.2.4. Note that the consistency with the thermodynamic equilibrium is not trivially fulfilled. There are several generalizations of the Scharfetter–Gummel scheme for generalized Einstein relations (e.g., Refs. [149, 239, 293]) that violate the equilibrium condition and yield an unphysical steady state dissipation in the discrete system.

In the following, generalizations of the Scharfetter–Gummel scheme are considered for carrier ensembles obeying Fermi–Dirac statistics with an arbitrary (non-negative) density of states function $D(E)$. The electron density is assumed as

$$n = \int_{\mathbb{R}} dE D_c(E) f\left(\frac{E - q\phi + q\phi_n}{k_B T}\right) = N_c(T) \mathcal{F}(\eta_n)$$

with $D_c(E) \geq 0$, $\mathcal{F} \geq 0$, $\mathcal{F}(\eta_n \rightarrow -\infty) \sim e^{\eta_n}$ and $\eta_n = (-E_c + q\phi - q\phi_n)/(k_B T)$.² The applications considered throughout this thesis assume the case $\mathcal{F}(\eta) = F_{1/2}(\eta)$, but the methods outlined below are also applicable to the Gauss–Fermi integral (in organic semiconductors) [206], dimension-reduced nanostructures (e.g., quantum wells with $\mathcal{F}(\eta) = F_0(\eta)$) or the Blakemore approximation for modest degeneracy [32, 69, 172].

3.3.2.1 Modified thermal voltage scheme

Following Refs. [27, 173, 174], the problem (3.6) can be solved approximately by taking a suitable average of the degeneracy factor along the edge $\mathbf{r}_{K,L}$ such that Eq. (3.6a) becomes

$$\frac{q(\phi_L - \phi_K)}{k_B T} \approx g_{n,K,L} \int_{\mathbf{r}_K}^{\mathbf{r}_L} d\mathbf{r} \cdot \frac{1}{\frac{j_{n,K,L}}{qM_n(\phi_L - \phi_K)} + n} \nabla n.$$

This can be solved along the same lines presented in Sec. 3.3 and lead to

$$j_{n,K,L}^{\text{mod}U_T} = M_n k_B T g_{n,K,L} \left(n_L B \left(\frac{q(\phi_L - \phi_K)}{k_B T g_{n,K,L}} \right) - n_K B \left(-\frac{q(\phi_L - \phi_K)}{k_B T g_{n,K,L}} \right) \right). \quad (3.11)$$

This corresponds to a formal rescaling of the thermal voltage $U_T = k_B T/q \rightarrow k_B T g_{n,K,L}/q$, such that Eq. (3.11) is referred to as the *modified thermal voltage scheme*. By taking the edge averaged degeneracy factor as

$$g_{n,K,L} = \frac{\mathcal{F}^{-1}(n_K/N_c) - \mathcal{F}^{-1}(n_L/N_c)}{\log(n_K/n_L)} = \frac{\eta_{n,K} - \eta_{n,L}}{\log(\mathcal{F}(\eta_{n,K})/\mathcal{F}(\eta_{n,L}))}, \quad (3.12)$$

the scheme (3.11) vanishes exactly under equilibrium conditions [174]. For, without loss of generality, $\eta_{n,K} \leq \eta_{n,L}$, the edge averaged degeneracy factor satisfies the inequality

$$g_{n,K} \leq g_{n,K,L} \leq g_{n,L} \quad (3.13)$$

² In general, the meaning of E_c depends on the context.

(or vice versa for $\eta_{n,K} \geq \eta_{n,L}$) with the nodal values $g_{n,K} = g(n_K/N_c)$, $g_{n,L} = g(n_L/N_c)$ and $g(x)$ as defined in Eq. (2.13). Therefore, the scheme (3.11) with $g_{n,K,L}$ replaced by the nodal values $g_{n,K}$, $g_{n,L}$ provides a lower and upper bound for the exact solution of Eq. (3.6). Moreover, Eq. (3.11) asymptotically approaches a modified version of the central difference scheme (3.9) (with the nonlinear diffusion constant $D_{n,K,L} = M_n k_B T g_{n,K,L}/q$)

$$j_{n,K,L}^{\text{cd,mod } U_T} = \lim_{\phi_L \rightarrow \phi_K} j_{n,K,L}^{\text{mod } U_T} = M_n k_B T g_{n,K,L} (n_L - n_K) \quad (3.14)$$

and the upwind scheme (3.10) in the corresponding diffusion- und drift-dominated limits.

3.3.2.2 Modified effective density of states scheme

Another generalization of the Scharfetter–Gummel scheme is obtained by substituting $n = N_c \mathcal{F}(\eta_n)$ and $g(n/N_c) = g(\mathcal{F}(\eta_n)) = \mathcal{F}(\eta_n)/\mathcal{F}'(\eta_n)$ (cf. Eq. (2.14)) in Eq. (3.6), such that

$$\frac{q(\phi_L - \phi_K)}{k_B T} = \int_{\mathbf{r}_K}^{\mathbf{r}_L} d\mathbf{r} \cdot \frac{1}{1 + \frac{j_{n,K,L}}{q M_n (\phi_L - \phi_K) N_c \mathcal{F}(\eta_n)}} \nabla \eta_n.$$

With the help of the *correction factor*

$$\gamma(\eta) = \mathcal{F}(\eta) e^{-\eta}, \quad (3.15)$$

$0 < \gamma < 1$, the function \mathcal{F} can be mapped on an exponential. By freezing the correction factor on a suitable average value $\gamma_{n,K,L}$ along the edge, the integral can be solved by partial fraction decomposition. Finally, the discrete flux formula is obtained as

$$j_{n,K,L}^{\text{mod } N_c} = M_n k_B T \gamma_{n,K,L} \left(\frac{n_L}{\gamma_{n,L}} B \left(\frac{q(\phi_L - \phi_K)}{k_B T} \right) - \frac{n_K}{\gamma_{n,K}} B \left(-\frac{q(\phi_L - \phi_K)}{k_B T} \right) \right) \quad (3.16)$$

with the nodal values $\gamma_{n,L} = \gamma(\eta_{n,L})$, $\gamma_{n,K} = \gamma(\eta_{n,K})$ of the correction factor. This approach is used in, e.g., electrochemistry [77]. In analogy to the scheme described above, it is referred to as the *modified effective density of states scheme* [67]. The scheme is consistent with the thermodynamic equilibrium independent of the choice of $\gamma_{n,K,L}$. However, the asymptotic correctness in the limiting cases of pure drift or diffusive currents is violated in general [67]. Typical choices of the edge averaged correction factor are arithmetic and geometric averages of the nodal values $\gamma_{n,K,L}^{(\text{geom})} = \sqrt{\gamma_{n,K} \gamma_{n,L}}$ or $\gamma_{n,K,L}^{(\text{arith})} = (\gamma_{n,K} + \gamma_{n,L})/2$.

3.3.2.3 Modified advection scheme

The current density with the generalized Einstein relation (2.10a) can be written as [90, 286, 301, 329]

$$\mathbf{j}_n = -q M_n n \nabla \left(\phi + \frac{k_B T}{q} \log \gamma(\eta_n) \right) + q \frac{M_n k_B T}{q} \nabla n, \quad (3.17)$$

where the nonlinear correction of the diffusion constant was rewritten as a modification of the electric field $\nabla \phi \rightarrow \nabla \left(\phi + \frac{k_B T}{q} \log \gamma(\eta_n) \right)$ by using the correction factor (3.15) and $g(n/N_c) = 1 - n/\gamma(\eta_n) \frac{\partial}{\partial n} \gamma(\eta_n)$. The discretization of Eq. (3.17) is obtained by integrating the projection of the current along the edge $\mathbf{r}_{K,L}$ under the assumption that

$\log \gamma(\eta_n)$ is linear along the segment. From

$$1 = \int_{\mathbf{r}_K}^{\mathbf{r}_L} d\mathbf{r} \cdot \frac{\nabla n}{\frac{j_{n,K,L}}{M_n k_B T} + n \left(\frac{q(\phi_L - \phi_K)}{k_B T} + \log \left(\frac{\gamma(\eta_{n,L})}{\gamma(\eta_{n,K})} \right) \right)}$$

one obtains (along the same lines as in Sec. 3.3.1) the modified Scharfetter–Gummel scheme

$$j_{n,K,L}^{\text{mod.con.}} = M_n k_B T \left(n_L B \left(\frac{q(\phi_L - \phi_K)}{k_B T} + \log \left(\frac{\gamma(\eta_{n,L})}{\gamma(\eta_{n,K})} \right) \right) - n_K B \left(- \left[\frac{q(\phi_L - \phi_K)}{k_B T} + \log \left(\frac{\gamma(\eta_{n,L})}{\gamma(\eta_{n,K})} \right) \right] \right) \right). \quad (3.18)$$

In the following, Eq. (3.18) is called the *modified advection scheme*. It is exact in the thermodynamic equilibrium and asymptotically approaches the upwind scheme (3.10) at high electric fields along the edge. However, if at least one of the nodal carrier density values n_K, n_L is high (such that $\mathcal{F}^{-1}(n/N_c) \gg \log(n/N_c)$) and their gradient along the edge is large $n_K \ll n_L$ (or vice versa), the convergence to the upwind scheme is slow, i.e.,

$$j_{n,K,L}^{\text{mod.con.}} \underset{\phi_L - \phi_K \rightarrow \infty}{\sim} -q M_n \left(\phi_L - \phi_K + \frac{k_B T}{q} \log \left(\frac{e^{\mathcal{F}^{-1}(\frac{n_K}{N_c}) - \mathcal{F}^{-1}(\frac{n_L}{N_c})}}{n_K/n_L} \right) \right) n_K.$$

A variant of the approach is considered in Refs. [13, 80, 83].

3.3.2.4 Exact solution and comparison with approximate schemes

Following Refs. [65, 84, 172], the problem (3.6) can be written as an integral equation

$$\frac{q(\phi_L - \phi_K)}{k_B T} = \int_{\eta_K}^{\eta_L} \frac{d\eta}{1 + \frac{j_{n,K,L}^{\text{exact}}}{q M_n (\phi_L - \phi_K) N_c \mathcal{F}(\eta)}}, \quad (3.19)$$

which implicitly defines the current $j_{n,K,L}^{\text{exact}} = j_{n,K,L}^{\text{exact}}(\phi_L - \phi_K, \eta_K, \eta_L)$. For a given triple $(\phi_L - \phi_K, \eta_K, \eta_L)$, the problem (3.19) can be solved by a Newton iteration in $j_{n,K,L}$, where the integral is evaluated by Gaussian quadrature [68]. This yields a numerically exact reference value to assess the quality of the approximate schemes (3.11), (3.16) and (3.18).

The numerically exact solution of Eq. (3.19) is shown along with the classical Scharfetter–Gummel scheme (3.7) and the modified schemes (3.11), (3.16), (3.18) in Fig. 3.5. The plot compares the schemes at very high carrier densities $n_K = 1 \times 10^{18} \text{ cm}^{-3}$ and $n_L = 3 \times 10^{18} \text{ cm}^{-3}$ (for GaAs data [232]), such that strong degeneration effects are enforced and discrepancies due to the different treatment of the nonlinear diffusion are enhanced (in particular at low T). At low carrier densities, the degeneration effects are negligible and all considered schemes recover the classical Scharfetter–Gummel result (3.7).

First, all generalized Scharfetter–Gummel schemes (3.11), (3.16) (for any average of the correction factor) and (3.18) match the exact result in the thermodynamic equilibrium³ (indicated by black dotted lines). The classical Scharfetter–Gummel scheme (3.7) is valid for Maxwell–Boltzmann statistics and therefore predicts a wrong equilibrium solution in the degenerate case. Consequently, this yields a finite current in the actual equilibrium.

³ For given nodal values of the electron density n_K, n_L and identical quasi-Fermi potentials, the thermodynamic equilibrium corresponds to a finite built-in electric field $\sim (\phi_L - \phi_K)$ along the edge.

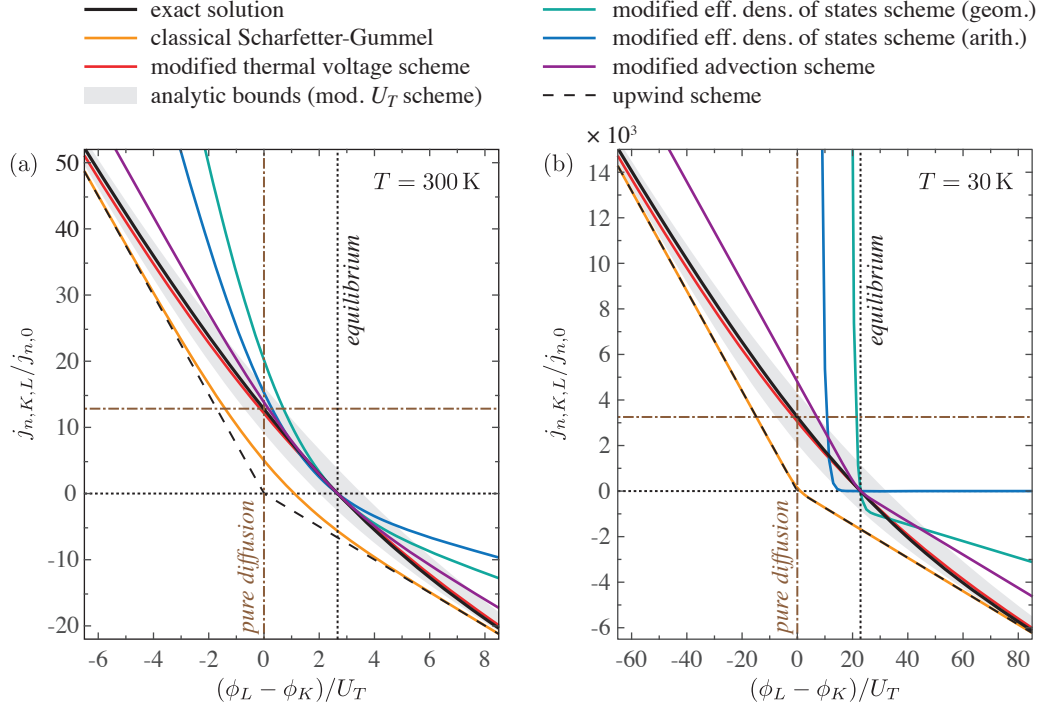


Fig. 3.5 Plot of the generalized Scharfetter–Gummel schemes for the discrete current density. The exact solution of the integral equation (3.19) is plotted along with the approximate solutions (3.11), (3.16) and (3.18). The classical Scharfetter–Gummel scheme (3.7) is shown for comparison. The plot indicates the position of the thermodynamic equilibrium ($j_{n,K,L}^{\text{exact}} = 0$, dotted black lines), the pure diffusion limit ($\phi_L - \phi_K = 0$, dash-dotted lines) and the drift-dominated limit (upwind scheme (3.10), dashed line). The shaded region indicates the analytical bounds obtained from the modified thermal voltage scheme (3.11) with nodal values of the degeneracy factors. The schemes are compared at two different temperatures: (a) $T = 300$ K and (b) $T = 30$ K. The nodal values of the electron density adjacent to the segment are $n_K = 1 \times 10^{18} \text{ cm}^{-3}$ and $n_L = 3 \times 10^{18} \text{ cm}^{-3}$. GaAs material parameters are taken for $N_c(T) \sim (m_e^*(T)T)^{3/2}$ and $E_c = E_c(T)$ [232]. The current density projection is non-dimensionalized with $j_{n,0} = M_n k_B T N_c(T)$.

Next, the behavior at strong electric fields $(\phi_L - \phi_K) \rightarrow \pm\infty$ shall be analyzed. In this case, the modified thermal voltage scheme (3.11) as well as the exact solution approach the upwind scheme (3.10), which becomes asymptotically exact in the limit of an infinite voltage drop along the edge $\mathbf{r}_{K,L}$. As degeneration effects become increasingly meaningless in this drift-dominated limit, also the classical Scharfetter–Gummel scheme (3.7) is pretty accurate in the high-field limit. On the other hand, the modified density of states schemes (3.16) completely fail in the high-field limit: They do not become asymptotically independent of the correction factors (3.15) in the high-field limit and thereby do not approach the upwind scheme (3.10). The error becomes even more dramatic, if the temperature is decreased (see Fig. 3.5 (b)). In the low temperature case the mapping of the Fermi–Dirac integral on an exponential via Eq. (3.15) becomes even worse ($\gamma \rightarrow 0$) and the scheme is more sensitive to the (enlarged) mismatch between the two nodal values $\gamma_{n,K}$, $\gamma_{n,L}$ and the edge average $\gamma_{n,KL}$. Therefore, the usage of the modified density of states schemes (3.16) is restricted to very fine meshes, such that the electric potential differences along the edges can remain small. This is a seriously impractical restriction for the simulation of semiconductor devices,

where one typically has to deal with strong internal fields at p-n junction and material interfaces. The high-field limit clearly discriminates the schemes (3.11) and (3.16), where the modified thermal voltage scheme (3.11) is superior as it provides high accuracy already on rather coarse grids. The relative error of the modified advection scheme (3.18) becomes small at very high electric fields, however, at high carrier densities there is a significant deviation from the upwind scheme as both curves have constant offset in Fig. 3.5 (a) and (b). This slow convergence to the upwind scheme has been noticed in Sec. 3.3.2.3 already.

Finally, the purely diffusive limit at $\phi_L - \phi_K = 0$ is indicated by a dash-dotted line in Fig. 3.5. The modified thermal voltage scheme (3.11) provides a good approximation of the exact solution (note that it is however not exact). As before, the modified density of states schemes (3.16) and the modified advection scheme (3.18) are less accurate in this limit. The classical Scharfetter–Gummel scheme (3.7) is of course far away from the exact result, since the treatment of the nonlinear diffusion is crucial in this case.

Details on the accuracy of the generalized Scharfetter–Gummel schemes (3.11) and (3.16) including analytical error estimates can be found in Refs. [67, 68]. The different schemes are implemented in the semiconductor simulation package *ddfermi* [59].

3.4 Structure preserving properties of the discretization

The overall goal of numerical simulations is the approximate solution of mathematical models (e.g., partial differential equations) that can not be solved by elementary means. The quality of the numerical results is to a large extent determined by the discretization method. A discretization is called *structure preserving*, if essential features of the continuous model are reflected in its discrete counterpart. This includes, e.g., the validity of conservation laws on the discrete level, without additional smallness assumptions on the mesh size.

The finite volume Scharfetter–Gummel discretization of the van Roosbroeck system outlined above is an outstanding example for a structure preserving discretization. This comprises the conservation of charge Eq. (2.49a), whose discrete counterpart (in the sense of the weak formulation) is easily obtained by the subtracting Eqs. (3.4c) and (3.4b). Moreover, the Scharfetter–Gummel currents subject to Sec. 3.3.2 obey the detailed balance principle in the thermodynamic equilibrium as they vanish exactly under equilibrium conditions (see Fig. 3.5). The same holds true for the discrete recombination rate (3.5). Also the consistency with the second law of thermodynamics survives on the discrete level, as the discrete entropy production rate

$$\begin{aligned} \frac{dS_{\text{tot}}^{(i)}}{dt} = \frac{1}{T} \sum_{r,K} \left[|\Omega_K \cap \Omega_r| q(\phi_{p,K}^{(i)} - \phi_{n,K}^{(i)}) R_{K,r}^{(i)} + \right. \\ \left. + \frac{1}{2} \sum_{L \in \mathcal{N}(K)} s_{K,L,r} \left(j_{n,K,L,r}^{(i)} (\phi_{n,K}^{(i)} - \phi_{n,L}^{(i)}) + j_{p,K,L,r}^{(i)} (\phi_{p,K}^{(i)} - \phi_{p,L}^{(i)}) \right) \right] \geq 0 \end{aligned} \quad (3.20)$$

is strictly non-negative for all Scharfetter–Gummel schemes consistent with the thermodynamic equilibrium (in particular those studied in Sec. 3.3.2). This is proved by casting all terms in Eq. (3.20) into the form $x(1 - e^{-x}) \geq 0$ (multiplied by a positive factor), where x is the non-dimensionalized Fermi voltage that drives the corresponding process.⁴

⁴ Note that in the discrete system all contributions are of the form $x(1 - e^{-x}) \geq 0$, whereas Joule heating is quadratic in the continuous case (cf. Sec. 2.3.2.3).

In the thermodynamic equilibrium, the discrete dissipation vanishes exactly. Therefore, the global stability of the thermodynamic equilibrium is guaranteed in the discrete case. Following Refs. [84, 86], also the uniqueness of the discrete solution at small voltages can be shown. A discrete analogue of the continuous maximum principle holding for elliptic and parabolic partial differential equations is encoded in the M-matrix property of the discrete Jacobian [81, 84].

3.5 Nonlinear iteration method

The discrete van Roosbroeck system is a system of coupled nonlinear algebraic equations

$$\mathbf{F}(\mathbf{u}) = 0, \quad (3.21)$$

where $\mathbf{F} = (F_{\phi_1} \dots F_{\phi_{N_{\text{nodes}}}}, F_{\phi_{n,1}} \dots F_{\phi_{n,N_{\text{nodes}}}}, F_{\phi_{p,1}} \dots F_{\phi_{p,N_{\text{nodes}}}})^T$ is given by Eq. (3.4).

Throughout this thesis, the vector of unknowns \mathbf{u} is given by the nodal values of the electrostatic potential ϕ and the quasi-Fermi potentials ϕ_n and ϕ_p as

$$\mathbf{u} = (\phi_1 \dots \phi_{N_{\text{nodes}}}, \phi_{n,1} \dots \phi_{n,N_{\text{nodes}}}, \phi_{p,1} \dots \phi_{p,N_{\text{nodes}}})^T.$$

In other works, the carrier densities n and p have been taken as basic variables of the discrete system [204, 278]. However, the usage of quasi-Fermi potentials has important advantages. Most important, the positivity of the discrete carrier densities is trivially guaranteed by the positivity of the Fermi–Dirac integral (or exponential in the Maxwell–Boltzmann case). This is not ensured if discrete carrier densities are used as basic variables instead, since the updates in the iteration procedure may overshoot to negative values. Moreover, the usage of quasi-Fermi potentials improves the scaling of the solution vector as all variables have identical physical dimension and take values on a similar order of magnitude. Hence, the numerical solution is expected to be more robust to round-off errors. Another practical advantage, which is important in the case of Fermi–Dirac statistics, addresses the assembly of the right hand side \mathbf{F} and the Jacobian J : When using quasi-Fermi potentials, only the numerical evaluation of the Fermi–Dirac integral $F_{1/2}$ and its derivative $F_{-1/2}$ is required, whereas when using carrier densities, additionally routines for the evaluation of the inverse $F_{1/2}^{-1}$ and its derivative $(F_{1/2}^{-1})'$ (see Eq. (3.12)) are needed.⁵ Finally, quasi-Fermi potentials simplify the initialization of the thermodynamic equilibrium problem as the exact solution $\phi_{n,K}^{\text{eq}} \equiv \phi_{p,K}^{\text{eq}} \equiv -\mu_{\text{eq}}/q \forall K \in \{1 \dots N_{\text{nodes}}\}$ is a global constant.

The system (3.21) can be solved iteratively by Newton’s method

$$\mathbf{u}^{(i+1)} = \mathbf{u}^{(i)} - J^{-1}(\mathbf{u}^{(i)})\mathbf{F}(\mathbf{u}^{(i)}),$$

where the Jacobian matrix reads

$$J = \begin{pmatrix} \frac{\partial F_{\phi_K}}{\partial \phi_L} & \frac{\partial F_{\phi_K}}{\partial \phi_{n,L}} & \frac{\partial F_{\phi_K}}{\partial \phi_{p,L}} \\ \frac{\partial F_{\phi_{n,K}}}{\partial \phi_L} & \frac{\partial F_{\phi_{n,K}}}{\partial \phi_{n,L}} & \frac{\partial F_{\phi_{n,K}}}{\partial \phi_{p,L}} \\ \frac{\partial F_{\phi_{p,K}}}{\partial \phi_L} & \frac{\partial F_{\phi_{p,K}}}{\partial \phi_{n,L}} & \frac{\partial F_{\phi_{p,K}}}{\partial \phi_{p,L}} \end{pmatrix}_{K,L=1 \dots N_{\text{nodes}}}. \quad (3.22)$$

⁵ There exist several approximations for $F_{1/2}^{-1}$ [46, 148, 227, 310], however their accuracies are below IEEE double precision and they do not match the economic approximations of $F_{1/2}$ (cf. Appx. A.3). While this may be acceptable for room temperature simulations, the deviations become significant at cryogenic temperatures. The derivative of the inverse can be computed by $(F_{1/2}^{-1})'(x) = (F_{-1/2}(F_{1/2}^{-1}(x)))^{-1}$, where $F_{1/2}^{-1}$ can be obtained by a Newton iteration using routines for $F_{1/2}$ and $F_{-1/2}$.

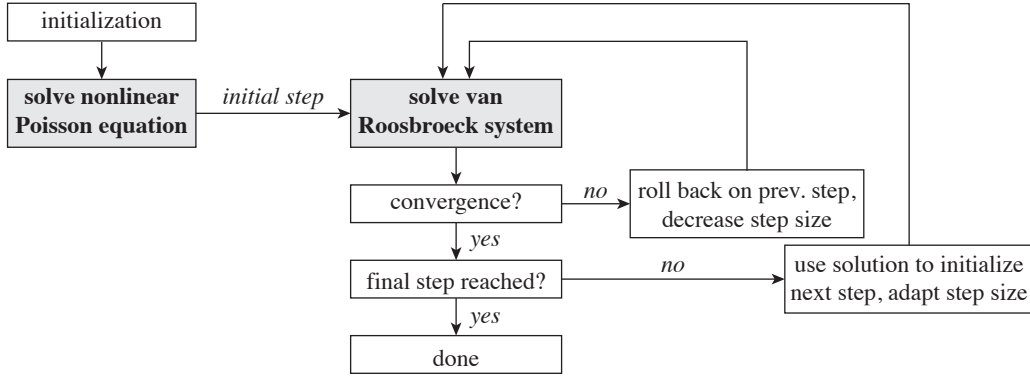


Fig. 3.6 Workflow for the computation of non-equilibrium states of the van Roosbroeck system. Starting from a suitable initialization, the thermodynamic equilibrium problem (nonlinear Poisson equation) is solved. Then, the van Roosbroeck system is solved repeatedly by Newton’s method while gradually changing the boundary conditions and constantly using the previously obtained solutions as a starting guess. The continuation procedure stops when the final step is reached.

Newton’s method converges quadratically if the starting guess $\mathbf{u}^{(0)}$ is sufficiently close to the solution [58]. This is a major advantage over other methods and allows to obtain highly accurate solutions after a few iteration steps at low computational cost. On the other hand, Newton’s method might converge very slow or even fail to converge if the starting guess is too far from the actual solution. The convergence region can be increased via (adaptive) damping [58], which however reduces the convergence rate. As an alternative to the full Newton iteration, Gummel suggested a decoupled approach that alternates between the solution of Poisson’s equation and the continuity equations [115]. The Gummel iteration method has a slower convergence rate but an increased convergence region in comparison to Newton’s method [79, 80].

The typical workflow in numerical semiconductor device simulation is depicted in Fig. 3.6. The method starts with the solution of the thermodynamic equilibrium problem from a suitable initialization. In this step only the nonlinear Poisson equation needs to be solved. Due to the strict monotonicity of the right hand side of Eq. (3.4a), the Newton method always converges. A useful initialization can be obtained from the local charge neutrality condition (2.20). Non-equilibrium solutions are obtained by solving the full system (3.4) using the thermodynamic equilibrium solution as a starting guess and slowly changing the Dirichlet boundary data (applied voltages, see Eq. (2.21)). The procedure is continued by gradually increasing the voltage and repeatedly using the previously obtained solutions as initialization, until the target state is reached. The procedure is shown in Fig. 3.6.

An important feature of the finite volume (or finite element) discretization is that it yields only next neighbor couplings in the discrete system. The Jacobian matrix is therefore sparsely populated such that economic storage schemes and sparse linear solver routines can be used. In 2D applications typically direct solvers such as UMFPACK [55] or PARDISO [235] can be used, which compute the LU-decomposition of the Jacobian. For very large systems (e.g., many vertices in 3D applications), the memory requirements and computational time of direct solvers increase, such that the usage of preconditioned (and precisely tuned) Krylov subspace methods [260] is beneficial [69].

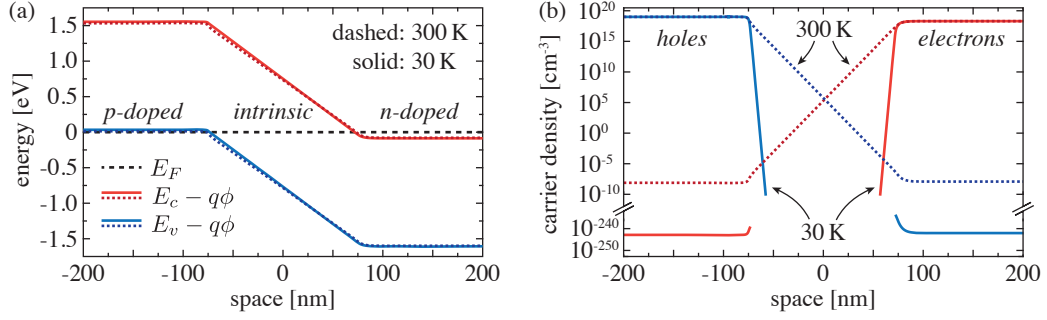


Fig. 3.7 Comparison of the thermodynamic equilibrium solution in a 1D pin-diode at 30 K and 300 K. Even though (a) the built-in potential and the energy bands differ only slightly, (b) the carrier density profiles vary drastically when passing from room temperature to the cryogenic case. The nonlinear Poisson equation is solved for a piecewise constant doping profile with $N_D^+ = 2 \times 10^{18} \text{ cm}^{-3}$, $N_A^- = 1 \times 10^{19} \text{ cm}^{-3}$ and low- T GaAs parameters $E_g = 1.52 \text{ eV}$, $\epsilon_r = 12.9$, $m_e^* = 0.063 m_0$, $m_h^* = 0.5 m_0$ (m_0 is the free electron mass). © 2016 Springer Science+Business Media. Reprinted, with permission, from Ref. [158].

3.6 Annealing method for simulation at cryogenic temperatures

At cryogenic operation temperatures, the numerical solution of the van Roosbroeck system is subject to serious convergence issues using the standard method described above. This is mainly caused by the extreme depletion of the minority carriers, which causes stiff boundary layers at p-n junctions and numerical underflow in finite precision arithmetics.

In the following, a one-dimensional pin-diode with low-temperature GaAs parameters (see captions of Figs. 3.7–3.8) is considered as a guiding example to the problem. The built-in potential and the equilibrium carrier density profiles are obtained by solving the nonlinear Poisson equation. The solutions are shown in Fig. 3.7 at $T = 300 \text{ K}$ and $T = 30 \text{ K}$. The built-in potential (see Fig. 3.7 (a)) is only weakly affected by the temperature, since complete dopant ionization due to the metal-insulator transition is assumed in the simulation (cf. Appx. A.1). The carrier density profiles depicted in Fig. 3.7 (b) range over many orders of magnitude and the minority carrier densities tend to become extremely small (scaling as $n_{\text{minor}} \approx n_{\text{intr}}^2/p_{\text{major}}$ in the p-doped domain) at cryogenic temperature. For comparison: The characteristic 300 K value of $n_{\text{minor}} \sim 10^{-8} \text{ cm}^{-3}$ drops down to around $n_{\text{minor}} \sim 10^{-240} \text{ cm}^{-3}$ at 30 K. This is caused by the high sensitivity of the carrier density on the position of the Fermi level with respect to the band gap, since the Fermi function (2.4) approaches a step function in the limit $T \rightarrow 0 \text{ K}$. This results in a strong temperature dependence of the intrinsic carrier density $n_{\text{intr}} \sim T^{3/2} \exp[-E_g(T)/(2k_B T)]$ (cf. Fig. 2.2 (b)) and the formation of extremely sharp layers between the intrinsic and doped regions (see Fig. 3.7 (b)). In order to highlight the temperature-induced degeneracy effects, only the explicit temperature-dependence in the carrier density expressions (2.6) is taken into account, whereas material parameters are kept constant throughout this section.

Because of the extreme depletion of the minority carriers at cryogenic temperatures, the typical workflow described in Sec. 3.5 leads to serious convergence issues close to the thermodynamic equilibrium. The Jacobian matrix (3.22) becomes practically singular to finite precision arithmetics as several rows belonging to the discrete continuity equations (3.4b)–(3.4c) contain solely close-to-zero values. The corresponding linear system is ill-

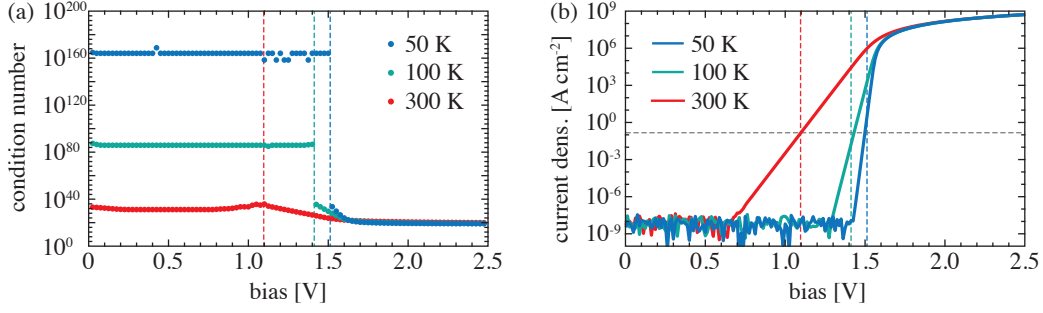


Fig. 3.8 (a) Condition number estimate $\kappa(J)$ of the Jacobian for the pin-diode problem at different temperatures and corresponding (b) current-voltage curves. The sudden drop of the condition number appears at the diode's threshold voltage. Next to the parameters listed in the caption of Fig. 3.7, the mobilities are $M_n = 20000 \text{ cm}^2 \text{ V}^{-1} \text{ s}^{-1}$, $M_p = 300 \text{ cm}^2 \text{ V}^{-1} \text{ s}^{-1}$ and the SRH life times are $\tau_n = 70 \text{ } \mu\text{s}$, $\tau_p = 200 \text{ } \mu\text{s}$ (other recombination channels are switched off). © 2016 Springer Science+Business Media. Reprinted, with permission, from Ref. [158].

conditioned and the matrix can not be inverted. As an indicator for the ill-posedness of the problem, the condition number $\kappa(J) = \|J^{-1}\| \cdot \|J\|$ of the Jacobian matrix is estimated by using an iterative procedure for the computation of the 1-norm $\|J^{-1}\|_1$ [118, 136]. Fig. 3.8 (a) shows a tremendous increase of $\kappa(J)$ in the vicinity of the thermodynamic equilibrium (zero bias) for decreasing temperature. For large values of $\kappa(J) \gg 1$, the solution of the linear corresponding system becomes highly sensitive to round-off errors and cancellation effects, such that no reliable updates for the Newton iteration can be obtained. As a consequence, the standard numerical continuation procedure shown in Fig. 3.6 can not be applied straightforwardly. To tackle this problem, Richey et al. [248] suggested the usage of extended-precision arithmetics, which is however computationally expensive and requires extensive modifications of existing codes.

On the other hand, Fig. 3.8 (a) shows a sudden drop of $\kappa(J)$ for the cryogenic temperature cases at bias values beyond the diode's threshold voltage. The drop in $\kappa(J)$ correlates with the onset of current flow through the diode (where the current density exceeds around 0.1 A cm^{-2} , see Fig. 3.8 (b)) and is explained by the increasing minority carrier density in the previously depleted domains. As the condition number of the cryogenic problems becomes comparable to the corresponding 300 K problems in this parameter regime, the simulations can be carried out by using standard methods.

This observation of the behavior of the condition number provides the basis for the two-step temperature-embedding scheme suggested in Ref. [158]. The approach is illustrated in Fig. 3.9 (a) and works as follows: First, at a moderate temperature a bias sweep from the thermodynamic equilibrium to an arbitrary target bias point beyond the expected threshold voltage is performed (red line in Fig. 3.9 (a)). In a second step, the temperature is gradually decreased until the desired cryogenic operation point is reached (green line in Fig. 3.9 (a)). In the following, the actual computations of interest (blue line in Fig. 3.9 (a)), e.g., voltage sweeps, small/ large signal analysis etc., can be carried out by using the standard continuation method discussed in Sec. 3.5. This temperature-embedding approach is particularly suitable for opto-electronic devices, where one is mainly interested in the behavior close to flat band conditions. Moreover it works well for transient simulations, as the finite carrier life times and mobilities counteract the rapid depletion below the diode's threshold voltage. During the annealing phase, all temperature-dependent material parameters need to be updated iteratively (or should be set to the cryogenic values in the

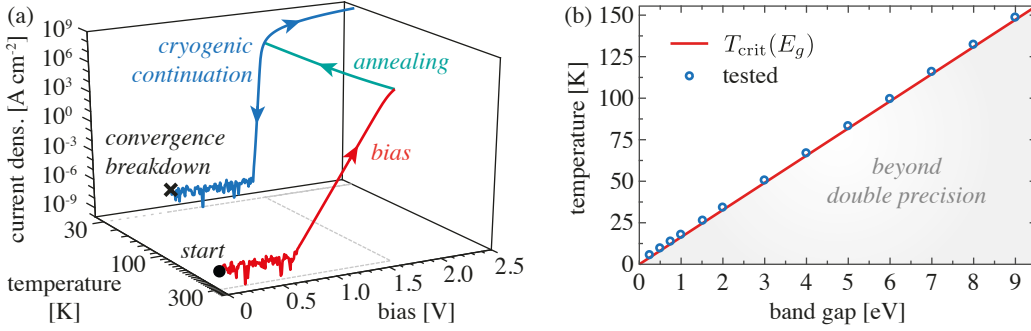


Fig. 3.9 Annealing method for the simulation of the van Roosbroeck system at cryogenic temperatures. (a) Path following scheme of the annealing method for the pin-diode problem. Starting from the thermodynamic equilibrium at room temperature ($T = 300$ K), the diode is driven to flat band conditions (red line). By gradually decreasing the temperature in the annealing phase (green line), a cryogenic target point beyond the diode's threshold voltage is reached. Finally, the calculations of interest can be carried out in the cryogenic regime using standard methods. © 2016 Springer Science+Business Media. Reprinted, with permission, from Ref. [158]. (b) Minimal attainable temperature vs. band gap parameter using the annealing method. The red line shows the IEEE double precision limit given in Eq. (3.23). The blue dots indicate the lowest temperature points reached by convergent Newton steps. The bias was set to $\Delta U_{\text{appl}} = 1.1 \times qE_g$ for each realization. The material and doping parameters are the same as listed in the captions of Figs. 3.7 and 3.8.

very beginning). Note that this includes also an update of the temperature-dependent boundary values at the ohmic contacts, cf. Sec. 2.1.5, in each temperature step. For the parameters used, the approach works well down to $T \approx 27$ K using IEEE double precision – also for higher dimensional device geometries (2D, 3D). Each successful Newton iteration showed quadratic convergence, however for lower temperatures the step size needs to be gradually decreased. As a rule, the lowest achievable temperature using double precision (IEEE floating point arithmetics with 11 exponent bits [331]) is determined by the band gap and can be estimated by

$$T_{\text{crit}}(E_g) \approx \frac{E_g}{k_B} \times \frac{\log_{10} e}{308}. \quad (3.23)$$

This estimate is greatly verified by the test calculations shown in Fig. 3.9 (b), where the minimal temperature reached using the annealing method is shown for different band gap values. For the solutions of the linear system UMFPACK [55] was used.

3.7 Simulation of wide band gap semiconductors using the annealing method

The convergence issues caused by the strong depletion of minority carriers also arise in the simulation of wide band gap semiconductors (e.g., III-nitrides, SiC). In this case, however, the problem occurs already at room temperature. Shah et al. [280] suggested an embedding procedure based on the gradual increase of the band gap (starting from an artificially narrowed band gap). However, this method requires an alternating iteration between increments of the band gap and the applied bias. The latter is necessary in order to

maintain the device in the on-state (beyond the threshold voltage) to avoid the troublesome depletion. Since the threshold voltage strongly depends on the band gap, increments of the band gap must be balanced by increments of the bias. The annealing method discussed in Sec. 3.6 and introduced in Ref. [158] does not require the secondary iteration over the applied bias, as the threshold voltage depends only weakly on the temperature (cf. Fig. 3.8). Hence, the simple one-parametric sweep in the annealing method simplifies the simulation of wide gap semiconductors (see also Fig. 3.9 (b)) as it does not require the staircase-like iteration between consecutive bias and band gap increments.

3.8 Conclusions

At cryogenic temperatures, the standard numerical simulation method for the van Roosbroeck system must be modified. First, the consideration of degeneration effects such as nonlinear diffusion, requires an extension of the finite volume Scharfetter–Gummel discretization scheme towards Fermi–Dirac statistics. The generalized Scharfetter–Gummel scheme proposed in Refs. [27, 174] (the *modified thermal voltage scheme*) allows for an accurate numerical approximation of the nonlinear diffusion at low computational costs and thereby outperforms other approaches. Moreover, the scheme preserves the essential structural properties of the classical Scharfetter–Gummel method. Second, due to numerical underflow in finite precision arithmetics, the standard continuation method for bias sweeps is not straightforwardly applicable at cryogenic temperatures. The annealing method proposed in Ref. [158] allows to circumvent the numerically intractable parameter regimes and enables the transport simulation at very low temperatures and close to flat band conditions. Finally, the annealing method has potential advantages in the simulation of wide gap semiconductors.

Chapter 4

Current injection into oxide-confined single-photon emitting diodes

In this chapter the van Roosbroeck system is applied to investigate the current flow in an electrically driven QD-based single-photon emitting diode. The device features an oxidized aperture for the site-controlled QD nucleation, which is also intended to improve the confinement of the injection current. The experimentally recorded electroluminescence, however, shows the counterintuitive light emission from parasitic QDs far away from the aperture, which contradicts the expected current confining property. The experimental observations are reproduced by a theoretical model, that predicts a rapid lateral current spreading above the oxide layer. This phenomenon is thoroughly investigated and traced back to the absence of carrier recombination above the oxide layer in the low-injection regime at cryogenic temperatures. Finally, by a revision of the doping design, a superior current confinement is achieved, that enables the highly selective excitation of a small domain above the aperture – in particular it allows for the electrical pumping of single QDs. This is evidenced by numerical simulations under stationary and pulsed excitation.

The results reported in this chapter are published in Ref. [156] and are reprinted with permission. ©2016 IEEE. The results represent the first successful application of the van Roosbroeck system to single-photon sources known in the literature. Moreover, to the best of the author’s knowledge, the simulations are conducted at the lowest temperature ($T = 30$ K) reported in the literature on numerical simulation of GaAs-based devices.

4.1 Introduction

The efficient electrical pumping of sub-micrometer sized domains is essential to achieve deterministic control over the carrier population within optically active nanostructures such as QDs. This is of high importance in electrically driven sources of single photons and entangled photon pairs for quantum information processing [41, 263], quantum cryptography [99, 133] etc. (see Sec. 1.2). In vertical-cavity surface-emitting lasers (VCSELs), the lateral current (and optical mode) confinement is achieved by laterally oxidized apertures near the optically active region [207], where the insulating nature of the oxide leads to a funneling of charge carriers into the aperture within the oxide. Moreover, the strain field in the vicinity of the aperture is modified in the oxidation step, which can be exploited to achieve

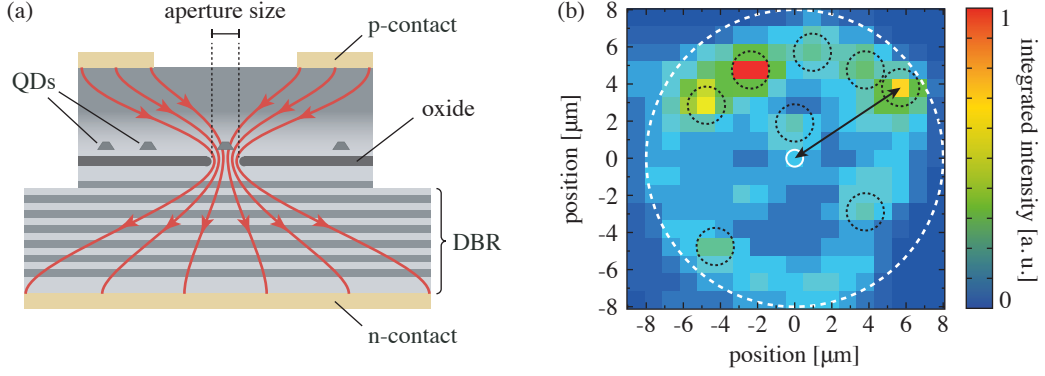


Fig. 4.1 (a) Schematic cross section of the single-photon source. The device is an axisymmetric, GaAs-based vertical pin-structure with a $\text{Al}_x\text{Ga}_{1-x}\text{As}/\text{GaAs}$ DBR section at the bottom. The oxidized aperture controls the strain-induced QD nucleation and the current confinement. The QD positions are indicated by capped grey triangles and the naively expected current flow is shown by red lines. (b) Electroluminescence map of a mesa with several parasitic QDs at low DC injection (10 nA) recorded at a lateral resolution of 1 μm . The white circle indicates the aperture (around 800 nm diameter) and the arrow corresponds to a distance of 6.7 μm between a parasitic QD and the aperture center. The figure shows a device where the emission intensity of central QDs is a factor of 30 weaker than from parasitic QDs in the outer region of the mesa. The dashed black circles highlight the positions of several parasitic QDs. © 2016 IEEE. Reprinted, with permission, from Ref. [156].

a self-alignment of single QDs above the aperture in a two-step epitaxial process [296, 297]. This approach has been successfully used to deterministically nucleate single QDs above such apertures for electrically driven single-photon sources [305]. Based on the experience with the current confinement due to oxidized apertures in VCSELs, the design is expected to provide a very efficient current injection into single QDs. However, the experimental and theoretical findings reveal a minor effect of the aperture on the lateral current distribution in the low-injection regime at cryogenic temperatures.

4.2 Device design and site-controlled quantum dot nucleation

The cross section of a pin-diode structure, that has been demonstrated to work as an electrically driven single-photon source [305], is schematically shown in Fig. 4.1 (a). The device features self-aligned QDs above an oxidized aperture, a (bottom) distributed Bragg reflector (DBR) and can be grown in a two-step epitaxial as follows [306]: First, a 24-fold n-doped $\text{Al}_x\text{Ga}_{1-x}\text{As}/\text{GaAs}$ double layer structure forming the DBR is grown followed by an Al-rich $\text{Al}_x\text{Ga}_{1-x}\text{As}/\text{AlAs}$ “sandwich” structure which later on forms aperture. The DBR mirror section is intended to provide a directed optical output through the surface of the device. Afterwards, the mesa structure is processed by dry etching, which allows for the subsequent partial oxidation of the $\text{Al}_x\text{Ga}_{1-x}\text{As}/\text{AlAs}$ -layers from the mesa side walls. The partially oxidized $\text{Al}_x\text{Ga}_{1-x}\text{As}/\text{AlO}_x$ -layers leave a conducting domain at the mesa center behind, which is intended to serve as an aperture for the current confinement. In a second epitaxial step, the structure is overgrown by a thin $\text{In}_x\text{Ga}_{1-x}\text{As}$ layer and a GaAs cap layer. Due to lateral variations of the mechanical strain distribution

at the $\text{Al}_x\text{Ga}_{1-x}\text{As}/\text{AlO}_x$ interface, the InAs growth is preferred at the local tensile strain maxima of the GaAs surface [296]. For small aperture diameters a single tensile strain maximum is formed directly above the aperture, leading to a self-aligned QD nucleation in the center of the mesa with high selectivity to its surroundings [296]. The formation of the QDs itself is based on a strain driven 2D to 3D growth transition (Stranski–Krastanov growth mode [29]) and occurs at a certain critical layer thickness of about 1.7 monolayers for $\text{In}_{0.65}\text{Ga}_{0.35}\text{As}/\text{GaAs}$ [134]. However, as fluctuations of the $\text{In}_x\text{Ga}_{1-x}\text{As}$ deposition across the lateral extension of the p-n junction region can hardly be avoided, further *parasitic* QDs can nucleate above the oxide layer, cf. Fig. 4.1 (a). More details on the growth and processing steps to manufacture the device can be found in Ref. [306]. Recently, the buried stressor approach was combined with a deterministically fabricated microlens [112] to further enhance the photon extraction and optical fiber coupling [155].

4.3 Electroluminescence of parasitic quantum dots and current spreading

An electroluminescence map¹ of a pin-diode mesa structure with $16\ \mu\text{m}$ diameter is shown in Fig. 4.1 (b). The emission spectrum recorded directly above the aperture reveals a weak luminescence of a few (about 2–4) QDs, whose intensity is a factor of 30 weaker than the emission intensity originating from parasitic QDs in the outer part of the mesa. Hence, the measurement shown in Fig. 4.1 (b) clearly indicates an insufficient current confinement by the oxidized aperture as parasitic QDs located about $6.7\ \mu\text{m}$ away from the mesa center can be electrically excited. The experimental observation obviously contradicts the naively expected current paths indicated in Fig. 4.1 (a) and rapid lateral current spreading above the aperture must be considered.

4.4 Numerical simulation of the carrier injection

As the lateral carrier density distributions and the current flow in the device are not directly accessible by experiments (only indirect observation, e.g., via electroluminescence measurements), the origin for the rapid lateral current spreading must be investigated theoretically by means of numerical simulations. While there is an extensive literature on electronic transitions between continuum states of a macroscopic carrier reservoir and discrete QDs states [48, 71, 201, 226], only a few recent publications consider the transport of the continuum carriers to the optically active QDs [98, 105, 171, 175] – however, always for macroscopic ensembles of QDs. As the impact of a few, isolated QDs on the macroscopic carrier transport is considered to be small on large scales, the current flow can be calculated by means of fully 3D simulation of the van Roosbroeck system (2.1) without QDs. The impact of the QDs can be estimated perturbationally.

In order to investigate the lateral current spreading above the aperture, the computational domain is restricted to the interesting region ranging from 200 nm below to 270 nm above the aperture. By further exploiting the rotational symmetry of the mesa, it is sufficient to analyze the current flow in the 2D cross section of the pin-diode shown in Fig. 4.2 (a) (the axial symmetry is encoded in rotated geometry factors, cf. Sec. 3.1.1 and Fig. 3.2). In the following, the conventional pin-design will be compared with the ppn-design shown in Fig. 4.2 (b), where only the doping profile has been altered. The layer thicknesses and

¹The experimental measurements reported in this section have been carried out by Jan-Hindrik Schulze at Technical University Berlin.

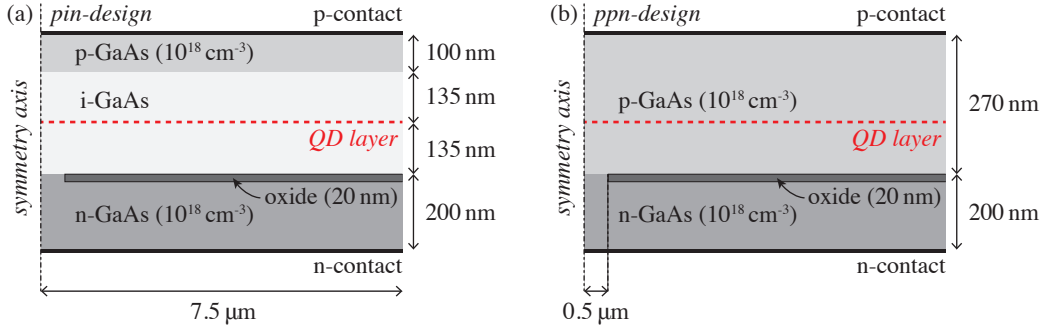


Fig. 4.2 Cross sections of the two simulated axisymmetric device structures. (a) The pin-design contains a 270 nm thick intrinsic layer between the n- and p-doped regions. The QD layer is embedded in the center of the intrinsic domain, indicated as a dashed red line. In the macroscopic transport calculations, the QDs are not taken into account (see text for details). The thickness of the current-blocking oxide layer on top of the n-doped domain is set to 20 nm and the radius of the aperture at the symmetry axis is chosen as 0.5 μm . Except for the oxide, the material is GaAs throughout. Ohmic contact conditions hold on the top and bottom boundaries, while homogeneous Neumann boundary conditions are imposed on the remaining boundaries (left and right). On the oxide domain only Poisson's equation is solved. (b) In the ppn-design the p-doping is employed down to the oxide, replacing the former intrinsic layer.

doping parameters are chosen close to the experimental structure and can be found in Fig. 4.2 (and the corresponding caption). As already stated above, the QD layer located 135 nm above the oxide layer is omitted in the simulation. The vertical positioning of the QD layer in the center of the intrinsic zone maximizes the overlap of the QDs with the optical mode [306]. Some details of the experimental structure shown in Fig. 4.2 (a) have a minor influence on the current distribution between aperture and the QD layer and are therefore simplified in the model. In particular the highly p-doped cap layer is replaced by an ohmic contact boundary condition, neglecting the small potential drop across the layer. The same is done with the entire bottom DBR section. Thereby, the current flow between the aperture and the QD layer is decoupled from the complex phenomena in the top and bottom layers of the device. For the same reason, the detailed multi-layer $\text{Al}_x\text{Ga}_{1-x}\text{As}/\text{AlAs}$ sandwich structure of the aperture region in the real device is reduced to a single GaAs-layer with a hole radius of 0.5 μm and a thickness of 20 nm. To include the effect of cryogenic operation temperatures, the device temperature is set to $T = 30\text{ K}$ throughout this section. This is close to the critical low temperature limit Eq. (3.23) of the annealing method for GaAs parameters (see Sec. 3.6).

4.4.1 Stationary injection in the pin-design

At stationary operation, the carrier density at the QD layer is very sensitive to the applied voltage and rapidly increases as the bias is increased. This is shown in Fig. 4.3 (a), where the radial profile of the carrier density distribution at the QD layer is plotted for different applied voltages. The strong sensitivity of the carrier density on the applied voltage is particularly pronounced at cryogenic temperatures, where the transition from full depletion to a high carrier density occurs within a very small bias range (cf. Fig. 3.8 (b)). Moreover, Fig. 4.3 (a) shows how the carrier distribution changes radially when passing from the low-injection to the high-injection regime. First, in the low-injection regime, the carrier density is nearly constant at the QD layer (blue curve in Fig. 4.3 (a) for $U = 1.46\text{ V}$).

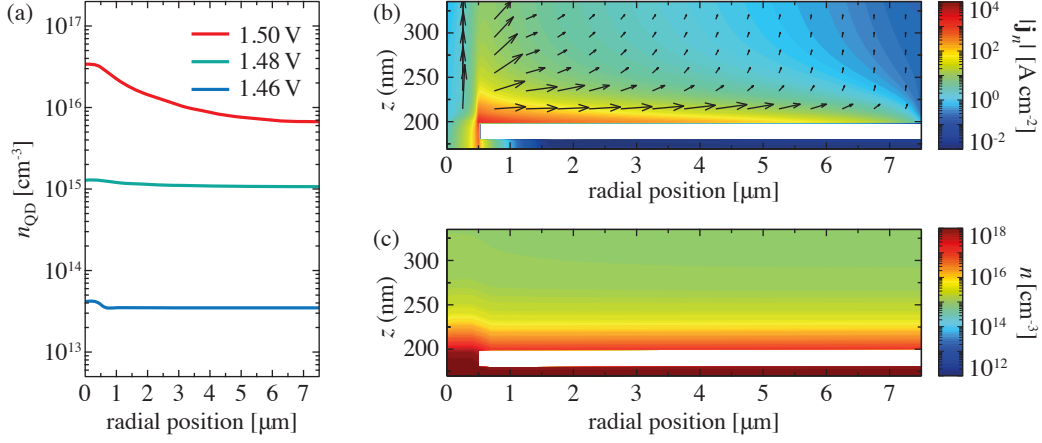


Fig. 4.3 Analysis of current flow and carrier density distributions in the pin-design. (a) Radial profile of the carrier density distribution at the QD layer for different applied voltages (stationary). The electron and hole densities are identical since the QD layer is centered in the intrinsic layer and the p- and n-doping densities are equal. (b) Electron current density distribution between the oxide (white) and the QD layer (top border, at $z = 335$ nm) at an applied voltage of $U = 1.48$ V. The magnitude of the current density is color-coded and the arrows point into the direction of electron flow. (c) Electron density distribution in the same domain as (b). The parameters in the calculation are $E_c = 1.5$ eV, $E_v = 0$ eV, $m_e^* = 0.063 m_0$, $m_h^* = 0.51 m_0$, $\epsilon_r = 12.9$. The SRH life times are $\tau_n = 10$ ns, $\tau_p = 34$ ns, the bimolecular recombination coefficient is $B = 10^{-8} \text{ cm}^3 \text{ s}^{-1}$ and the Auger coefficients are set to $C_{\text{Au}}^n = C_{\text{Au}}^p = 10^{-30} \text{ cm}^6 \text{ s}^{-1}$. The carrier mobilities in the intrinsic region are $M_n^{(\text{intr})} = 10^4 \text{ cm}^2 \text{ V}^{-1} \text{ s}^{-1}$, $M_p^{(\text{intr})} = 300 \text{ cm}^2 \text{ V}^{-1} \text{ s}^{-1}$ and $M_n^{(\text{dop})} = 6400 \text{ cm}^2 \text{ V}^{-1} \text{ s}^{-1}$, $M_p^{(\text{dop})} = 130 \text{ cm}^2 \text{ V}^{-1} \text{ s}^{-1}$ in the doped domains. The parameters are based on Ref. [232]. Because of the heavy doping $N_D = -N_A = 10^{18} \text{ cm}^{-3}$, complete ionization is assumed due to the Mott transition (see Appx. A.1). © 2016 IEEE. Reprinted, with permission, from Ref. [156].

As the capture rate to the QDs is assumed to be proportional to the carrier density [226, 322], and the latter is roughly independent of the radial position, the occupation of the QDs in the low-injection regime is expected to be homogeneous within the whole layer. This assumption agrees well with the experimentally observed excitation of parasitic QDs far away from the aperture reported in Sec. 4.3. The underlying mechanism is shown in Fig. 4.3 (b), which shows how the electrons flow around the aperture and then diffuse outwards within a thin layer right above the oxide. In this thin layer, the electron density reaches nearly 10^{18} cm^{-3} and is practically independent of the radial position, see Fig. 4.3 (c). Therefore, the quasi-homogeneous and highly conductive thin layer acts like an equipotential plane. As a consequence, also the electron distribution everywhere above it (and thus the injection into the QDs) is almost homogeneous along the radial direction.

At first glance, the rapid lateral current spreading might be caused by the high electron mobility in the intrinsic region. Hence, a reversal of the doping profile should help to impede the current spreading above the oxide as the mobility of holes is much smaller (see the parameters listed in the caption of Fig. 4.3). However, the simulation of the corresponding nip-design showed almost no improvement, as also the holes radially spread out along the mesa, irrespective of their shorter diffusion length (not shown). In conclusion, the carrier mobility does not sufficiently explain the rapid lateral current spreading in the low-injection regime. Another possible reason for the current spreading is found, when returning to the analysis of the pin-design, in the thin, highly conductive layer above the

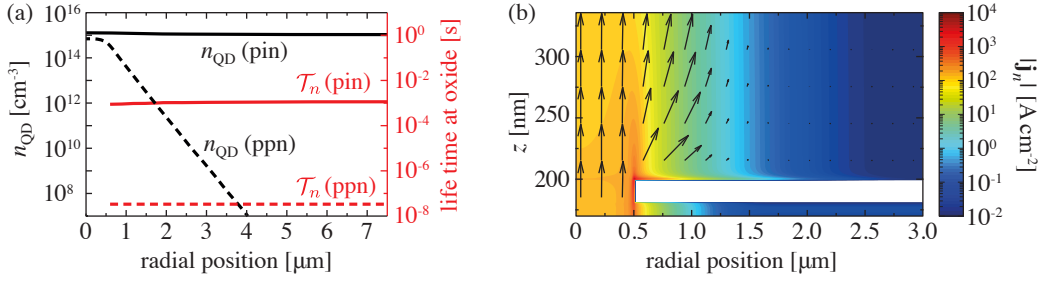


Fig. 4.4 (a) Radial distributions of the electron density $n_{\text{QD}}(r)$ at the QD layer (black) and the electron life time $\mathcal{T}_n(r)$ directly above the oxide (red). The solid lines correspond to the pin-design, dashed lines show the results obtained for the ppn-design (cf. Fig. 4.2). The maximum electron density in the QD layer $n_{\text{QD}}(r=0) \approx 10^{15} \text{ cm}^{-3}$ is reached at the symmetry axis in both designs. (b) Electron current density distribution between the oxide (white) and the QD layer (top border) in the ppn-design. The arrows indicate the direction of electron flow and the magnitude of the current density color-coded. © 2016 IEEE. Reprinted, with permission, from Ref. [156].

oxide. There, the density of electrons exceeds the density of holes by several orders of magnitude. As a result, the recombination rate R is very small and the electron life time $\mathcal{T}_n = n/R$ becomes extremely long. For the pin-design, the simulations lead to life times \mathcal{T}_n up to milliseconds, see Fig. 4.4 (a). With such long life times, the electron diffusion length $L_{D,n} = \sqrt{D_n \mathcal{T}_n} \approx 1.6 \text{ mm}$ (with $D_n(T=30 \text{ K}) \approx 26 \text{ cm}^2 \text{ s}^{-1}$, cf. caption of Fig. 4.3, and $\mathcal{T}_n \approx 1 \text{ ms}$, cf. Fig. 4.4) reaches the order of millimeters and thereby exceeds the mesa radius by two orders of magnitude. As a result, the electrons can easily occupy the whole mesa area.

It shall be stressed, that the current spreading above the aperture in the low-injection regime at cryogenic temperatures is not a feature of a specific doping design but rather a general phenomenon that arises in any design containing a sufficiently thick intrinsic layer. The tiny minority carrier density above the oxide leads to a small recombination rate and consequently to a long diffusion length of the majority species. Hence, the lateral current spreading is inevitably caused by the intrinsic region above the aperture layer. On the other hand, in the high-injection regime, the onset of recombination decreases the carrier life times such that the current spreading is reduced. This regime is important for VCSELs and LEDs, where the current confinement induced by the oxidized aperture is supported by recombination-guided current densities. Moreover, VCSELs and LEDs are typically operated at room temperature, where the depletion of minority carrier densities is less extreme.

4.4.2 Impact of QDs on free carrier densities

It is challenging to properly model the physics in the QD layer and to include it in the transport model (2.1). The QD positions are randomly distributed in the plane, and the corresponding wetting layer is expected to have a randomly fluctuating, discontinuous structure. First, the ideal case is discussed, where the QD layer consists only of a single, central InAs-QD. The influence of the QD on the current flow can be taken into account by supplementing the right-hand sides of the continuity equations (2.1b)–(2.1c) with the losses due to scattering of continuum carrier to discrete QD states (see, e.g., Ref. [175]). It can be assumed, that these capture processes are restricted to the domain $\Omega_{\text{QD}} \subset \Omega$,

where continuum states and discrete QD states coexist. The corresponding capture rate for electrons, which appears as an additional loss term on the right hand side of the continuity equation (2.1b), can be modeled as [156]

$$S_n(\mathbf{r}) = \frac{1}{\tau_{n,\text{cap}}} n(\mathbf{r})(1 - f_n), \quad \mathbf{r} \in \Omega_{\text{QD}}, \quad (4.1)$$

within Ω_{QD} and zero outside. Here, $\tau_{n,\text{cap}}$ is the characteristic capture time of the individual QD and $f_n \in [0, 1]$ is the occupation probability. The model (4.1) accounts for Pauli blocking due to filling of the QD level. The corresponding expression for holes is analogous and the generalization to multiple, isolated QDs is straightforward. The model (4.1) neglects the escape of carriers, which is however negligible at cryogenic temperatures.

The characteristic capture time can be obtained from photoluminescence measurements. In Ref. [56], the relaxation of off-resonantly excited carriers in GaAs to a layer of embedded InAs-QDs has been measured experimentally and modeled by rate equations. The authors conclude a mean capture rate per volume $\langle S_n \rangle = \gamma_n \langle n \rangle$ in the QD layer domain of the empty QDs ($f_n \approx 0$) with a characteristic ensemble capture coefficient $\gamma_n \approx 10 \text{ ns}^{-1}$. The capture rate per QD is estimated by relating the capture coefficient γ_n with the volume filling factor $F = n_S V_{\text{QD}}/h$ of the QDs within the QD-layer (with the volume of the QD domain $V_{\text{QD}} = \int_{\Omega_{\text{QD}}} d^3r$). Following Ref. [56], the sheet density of QDs is taken as $n_S \approx 10^{10} \text{ cm}^{-2}$, the layer height is assumed as $h \approx 10 \text{ nm}$ and the QD volume is $V_{\text{QD}} \approx (10 \text{ nm})^3$. Hence, the filling factor estimate yields $F \approx 10^{-2}$. Finally, one obtains the order-of-magnitude estimate for the characteristic capture time of a single QD as $\tau_{n,\text{cap}} = F/\gamma_n \approx 1 \text{ ps}$. This estimate for the capture time is in good agreement with previously reported values in the literature [226, 300, 322] and is about three orders of magnitude smaller than the typical radiative life time $\tau_{\text{rad}} \approx 1 \text{ ns}$ of excitons in InGaAs-QDs.

The internal kinetics of the bound carrier population can be described by a simple rate equation of the form

$$\partial_t f_n = \int_{\Omega_{\text{QD}}} d^3r S_n - \frac{1}{\tau_{\text{rad}}} f_n f_p \approx \frac{1}{\tau_{n,\text{cap}}} V_{\text{QD}} \langle n \rangle (1 - f_n) - \frac{1}{\tau_{\text{rad}}} f_n f_p, \quad (4.2)$$

(the equation for the bound hole population f_p is analogous) where the spatially integrated capture rate (4.1) represents the pump rate. The second term is the radiative recombination rate (with the radiative life time τ_{rad}), which represents the dominant decay process. Under stationary conditions, the pump and decay rates are balanced in time average. At large bulk carrier densities in the vicinity of the QD, the occupations f_n, f_p saturate slightly below unity due to recombination losses. The corresponding bulk density $\langle n \rangle_{\text{sat}}$ at which saturation sets in can roughly be estimated by equating the capture rate of the empty QD with the radiative decay rate of the fully occupied QD. One obtains the order of magnitude estimate $\langle n \rangle_{\text{sat}} = V_{\text{QD}}^{-1} \tau_{n,\text{cap}}/\tau_{\text{rad}} \approx 10^{15} \text{ cm}^{-3}$. If the bulk density in the vicinity of the QD is driven beyond $\langle n \rangle_{\text{sat}}$, the recombination from the bound QD states saturates but continues growing in the rest of the device, which lowers the quantum efficiency. On the other hand, bulk densities below $\langle n \rangle_{\text{sat}}$ reduce the number of generated photons, which is also unfavorable. In conclusion, an average bulk density $\langle n \rangle \approx \langle n \rangle_{\text{sat}}$ in the vicinity of the QD represents a certain optimum, which is considered as the target carrier density in the numerical simulations studied in this section.

Finally, the impact of the capture rate term (4.1) on the macroscopic density distributions shall be discussed. The influence of the QD on the bulk carrier distributions is most significant if the QD is empty ($f_n, f_p = 0$). In this case, it acts as an additional

recombination center (deep trap in the domain Ω_{QD}) with an extremely small recombination life time $\tau_{n,\text{cap}} = 1$ ps. This represents a huge rate such that strong spatial hole burning could be expected. However, the diffusion spreads the extension of the depleted domain to the order of the diffusion length $L_{D,n}$, which exceeds the size of the QD by several (around five) orders of magnitude. As a consequence, the bulk carrier density is only slightly affected in comparison to simulations neglecting the QD as an additional recombination center. This approximation is confirmed by the detailed treatment of this problem given in Chap. 5 and 6.

4.4.3 Current confinement in the ppn-design

4.4.3.1 Stationary operation

The central insight of Sec. 4.4.1 is that the lateral current spreading above oxidized apertures is inevitable in the low-injection regime as long as the active region is undoped. Hence, doping of the active region containing the QD layer will likely be helpful to suppress the lateral current spreading. This assumption is confirmed by the numerical simulation of the electron current flow in the ppn-design (cf. Fig. 4.2 (b)) shown in Fig. 4.4 (b). Due to the availability of holes as recombination partners in the active region, the electron life time is reduced (cf. Fig. 4.4 (a)) such that the lateral current spreading is drastically decreased because of the reduced diffusion length. Accordingly, the radial electron density distribution in the QD layer drops exponentially $n_{\text{QD}}(r) \sim \exp(-r/r_0)$ with increasing r (cf. Fig. 4.4 (a), radial decay constant $r_0 \approx 0.19 \mu\text{m}$), such that the excitation of parasitic QDs far away from the aperture is suppressed.

Interestingly, the diffusion length in the ppn-design $L_{D,n}^{(\text{ppn})} \approx 7 \mu\text{m}$ (with $D_n^{(\text{ppn})} \approx 16.5 \text{ cm}^2 \text{ s}^{-1}$ and $\mathcal{T}_n^{(\text{ppn})} \approx 3 \times 10^{-8} \text{ s}$ at the oxide) is still 1–2 orders of magnitude larger than the observed radial decay constant r_0 of $n_{\text{QD}}(r)$ in Fig. 4.4 (a). The latter indicates an even shorter electron life time on the order of a few tens of picoseconds. The corresponding additional confinement can be explained by the close proximity of the QD layer to the p-contact (only 235 nm between the QD layer and the top contact, cf. Fig. 4.2) since a considerable amount of the injected electrons escapes through the p-contact which is further reducing the mean life time. The contact induced life time can be estimated as $\tau_{\text{cont}} \approx d^2/D_n^{(\text{ppn})} \approx 34 \text{ ps}$ (where $d = 235 \text{ nm}$ is the distance to the QD layer), which is around 3 orders of magnitude smaller than the electron life time $\mathcal{T}_n^{(\text{ppn})}$ in the QD layer (cf. Fig. 4.4 (a)) and therefore explains the steep radial decrease of $n_{\text{QD}}(r)$.

In conclusion, the simulation of the current flow in the ppn-design further confirms the hypothesis on the origin of the lateral current spreading in the pin-design. By using a sufficiently strong p-doping in the active region (here $N_A \approx N_A^- = 10^{18} \text{ cm}^{-3}$) in combination with a thin p-doped top layer, the diffusion length of the electrons can be significantly reduced leading to a tightly confined radial density profile of the injected electrons. Thereby, the selective excitation of the central QD can be achieved even in the low-injection regime. Because of the increased recombination of bulk carriers in the ppn-design, the total current to achieve the target density $n_{\text{QD}}(r=0) \approx \langle n \rangle_{\text{sat}} \approx 10^{15} \text{ cm}^{-3}$ is increased (in the simulations it doubles approximately which is acceptable in view of the excellent current funneling). Furthermore, doping of the active region will modify the emission properties of the QDs. Due to the p-doping, the photon emission from the decay of positively charged complexes (e.g., trions) will certainly become more likely. However, as the trion ground state emission of QDs exhibits no fine structure splitting [19, 162, 304] this may be even advantageous for single-photon generation.

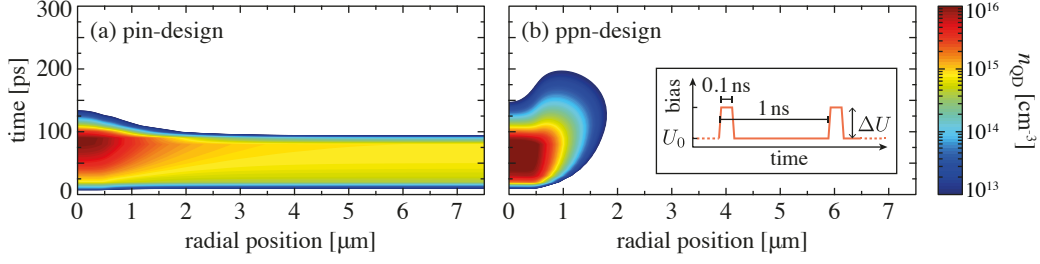


Fig. 4.5 Time evolution of the radial electron density distribution in the QD layer in response to a periodically pulsed contact voltage for the (a) pin-design ($U_0 = 1.43$ V, $\Delta U = 70$ mV) and the (b) ppn-design ($U_0 = 1.48$ V, $\Delta U = 30$ mV). The onset of the bias pulse is at $t = 0$ ps. The electron density is color-coded, white areas indicate small electron densities below 10^{13} cm $^{-3}$. The inset shows the voltage pulse train for transient excitation. ©2016 IEEE. Reprinted, with permission, from Ref. [156].

4.4.3.2 Pulsed operation

For many practical applications it is essential to generate single photons in response to an externally triggered excitation [41]. Therefore, this section deals with the performance of the two different designs shown in Fig. 4.2 in the pulsed excitation mode. More precisely, it is investigated whether the design rules for the reduction of the lateral current spreading under stationary operation still apply in the dynamic case of pulsed excitation.

The repetition frequency of pulse-driven single-photon sources is limited by the radiative life time of the electronic transition in the QD used for the single-photon generation. For $\text{In}_x\text{Ga}_{1-x}\text{As}$ -QDs embedded in low Q resonators with only a weak Purcell enhancement, a reasonable repetition rate is around 1 GHz at maximum. To study the dynamic behavior of the device, short voltage pulses ($\Delta t_{\text{pulse}} = 100$ ps) with amplitude ΔU superimposed on a constant bias U_0 with a repetition frequency of 1 GHz are numerically simulated (see inset of Fig. 4.5 (b)). For each design, the corresponding DC bias U_0 is chosen such that the electron density in the QD layer is slightly below 10^{12} cm $^{-3}$. Then, the capture rate of the empty QD is around $\Gamma_n = \int_{\Omega_{\text{QD}}} d^3r S_n \approx 10^{-6}$ s $^{-1}$, which is low enough to effectively suppress the electron capture between subsequent pulses. The pulse amplitude ΔU is chosen such that the capture rate during the excitation reaches the inverse pulse length $\Gamma_n = 10$ GHz, i.e., the bulk carrier density in the QD layer reaches $n_{\text{QD}} \approx 10^{16}$ cm $^{-3}$. The rise and fall times of the pulses are assumed to be 20 ps each.

The time evolution of the radial electron density distribution in the QD layer in response to a periodically pulsed contact voltage is shown in Fig. 4.5. In both designs, the carrier density follows the pulses with a short delay of only a few picoseconds. Therefore, the internal time scale of the carrier transport processes to pump the QDs is sufficiently fast to allow for very high repetition rates beyond the GHz scale. However, external effects like parasitic capacitances and inductivity of bond wires, which are not included here, will lead to limitations in real devices. The radial electron density distribution $n_{\text{QD}}(r, t)$ differs drastically between both designs. In the pin-design, the lateral current spreading quickly leads to a homogeneous electron density distribution in the QD layer until $n_{\text{QD}} \approx 10^{15}$ cm $^{-3}$ is reached in the whole plane. Close to the end of the excitation pulse, a peak density of $n_{\text{QD}} \approx 10^{16}$ cm $^{-3}$ is reached only above the aperture, while the electron density above the oxide saturates at $n_{\text{QD}} \approx 10^{15}$ cm $^{-3}$. Hence, just as in the stationary case (cf. Fig. 4.3(a)), a small drop (around one order of magnitude) in the radial electron density distribution can be observed at voltages close to the diodes threshold

voltage ($U \approx 1.5$ V). According to Eq. (4.2), the probability to capture an electron per excitation cycle

$$P_n = \int_0^{1 \text{ ns}} dt \Gamma_n(t)$$

is close to 100 % for central QDs and around 10 % for parasitic QDs far away from the aperture. While this represents a noticeable reduction of the capture rate for parasitic QDs compared to the case of stationary operation, it is probably not very satisfying for a pulsed single-photon source. The pulse-response of the ppn-design shown in Fig. 4.5(b) is tightly confined to the central part of the mesa directly above the aperture. The radial range in which the electron capture probability to a QD exceeds 1 % is restricted to $r < 1.5$ μm . Hence, both under stationary and pulsed operation, the ppn-design is distinctly better suited for efficient current injection into the central QD than the pin-design.

4.5 Conclusions

The van Roosbroeck system has been applied to the numerical simulation of a single-photon emitting diode for the first time in literature [156]. The analysis of the current flow yields an explanation of the experimentally observed optical activity of parasitic QDs in the oxide-confined diode structure under investigation:

The current confining property of oxide apertures can get lost at low injection currents and cryogenic temperatures, if the domain above the oxide layer is undoped. The absence of recombination in the intrinsic domain above the oxide leads to long carrier life times and a strongly increased carrier diffusion length in that region. This causes a rapid lateral current spreading above the oxide, which results in the excitation of parasitic QDs far away from the aperture. By a revision of the doping design, the current spreading can be suppressed, such that the highly selective electrical excitation of the central QDs above the aperture is possible. The revised design has superior confinement properties in both the stationary and the pulsed excitation mode.

Chapter 5

Hybrid quantum-classical modeling of electrically driven quantum light sources

This chapter describes a comprehensive modeling approach for the simulation of quantum dot-based electrically driven quantum light sources, by coupling the van Roosbroeck system to a quantum master equation in Lindblad form. In Sec. 5.2, the Lindblad master equation for a quantum system weakly coupled to a carrier reservoir is derived under the additional constraint of a charge conserving system-reservoir interaction. In Sec. 5.3, a new *hybrid quantum-classical* model system is constructed, that allows for a self-consistent description of the dynamics of the QD-photon system and the carrier transport in realistic semiconductor device geometries. Thereby, the quantum optical figures of merit and the spatially resolved current flow can be calculated out of one box. The hybrid model is investigated with respect to its thermodynamic properties and is shown to obey fundamental principles of (non-)equilibrium thermodynamics. In Sec. 5.4 the hybrid model is discussed from the viewpoint of the *GENERIC* formalism on thermodynamically consistent modeling of multi-physics problems. The main results of this chapter are published in Ref. [160] and are reprinted with permission. ©2017 American Physical Society.

5.1 Motivation

In the last decades, the research in semiconductor quantum optics has greatly advanced our understanding of the quantum nature of light and its interaction with matter. This development was considerably supported by the advent of semiconductor QDs, which enable a three-dimensional confinement of the carrier wave functions and show (tunable) atom-like energy spectra (cf. Sec. 1.1). Since QDs can be directly integrated into dielectric micro-cavities by standard growth techniques, they are promising candidates for novel semiconductor lasers [48, 295] and quantum light sources [31, 41, 194]. Driven by these technological applications, nowadays semiconductor quantum optics is on the leap from the lab to commercial applications [298]. For the design of electrically driven devices, which are desirable for practical applications [35], efficient mathematical models and simulation tools are needed to optimize particular designs and reduce the development

cost. A large class of device concepts for electrically driven quantum light sources [37, 126, 132, 246, 272, 305, 316, 330] and nanolasers [244, 246] is based on a single or a few QDs as optically active elements embedded in a macroscopic semiconductor structure (predominantly pin-diode-like structures). In such devices the van Roosbroeck system (2.1) can be used to model the charge transport for the purpose of device optimization. For example, in Chap. 4 the van Roosbroeck system has been employed for the optimization of a QD-based single-photon source, where a modification of the doping design in a vertical p-n junction significantly improved the carrier injection into the optically active QD [156].

A serious shortcoming of semi-classical transport models is that they make, of course, no predictions about the quantum optical properties of the radiation generated by the device. For example, to characterize the quality of a single-photon source it is required to examine the second-order correlation function, which discriminates non-classical from classical light emitters (see Sec. 1.2). The quantum optical properties can be described by microscopic models for the emitter-photon system in the framework of cavity quantum electrodynamics, which describes the light-matter interaction on the fundamental level [44]. Hence, in order to achieve a comprehensive device-scale simulation of electrically driven quantum light sources that goes beyond the scope presented in Chap. 4, a combination of quantum mechanical models and classical device physics is required.

The dynamics of open quantum systems, such as QD-confined carriers coupled to a macroscopic semiconductor environment, can be described by quantum master equations [39]. These are equations of motion for the quantum mechanical density matrix, that describe its evolution in the presence of dissipative system-reservoir interactions such as, e.g., the exchange of energy and charge via carrier capture or photon emission. Quantum master equations have proven to be a powerful tool in quantum optics [39, 44], quantum measurement theory [324] and quantum thermodynamics [89, 176]. The overall goal of this chapter is the construction of a *hybrid quantum-classical model* that self-consistently couples the van Roosbroeck system with a quantum master equation in Lindblad form for the comprehensive simulation of QD-based electrically driven quantum optical devices.

5.2 Lindblad equation for grand canonical reservoirs

5.2.1 Open quantum systems

The theory of open quantum systems deals with the description of an open quantum system S that is coupled to another quantum system R , which is called the *reservoir* or *environment*. The system S represents a subsystem of the composite quantum system $S + R$, which is assumed to be closed and isolated, see Fig. 5.1 (a). The state space of the open system is given by the Hilbert space \mathcal{H}_S , whereas \mathcal{H}_R denotes the Hilbert space of the surrounding reservoir. The Hilbert space of the combined system $S + R$ is given by the tensor product space $\mathcal{H} = \mathcal{H}_S \otimes \mathcal{H}_R$ [39, 266]. The state of the total system is described by the density matrix ρ , which – as the combined system is assumed to be closed – obeys a unitary time evolution $\rho(t) = U(t, 0) \rho(0) U^\dagger(t, 0)$. The unitary time evolution operator $U = U^\dagger$ obeys Schrödinger's equation $i\hbar \partial_t U(t, t_0) = H U(t, t_0)$, $U(t_0, t_0) = I$ where H is the Hamiltonian of the composite system. The Hamiltonian can be decomposed as [39, 253, 266]

$$H = H_S \otimes I_R + I_S \otimes H_R + H_{SR}, \quad (5.1)$$

where $H_S \in \mathcal{H}_S$ is the Hamiltonian of the system S , $H_R \in \mathcal{H}_R$ is the Hamiltonian of the free reservoir and $I_{S/R}$ are the respective identity operators. The interaction Hamiltonian $H_{SR} \in \mathcal{H}_S \otimes \mathcal{H}_R$ lives on the tensor product space and describes the system-reservoir

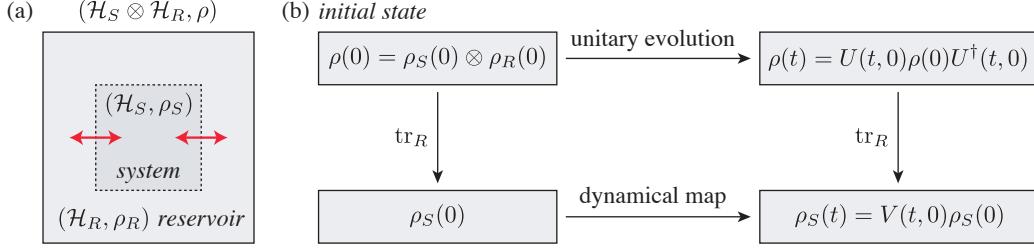


Fig. 5.1 (a) The open quantum system S is embedded in a reservoir R with which it can exchange energy and charge. The composite system $S + R$ is closed and isolated. (b) The total system follows Hamiltonian dynamics via the unitary time evolution operator $U(t, t_0)$, whereas the (reduced) open quantum system is propagated by the dynamical map $V(t, t_0)$ [39].

coupling. If the Hamiltonian of the total system is time-independent (isolated system), the time evolution operator is explicitly given as $U(t, 0) \equiv U(t) = e^{-\frac{i}{\hbar}Ht}$. The corresponding equation of motion for the total density matrix is the Liouville–von Neumann equation

$$\partial_t \rho(t) = -\frac{i}{\hbar} [H, \rho(t)]. \quad (5.2)$$

The state space of the composite system is typically very large. One of the central objectives in the theory of open quantum system is to reduce the Liouville–von Neumann Eq. (5.2) for the full system $S + R$ to an effective equation of motion for a reduced density matrix, that describes only the relevant observables and degrees of freedom associated with S [39]. The reduced density matrix of the open quantum system $\rho_S(t) = \text{tr}_R(\rho(t))$ is obtained by taking the partial trace over the reservoir’s degrees of freedom. As the interaction between both subsystems S and R (mediated by H_{SR}) leads to correlations between the open system and its environment, the dynamics of S can no longer be described by a unitary time evolution. Instead, the time evolution of the open system

$$\rho_S(t) = V(t, 0) \rho_S(0) = \text{tr}_R(U(t, 0) \rho(0) U^\dagger(t, 0)) \quad (5.3)$$

is described by the dynamical map V that depends on the global propagator U and the state of the reservoir $\rho_R = \text{tr}_S(\rho)$, see Fig. 5.1 (b) [253]. By employing a series of approximations (see below), the generator \mathcal{L} of the dynamical map V can be found. Both are related as

$$\partial_t V(t, 0) = \mathcal{L}(t) V(t, 0). \quad (5.4)$$

The generator \mathcal{L} is called the *Liouvillian superoperator* and governs the evolution of the reduced density matrix

$$\partial_t \rho_S(t) = \mathcal{L}(t) \rho_S(t). \quad (5.5)$$

5.2.2 Derivation of the Lindblad equation in the weak-coupling limit with charge conservation constraint

In this section, the quantum master equation for an open quantum system weakly coupled to a carrier reservoir is derived in the Born-Markov-Secular (BMS) approximation. Since the central objective of this chapter is the description of electrically driven QD-based quantum light sources, the open quantum system S shall be identified with the coupled QD-photon system later on. The reservoir R will be later on identified with the (spatio-

temporally resolved) freely roaming electrons and holes evolving according to the van Roosbroeck system in the environment of the QD. Furthermore, the reservoir R may comprise the thermal radiation surrounding the device and the phonons of the crystal lattice. As the electron-hole plasma subject to the van Roosbroeck system is described by quasi-equilibrium distributions (see Secs. 2.1.2 and 2.3.1), the corresponding density matrix is a grand canonical ensemble state, see Eq. (2.29). The total reservoir is a tensor product of (uncorrelated) Gibbs states.

The open quantum system considered in this chapter can exchange next to energy also charge with its environment. As the total charge of the composite system $S + R$ must be conserved, the problem has an additional symmetry. This case goes beyond the standard textbook [39] derivation of the Lindblad master equation, which must be extended by the inclusion of an additional constraint. More precisely, the evolution of the composite quantum system is subject to the system-reservoir Hamiltonian (5.1) and the conditions

$$[H_S, N_S] = 0, \quad (5.6a)$$

$$[H_R, N_R] = 0, \quad (5.6b)$$

$$[H_{SR}, N_S + N_R] = 0, \quad (5.6c)$$

where N_S is the charge number operator of the open system and N_R is the charge number operator of the reservoir. The Hamiltonian evolution of the (uncoupled) system S and reservoir R leaves the charge state in the respective subsystems invariant, which is encoded by Eqs. (5.6a)–(5.6b). The conservation of the total charge by the system-reservoir interaction is enforced by Eq. (5.6c). As a consequence, it holds $[H, N] = 0$, such that the total charge is conserved in the composite system $S + R$, where $N = N_S + N_R$ is the total charge number operator. However, due to (in general) $[H_{SR}, N_S] \neq 0$ and $[H_{SR}, N_R] \neq 0$, non-trivial evolution arises as both systems can exchange charge according to Eq. (5.6c) via the system-reservoir interaction, cf. Ref. [265].

The derivation of the Lindblad master equation starts from the Liouville–von Neumann equation of the composite system in the interaction picture [39]

$$\partial_t \boldsymbol{\rho}(t) = -\frac{i}{\hbar} [\mathbf{H}_{SR}(t), \boldsymbol{\rho}(t)], \quad \boldsymbol{\rho}(0) = \rho(0), \quad (5.7)$$

where interaction picture operators are indicated by bold symbols. The transition to the interaction picture, where the time-dependency is partially carried by both the observables and the density matrix, is based on a factorization of the unitary time evolution operator $U(t) = U_0(t) \mathbf{U}(t)$. The propagator U_0 obeys the non-interacting Schrödinger equation

$$i\hbar \partial_t U_0(t) = (H_S + H_R) U_0(t), \quad U_0(0) = I, \quad (5.8)$$

yielding $U_0(t) = e^{-\frac{i}{\hbar}(H_S + H_R)t}$. The time evolution operator $\mathbf{U}(t)$ satisfies

$$i\hbar \partial_t \mathbf{U}(t) = \mathbf{H}_{SR}(t) \mathbf{U}(t), \quad \mathbf{U}(0) = I,$$

with the interaction picture representation of the coupling Hamiltonian

$$\mathbf{H}_{SR}(t) = U_0^\dagger(t) H_{SR} U_0(t).$$

The corresponding interaction picture density matrix reads

$$\boldsymbol{\rho}(t) = \mathbf{U}(t) \rho(0) \mathbf{U}^\dagger(t) = U_0^\dagger(t) \rho(t) U_0(t).$$

Time integration of Eq. (5.7) yields the formal solution

$$\boldsymbol{\rho}(t) = \boldsymbol{\rho}(0) - \frac{i}{\hbar} \int_0^t dt' [\mathbf{H}_{SR}(t'), \boldsymbol{\rho}(t')],$$

which can be iteratively substituted into Eq. (5.7), yielding a series expansion in terms of the interaction Hamiltonian. For a weak system-reservoir coupling, the expansion can be truncated at second order. Following Ref. [265], the charge conservation constraints (5.6), are considered by substituting

$$\mathbf{H}_{SR}(t) = e^{-i\alpha(N_S+N_R)t} \mathbf{H}_{SR}(t) e^{i\alpha(N_S+N_R)t}, \quad \alpha \in \mathbb{R}.$$

The above relation follows from Eq. (5.6) and (5.8). By taking the partial trace over the reservoirs degrees of freedom, this yields the (still exact) equation of motion

$$\begin{aligned} \partial_t \boldsymbol{\rho}_S(t) = & -\frac{i}{\hbar} \text{tr}_R([\mathbf{H}_{SR}(t), \boldsymbol{\rho}(0)]) - \\ & - \frac{1}{\hbar^2} \int_0^t d\tau \text{tr}_R([\mathbf{H}_{SR}(t) e^{i\alpha(N_S+N_R)t}, \dots \\ & \dots [e^{-i\alpha(N_S+N_R)(t-\tau)} \mathbf{H}_{SR}(t-\tau) e^{i\alpha(N_S+N_R)(t-\tau)}, \boldsymbol{\rho}(t-\tau)])]. \end{aligned}$$

The parameter α is still free and will be chosen later on.

The above equation still depends on the full density matrix of the composite system. The problem is greatly simplified by assuming a weak system-reservoir coupling, such that the correlations between both subsystems are negligible. This implies the factorization

$$\boldsymbol{\rho}(t) = \rho_S(t) \otimes \rho_R(t) \quad (5.9)$$

which is called the *Born approximation* [39]. Here and in the following, the time-dependency of the reservoir is parametric, e.g., due to an externally controlled chemical potential with prescribed time-dependency (cf. Eq. (2.29)). To fully exploit the factorization of the density matrix (5.9), a tensor product decomposition of the interaction Hamiltonian is convenient in the following. The most general form of the system-reservoir interaction Hamiltonian is given by [39]

$$\mathbf{H}_{SR} = \sum_{\nu} \mathcal{A}_{\nu} \otimes B_{\nu} \quad (5.10)$$

with Hermitian coupling operators $\mathcal{A}_{\nu} = \mathcal{A}_{\nu}^{\dagger} \in \mathcal{H}_S$ and $B_{\nu} = B_{\nu}^{\dagger} \in \mathcal{H}_R$ [39].¹ With Eq. (5.9) and $\mathbf{H}_{SR}(t) = \sum_{\nu} \mathcal{A}_{\nu}(t) \otimes B_{\nu}(t)$, one arrives at

$$\begin{aligned} \partial_t \boldsymbol{\rho}_S(t) = & -\frac{i}{\hbar} \sum_{\nu} [\mathcal{A}_{\nu}(t), \rho_S(0)] \text{tr}_R(B_{\nu}(t) \rho_R(0)) \\ & + \sum_{\mu, \nu} \int_0^t d\tau \left[e^{-i\alpha N_S(t-\tau)} \mathcal{A}_{\nu}(t-\tau) e^{i\alpha N_S(t-\tau)} \rho_S(t-\tau) e^{-i\alpha N_S t} \mathcal{A}_{\mu}(t) e^{i\alpha N_S t} - \right. \\ & \left. - e^{-i\alpha N_S t} \mathcal{A}_{\mu}(t) e^{i\alpha N_S \tau} \mathcal{A}_{\nu}(t-\tau) e^{i\alpha N_S(t-\tau)} \rho_S(t-\tau) \right] \times \\ & \times \frac{1}{\hbar^2} \text{tr}_R(e^{-i\alpha N_R t} B_{\mu}(t) e^{i\alpha N_R \tau} B_{\nu}(t-\tau) e^{i\alpha N_R(t-\tau)} \rho_R(t-\tau)) + \text{h.c.} \end{aligned}$$

¹ For (anti-commuting) fermionic coupling operators the tensor product decomposition is achieved by the Jordan–Wigner transformation, see Refs. [266, 267].

The first term can be omitted by assuming $\text{tr}_R(\mathbf{B}_\nu(t)\rho_R(0)) = 0$, which is readily fulfilled in many problems. Otherwise it can always be achieved by a suitable transformation [266].

The above equation of motion still depends on the entire history of the system, making its solution very difficult. The evolution of the reduced system S depends on its own history as its earlier states become imprinted in the reservoir via the system-reservoir interaction. However, if the reservoir R has a large number of degrees of freedom with a (quasi-)continuous energy spectrum and is always close to a Gibbs state, the changes in R induced by S will decay on a time scale that is very fast in comparison to the system's internal dynamics [45]. Then the integral is non-zero only in a close vicinity of $\tau \approx 0$ such that it is justified to replace $\rho_{S/R}(t-\tau) \rightarrow \rho_{S/R}(t)$ and shift the upper integral boundary to infinity. This is called the *Markov approximation* which yields the *Redfield equation* [39]

$$\begin{aligned} \partial_t \rho_S(t) = & \sum_{\mu,\nu} \int_0^\infty d\tau \left[e^{-i\alpha N_S(t-\tau)} \mathcal{A}_\nu(t-\tau) e^{i\alpha N_S(t-\tau)} \rho_S(t) e^{-i\alpha N_S t} \mathcal{A}_\mu(t) e^{i\alpha N_S t} \right. \\ & \left. - e^{-i\alpha N_S t} \mathcal{A}_\mu(t) e^{i\alpha N_S \tau} \mathcal{A}_\nu(t-\tau) e^{i\alpha N_S(t-\tau)} \rho_S(t) \right] \times \quad (5.11) \\ & \times \frac{1}{\hbar^2} \text{tr}_R \left(e^{-i\alpha N_R t} \mathbf{B}_\mu(t) e^{i\alpha N_R \tau} \mathbf{B}_\nu(t-\tau) e^{i\alpha N_R(t-\tau)} \rho_R(t) \right) + \text{h.c.}, \end{aligned}$$

that describes the evolution of the reduced system on a coarse-grained time-scale (slower than the decay time of the reservoir correlation functions).

The *secular approximation* is conveniently performed using a spectral decomposition of the coupling operator \mathcal{A}_ν . Assuming the spectra of H_S and N_S to be discrete, they can be represented in terms of projection operators

$$H_S = \sum_\varepsilon \varepsilon \Pi_{H_S}(\varepsilon), \quad N_S = \sum_\ell \ell \Pi_{N_S}(\ell),$$

where the projectors $\Pi_{H_S}(\varepsilon)$ and $\Pi_{N_S}(\ell)$ map on the eigenspaces of the corresponding energy eigenvalue $\varepsilon \in \mathbb{R}$ or charge number $\ell \in \mathbb{Z}$, respectively. The projectors satisfy

$$\Pi_{H_S}(\varepsilon) \Pi_{H_S}(\varepsilon') = \delta_{\varepsilon,\varepsilon'} \Pi_{H_S}(\varepsilon'), \quad \Pi_{N_S}(\ell) \Pi_{N_S}(\ell') = \delta_{\ell,\ell'} \Pi_{N_S}(\ell'), \quad (5.12)$$

the commutator $[\Pi_{H_S}(\varepsilon), \Pi_{N_S}(\ell)] = 0$ (due to Eq. (5.6a)) and the completeness relations

$$\sum_\varepsilon \Pi_{H_S}(\varepsilon) = I_S, \quad \sum_\ell \Pi_{N_S}(\ell) = I_S. \quad (5.13)$$

Finally, one introduces the spectrally filtered coupling operator

$$A_\nu(\omega, \ell) = \sum_{\varepsilon' - \varepsilon = \hbar\omega} \sum_{m' - m = \ell} \Pi_{H_S}(\varepsilon) \Pi_{N_S}(m) \mathcal{A}_\nu \Pi_{N_S}(m') \Pi_{H_S}(\varepsilon'), \quad (5.14)$$

where the summation is extended over all energy eigenvalues $\varepsilon, \varepsilon'$ of H_S with a fixed energy difference $\hbar\omega$ and all eigenvalues m, m' of N_S with a fixed charge difference ℓ . Note that Eq. (5.14) extends the standard definition [39] to the case of open quantum systems with variable charge. In the Lindblad master equation, which will be the final result at the end of the section, the operators $A_\nu(\omega, \ell)$ will occur as *quantum jump operators* mediating certain dissipative transitions (labeled by ν), where the system S exchanges the energy $\hbar\omega$ and the charge ℓ with its environment. With the properties of the projection operators

detailed above, the definition (5.14) immediately yields the relations [160]

$$[H_S, A_\nu(\omega, \ell)] = -\hbar\omega A_\nu(\omega, \ell), \quad (5.15a)$$

$$[N_S, A_\nu(\omega, \ell)] = -\ell A_\nu(\omega, \ell), \quad (5.15b)$$

and
$$A_\nu^\dagger(\omega, \ell) = A_\nu(-\omega, -\ell). \quad (5.16)$$

The operators $A_\nu(\omega, \ell)$ and $A_\nu^\dagger(\omega, \ell)$ are therefore called *eigenoperators* of H_S and N_S to the respective eigenvalues $\pm\hbar\omega$ and $\pm\ell$. From Eqs. (5.12)–(5.14) one obtains

$$[H_S, A_\mu^\dagger(\omega, \ell) A_\nu(\omega, \ell)] = 0, \quad (5.17)$$

and the spectral decomposition of the coupling operator

$$\mathcal{A}_\nu = \sum_{\omega, \ell} A_\nu(\omega, \ell) = \sum_{\omega, \ell} A_\nu^\dagger(\omega, \ell). \quad (5.18)$$

Using *Hadamard's lemma* of the Baker–Campbell–Hausdorff formula [321], Eqs. (5.15a) and (5.18), a simple interaction picture representation of the coupling operator is obtained:

$$\mathcal{A}_\nu(t) = U_0^\dagger(t) A_\nu U_0(t) = \sum_{\omega, \ell} e^{-i\omega t} A_\nu(\omega, \ell).$$

Similarly, from Eq. (5.15b) it follows that $e^{-i\alpha N_S t} A_\nu(\omega, \ell) e^{i\alpha N_S t} = e^{i\alpha \ell t} A_\nu(\omega, \ell)$. As a result, the above quantum master equation can be cast in the form

$$\begin{aligned} \partial_t \rho_S(t) &= \sum_{\mu, \nu} \sum_{\omega, \omega'} \sum_{\ell, \ell'} e^{-i(\omega - \omega')t} e^{i\alpha(\ell - \ell')t} \Gamma_{\mu, \nu}(\omega, \ell, t) \times \\ &\quad \times (A_\nu(\omega, \ell) \rho_S(t) A_\mu^\dagger(\omega', \ell') - A_\mu^\dagger(\omega', \ell') A_\nu(\omega, \ell) \rho_S(t)) + \text{h.c.} \end{aligned}$$

with the one-sided Fourier transform of the reservoir correlation function

$$\begin{aligned} \Gamma_{\mu, \nu}(\omega, \ell, t) &= \frac{1}{\hbar^2} \int_0^\infty d\tau e^{i(\omega - \alpha\ell)\tau} \times \\ &\quad \times \text{tr}_R(\mathbf{B}_\mu(t) e^{i\alpha N_R \tau} \mathbf{B}_\nu(t - \tau) e^{-i\alpha N_R \tau} e^{i\alpha N_R t} \rho_R(t) e^{-i\alpha N_R t}). \end{aligned}$$

The reservoir is assumed to be in a grand canonical ensemble state (cf. Eq. (2.29))

$$\rho_R(t) = \frac{1}{Z_R(t)} e^{-\beta(H_R - \mu_R(t)N_R)}, \quad (5.19)$$

where the time-dependency is carried by the externally controlled chemical potential μ_R . Then, by exploiting the commutator relation (5.6b), the above expression reduces to

$$\Gamma_{\mu, \nu}(\omega, \ell, \mu_R) = \frac{1}{\hbar^2} \int_0^\infty d\tau e^{\frac{i}{\hbar}(\hbar\omega - \mu_R \ell)\tau} \langle e^{-\frac{i}{\hbar}\mu_R N_R \tau} \mathbf{B}_\mu(\tau) e^{\frac{i}{\hbar}\mu_R N_R \tau} \mathbf{B}_\nu \rangle_{\rho_R}, \quad (5.20)$$

where $\Gamma_{\mu, \nu}$ is now written as a function of μ_R . Moreover, α was set to μ_R/\hbar . The reservoir correlation function is taken with respect to the Schrödinger picture density matrix

$$\langle e^{-\frac{i}{\hbar}\mu_R N_R \tau} \mathbf{B}_\mu(\tau) e^{\frac{i}{\hbar}\mu_R N_R \tau} \mathbf{B}_\nu \rangle_{\rho_R} = \text{tr}_R(e^{-\frac{i}{\hbar}\mu_R N_R \tau} \mathbf{B}_\mu(\tau) e^{\frac{i}{\hbar}\mu_R N_R \tau} \mathbf{B}_\nu \rho_R).$$

Eventually, the *secular approximation* is performed by discarding all terms with $\omega \neq \omega'$ in the above master equation. This is justified if the non-secular terms with $\omega \neq \omega'$ oscillate very rapidly during the time on which ρ_S varies appreciably [39, 45]. With the same arguments, all terms with $\ell \neq \ell'$ are neglected in the following. This approximation is typically well fulfilled in quantum optical systems, where it is known as *rotating wave approximation* [45, 276]. The approximation yields

$$\begin{aligned} \partial_t \rho_S(t) &= \sum_{\mu, \nu} \sum_{\omega, \ell} \Gamma_{\mu, \nu}(\omega, \ell, \mu_R) (A_\nu(\omega, \ell) \rho_S(t) A_\mu^\dagger(\omega, \ell) - A_\mu^\dagger(\omega, \ell) A_\nu(\omega, \ell) \rho_S(t)) \\ &+ \text{h.c.} \end{aligned}$$

Finally, Eq. (5.20) is decomposed as

$$\Gamma_{\mu, \nu}(\omega, \ell, \mu_R) = \frac{1}{2} \gamma_{\mu, \nu}(\omega, \ell, \mu_R) + \frac{i}{\hbar} \sigma_{\mu, \nu}(\omega, \ell, \mu_R)$$

with the Hermitian matrices

$$\begin{aligned} \gamma_{\mu, \nu}(\omega, \ell, \mu_R) &= \gamma_{\nu, \mu}^*(\omega, \ell, \mu_R) = \Gamma_{\mu, \nu}(\omega, \ell, \mu_R) + \Gamma_{\nu, \mu}^*(\omega, \ell, \mu_R) \\ &= \frac{1}{\hbar^2} \int_{-\infty}^{\infty} d\tau e^{\frac{i}{\hbar}(\hbar\omega - \mu_R \ell)\tau} \langle e^{-\frac{i}{\hbar}\mu_R N_R \tau} \mathbf{B}_\mu(\tau) e^{\frac{i}{\hbar}\mu_R N_R \tau} B_\nu \rangle_{\rho_R}, \end{aligned} \quad (5.21)$$

and

$$\begin{aligned} \sigma_{\mu, \nu}(\omega, \ell, \mu_R) &= \sigma_{\nu, \mu}^*(\omega, \ell, \mu_R) = \frac{\hbar}{2i} (\Gamma_{\mu, \nu}(\omega, \ell, \mu_R) - \Gamma_{\nu, \mu}^*(\omega, \ell, \mu_R)) \\ &= \frac{1}{2i\hbar} \int_{-\infty}^{\infty} d\tau \text{sign}(\tau) e^{\frac{i}{\hbar}(\hbar\omega - \mu_R \ell)\tau} \langle e^{-\frac{i}{\hbar}\mu_R N_R \tau} \mathbf{B}_\mu(\tau) e^{\frac{i}{\hbar}\mu_R N_R \tau} B_\nu \rangle_{\rho_R}. \end{aligned} \quad (5.22)$$

This yields the Lindblad master equation² [102, 191]

$$\partial_t \rho_S(t) = \mathcal{L}(\mu_R) \rho_S(t) = -\frac{i}{\hbar} [\mathbf{H}_{\text{LS}}(\mu_R), \rho_S(t)] + \mathcal{D}(\mu_R) \rho_S(t) \quad (5.23)$$

with the interaction picture Lamb shift Hamiltonian

$$\mathbf{H}_{\text{LS}}(\mu_R) = \sum_{\mu, \nu} \sum_{\omega, \ell} \sigma_{\mu, \nu}(\omega, \ell, \mu_R) A_\mu^\dagger(\omega, \ell) A_\nu(\omega, \ell) \quad (5.24)$$

and the *dissipation superoperator*

$$\begin{aligned} \mathcal{D}(\mu_R) \rho_S(t) &= \sum_{\mu, \nu} \sum_{\omega, \ell} \gamma_{\mu, \nu}(\omega, \ell, \mu_R) \times \\ &\times (A_\nu(\omega, \ell) \rho_S(t) A_\mu^\dagger(\omega, \ell) - \frac{1}{2} \{A_\mu^\dagger(\omega, \ell) A_\nu(\omega, \ell), \rho_S(t)\}), \end{aligned} \quad (5.25)$$

where $\{\cdot, \cdot\}$ denotes the anti-commutator and \mathcal{L} is the Liouvillian. The Hamiltonian (5.24) and the dissipation superoperator (5.25) depend on the state of the macroscopic environment, which is defined by the chemical potential μ_R . The dissipation superoperator

² Sometimes it is also referred to as the Gorini–Kossakowski–Sudarshan–Lindblad master equation.

can be diagonalized by a unitary transformation of the jump operators [39]

$$A_\nu(\omega, \ell) = \sum_\alpha u_{\nu, \alpha}(\omega, \ell) \bar{A}_\alpha(\omega, \ell), \quad A_\mu^\dagger(\omega, \ell) = \sum_\beta \bar{A}_\beta^\dagger(\omega, \ell) u_{\beta, \mu}^*(\omega, \ell)$$

such that via $\delta_{\alpha, \beta} \bar{\gamma}_\alpha(\omega, \ell, \mu_R) = \sum_{\mu, \nu} u_{\beta, \mu}^*(\omega, \ell) \gamma_{\mu, \nu}(\omega, \ell, \mu_R) u_{\nu, \alpha}(\omega, \ell)$ the transition rate matrix becomes diagonal. The diagonalized dissipation superoperator reads

$$\mathcal{D}(\mu_R) \rho_S(t) = \sum_\alpha \sum_{\omega, \ell} \bar{\gamma}_\alpha(\omega, \ell, \mu_R) L_{\bar{A}_\alpha(\omega, \ell)} \rho_S(t), \quad (5.26)$$

where the *Lindblad superoperator* was introduced as

$$L_A \rho = A \rho A^\dagger - \frac{1}{2} \{A^\dagger A, \rho\}. \quad (5.27)$$

The Lindblad master equation (5.23) has many appealing properties. Most important, it preserves the trace of the reduced density matrix (because the Lindblad superoperator (5.27) is trace-free $\text{tr}(L_A(\rho)) = 0$, independent of $\text{tr}(\rho)$). Moreover, the Lindblad master equation preserves the self-adjointness $\rho = \rho^\dagger$ and the (complete) positivity of ρ_S [39]. Note that these properties are non-trivial as, e.g., the Redfield equation (5.11) does not guarantee the positivity of the density matrix [61].

5.2.3 Thermodynamic properties

5.2.3.1 Generalized Kubo–Martin–Schwinger condition

The reservoir correlation function satisfies the *generalized* Kubo–Martin–Schwinger (KMS) condition

$$\begin{aligned} \langle e^{-\frac{i}{\hbar} \mu_R N_R \tau} \mathbf{B}_\mu(\tau) e^{\frac{i}{\hbar} \mu_R N_R \tau} \mathbf{B}_\nu \rangle_{\rho_R} \\ = \langle \mathbf{B}_\nu e^{-\frac{i}{\hbar} \mu_R N_R (\tau + i\beta \hbar)} \mathbf{B}_\mu(\tau + i\beta \hbar) e^{\frac{i}{\hbar} \mu_R N_R (\tau + i\beta \hbar)} \rangle_{\rho_R}. \end{aligned} \quad (5.28)$$

The KMS condition (5.28) relies on the formal identification of the thermal Gibbs state ρ_R with an evolution operator $\rho_R \sim U_0(-i\beta \hbar)$ in imaginary time, where $\beta^{-1} = k_B T$ is the inverse temperature. For the reservoir density matrix (5.19), the relation (5.28) can be checked by straightforward calculation. The KMS condition plays an important role in thermal quantum field theory, where it provides an abstract definition of equilibrium states [117, 177, 288]. In Eq. (5.28) the usual KMS condition for (bosonic) heat baths [39] is extended to carrier reservoirs and charge preserving system–environment interactions.

5.2.3.2 Quantum detailed balance relation

The forward and backward transition rates (5.21) in the dissipation superoperator (5.25) are related by the KMS condition (5.28). First, it holds

$$\begin{aligned} \gamma_{\nu, \mu}(\mu_R, -\omega, -\ell) &= \frac{1}{\hbar^2} \int_{-\infty}^{\infty} d\tau e^{-\frac{i}{\hbar} (\hbar \omega - \mu_R \ell) \tau} \langle e^{-\frac{i}{\hbar} \mu_R N_R \tau} \mathbf{B}_\nu(\tau) e^{\frac{i}{\hbar} \mu_R N_R \tau} \mathbf{B}_\mu \rangle_{\rho_R} \\ &= \frac{1}{\hbar^2} \int_{-\infty}^{\infty} d\tau e^{-\frac{i}{\hbar} (\hbar \omega - \mu_R \ell) \tau} \times \\ &\quad \times \langle \mathbf{B}_\mu e^{-\frac{i}{\hbar} \mu_R N_R (\tau + i\beta \hbar)} \mathbf{B}_\nu(\tau + i\beta \hbar) e^{\frac{i}{\hbar} \mu_R N_R (\tau + i\beta \hbar)} \rangle_{\rho_R}. \end{aligned}$$

By the complex substitution $s = -\tau - i\beta\hbar$, one arrives at

$$\begin{aligned}\gamma_{\nu,\mu}(\mu_R, -\omega, -\ell) &= \frac{1}{\hbar^2} \int_{-\infty - i\beta\hbar}^{\infty - i\beta\hbar} ds e^{-\frac{i}{\hbar}(\hbar\omega - \mu_R\ell)(-s - i\beta\hbar)} \times \\ &\quad \times \langle B_\mu e^{\frac{i}{\hbar}\mu_R N_{RS}} B_\nu(-s) e^{-\frac{i}{\hbar}\mu_R N_{RS}} \rangle_{\rho_R} \\ &= e^{-\beta(\hbar\omega - \mu_R\ell)} \frac{1}{\hbar^2} \int_{-\infty}^{\infty} ds e^{\frac{i}{\hbar}(\hbar\omega - \mu_R\ell)s} \times \\ &\quad \times \langle e^{-\frac{i}{\hbar}\mu_R N_{RS}} B_\mu(s) e^{\frac{i}{\hbar}\mu_R N_{RS}} B_\nu \rangle_{\rho_R},\end{aligned}$$

which finally yields the relation between forward and backward transition rates as

$$\gamma_{\nu,\mu}(\mu_R, -\omega, -\ell) = e^{-\beta(\hbar\omega - \mu_R\ell)} \gamma_{\mu,\nu}(\mu_R, \omega, \ell). \quad (5.29)$$

For certain processes, which leave the charge invariant ($\ell = 0$) and run independent of the state of the carrier reservoir (e.g., spontaneous emission or out-coupling of cavity photons), the relation (5.29) simplifies to $\gamma_{\nu,\mu}(\mu_R, -\omega, 0) = e^{-\beta\hbar\omega} \gamma_{\mu,\nu}(\mu_R, \omega, 0)$. With Eq. (5.29) the (Schrödinger picture) dissipation superoperator (5.25) takes the form

$$\begin{aligned}\mathcal{D}(\mu_R) \rho_S(t) &= \sum_{\mu,\nu} \sum_{\omega>0} \sum_{\ell} \gamma_{\mu,\nu}(\omega, \ell, \mu_R) \times \\ &\quad \times (A_\nu(\omega, \ell) \rho_S(t) A_\mu^\dagger(\omega, \ell) - \frac{1}{2} \{A_\mu^\dagger(\omega, \ell) A_\nu(\omega, \ell), \rho_S(t)\}) \\ &\quad + e^{-\beta(\hbar\omega - \mu_R\ell)} \gamma_{\mu,\nu}(\omega, \ell, \mu_R) \times \\ &\quad \times (A_\mu^\dagger(\omega, \ell) \rho_S(t) A_\nu(\omega, \ell) - \frac{1}{2} \{A_\nu(\omega, \ell) A_\mu^\dagger(\omega, \ell), \rho_S(t)\}).\end{aligned}$$

In the thermodynamic equilibrium the open system S approaches the Gibbs state

$$\rho_S^{\text{eq}} = \frac{1}{Z_S} e^{-\beta(H_S - \mu_{\text{eq}} N_S)} \quad (5.30)$$

with $Z_S = \text{tr}_S (e^{-\beta(H_S - \mu_{\text{eq}} N_S)})$ and the equilibrium chemical potential μ_{eq} . In this case the Hamiltonian part of the Lindblad Eq. (5.23) vanishes (microscopic reversibility; Eq. (5.17) implies $[H_S, H_{\text{LS}}(\mu_R)] = 0$)

$$[H_S + H_{\text{LS}}(\mu_R), \rho_S^{\text{eq}}] = 0 \quad (5.31)$$

and one obtains

$$\rho_S^{\text{eq}} A_\nu(\omega, \ell) = e^{\beta(\hbar\omega - \mu_{\text{eq}}\ell)} A_\nu(\omega, \ell) \rho_S^{\text{eq}}.$$

Hence, if the system S is in equilibrium, the dissipation superoperator reduces to

$$\begin{aligned}\mathcal{D}(\mu_R) \rho_S^{\text{eq}} &= \sum_{\mu,\nu} \sum_{\omega>0} \sum_{\ell} \gamma_{\mu,\nu}(\omega, \ell, \mu_R) (1 - e^{\beta(\mu_R - \mu_{\text{eq}})\ell}) \times \\ &\quad \times (A_\nu(\omega, \ell) \rho_S^{\text{eq}} A_\mu^\dagger(\omega, \ell) - e^{-\beta(\hbar\omega - \mu_{\text{eq}}\ell)} A_\mu^\dagger(\omega, \ell) \rho_S^{\text{eq}} A_\nu(\omega, \ell)).\end{aligned}$$

The dissipator $\mathcal{D}(\mu_R) \rho_S^{\text{eq}}$ vanishes due to pairwise cancellation of forward and backward scattering processes if the system and the reservoir simultaneously approach the thermodynamic equilibrium $\rho_S \rightarrow \rho_S^{\text{eq}}$ and $\mu_R \rightarrow \mu_{\text{eq}}$. This is called the *quantum detailed balance relation*, that is a direct consequence of the generalized KMS condition (5.28) [5, 177, 288].

5.2.3.3 Entropy production and the second law of thermodynamics

The theory of open quantum systems is intimately connected with the field of *quantum thermodynamics*, which deals with the emergence of thermodynamic laws from quantum mechanics on the nanoscale. Quantum thermodynamics differs from quantum statistical mechanics as it focuses on the investigation of irreversible dynamical processes out of equilibrium [89, 176]. For an open quantum system that obeys the Lindblad master Eq. (5.23) it can be shown [192] that the so-called *relative entropy*

$$\mathcal{S}_{\text{rel}}(\rho_S, \rho_S^{\text{eq}}) = k_B \text{tr}_S (\rho_S \log \rho_S - \rho_S \log \rho_S^{\text{eq}}) \quad (5.32)$$

is contractive over time

$$\mathcal{S}_{\text{rel}}(V(t, 0) \rho_S(0), V(t, 0) \rho_S^{\text{eq}}) = \mathcal{S}_{\text{rel}}(\rho_S(t), \rho_S^{\text{eq}}) \leq \mathcal{S}_{\text{rel}}(\rho_S(0), \rho_S^{\text{eq}}). \quad (5.33)$$

Here, V is the dynamical map generated by the Liouvillian of the Lindblad equation (see Eq. (5.23)) and ρ_S^{eq} is a stationary state of the system, i.e., $V(t, 0) \rho_S^{\text{eq}} \equiv \rho_S^{\text{eq}}$. The equality in Eq. (5.33) holds only if $\rho_S = \rho_S^{\text{eq}}$ [192]. The proof of Eq. (5.33) relies on the strong sub-additivity property of the von Neumann entropy [192]

$$\mathcal{S}(\rho_S) = -k_B \text{tr}_S (\rho_S \log \rho_S). \quad (5.34)$$

Using the parameter differentiation of operator logarithms [321], Eq. (5.33) yields an inequality for the time derivative of the relative entropy (5.32)

$$-\frac{d}{dt} \mathcal{S}_{\text{rel}}(\rho_S(t) | \rho_S^{\text{eq}}) = k_B \text{tr}_S ((\log \rho_S^{\text{eq}} - \log \rho_S(t)) \mathcal{L}(t) \rho_S(t)) \geq 0 \quad (5.35)$$

which is known as *Spohn's inequality* [287, 288]. As the relative entropy is closely related to the grand potential $\Phi_S(\rho_S) = \text{tr}_S (H_S \rho_S) + k_B T \text{tr}_S (\rho_S \log \rho_S) - \mu_{\text{eq}} \text{tr}_S (N_S \rho_S)$

$$-\frac{d}{dt} \mathcal{S}_{\text{rel}}(\rho_S, \frac{1}{Z_S} e^{-\beta(H_S - \mu_{\text{eq}} N_S)}) = -\frac{1}{T} \frac{d\Phi_S(\rho)}{dt} = \frac{d\mathcal{S}_{\text{tot}}}{dt} \geq 0,$$

the corresponding total entropy production rate is always non-negative. Thus, Spohn's inequality states the second law of thermodynamics. For the Liouvillian (5.23), the entropy production rate is independent of the Hamiltonian part such that (use cyclic permutations and Eq. (5.31))

$$\dot{\mathcal{S}}_{\text{tot}} = k_B \text{tr}_S ((\log \rho_S^{\text{eq}} - \log \rho_S(t)) \mathcal{D}(\mu_R) \rho_S(t)) \geq 0. \quad (5.36)$$

5.3 Hybrid quantum-classical model for electrically driven quantum light sources

The comprehensive device-scale simulation of electrically driven QD-based quantum light emitters requires a combination of semi-classical carrier transport theory with models from cavity quantum electrodynamics. This was pointed out in Sec. 5.1. Following a multi-species ansatz [175, 289], that separates the freely roaming continuum carriers from the confined carriers bound to the QDs, this can be achieved by the self-consistent coupling of the van Roosbroeck system (2.1) and a Lindblad type master equation (5.23). The separation of bound and continuum carriers corresponds to the Born approximation (5.9),

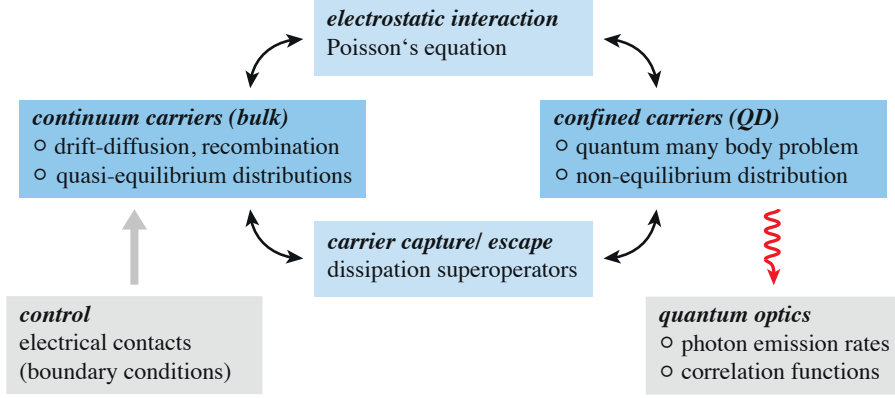


Fig. 5.2 Schematic representation of the hybrid quantum-classical model (5.37). The coupling is based on the separation of continuum and QD-confined carriers. Both subsystems interact via electrostatics and the dissipative exchange of charge carriers. The hybrid model allows to investigate the evolution of the open quantum system in response to the excitation of the device at the electrical contacts. Reprinted with permission from Ref. [160]. ©2017 American Physical Society.

which is typically well justified for opto-electronic devices working in the vicinity of flat band conditions. The resulting *hybrid quantum-classical model* system reads [160]

$$-\nabla \cdot \varepsilon \nabla \phi = q(p - n + C + Q(\rho_S)), \quad (5.37a)$$

$$\partial_t n - \frac{1}{q} \nabla \cdot \mathbf{j}_n = -R - S_n(\mu_c, \mu_v, \phi, \rho_S), \quad (5.37b)$$

$$\partial_t p + \frac{1}{q} \nabla \cdot \mathbf{j}_p = -R - S_p(\mu_c, \mu_v, \phi, \rho_S), \quad (5.37c)$$

$$\partial_t \rho_S = \mathcal{L}(\mu_c, \mu_v, \phi) \rho_S = -\frac{i}{\hbar} [\hat{H}, \rho_S] + \mathcal{D}(\mu_c, \mu_v, \phi) \rho_S, \quad (5.37d)$$

where Eqs. (5.37a)–(5.37c) constitute an extended van Roosbroeck system, which contains additional terms that describe the coupling to the quantum system. Here and in the following, the *quantum system* refers to the coupled QD-photon system subject to the Lindblad master equation (5.37d). The novel coupling terms in Eqs. (5.37a)–(5.37c) model the charge density and its exchange between the macroscopic and the quantum system. First, the quantum system may be in a charged state (e.g., the QD is occupied by a single electron/hole or a trion) described by the charge density $qQ(\rho_S)$, which contributes to the generation of the self-consistent electrostatic field. Hence, it contributes to the right hand side of Poisson's Eq. (5.37a). Second, the electrons and holes can be scattered from the continuum states to the QD states (and back), which changes the continuum carrier density subject to the van Roosbroeck system. This is reflected by the macroscopic scattering rates S_n and S_p on the right hand side of the continuity Eqs. (5.37b)–(5.37c), respectively. Note that these scattering rates account for the net-process and thereby include both the capture and escape of carriers (just like the net-recombination rate R , cf. Sec. 2.1.4).

The time evolution of the quantum system is described by the Lindblad master equation (5.37d) for the reduced density matrix ρ_S . As the quantum system self-consistently interacts with the spatio-temporally resolved electron-hole plasma in its environment, the dissipation superoperator is a functional of the state (μ_c, μ_v, ϕ) of the macroscopic system. In the

following, occasionally the short notation $u = (\mu_c, \mu_v, \phi)$ will be used. The Hamiltonian \hat{H} in Eq. (5.37d) is a (simplified) Schrödinger–Poisson-like Hamiltonian

$$\hat{H} = H_S - q\langle\phi\rangle_w N_S, \quad (5.38)$$

where the second term yields a shift of the energy eigenvalues due to the electrostatic interaction with the macroscopic environment. The Lamb shift is neglected here and in the following. The coupling scheme is illustrated in Fig. 5.2.

The system (5.37) goes beyond existing approaches in the literature. While there is an extensive literature on microscopic models for QDs and the dynamics of the QD-photon system (see, e.g., Ref. [48] for a review), only few of them [98, 105, 175] take the transport in the environment into account. These approaches are, however, all based on classical rate equations for large QD ensembles and can not be employed for single QD problems. The essential reason for this is the different treatment of the Pauli exclusion principle in Master equations and (Boltzmann-like) classical rate equations [109]. The latter describe the QD population in terms of single-particle distribution functions, that provide a mean field description of the population with independently taken ensemble averages. Therefore, transitions between microscopic configurations are not described accurately, which is essential for single QDs (see also Refs. [94, 291]). In this respect, single QDs differ from any higher dimensional semiconductor nanostructure (quantum wires, quantum wells) and also from QD ensembles with a high QD sheet density [109].

5.3.1 Modeling of the quantum system

The open quantum system considered throughout this section is an interacting many-body system. The number of particles fluctuates, as the quantum system is allowed to exchange energy and charge with its environment. This is conveniently described by the second quantization formalism [119, 130], where the Hamiltonian and other observables of the quantum system are formulated in terms of annihilation and creation operators. In order to be more illustrative, an exemplary (and rather general) Hamiltonian is considered, that covers many problems in semiconductor QD electronics and quantum optics (see Ref. [48])

$$\begin{aligned} H_S = & \sum_i \varepsilon_{c,i} e_i^\dagger e_i - \sum_i \varepsilon_{v,i} h_i^\dagger h_i + \sum_j \hbar\omega_j a_j^\dagger a_j, \\ & + \frac{1}{2} \sum_{i,j,kl} \left(V_{i,j,k,l}^{e,e} e_i^\dagger e_j^\dagger e_k e_l + V_{i,j,k,l}^{h,h} h_i^\dagger h_j^\dagger h_k h_l - 2V_{i,j,k,l}^{e,h} e_i^\dagger h_j^\dagger h_k e_l \right) \\ & + \sum_{i,j,k} \left(\hbar g_{i,j,k} e_i^\dagger h_j^\dagger a_k + \hbar g_{i,j,k}^* a_k^\dagger h_j e_i \right). \end{aligned} \quad (5.39)$$

The first line describes the single-particle energies $\varepsilon_{c,i}$ and $\varepsilon_{v,i}$ of the bound QD electrons and holes and the energy of the cavity photons with angular frequencies ω_i . For the sake of simplicity, the discussion is restricted to a single QD coupled to the radiation field. The generalization to multiple QDs is straightforward. The multi-index i labels either the single-particle energy level and spin state of the fermions or the mode and polarization index of the photons (for the optical modes considered part of the quantum system), respectively. The fermionic creation and annihilation operators satisfy the anti-commutator relations

$$\begin{aligned} \{e_i, e_j^\dagger\} &= \delta_{i,j}, & \{e_i, e_j\} &= \{e_i^\dagger, e_j^\dagger\} = 0, \\ \{h_i, h_j^\dagger\} &= \delta_{i,j}, & \{h_i, h_j\} &= \{h_i^\dagger, h_j^\dagger\} = 0, \end{aligned} \quad (5.40)$$

and $\{h_i, e_j^\dagger\} = \{h_i, e_j\} = \{h_i^\dagger, e_j^\dagger\} = 0$. The creation and annihilation operators of the cavity photons obey the canonical commutator relations

$$[a_i, a_j^\dagger] = \delta_{i,j}, \quad [a_i, a_j] = [a_i^\dagger, a_j^\dagger] = 0. \quad (5.41)$$

The second line of the Hamiltonian (5.39) describes the Coulomb interaction between the bound electrons and holes (configuration interaction [11]). The first two terms model the repulsive electrostatic interaction between equally charged carriers (which increases the energy of the bound complexes) whereas the third yields an attractive electron-hole binding energy. The Coulomb matrix elements $V_{i,j,k,l}^{\lambda,\lambda'}$, $\lambda, \lambda' \in \{e, h\}$, are computed from the single-particle wave functions (see Appx. A.6) and possibly take screening effects into account [119, 130, 264]. The third line of the Hamiltonian (5.39) is a Jaynes–Cummings-like light-matter interaction Hamiltonian, that describes the coupling of the QD carriers to the quantized radiation field in the dipole- and rotating wave approximation [276]. The light-matter coupling constant $g_{i,j,k}$ depends on the optical frequency, the wave function overlap, the orientation of the dipole moment of the emitter and the polarization vector of the radiation field mode. Moreover, it contains the optical selection rules related to the conservation of angular momentum.

The charge number operator of the open system reads

$$N_S = n_e - n_h \quad (5.42)$$

with $n_e = \sum_i e_i^\dagger e_i$ and $n_h = \sum_i h_i^\dagger h_i$. A straightforward calculation shows that the Hamiltonian (5.39) satisfies the charge conservation property $[H_S, N_S] = 0$ (cf. Eq. (5.6a)).

5.3.2 Confined charge density and charge conservation

The charge density of a single QD (see above) is approximated as [160]

$$qQ(\rho_S) = -qw(\mathbf{r}) \text{tr}_S(N_S \rho_S), \quad (5.43)$$

where $\langle N_S \rangle = \text{tr}_S(N_S \rho_S)$ is the expectation value of the charge number operator (5.42) and w is called the (normalized) *spatial profile function*. The function w satisfies

$$\int_{\Omega} d^3r w(\mathbf{r}) = 1 \quad (5.44)$$

and phenomenologically replaces the complicated many-body wave functions that arise from the microscopically exact construction using the respective fermionic field operators [130]. The actual spatial distributions of the confined carriers vary only on a short length scale, that can be safely neglected in the simulation of macroscopic charge transport. With Eq. (5.43), the model (5.37) accounts for long-range electrostatic correlations.

By taking the time derivative of Poisson's equation (5.37a) and assuming the bound charge density as in Eq. (5.43), one arrives by substituting Eqs. (5.37b)–(5.37d) at the local balance equation for the total charge density

$$q(w(\mathbf{r}) \text{tr}_S(N_S \mathcal{D}(u) \rho_S) + S_p(u, \rho_S) - S_n(u, \rho_S)) + \nabla \cdot (\mathbf{j}_n + \mathbf{j}_p + \partial_t \mathbf{D}) = 0. \quad (5.45)$$

Here, a stationary doping profile C was assumed. The dependency of the scattering rates $S_{n/p}$ and the dissipator \mathcal{D} on the state of the macroscopic system is indicated by $u = (\mu_c, \mu_v, \phi)$. The local continuity equation for the charge density of the van Roosbroeck

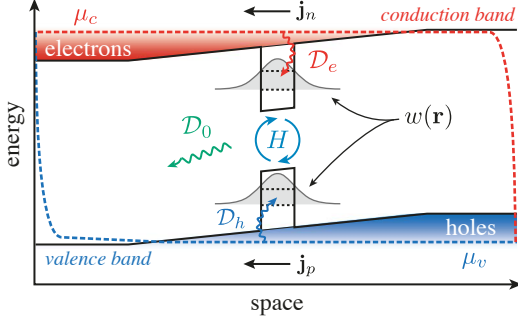


Fig. 5.3 Illustration of the coupling scheme and the spatial profile function $w(\mathbf{r})$ for a single QD embedded in a pin-diode structure. Reprinted with permission from Ref. [160]. ©2017 American Physical Society.

system (2.49) is recovered only if the charge exchange between the quantum system and its macroscopic environment obeys the local balance equation

$$w(\mathbf{r}) \operatorname{tr}_S (N_S \mathcal{D}(u) \rho_S) = S_n(u, \rho_S) - S_p(u, \rho_S). \quad (5.46)$$

In general, by integration over the computational domain Ω and using Kirchhoff's circuit law $\oint_{\partial\Omega} d\mathbf{A} \cdot (\mathbf{j}_n + \mathbf{j}_p + \partial_t \mathbf{D}) = \sum_i I_i = 0$, one obtains a non-local version of Eq. (5.46)

$$\int_{\Omega} d^3r w(\mathbf{r}) \operatorname{tr}_S (N_S \mathcal{D}(u(\mathbf{r})) \rho_S) = \int_{\Omega} d^3r (S_n(u(\mathbf{r}), \rho_S) - S_p(u(\mathbf{r}), \rho_S)). \quad (5.47)$$

Here, the spatial dependency of the macroscopic environment $u = u(\mathbf{r})$ is stated explicitly.

5.3.3 Energy, charge and entropy balance

The quantum system and the continuum carriers represent an open quantum-classical system $S = S_{\text{cl}} + S_{\text{qm}}$ that is coupled to a reservoir R . The system S and the reservoir R are allowed to exchange energy and charge. The reservoir comprises the electric contact reservoirs $R_{i \geq 1}$ at the boundary of the device (characterized by their chemical potentials μ_i and temperature T , modeled by ohmic boundary conditions, see Sec. 2.1.5) and a heat bath R_0 with a fixed background temperature T . The latter includes the vibrations of the crystal lattice and weakly coupled (off-resonant) modes of the surrounding radiation field.

The following discussion extends the considerations of Sec. 2.3.2 to the framework of the hybrid model. The change of entropy due to the system-reservoir interaction is assumed as³

$$\Delta \mathcal{S}_{\text{tot}} = \Delta \mathcal{S}_S + \Delta \mathcal{S}_R \quad (5.48a)$$

and the conservation of energy and charge is expressed by

$$0 = \Delta \mathcal{E}_S + \Delta \mathcal{E}_R, \quad (5.48b)$$

$$0 = \Delta \mathcal{N}_S + \Delta \mathcal{N}_R. \quad (5.48c)$$

The change of the reservoir's thermodynamic potentials comes from the different subsystems

$$\Delta \mathcal{S}_R = \sum_{i \geq 0} \Delta \mathcal{S}_{R_i}, \quad \Delta \mathcal{E}_R = \sum_{i \geq 0} \Delta \mathcal{E}_{R_i}, \quad \Delta \mathcal{N}_R = \sum_{i \geq 1} \Delta \mathcal{N}_{R_i},$$

and similarly, the changes of the thermodynamic potentials of the system S result from

³ The additive structure relies on the weak coupling assumption and the Born approximation (5.9).

the changes in the classical and the quantum mechanical subsystem

$$\Delta\mathcal{S}_S = \Delta\mathcal{S}_{S_{\text{cl}}} + \Delta\mathcal{S}_{S_{\text{qm}}}, \quad \Delta\mathcal{E}_S = \Delta\mathcal{E}_{S_{\text{cl}}} + \Delta\mathcal{E}_{S_{\text{qm}}}, \quad \Delta\mathcal{N}_S = \Delta\mathcal{N}_{S_{\text{cl}}} + \Delta\mathcal{N}_{S_{\text{qm}}}.$$

The heat bath R_0 can exchange only energy with S , such that the corresponding change of entropy is

$$\Delta\mathcal{S}_{R_0} = \frac{1}{T} \Delta\mathcal{E}_{R_0}.$$

For the contact reservoirs R_i the respective change of entropy includes also the work performed by the exchange of charge such that

$$\Delta\mathcal{S}_{R_i} = \frac{1}{T} \Delta\mathcal{E}_{R_i} - \frac{\mu_i}{T} \Delta\mathcal{N}_{R_i}, \quad i \geq 1.$$

Using the energy conservation law (5.48b), the entropy balance (5.48a) can be written as

$$\Delta\mathcal{S}_{\text{tot}} = -\frac{1}{T} \Delta\mathcal{F}_S - \frac{1}{T} \sum_{i \geq 1} \mu_i \Delta\mathcal{N}_{R_i},$$

where $\Delta\mathcal{F}_S = \Delta\mathcal{E}_S - T\Delta\mathcal{S}_S$ is the change of the free energy of the system S . The second term describes the charge flux from the system to the reservoir. Finally, by using Eq. (2.46), the expression for the entropy production rate takes the form

$$\frac{d\mathcal{S}_{\text{tot}}}{dt} = -\frac{1}{T} \frac{d\mathcal{F}_S}{dt} + \frac{1}{qT} \sum_{i \geq 1} \mu_i \int_{\Gamma_{D,i}} d\mathbf{A} \cdot (\mathbf{j}_n + \mathbf{j}_p). \quad (5.49)$$

This is formally equivalent to the result obtained in Sec. 2.3.2, however, now also the quantum mechanical free energy contribution is included in $\mathcal{F}_S = \mathcal{F}_S(n, p, \rho_S)$.

5.3.4 Thermodynamic equilibrium

In the thermodynamic equilibrium, the entropy production rate takes a global minimum and vanishes to zero. Defining the (negative) total charge of the system S

$$q\mathcal{N}_S = q \int_{\Omega} d^3r (n - p - Q(\rho_S)) \quad (5.50)$$

and taking the total time derivative (substituting Eqs. (5.37b)–(5.37d)) one obtains

$$\begin{aligned} \frac{d}{dt} \mathcal{N}_S &= \int_{\Omega} d^3r (\partial_t n - \partial_t p + w(\mathbf{r}) \text{tr}_S (N_S \mathcal{D}(u(\mathbf{r})) \rho_S)) \\ &= \frac{1}{q} \oint_{\partial\Omega} d\mathbf{A} \cdot (\mathbf{j}_n + \mathbf{j}_p) + \\ &\quad + \int_{\Omega} d^3r (w(\mathbf{r}) \text{tr}_S (N_S \mathcal{D}(u(\mathbf{r})) \rho_S) + S_p(u(\mathbf{r}), \rho_S) - S_n(u(\mathbf{r}), \rho_S)) \\ &= \frac{1}{q} \sum_{i \geq 1} \int_{\Gamma_{D,i}} d\mathbf{A} \cdot (\mathbf{j}_n + \mathbf{j}_p), \end{aligned}$$

where the non-local charge balance condition (5.47) has been exploited. With equilibrated reservoir chemical potentials $\mu_i \equiv \mu_{\text{eq}}$ and the above result, one obtains the equilibrium

entropy production rate as

$$0 = \left. \frac{d\mathcal{S}_{\text{tot}}}{dt} \right|_{\text{eq}} = -\frac{1}{T} \frac{d\mathcal{F}_S}{dt} + \frac{\mu_{\text{eq}}}{qT} \sum_{i \geq 1} \int_{\Gamma_{D,i}} d\mathbf{A} \cdot (\mathbf{j}_n + \mathbf{j}_p) = -\frac{1}{T} \frac{d\Phi_S^{\text{eq}}}{dt}.$$

Hence, the thermodynamic equilibrium state can be found by minimizing the equilibrium *hybrid* grand potential $\Phi_S^{\text{eq}} = \mathcal{F}_S - \mu_{\text{eq}}\mathcal{N}_S$, where the *hybrid* free energy functional

$$\mathcal{F}_S(n, p, \rho_S) = \mathcal{F}_{S_{\text{cl}}}(n, p) + \mathcal{F}_{S_{\text{qm}}}(\rho_S) + \mathcal{E}_\phi(n, p, \rho_S) \quad (5.51)$$

comprises the free energy $\mathcal{F}_{S_{\text{cl}}}$ of the electron-hole gas in the continuum states (2.31), the free energy of the (uncoupled) quantum system $\mathcal{F}_{S_{\text{qm}}}(\rho_S) = \text{tr}_S((H_S + k_B T \log \rho_S) \rho_S)$ (using the von Neumann entropy (5.34)) and the electrostatic interaction energy \mathcal{E}_ϕ (see Sec. 2.3.1.2). The hybrid equilibrium grand potential takes the form

$$\begin{aligned} \Phi_S^{\text{eq}}(n, p, \rho_S) = & \int_{\Omega} d^3r \left[k_B T \left(n F_{1/2}^{-1} \left(\frac{n}{N_c} \right) - N_c F_{3/2} \left(F_{1/2}^{-1} \left(\frac{n}{N_c} \right) \right) \right) + E_c n + \right. \\ & \left. + k_B T \left(p F_{1/2}^{-1} \left(\frac{p}{N_v} \right) - N_v F_{3/2} \left(F_{1/2}^{-1} \left(\frac{p}{N_v} \right) \right) \right) - E_v p \right] \\ & + \text{tr}_S((H_S + k_B T \log \rho_S) \rho_S) + \mathcal{E}_\phi(q(p - n - Q(\rho_S))) \\ & - \mu_{\text{eq}} \int_{\Omega} d^3r (n - p - Q(\rho_S)). \end{aligned} \quad (5.52)$$

The minimum of Eq. (5.52) is obtained by expansion around the equilibrium state

$$\begin{aligned} \Phi_S^{\text{eq}}(n_{\text{eq}} + a\delta n, p_{\text{eq}}, \rho_S^{\text{eq}}) &= \Phi_S^{\text{eq}}(n_{\text{eq}}, p_{\text{eq}}, \rho_S^{\text{eq}}) + \\ &+ a \int_{\Omega} d^3r \left[k_B T F_{1/2}^{-1} \left(\frac{n_{\text{eq}}}{N_c} \right) + E_c - q\mu_{\text{eq}} - q\phi_{\text{eq}} \right] \delta n + \mathcal{O}(a^2), \\ \Phi_S^{\text{eq}}(n_{\text{eq}}, p_{\text{eq}} + a\delta p, \rho_S^{\text{eq}}) &= \Phi_S^{\text{eq}}(n_{\text{eq}}, p_{\text{eq}}, \rho_S^{\text{eq}}) + \\ &+ a \int_{\Omega} d^3r \left[k_B T F_{1/2}^{-1} \left(\frac{p_{\text{eq}}}{N_v} \right) - E_v + q\mu_{\text{eq}} + q\phi_{\text{eq}} \right] \delta p + \mathcal{O}(a^2), \\ \Phi_S^{\text{eq}}(n_{\text{eq}}, p_{\text{eq}}, \rho_S^{\text{eq}} + a\delta\rho) &= \Phi_S^{\text{eq}}(n_{\text{eq}}, p_{\text{eq}}, \rho_S^{\text{eq}}) + \\ &+ a \text{tr}_S([H_S - (q\langle\phi_{\text{eq}}\rangle_w + \mu_{\text{eq}})N_S + k_B T \log(\rho_S^{\text{eq}})]\delta\rho) + \mathcal{O}(a^2) \end{aligned}$$

with a small parameter $0 < a \ll 1$. One recovers the usual equilibrium carrier densities

$$\begin{aligned} n_{\text{eq}} &= N_c F_{1/2} \left(\frac{\mu_{\text{eq}} - E_c + q\phi_{\text{eq}}}{k_B T} \right), \\ p_{\text{eq}} &= N_v F_{1/2} \left(\frac{E_v - q\phi_{\text{eq}} - \mu_{\text{eq}}}{k_B T} \right), \end{aligned}$$

and the equilibrium density matrix

$$\rho_S^{\text{eq}} = \frac{1}{Z_S} e^{-\beta(H_S - q\langle\phi_{\text{eq}}\rangle_w N_S - \mu_{\text{eq}} N_S)} \quad (5.53)$$

with $Z_S = \text{tr}_S(e^{-\beta(H_S - q\langle\phi_{\text{eq}}\rangle_w N_S - \mu_{\text{eq}} N_S)})$. By comparison with the equilibrium density matrix of the uncoupled open quantum system (5.30) considered in Sec. 5.2, the equilibrium

state of the coupled (hybrid) system contains an additional contribution from the spatially averaged equilibrium electric potential, which results from the variational derivative of the electrostatic interaction energy functional, see Eq. (2.37). Note that the emergence of the spatial average

$$\langle \phi \rangle_w = \int_{\Omega} d^3r w(\mathbf{r}) \phi(\mathbf{r}, t), \quad (5.54)$$

where the spatial profile function w now occurs as a weight function, is a direct consequence of the ansatz (5.43) and the functional derivative (2.37). This result implies that the equilibrium quantum system interacts only with its spatially averaged environment. Here, the equilibrium electrostatic potential ϕ_{eq} solves the nonlinear Poisson equation (5.37a) with right hand side $\rho_Q^{\text{eq}} = q(p_{\text{eq}} - n_{\text{eq}} + Q(\rho_S^{\text{eq}}))$ and equilibrium boundary conditions, which is a nonlinear and nonlocal integral-boundary value problem:

$$\begin{aligned} -\nabla \cdot \varepsilon \nabla \phi_{\text{eq}} = & q \left(N_v F_{1/2} \left(\frac{E_v - q\phi_{\text{eq}} - q\mu_{\text{eq}}}{k_B T} \right) - N_c F_{1/2} \left(\frac{-E_c + q\phi_{\text{eq}} + q\mu_{\text{eq}}}{k_B T} \right) + C \right) \\ & - q w(\mathbf{r}) \frac{\text{tr}_S(N_S e^{-\beta(H_S - [\mu_{\text{eq}} + q \int_{\Omega} d^3r w(\mathbf{r}) \phi_{\text{eq}}] N_S})}}{\text{tr}_S(e^{-\beta(H_S - [\mu_{\text{eq}} + q \int_{\Omega} d^3r w(\mathbf{r}) \phi_{\text{eq}}] N_S})}}. \end{aligned}$$

Moreover, the *dressed* Hamiltonian (5.38) stated in Eq. (5.37d) naturally appears in the equilibrium density matrix, which can also be written as $\rho_S^{\text{eq}} = Z_S^{-1}(\phi_{\text{eq}}) e^{-\beta(\hat{H}(\phi_{\text{eq}}) - \mu_{\text{eq}} N_S)}$.

5.3.5 Macroscopic scattering rates

Based on the preceding considerations, this section aims at a definition of the macroscopic scattering rates $S_{n/p}$ in Eqs. (5.37b)–(5.37c). The dissipation superoperator in the hybrid system (5.37) takes the form

$$\mathcal{D}(u(\mathbf{r})) \rho_S = \sum_{\alpha \in \mathcal{I}} \sum_{\omega, \ell} \gamma_{\alpha}(\omega, \ell, u(\mathbf{r})) L_{A_{\alpha}(\omega, \ell)} \rho_S,$$

where the jump operators $A_{\alpha}(\omega, \ell)$ are defined in Eq. (5.14) and the index $\alpha \in \mathcal{I}$ labels the admitted system-environment interactions. The spatial dependency of the dissipation superoperator is entirely carried by the dependency of the transition rates γ_{α} on the state of the macroscopic system $u = u(\mathbf{r})$. For the sake of simplicity, the discussion is restricted to single-particle capture and escape processes ($\ell = \pm 1$), and processes that leave the charge invariant ($\ell = 0$). The index set is split into pairwise disjoint subsets $\mathcal{I} = \mathcal{I}_e \cup \mathcal{I}_h \cup \mathcal{I}_0$, where the index sets \mathcal{I}_e and \mathcal{I}_h comprise all processes that lead to the exchange of electrons or holes ($\ell = \pm 1$), respectively, between the quantum system and its macroscopic environment. The remaining, charge conserving processes ($\ell = 0$) are contained in \mathcal{I}_0 . With the additive structure of the dissipation superoperator (recall Eq. (5.26)), this yields the decomposition

$$\mathcal{D}(u) \rho_S = \mathcal{D}_e(u) \rho_S + \mathcal{D}_h(u) \rho_S + \mathcal{D}_0(u) \rho_S. \quad (5.55)$$

The essential property of the charge conserving dissipator \mathcal{D}_0 is

$$\text{tr}_S(N_S \mathcal{D}_0(u) \rho_S) = 0, \quad (5.56)$$

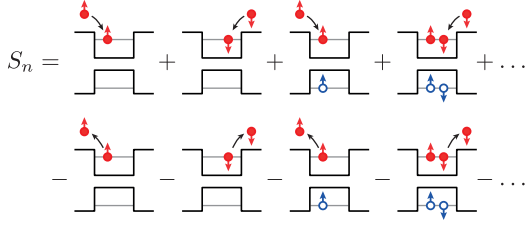


Fig. 5.4 The macroscopic scattering rates $S_{n/p}$ (5.58) collect all the individual microscopic charge transfer processes between the various multi-particle configurations of the quantum system and balance them on the right hand side of the macroscopic continuity Eqs. (5.37b)–(5.37c).

which is an immediate consequence of $[N_S, A_\alpha(\omega, \ell = 0)] = 0$ (recall Eq. (5.15b)). With the decomposition (5.55) and Eq. (5.56), the charge balance relation (5.47) takes the form

$$\int_{\Omega} d^3r w(\mathbf{r}) \text{tr}_S (N_S [\mathcal{D}_e(u(\mathbf{r})) + \mathcal{D}_h(u(\mathbf{r}))] \rho_S) = \int_{\Omega} d^3r (S_n(u(\mathbf{r}), \rho_S) - S_p(u(\mathbf{r}), \rho_S)).$$

The most simple expressions of S_n and S_p that satisfy this relation are obtained by assuming a simplified spatial dependency

$$\mathcal{D}(u(\mathbf{r})) \approx \mathcal{D}(u_w), \quad (5.57)$$

such that the microscopic transition rates $\gamma_\alpha(\omega, \ell, u(\mathbf{r})) = \gamma_\alpha(\omega, \ell, u_w)$ are driven only by the spatially averaged macroscopic environment $u_w = (\langle \mu_c \rangle_w, \langle \mu_v \rangle_w, \langle \phi \rangle_w)$ of the QD. The spatial average is taken according to Eq. (5.54). This simplification is motivated by the exact result (5.53) obtained in the previous section, which indicates that in the thermodynamic equilibrium the quantum system interacts only with its spatially averaged environment. Extending this observation as a paradigm to the non-equilibrium situation, one obtains a simple form for the macroscopic scattering rates

$$S_n(u_w, \rho_S) = +w(\mathbf{r}) \text{tr}_S (N_S \mathcal{D}_e(u_w) \rho_S), \quad (5.58a)$$

$$S_p(u_w, \rho_S) = -w(\mathbf{r}) \text{tr}_S (N_S \mathcal{D}_h(u_w) \rho_S). \quad (5.58b)$$

Note that with the simplified spatial dependency of the dissipator (5.57), the macroscopic scattering rates $S_{n/p}$ given in (5.58) even satisfy the local charge balance condition (5.46).

The form stated in Eq. (5.58) allows for an easy interpretation. The (net-)capture rates $S_{n/p}$ collect all microscopic charge transfer processes between the macroscopic and the quantum system: The trace involves a summation over all individual transitions between the various multi-particle configurations of the quantum system that are driven by charge transfer with its environment and balances them on the right hand side of the continuity Eqs. (5.37b)–(5.37c), see Fig. 5.4. The sum over the transition rates is weighted by the occupation probabilities of the initial states. The corresponding sign (plus for capture, minus for escape) arises from the structure of the dissipation superoperators $\mathcal{D}_{e/h}$ in a natural way. Moreover, just as the QD-confined charge density itself, also the scattering region is localized by the spatial profile function $w(\mathbf{r})$, see Fig. 5.3.

The thermodynamic consistency discussed in the subsequent sections does not crucially rely on the local charge balance property as ensured by Eqs. (5.58). With some modifications, the results can be generalized to cases where only the weaker non-local condition (5.47) is fulfilled. This allows, e.g., for macroscopic scattering rates with a more complicated spatial dependency than the ones stated in Eq. (5.58). However, since the discussion of the thermodynamic consistency is least technical in the case of local charge balance, the structural form (5.58) will be assumed in the following. The other cases can be treated analogously. An alternative structure of the macroscopic scattering rates, which

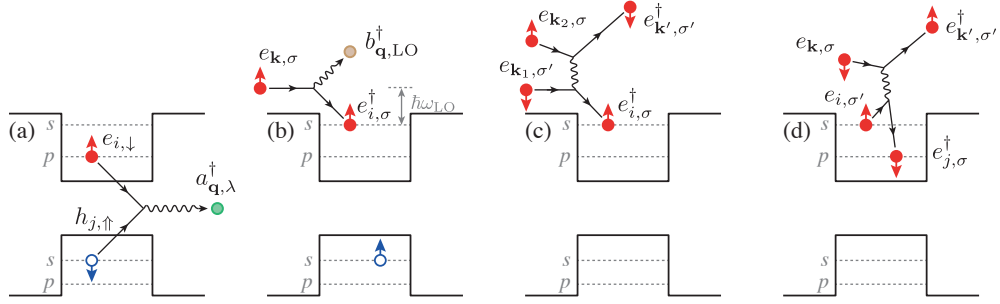


Fig. 5.5 Illustration of some important scattering processes. (a) Spontaneous emission of a photon due to recombination of a bound QD exciton. (b) Phonon-assisted capture of a continuum electron to a bound QD state. The scattering rate can be significantly altered if the QD contains further carriers (see the s-shell hole). (c) Auger-assisted capture via Coulomb interaction between bound and continuum electrons. (d) Auger-assisted relaxation of a QD electron from an excited state to the ground state. The annihilation and creation of carriers during scattering is indicated by the corresponding operators (see Sec. 5.3.1). QD carriers are labeled by the state index i , continuum carriers by their wave vector \mathbf{k} , σ is the spin index.

satisfies only the non-local condition (5.47) can be found in the Appx. A.5. Similarly, for different choices of $Q(\rho_S)$, e.g., with different localization profiles of the bound electrons and holes $Q(\rho_S) = w_h(\mathbf{r})\text{tr}_S(n_h\rho_S) - w_e(\mathbf{r})\text{tr}_S(n_e\rho_S)$ (with $w_{e/h}$ normalized), the local charge balance property is lost in general. However, the violation of local charge balance is restricted to a small spatial region $\nabla \cdot \mathbf{j}_{\text{tot}} \propto (w_e(\mathbf{r}) - w_h(\mathbf{r}))$ and is preserved globally, i.e., it holds $\int_{\Omega} d^3r \nabla \cdot \mathbf{j}_{\text{tot}} = 0$ with $\mathbf{j}_{\text{tot}} = \mathbf{j}_n + \mathbf{j}_p + \partial_t \mathbf{D}$.

5.3.6 Microscopic transition rates

This section is devoted to the microscopic scattering rates γ_{α} driving the irreversible processes (i.e., energy dissipation and decoherence) in the quantum system described by the dissipation superoperator in Eq. (5.37d). Via the macroscopic scattering terms $S_{n/p}$ considered in the previous section, the microscopic transitions in the quantum system also cause irreversible decay processes in the macroscopic environment.

In the framework of approximations underlying the Lindblad master equation (see Sec. 5.2.2), the microscopic transition rates γ_{α} are given by Fermi's golden rule. Following Ref. [6], this can be seen by evaluating the reservoir correlation function in the transition rate (5.21) (after diagonalization, see Eq. (5.26)) in the eigenbasis of the reservoir density matrix. The reservoir is assumed to be in a (tensor product) Gibbs state throughout this thesis (cf. Eq. (5.19)), such that its eigenbasis coincides with that of the Hamiltonian H_R and the charge number operator N_R (recall the charge conservation condition $[H_R, N_R] = 0$, see Eq. (5.6b)). With $(H_R - \mu_R N_R) |i\rangle = (E_i - \mu_R \ell_i) |i\rangle$ one obtains

$$\begin{aligned} \langle e^{-\frac{i}{\hbar}\mu_R N_{R\tau}} \mathbf{B}_{\alpha}(\tau) e^{\frac{i}{\hbar}\mu_R N_{R\tau}} \mathbf{B}_{\alpha} \rangle_{\rho_R} &= \frac{1}{Z_R} \text{tr}_R (e^{-\frac{i}{\hbar}\mu_R N_{R\tau}} \mathbf{B}_{\alpha}(\tau) e^{\frac{i}{\hbar}\mu_R N_{R\tau}} \mathbf{B}_{\alpha} e^{-\beta(H_R - \mu_R N_R)}) \\ &= \sum_{i,f} e^{\frac{i}{\hbar}([E_f - E_i] - \mu_R[\ell_f - \ell_i])\tau} |\langle f | \mathbf{B}_{\alpha} | i \rangle|^2 \rho_{R,f} \end{aligned}$$

where $|i\rangle, |f\rangle$ are eigenstates of the macroscopic environment and $\rho_{R,f}$ is an element of the density matrix $\rho_{R,f} = \langle f | \rho_R | f \rangle = e^{-\beta(E_f - \mu_R \ell_f)} / (\sum_j e^{-\beta(E_j - \mu_R \ell_j)})$. As a result, the

transition rate (5.21) takes the form

$$\gamma_\alpha(\omega, \ell, \mu_R) = \frac{1}{\hbar^2} \sum_{i,f} |\langle f|B_\alpha|i\rangle|^2 \rho_{R,f} \int_{-\infty}^{\infty} d\tau e^{\frac{i}{\hbar}([\hbar\omega + E_f - E_i] - \mu_R[\ell + \ell_f - \ell_i])\tau} = \sum_{i,f} R_{i \rightarrow f}^\alpha$$

with

$$R_{i \rightarrow f}^\alpha = R_{i \rightarrow f}^\alpha(\omega, \ell, \mu_R) = \frac{2\pi}{\hbar} |B_{f,i}|^2 \rho_{R,f} \delta(\hbar\omega - [E_i - E_f] - \mu_R[\ell - (\ell_i - \ell_f)]). \quad (5.59)$$

This expression for the transition rate coincides with Fermi's golden rule (in the long-time limit), where $|B_{f,i}|^2 = |\langle f|B_\alpha|i\rangle|^2$ is the transition matrix element for the jump from an initial state i to a final state f . The density of states of the admitted final states is given by $\rho_{R,f} \delta(\hbar\omega - (E_i - E_f) - \mu_R[\ell - (\ell_i - \ell_f)])$.

For the description of QD-based devices, the most important scattering processes that need to be modeled are the recombination of bound electron-hole pairs and the capture of continuum carriers to the bound QD states. As a rule of thumb, at low continuum carrier densities, (multi-)phonon-assisted processes provide a very efficient scattering channel for carrier capture, whereas at elevated carrier densities Auger processes become increasingly dominant [54, 73, 226]. Moreover, the description of intra-dot carrier relaxation processes and dephasing are of high importance. Some scattering processes are illustrated in Fig. 5.5.

Auger processes

There is an extensive literature on the calculation of Auger-assisted capture and relaxation times to self-assembled InGaAs-QDs based on Fermi's golden rule. Auger scattering refers to carrier-carrier scattering processes (due to Coulomb interaction, see Fig. 5.5 (c, d)), which have proven to be a very fast scattering channel reaching rapid capture and relaxation rates on the order of 10^{12} s^{-1} to 10^{14} s^{-1} [34, 71, 226, 307, 308, 319, 322]. The scattering rates depend on the temperature [38, 101], the QD level splitting (i.e., QD size and shape) [34, 202, 307] and the reservoir's dimensionality (2D or 3D) [319, 322]. Moreover, there is a characteristic nonlinear dependency on the continuum carrier density, that depends on the microscopic details of the particular QD and the wave function model employed [203, 226, 322]. The model calculations typically assume a thermalized (Maxwell-Boltzmann or Fermi-Dirac) electron gas in the reservoir and consider screened Coulomb interaction in second-order Born approximation [130], taking direct and exchange Coulomb effects into account [48, 197, 226]. Calculations have shown that the most efficient scattering process that transfers continuum carriers to the QD ground state is indeed a cascade: First, the carriers are captured to an excited state (e.g., p-shell, see Fig. 5.5 (c)) and then relax by a secondary Auger process to the ground state (s-shell, see Fig. 5.5 (d)) [48, 226]. This cascade is more efficient than direct scattering from the continuum level to the QD ground state [48, 226]. Next to capture and intra-dot relaxation, Auger scattering significantly impacts the exciton dephasing rate and leads to line broadening [54, 175, 197, 309, 322]. The description of Auger processes within the framework of the Lindblad master equation has been investigated in Ref. [291].

Phonon-assisted processes

Phonons play an important role in the physics of carrier scattering in QDs. In principle, carrier relaxation is possible due to the interaction with LA (longitudinal acoustic) or LO (longitudinal optical) phonons, where the coupling is most efficient for phonons with small momenta [48, 264]. From the viewpoint of Fermi's golden rule, the Fröhlich interaction with the (nearly) dispersionless LO phonons is strongly suppressed due to the strict energy

conservation requirement imposed by the Dirac delta function in Eq. (5.59). The energy conservation constitutes a significant constraint in quasi zero-dimensional systems (such as QDs) with energy splittings different from the LO phonon energy and is in general not fulfilled [48, 72]. On the other hand, the deformation potential coupling [264] of carriers with LA phonons, which have an approximately linear energy dispersion relation, is, however, very inefficient as the energy transferred in the one-phonon scattering event is very small and multiple phonons are needed to match the QD level splitting [48]. These considerations, that are based on a perturbational treatment of the carrier-phonon interaction, have led to vibrant discussions about the so-called *phonon relaxation bottleneck* [23, 24, 33, 141]. A more advanced treatment of the carrier-phonon interaction in QDs is based on the observation of strong carrier-phonon coupling [123] and describes the dynamics in the *polaron picture* [257] using quantum kinetic approaches [129, 130, 264] beyond the weak coupling and Markov approximation [48, 154, 183, 277]. Next to relaxation, the quantum kinetic approach allows for an accurate description of phonon-induced dephasing processes that are an important source of decoherence in QDs [153, 154, 194]. The non-perturbative, quantum kinetic treatment can be combined with the Lindblad formalism as carried out in Ref. [290].

For some processes, in particular the *primary* capture of carriers from the continuum to *shallow* QD states (provided the QD state is less than $\hbar\omega_{\text{LO}}$ below the continuum band edge), see Fig. 5.5 (b), reasonable results are obtained using Fermi's golden rule [71, 73, 201]. The capture rate of quasi-resonant free carriers shows a strong dependency on the dot geometry and size, the temperature and the continuum carrier density [71, 201]. Characteristic capture rates due to LO phonon emission reach 10^{12} s^{-1} to 10^{13} s^{-1} [73]. The LO phonon-assisted capture rate is significantly altered, if the QD is initially occupied by other carriers (cf. Fig. 5.5 (b)) [71]. While the Coulomb interaction energy between continuum and bound carriers is typically very low, it reaches a few tens of meV between bound states [11] (cf. Appx. A.6). Therefore, the additional binding (or repulsive) energy in the final state leads to an enhancement (or suppression) of the transition rate – provided the transition remains allowed. These effects are referred to as *Coulomb blockade*, *Coulomb inhibition* and *Coulomb enhancement* or *suppression*, respectively [73].

Radiative transitions

The radiative recombination of electron-hole pairs in QDs, see Fig. 5.5 (a), strongly depends on the photonic environment. For QDs embedded in low Q cavities, the light-matter interaction is weak and can be treated by perturbation theory (i.e., Fermi's golden rule). In this case the Weisskopf–Wigner theory [317] for the spontaneous emission of a two-level system in free space can be adopted [12, 194, 263], where the radiative decay rate dominantly depends on the interband dipole moment, the background refractive index and the recombination energy. Moreover, in QDs the (intrinsic) radiative life time of the various optically active (neutral and charged) excitons depends on the QD geometry [225] and is typically on the order of around one nanosecond [194, 225]. By embedding the QD in a high Q cavity, the spontaneous emission rate can be significantly enhanced. This results from an increased local density of photonic states at the emitter location and is denoted as *Purcell effect* [240]. The enhancement is quantified by the *Purcell factor*, which relates the radiative life time in a resonator to the free space life time. The enhancement of the spontaneous emission rate by embedding the QD into either photonic crystals [64, 195] or micro-pillars [35, 245] is one of the major objectives in the design of QD-based single-photon sources as it yields an increased photon generation efficiency.

In the strong-coupling regime the perturbative approach to describe the light-matter interaction breaks down [48]. In this regime the energy is periodically exchanged between

the emitter and the optical field which leads to Rabi oscillations and the formation of exciton-polaritons that need to be described by the Jaynes–Cummings model [276]. The reversible light-matter interaction must be included in the system’s Hamiltonian (5.10) and can not be described by a Lindblad-like dissipation superoperator.

The microscopic calculation of scattering rates is beyond the scope of this thesis and is a subject on its own right. The goal of this work is the coupling of macroscopic and microscopic evolution equations in a hybrid model (5.37) by using already known results from microscopic scattering theory. Therefore a suitable parametrization of microscopically calculated transition rates in terms of the macroscopic state variables is required. This can be achieved by a fit of the transition rates in terms of continuum carrier densities or chemical potentials (cf. Refs. [198, 199]), which can then be included phenomenologically in the coupled system (5.37). Moreover, by “hard-wiring” the quantum detailed balance relation (5.29) it is sufficient to model only the *forward* scattering process. The dissipation superoperators considered in the following take the form⁴

$$\mathcal{D}_e(u_w)\rho_S = \sum_{\alpha \in \mathcal{I}_e} \sum_{\omega < 0} \gamma_\alpha(\omega, u_w) (L_{A_\alpha(\omega, -1)}\rho_S + e^{-\beta(\hbar\omega + [q\langle\phi\rangle_w + \langle\mu_c\rangle_w])} L_{A_\alpha^\dagger(\omega, -1)}\rho_S), \quad (5.60a)$$

$$\mathcal{D}_h(u_w)\rho_S = \sum_{\alpha \in \mathcal{I}_h} \sum_{\omega > 0} \gamma_\alpha(\omega, u_w) (L_{A_\alpha(\omega, +1)}\rho_S + e^{-\beta(\hbar\omega - [q\langle\phi\rangle_w + \langle\mu_v\rangle_w])} L_{A_\alpha^\dagger(\omega, +1)}\rho_S), \quad (5.60b)$$

$$\mathcal{D}_0(u_w)\rho_S = \sum_{\alpha \in \mathcal{I}_0} \sum_{\omega > 0} \gamma_\alpha(\omega, u_w) (L_{A_\alpha(\omega, 0)}\rho_S + e^{-\beta\hbar\omega} L_{A_\alpha^\dagger(\omega, 0)}\rho_S). \quad (5.60c)$$

The thermodynamic consistency considered in the following section relies merely on the detailed balance relation (5.29) and the non-negativity of the transition rates γ_α .

5.3.7 Entropy production and the second law of thermodynamics

This section generalizes the results on the consistency of the van Roosbroeck system with the second law of thermodynamics to the case of the hybrid system (5.37). Therefore the considerations on the van Roosbroeck system detailed in Sec. 2.3.2 will be combined with the thermodynamic properties of the Lindblad equation discussed in Sec. 5.2.3.

Starting from Eq. (5.49) and the hybrid free energy functional (5.51), the entropy production rate of the hybrid system (5.37) is written as

$$\begin{aligned} \dot{S}_{\text{tot}} = & -\frac{1}{T} \int_{\Omega} d^3r \left([\mu_c + q\phi] \frac{\partial n}{\partial t} - [\mu_v + q\phi] \frac{\partial p}{\partial t} \right) - \frac{1}{T} \text{tr}_S ([H_S + k_B T \log \rho_S] \mathcal{L}(u_w)\rho_S) \\ & - \frac{q}{T} \int_{\Omega} d^3r \phi \frac{\partial}{\partial t} (p - n + Q(\rho_S)) + \frac{1}{qT} \sum_{i \geq 1} \mu_i \int_{\Gamma_{D,i}} d\mathbf{A} \cdot (\mathbf{j}_n + \mathbf{j}_p). \end{aligned}$$

With the confined charge density (5.43) and the equations of motion (5.37b)–(5.37d) one

⁴ A remark on the sign conventions: All *forward* processes considered here are chosen such that they reduce the energy of the total system. In the case of hole capturing (i.e., relaxation of valence band electrons) and, e.g., the recombination of an electron-hole pair this is connected with a reduction of the energy contained in the open quantum system. This corresponds to a positive transition energy $\omega > 0$. For the capture of electrons, however, the energy of the open quantum system increases (negative transition energy $\omega < 0$) even though the total energy of the full system is reduced.

arrives at

$$\begin{aligned} \dot{S}_{\text{tot}} = & \frac{1}{T} \int_{\Omega} d^3r (\mu_c - \mu_v) R + \frac{1}{T} \int_{\Omega} d^3r (\mu_c S_n - \mu_v S_p) - \frac{1}{qT} \int_{\Omega} d^3r (\mu_c \nabla \cdot \mathbf{j}_n + \mu_v \nabla \cdot \mathbf{j}_p) \\ & - \frac{1}{T} \text{tr}_S ([H_S - q \langle \phi \rangle_w N_S + k_B T \log \rho_S] \mathcal{D}(u_w) \rho_S) + \frac{1}{qT} \sum_{i \geq 1} \mu_i \int_{\Gamma_{D,i}} d\mathbf{A} \cdot (\mathbf{j}_n + \mathbf{j}_p). \end{aligned}$$

Using the macroscopic scattering rates stated in Eq. (5.58) and partial integration, the entropy production rate takes the form

$$\begin{aligned} \dot{S}_{\text{tot}} = & \frac{1}{T} \int_{\Omega} d^3r (\mu_c - \mu_v) R + \frac{1}{T} \langle \mu_c \rangle_w \text{tr}_S (N_S \mathcal{D}_e(u_w) \rho_S) + \frac{1}{T} \langle \mu_v \rangle_w \text{tr}_S (N_S \mathcal{D}_h(u_w) \rho_S) \\ & - \frac{1}{qT} \oint_{\partial\Omega} d\mathbf{A} \cdot (\mu_c \mathbf{j}_n + \mu_v \mathbf{j}_p) + \frac{1}{qT} \int_{\Omega} d^3r (\mathbf{j}_n \cdot \nabla \mu_c + \mathbf{j}_p \cdot \nabla \mu_v) \\ & - \frac{1}{T} \text{tr}_S ([H_S - q \langle \phi \rangle_w N_S + k_B T \log \rho_S] \mathcal{D}(u_w) \rho_S) + \frac{1}{qT} \sum_{i \geq 1} \mu_i \int_{\Gamma_{D,i}} d\mathbf{A} \cdot (\mathbf{j}_n + \mathbf{j}_p). \end{aligned}$$

This expression is simplified by exploiting the decomposition of the dissipation superoperator (5.55) and the charge conserving property of \mathcal{D}_0 (5.56)

$$\begin{aligned} \dot{S}_{\text{tot}} = & \frac{1}{T} \int_{\Omega} d^3r (\mu_c - \mu_v) R + \frac{1}{qT} \int_{\Omega} d^3r (\mathbf{j}_n \cdot \nabla \mu_c + \mathbf{j}_p \cdot \nabla \mu_v) \\ & - \frac{1}{T} \text{tr}_S ([H_S - q \langle \phi \rangle_w N_S - \langle \mu_c \rangle_w N_S + k_B T \log \rho_S] \mathcal{D}_e(u_w) \rho_S) \\ & - \frac{1}{T} \text{tr}_S ([H_S - q \langle \phi \rangle_w N_S - \langle \mu_v \rangle_w N_S + k_B T \log \rho_S] \mathcal{D}_h(u_w) \rho_S) \\ & - \frac{1}{T} \text{tr}_S ([H_S + k_B T \log \rho_S] \mathcal{D}_0(u_w) \rho_S), \end{aligned}$$

where the surface integrals have canceled out as a consequence of the ohmic boundary conditions detailed in Sec. 2.1.5. Next, the *auxiliary* density matrices

$$\rho_e^*(u_w) = \frac{e^{-\beta(H_S - [q \langle \phi \rangle_w + \langle \mu_c \rangle_w] N_S)}}{\text{tr}_S(e^{-\beta(H_S - [q \langle \phi \rangle_w + \langle \mu_c \rangle_w] N_S)}), \quad \rho_h^*(u_w) = \frac{e^{-\beta(H_S - [q \langle \phi \rangle_w + \langle \mu_v \rangle_w] N_S)}}{\text{tr}_S(e^{-\beta(H_S - [q \langle \phi \rangle_w + \langle \mu_v \rangle_w] N_S)}),$$

and

$$\rho_0^* = \frac{e^{-\beta H_S}}{\text{tr}_S(e^{-\beta H_S})},$$

are introduced, which are stationary (non-)equilibrium states of dissipation superoperators $\mathcal{D}_\nu(u_w) \rho_\nu^*(u_w) \equiv 0$ ($\nu \in \{0, e, h\}$) given in Eq. (5.60). This follows essentially from the eigenoperator relations (5.15) (cf. Sec. 5.2.3.2). The auxiliary density matrices enable a simple representation of the entropy production rate:

$$\begin{aligned} \dot{S}_{\text{tot}} = & \frac{1}{T} \int_{\Omega} d^3r (\mu_c - \mu_v) R + \frac{1}{qT} \int_{\Omega} d^3r (\mathbf{j}_n \cdot \nabla \mu_c + \mathbf{j}_p \cdot \nabla \mu_v) \\ & + k_B \text{tr}_S ([\log \rho_e^*(u_w) - \log \rho_S] \mathcal{D}_e(u_w) \rho_S) \\ & + k_B \text{tr}_S ([\log \rho_h^*(u_w) - \log \rho_S] \mathcal{D}_h(u_w) \rho_S) \\ & + k_B \text{tr}_S ([\log \rho_0^* - \log \rho_S] \mathcal{D}_0(u_w) \rho_S). \end{aligned} \tag{5.61}$$

The first line is the entropy production rate of the uncoupled van Roosbroeck system (see Sec. 2.3.2.3), the second and third line represents the dissipation rate due to the irreversible charge transfer between the continuum states and the quantum system and the fourth line is the entropy production rate of the charge preserving dissipative processes in the open quantum system. Note that all terms are products of (abstract) fluxes with their respective driving force. Using the structural form of the (net-)recombination rate R (2.15), the current density expressions (2.10) and Spohn's inequality (5.35), all terms in Eq. (5.61) are evidently non-negative for any (stationary) bias. Moreover, with the same arguments, the entropy production rate vanishes only in the thermodynamic equilibrium. Hence, the hybrid model systems obeys the second law of thermodynamics [160]:

$$\dot{\mathcal{S}}_{\text{tot}} \geq 0.$$

This result follows from rather general structural features of the hybrid system, and is therefore independent of specific details of the Hamiltonian or the dissipation processes. Hence, it holds for a wide range of physical systems and indicates that the quantum-classical coupling has been constructed in a – at least thermodynamically – reasonable way.

5.4 Relation of the hybrid quantum-classical model to the *GENERIC* formalism

In non-equilibrium thermodynamics, the *GENERIC*⁵ formalism, provides a thermodynamically consistent way for the coupling of systems showing both reversible and irreversible dynamics. The concept has been originally introduced to describe the dynamics and thermodynamics of complex fluids [107, 231] and was extended later on to quantum mechanical problems [214, 215, 229, 230]. The *GENERIC* formalism denotes the theory built around the *GENERIC equation* for the evolution of a dynamic variable z

$$\frac{dz}{dt} = \mathbb{J}(z) D\mathcal{E}(z) + \mathbb{K}(z) D\mathcal{S}(z), \quad (5.62)$$

The variable z is an element of the state space \mathbf{Z} , which carries two geometric structures, namely the *Poisson structure* \mathbb{J} that generates the Hamiltonian evolution and the *Onsager operator* (or friction matrix) \mathbb{K} driving the dissipative dynamics. The Poisson structure is a symplectic form $\mathbb{J}(z) = -\mathbb{J}^\dagger(z)$ and satisfies Jacobi's identity⁶, whereas the Onsager operator is self-adjoint $\mathbb{K}(z) = \mathbb{K}^\dagger(z)$ and positive semi-definite $\mathbb{K}(z) \geq 0$ [214, 215]. Moreover, $\mathcal{E}(z)$ denotes the total energy functional of the system and $\mathcal{S}(z)$ describes its entropy. The dynamics in Eq. (5.62) are driven by the functional derivatives of the thermodynamic potentials in the sense of $\langle \delta z, D\mathcal{E}(z) \rangle = \lim_{a \rightarrow 0} \frac{1}{a} (\mathcal{E}(z + a\delta z) - \mathcal{E}(z))$ (cf. Sec. 2.3.1). The *GENERIC* system is supplemented by the *non-interaction conditions*

$$\mathbb{J}(z) D\mathcal{S}(z) = 0, \quad \mathbb{K}(z) D\mathcal{E}(z) = 0, \quad (5.63)$$

which describe the complementary degeneracy of reversible and irreversible processes and guarantee, together with the properties described above, the first and second law of

⁵ *GENERIC* is an acronym for *General Equation for Non-Equilibrium Reversible-Irreversible Coupling*.

⁶ Jacobi's identity reads $\{\{F_1, F_2\}_{\mathbb{J}}, F_3\}_{\mathbb{J}} + \{\{F_2, F_3\}_{\mathbb{J}}, F_1\}_{\mathbb{J}} + \{\{F_3, F_1\}_{\mathbb{J}}, F_2\}_{\mathbb{J}} = 0$ for all $F_i : \mathbf{Z} \rightarrow \mathbb{R}$, where the Poisson bracket is defined as $\{F, G\}_{\mathbb{J}}(z) = \langle DF(z), \mathbb{J}(z) DG(z) \rangle$ [214]. This is satisfied, e.g., for the Lie bracket operation $\mathbb{J}(\rho)\square = \frac{i}{\hbar} [\rho, \square]$ in the Liouville–von Neumann Eq. (5.2) [214, 215].

thermodynamics [107, 215, 216]:

$$\frac{d\mathcal{E}(z(t))}{dt} = \langle D\mathcal{E}(z), \mathbb{J}(z) D\mathcal{E}(z) + \mathbb{K}(z) D\mathcal{S}(z) \rangle = 0 + 0 = 0 \quad (5.64a)$$

$$\frac{d\mathcal{S}(z(t))}{dt} = \langle D\mathcal{S}(z), \mathbb{J}(z) D\mathcal{E}(z) + \mathbb{K}(z) D\mathcal{S}(z) \rangle = 0 + \langle D\mathcal{S}, \mathbb{K} D\mathcal{S} \rangle \geq 0. \quad (5.64b)$$

An important class of GENERIC systems are damped Hamiltonian systems with fixed temperature T , where the free energy $\mathcal{F}(z) = \mathcal{E}(z) - T\mathcal{S}(z)$ is a Lyapunov function. In this case, the GENERIC equation (5.62) reduces to

$$\frac{dz}{dt} = \left(\mathbb{J}(z) - \frac{1}{T} \mathbb{K}(z) \right) D\mathcal{F}(z), \quad (5.65)$$

which describes a gradient flow system that relaxes to the minimum of the free energy.

The hybrid quantum-classical system (5.37) can be interpreted as a damped Hamiltonian system in the sense of Eq. (5.65) [159]. The gradient structure underlying the van Roosbroeck system (2.1) was investigated in Ref. [213]. What was missing so far, is the gradient structure underlying the Lindblad master equation. A gradient structure for the Lindblad equation requires an Onsager operator $\mathbb{K}(\rho)$ that maps the derivative of the free energy functional $D\mathcal{F}(\rho) = H + k_B T \log \rho + k_B T I$ (where I is the identity operator) on the dissipation superoperator (5.25) such that

$$-\frac{1}{T} \mathbb{K}(\rho) D\mathcal{F}(\rho) = \mathcal{D}\rho. \quad (5.66)$$

This was recently achieved in Ref. [216] for Lindblad equations that satisfy the detailed balance principle (see Sec. 5.2.3). The Hamiltonian part is given by the symplectic commutator structure of the Liouville–von Neumann equation (5.2)

$$\mathbb{J}(\rho) D\mathcal{F}(\rho) = \frac{i}{\hbar} [\rho, D\mathcal{F}(\rho)] = \frac{i}{\hbar} [\rho, H]. \quad (5.67)$$

The Lindblad master equation (5.23) follows from Eqs. (5.66) and (5.67). These results can be readily extended to the hybrid quantum-classical system (5.37) with the state vector $z = (n, p, \rho)$ using the hybrid free energy functional (5.51).

The interpretation of the hybrid quantum-classical system as a gradient system is useful as it allows to draw connections to other branches of mathematical science. The investigation of entropic gradient structures goes back to Refs. [146, 147], where the Fokker–Planck equation for classical Markov processes was written as a gradient system with respect to the Wasserstein metric [216]. The Wasserstein metric defines a distance on the space of probability distributions [147, 312]. Thereby, the geometric interpretation of the dynamics provides a link to *optimal transport theory* [312]. The gradient structure imposed by the Onsager operator of the Lindblad equation represents a non-commutative analogue of the Wasserstein distance and extends the concept to the space of density matrices [216].

5.5 Conclusions

The device scale simulation of novel, electrically driven quantum optical devices requires modeling approaches that combine classical device physics with cavity quantum electrodynamics. As a step on this route, a *hybrid quantum-classical model system* was

introduced, that self-consistently couples the van Roosbroeck system with a Markovian quantum master equation in Lindblad form. The formalism allows to investigate the spatially resolved carrier transport in realistic semiconductor device structures together with the calculation of quantum optical figures of merit (e.g., photon generation rates, higher order correlation functions, emission spectra) in a unified way. Thereby, the hybrid system goes beyond existing modeling approaches (based on classical rate equations) in multi-scale semiconductor device simulation. The system allows to include a broad class of Hamiltonian operators and dissipation processes and can therefore be applied to the simulation of a wide range of devices – in particular quantum light sources and (single or few) quantum dot nanolasers. The coupling structure developed throughout this chapter preserves the essential thermodynamical features of its constituting subsystems and guarantees consistency with fundamental principles of (non-)equilibrium thermodynamics also on the level of the coupled system. In particular, the conservation of charge, the microscopic reversibility in the thermodynamic equilibrium and the consistency with the second law of thermodynamics have been addressed in detail. Finally, the hybrid system has been discussed from the viewpoint of the GENERIC approach to non-equilibrium thermodynamics.

An application of the approach, followed by a detailed discussion is found below in the next chapter.

Chapter 6

Hybrid simulation of an electrically driven single-photon source

This chapter provides a *proof-of-principle* application of the hybrid modeling approach presented in the previous chapter. An electrically driven single-photon source based on a single QD embedded in a pin-diode is investigated by numerical simulations. In Sec. 6.3 the numerical method introduced in Chap. 3 is extended towards the hybrid model. The simulation results for stationary and pulsed injection are given in Sec. 6.4 and Sec. 6.5, respectively. A critical discussion of the results and an outlook on possible extensions of the approach is given Sec. 6.6. The results presented in this chapter are published in Ref. [160] and are reprinted with permission. ©2017 American Physical Society.

6.1 Device structure

The pin-diode considered in this chapter is shown in Fig. 6.1. The device has a cylindrical symmetry and an etched top mesa structure. A single QD is placed on the symmetry axis within the center of the intrinsic zone. The electrical contacts are modeled as ohmic boundary conditions (2.21), while the remaining facets are considered as artificial boundaries (2.22). The bottom contact is assumed to consist of a highly reflective metal such that it simultaneously acts as a mirror. This leads to a directed optical emission in vertical direction. The p-contact is assumed to be made of an optically transparent material (e.g., ITO), such that the structure forms a leaky, low Q optical resonator. The layer thicknesses and other geometric features are indicated in Fig. 6.1. The doping concentrations are set to $N_D^+ = 2 \times 10^{18} \text{ cm}^{-3}$ and $N_A^- = 10^{19} \text{ cm}^{-3}$ in the n- and p-domain, respectively. The numerical simulation exploits the rotational symmetry of the device, such that the computational domain reduces to a 2D cross section with adapted geometry factors, cf. Fig. 3.2. The wetting layer indicated in Fig. 6.1 is neglected in the simulation.

The temperature is set to $T = 50 \text{ K}$ in the following. In view of practical applications, such a temperature can be achieved by compact (and comparably inexpensive) Stirling cryocoolers [271]. A temperature around $T = 50 \text{ K}$ is considered an upper limit for the operation of self-assembled Stranski–Krastanov InGaAs-QDs, where the phonon-induced line broadening and dephasing are still acceptable [271]. Theoretical studies predict the persistence of entanglement in this material system up to around $T = 80 \text{ K}$ [43].

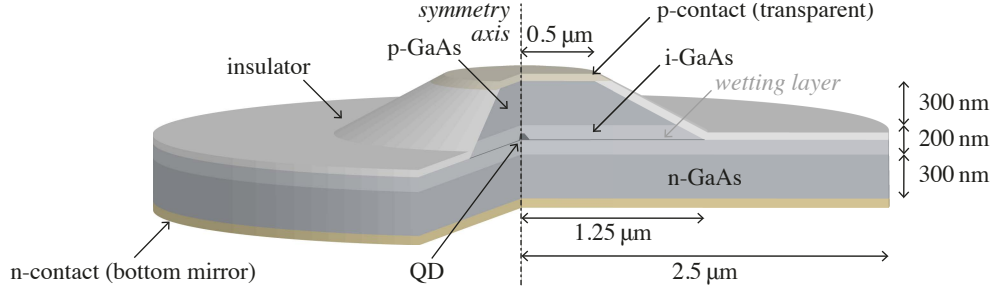


Fig. 6.1 Schematic illustration of the example device considered throughout this chapter. A single QD is placed within the center of the intrinsic zone on the symmetry axis of an axisymmetric GaAs-based pin-diode with an etched mesa structure on top. The bottom mirror leads to a directed emission in vertical direction. Due to the lack of a top mirror, the device forms a leaky photonic cavity with low Q factor. Ohmic contacts are attached at the top and the bottom facets.

6.2 Model specification

The numerical simulations presented in this chapter are based on the hybrid quantum-classical model (5.37) introduced in Chap. 5. For the application to the structure depicted in Fig. 6.1, the Hamiltonian H_S of the quantum system and the dissipative system-environment interactions need to be specified. Moreover, the transition rate models for carrier capture/escape and radiative decay employed in the dissipators must be declared.

6.2.1 Hamiltonian

The Hamiltonian H_S describes the single-particle energy contributions of the particles, which are considered part of the quantum system S , and their respective interaction energies, see Sec. 5.3.1. In order to specify H_S , the separation (in the sense of relevant degrees of freedom) between system S and reservoir R must be declared. The device shown in Fig. 6.1 is a leaky resonator with a low Q factor supporting a broadband emission spectrum. In such devices, the light-matter interaction is weak and dominated by (irreversible) spontaneous emission. Hence, the reversible (Jaynes–Cummings-like) light-matter coupling included in the Hamiltonian (5.39) can be omitted, such that a purely electronic Hamiltonian is considered in the following. By assuming a single (spin-degenerate) one-particle energy level for both the electrons and holes, the Hamiltonian reads

$$\begin{aligned}
 H_S = & \sum_{\sigma} \varepsilon_c e_{\sigma}^{\dagger} e_{\sigma} - \sum_{\sigma} \varepsilon_v h_{\sigma}^{\dagger} h_{\sigma} \\
 & + \frac{1}{2} \sum_{\sigma, \sigma'} (V_{c,c} e_{\sigma}^{\dagger} e_{\sigma'}^{\dagger} e_{\sigma'} e_{\sigma} + V_{v,v} h_{\sigma}^{\dagger} h_{\sigma'}^{\dagger} h_{\sigma'} h_{\sigma} - 2V_{c,v} e_{\sigma}^{\dagger} h_{\sigma'}^{\dagger} h_{\sigma'} e_{\sigma}),
 \end{aligned} \tag{6.1}$$

where ε_c is the one-particle electron level, ε_v is the one-particle (heavy) hole level and $V_{\lambda, \lambda'}$ ($\lambda, \lambda' \in \{c, v\}$) denotes the direct Coulomb interaction matrix elements $V_{\mu, \nu} = V_{\mu, \nu, \nu, \mu}$. The limitation to only direct Coulomb interaction results from the restriction to only a single one-particle level per carrier species and corresponds to full configuration interaction in this case. The creation and annihilation operators and their anti-commutator relations have been introduced in Sec. 5.3.1. Due to the Coulomb interaction, the model features several few-body states including the single-particle states, dark and bright excitons, charged trions and the biexciton listed in Tab. 6.1 and shown in Fig. 6.3. The spin index

symbol	config.	energy	symbol	config.	energy
$ 0\rangle$	$ 0, 0, 0, 0\rangle$	0	$ X_2\rangle$	$ 0, 1, 1, 0\rangle$	ε_X
$ e^\uparrow\rangle$	$ 1, 0, 0, 0\rangle$	ε_c	$ D_2\rangle$	$ 0, 1, 0, 1\rangle$	ε_X
$ e^\downarrow\rangle$	$ 0, 1, 0, 0\rangle$	ε_c	$ hh\rangle$	$ 0, 0, 1, 1\rangle$	$-2\varepsilon_v + V_{v,v}$
$ h^\uparrow\rangle$	$ 0, 0, 1, 0\rangle$	$-\varepsilon_v$	$ X_-^\uparrow\rangle$	$ 1, 1, 1, 0\rangle$	$\varepsilon_X + \varepsilon_c + V_{c,c} - V_{c,v}$
$ h^\downarrow\rangle$	$ 0, 0, 0, 1\rangle$	$-\varepsilon_v$	$ X_-^\downarrow\rangle$	$ 1, 1, 0, 1\rangle$	$\varepsilon_X + \varepsilon_c + V_{c,c} - V_{c,v}$
$ ee\rangle$	$ 1, 1, 0, 0\rangle$	$2\varepsilon_c + V_{c,c}$	$ X_+^\uparrow\rangle$	$ 1, 0, 1, 1\rangle$	$\varepsilon_X - \varepsilon_v + V_{v,v} - V_{c,v}$
$ D_1\rangle$	$ 1, 0, 1, 0\rangle$	ε_X	$ X_+^\downarrow\rangle$	$ 0, 1, 1, 1\rangle$	$\varepsilon_X - \varepsilon_v + V_{v,v} - V_{c,v}$
$ X_1\rangle$	$ 1, 0, 0, 1\rangle$	ε_X	$ B\rangle$	$ 1, 1, 1, 1\rangle$	$2\varepsilon_X + V_{c,c} + V_{v,v} - 2V_{c,v}$

Table 6.1 Eigenstates, occupation number configurations and energies of the Hamiltonian (6.1). The exciton energy is $\varepsilon_X = \varepsilon_c - \varepsilon_v - V_{c,v}$. The parameters used are $\varepsilon_c = 1.378$ eV, $\varepsilon_v = 44.7$ meV, $V_{c,c} = 23.2$ meV, $V_{v,v} = 24.5$ meV and $V_{c,v} = 23.7$ meV (see Appx. A.6 for details).

σ describes the z -component of the total angular momentum (orbital angular momentum and spin), which is $\sigma = \{\uparrow, \downarrow\}$ for the spin 1/2 conduction band electrons and $\{\uparrow, \downarrow\}$ for the pseudo-spin 3/2 heavy holes in the valence band [194]. The one-particle energy levels and the Coulomb matrix elements are obtained from Schrödinger's equation with an effective confinement potential for lens shaped InGaAs-QDs [325], see Appx. A.6. Using the commutator relations (5.40), the number operators $n_{e,\sigma} = e_\sigma^\dagger e_\sigma$, $n_{h,\sigma} = h_\sigma^\dagger h_\sigma$ and

$$n_e = \sum_{\sigma=\{\uparrow,\downarrow\}} n_{e,\sigma}, \quad n_h = \sum_{\sigma=\{\uparrow,\downarrow\}} n_{h,\sigma},$$

the Hamiltonian (6.1) can be written in the occupation number representation

$$H_S = \left(\varepsilon_c - \frac{1}{2}V_{c,c}\right)n_e - \left(\varepsilon_v + \frac{1}{2}V_{v,v}\right)n_h + \frac{1}{2}(V_{c,c}n_e^2 + V_{v,v}n_h^2 - 2V_{c,v}n_en_h). \quad (6.2)$$

The corresponding multi-particle eigenstates are the product states $|n_{e,\uparrow}, n_{e,\downarrow}, n_{h,\uparrow}, n_{h,\downarrow}\rangle = |n_{e,\uparrow}\rangle \otimes |n_{e,\downarrow}\rangle \otimes |n_{h,\uparrow}\rangle \otimes |n_{h,\downarrow}\rangle$. This enables the spectral representation

$$H_S = \sum_k \varepsilon_k |k\rangle \langle k|,$$

where $k = (n_{e,\uparrow}, n_{e,\downarrow}, n_{h,\uparrow}, n_{h,\downarrow})$ is a multi-index labeling the $2^4 = 16$ different electronic configurations shown in Fig. 6.3. If excited one-particle states are included and full configuration interaction is taken into account, the diagonalization of H_S is a non-trivial task. In this case, an approximative treatment of the Coulomb interaction in terms of number operators can be achieved by the Hartree-Fock approximation as given in Ref. [11].

6.2.2 Dissipation superoperators

The system-environment interactions, such as the capture and escape of carriers or the generation and absorption of photons, can be described by dissipation superoperators of Lindblad type. The aim of the model developed in this chapter is the description of the irreversible processes indicated by arrows in Fig. 6.3. In order to consider Coulomb effects in both the charge transfer as well as the recombination processes the various transitions

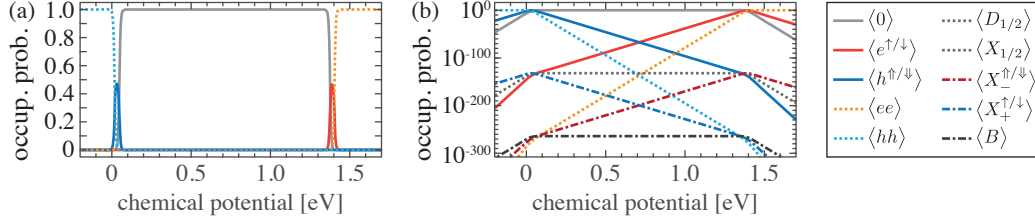


Fig. 6.2 Equilibrium occupation probability (5.53) of the quantum system at $T = 50$ K on (a) linear and (b) logarithmic scale. The equilibrium chemical potential μ_{eq} is controlled by the doping concentration at the QD position. For a QD in the p-domain $\mu_{\text{eq}} \rightarrow -\infty$ the two-hole state occupation probability $\langle hh \rangle = \langle hh | \rho_S | hh \rangle$ approaches 1 and analogously for $\mu_{\text{eq}} \rightarrow +\infty$ only the two-electron state $\langle ee \rangle = \langle ee | \rho_S | ee \rangle$ is occupied. In between the QD is most likely empty.

between the different many-body states must be considered by individual Lindblad terms.

The Hamiltonian of the quantum system (6.1) has a degenerate energy spectrum (due to spin degeneracy), which in general may give rise to eigenstate coherences and non-trivial interactions between diagonal and off-diagonal elements of the reduced density matrix. However, in the situation at hand, the evolution of coherences is decoupled from the evolution of populations because of the selection rules (Pauli-blocking, angular momentum conservation, see Fig. 6.3). Therefore, the resulting dynamical system reduces to a *Pauli master equation* for the populations [42, 266]. In this case, the jump operators $A(\omega, \ell)$ are simple projectors $|f\rangle\langle i|$, that describe the transition between two multi-particle states $|i\rangle$ and $|f\rangle$ separated by the transition energy $\hbar\omega = \varepsilon_i - \varepsilon_f$ and the charge number difference $\ell = \langle i | N_S | i \rangle - \langle f | N_S | f \rangle$. For example, the dissipator connected with $A = |X_1\rangle\langle h^\downarrow|$ describes the capture of a spin-up electron into a QD occupied by a single hole leading to the formation of the bright exciton state $|X_1\rangle$, see Fig. 6.3. In detail, the jump operators belonging to the dissipator \mathcal{D}_e are obtained from Eq. (5.14) using $\mathcal{A}_\alpha = \sum_\sigma (e_\sigma + e_\sigma^\dagger)$ as

$$\begin{aligned}
 A_{\alpha \in \mathcal{I}_e}(\omega, \ell) = & \delta_{\ell, -1} (\delta_{\hbar\omega, -\varepsilon_c} [|e^\uparrow\rangle\langle 0| + |e^\downarrow\rangle\langle 0|] + \delta_{\hbar\omega, -(\varepsilon_c + V_{c,c})} [|ee\rangle\langle e^\uparrow| + |ee\rangle\langle e^\downarrow|] \\
 & + \delta_{\hbar\omega, -(\varepsilon_c - V_{c,v})} [|D_1\rangle\langle h^\uparrow| + |X_1\rangle\langle h^\downarrow| + |X_2\rangle\langle h^\uparrow| + |D_2\rangle\langle h^\downarrow|] \\
 & + \delta_{\hbar\omega, -(\varepsilon_c + V_{cc} - V_{c,v})} [|X_-^\uparrow\rangle\langle D_1| + |X_-^\uparrow\rangle\langle X_2| + |X_-^\downarrow\rangle\langle X_1| + |X_-^\downarrow\rangle\langle D_2|] \\
 & + \delta_{\hbar\omega, -(\varepsilon_c - 2V_{c,v})} [|X_+^\uparrow\rangle\langle hh| + |X_+^\downarrow\rangle\langle hh|] \\
 & + \delta_{\hbar\omega, -(\varepsilon_c + V_{cc} - 2V_{c,v})} [|B\rangle\langle X_+^\uparrow| + |B\rangle\langle X_+^\downarrow|]) \\
 & + \delta_{\ell, +1} (\delta_{\hbar\omega, \varepsilon_c} [|0\rangle\langle e^\uparrow| + |0\rangle\langle e^\downarrow|] + \delta_{\hbar\omega, \varepsilon_c + V_{c,c}} [|e^\uparrow\rangle\langle ee| + |e^\downarrow\rangle\langle ee|] \\
 & + \delta_{\hbar\omega, \varepsilon_c - V_{c,v}} [|h^\uparrow\rangle\langle D_1| + |h^\downarrow\rangle\langle X_1| + |h^\uparrow\rangle\langle X_2| + |h^\downarrow\rangle\langle D_2|] \\
 & + \delta_{\hbar\omega, \varepsilon_c + V_{cc} - V_{c,v}} [|D_1\rangle\langle X_-^\uparrow| + |X_2\rangle\langle X_-^\uparrow| + |X_1\rangle\langle X_-^\downarrow| + |D_2\rangle\langle X_-^\downarrow|] \\
 & + \delta_{\hbar\omega, \varepsilon_c - 2V_{c,v}} [|hh\rangle\langle X_+^\uparrow| + |hh\rangle\langle X_+^\downarrow|] \\
 & + \delta_{\hbar\omega, \varepsilon_c + V_{cc} - 2V_{c,v}} [|X_+^\uparrow\rangle\langle B| + |X_+^\downarrow\rangle\langle B|]).
 \end{aligned}$$

The first five lines with $\ell = -1$ and negative transition energies $\hbar\omega < 0$ describe the electron capture processes whereas the last 5 lines represent the corresponding escape processes (with $\ell = +1$ and $\hbar\omega > 0$). The jump operators connected to the charge conserving processes in \mathcal{D}_0 and the hole transfer processes in \mathcal{D}_h follow analogously. As each projector is uniquely connected with a distinct transition energy and charge transfer number, the dissipation superoperators for all processes can be written in a compact form by using

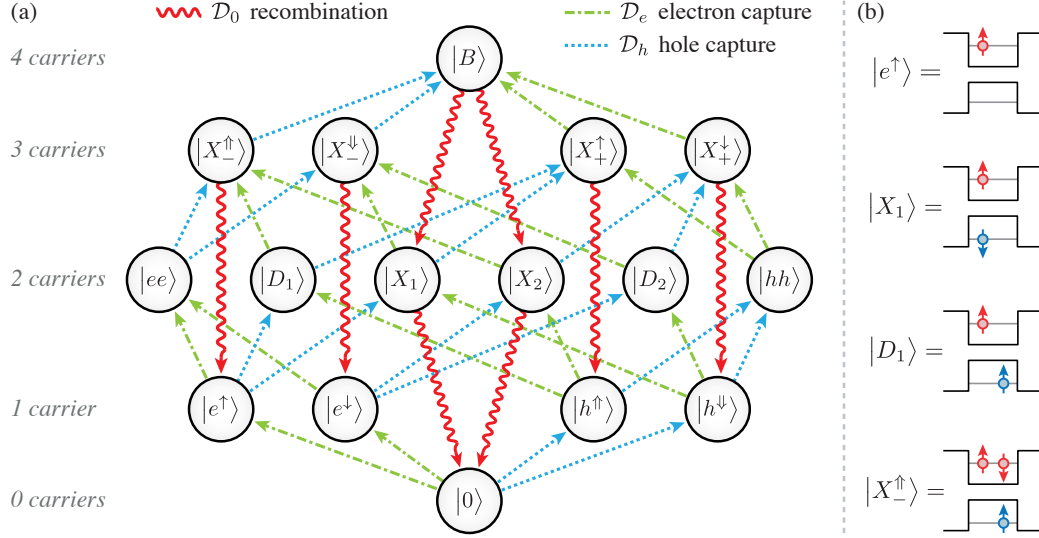


Fig. 6.3 (a) Diagram of electronic states of the Hamiltonian (6.1) and admitted (irreversible) transitions. The arrows indicate capture and recombination, for the corresponding reverse processes (escape, generation) the arrow directions need to be reversed. The multi-particle states are labeled by symbols given in Tab. 6.1. (b) Illustration of the QD occupation for some example states. Reprinted with permission from Ref. [160]. © 2017 American Physical Society.

adjacency matrices \mathbb{A} that encode the allowed transitions shown in Fig. 6.3 (a):

$$\mathcal{D}_e(u_w) \rho_S = \sum_{i,f} \mathbb{A}_{i,f}^e \gamma_{i \rightarrow f}^e(u_w) (L_{|f\rangle} \langle i| \rho_S + e^{-\beta(\varepsilon_i - \varepsilon_f + q\langle\phi\rangle_w + \langle\mu_c\rangle_w)} L_{|i\rangle} \langle f| \rho_S), \quad (6.3a)$$

$$\mathcal{D}_h(u_w) \rho_S = \sum_{i,f} \mathbb{A}_{i,f}^h \gamma_{i \rightarrow f}^h(u_w) (L_{|f\rangle} \langle i| \rho_S + e^{-\beta(\varepsilon_i - \varepsilon_f - q\langle\phi\rangle_w - \langle\mu_v\rangle_w)} L_{|i\rangle} \langle f| \rho_S), \quad (6.3b)$$

$$\mathcal{D}_0(u_w) \rho_S = \sum_{i,f} \mathbb{A}_{i,f}^0 \gamma_{i \rightarrow f}^0(u_w) (L_{|f\rangle} \langle i| \rho_S + e^{-\beta(\varepsilon_i - \varepsilon_f)} L_{|i\rangle} \langle f| \rho_S). \quad (6.3c)$$

Here, the indices i and f run over all multi-particle eigenstates. The relation between forward and backward transition rates is “hard-wired” according to the discussion in Sec. 5.3.6. As before, the dependency of the transition rate on the state of the spatially averaged macroscopic environment is indicated by the abbreviation $u_w = (\langle\mu_c\rangle_w, \langle\mu_v\rangle_w, \langle\phi\rangle_w)$. The adjacency matrix elements, which encode the Pauli blocking and the optical selection rules (conservation of total angular momentum), read

$$\mathbb{A}_{i,f}^e = \delta_{\langle i|n_e|i\rangle+1, \langle f|n_e|f\rangle} \prod_{\sigma=\{\uparrow,\downarrow\}} \delta_{\langle i|n_{h,\sigma}|i\rangle, \langle f|n_{h,\sigma}|f\rangle}, \quad (6.4a)$$

$$\mathbb{A}_{i,f}^h = \delta_{\langle i|n_h|i\rangle+1, \langle f|n_h|f\rangle} \prod_{\sigma=\{\uparrow,\downarrow\}} \delta_{\langle i|n_{e,\sigma}|i\rangle, \langle f|n_{e,\sigma}|f\rangle}, \quad (6.4b)$$

$$\begin{aligned} \mathbb{A}_{i,f}^0 &= \delta_{\langle i|n_{e,\uparrow}|i\rangle, \langle f|n_{e,\uparrow}|f\rangle} \delta_{\langle i|n_{e,\downarrow}|i\rangle-1, \langle f|n_{e,\downarrow}|f\rangle} \delta_{\langle i|n_{h,\uparrow}|i\rangle-1, \langle f|n_{h,\uparrow}|f\rangle} \delta_{\langle i|n_{h,\downarrow}|i\rangle, \langle f|n_{h,\downarrow}|f\rangle} + \\ &+ \delta_{\langle i|n_{e,\uparrow}|i\rangle-1, \langle f|n_{e,\uparrow}|f\rangle} \delta_{\langle i|n_{e,\downarrow}|i\rangle, \langle f|n_{e,\downarrow}|f\rangle} \delta_{\langle i|n_{h,\uparrow}|i\rangle, \langle f|n_{h,\uparrow}|f\rangle} \delta_{\langle i|n_{h,\downarrow}|i\rangle-1, \langle f|n_{h,\downarrow}|f\rangle}. \end{aligned} \quad (6.4c)$$



Fig. 6.4 Effective carrier capture cascade in a reduced model without an explicitly resolved wetting layer (WL). The transition rates between bulk, WL, excited QD states and QD ground states are summarized in the effective capture rate. Reprinted with permission from Ref. [160]. © 2017 American Physical Society.

Note that the above adjacency matrices encode a *directionality* and are therefore non-symmetric $A_{i,f} \neq A_{f,i}$. The matrix elements are only non-zero for the forward processes indicated by the arrow directions shown in Fig. 6.3 (a). The adjacency matrices for the corresponding backward processes are given by the adjoints of Eq. (6.4).

6.2.3 Transition rate models

This section describes the microscopic transition rate models employed in the simulation. Like already outlined above in Sec. 5.3.6, the microscopic calculation of scattering rates is beyond the scope of this thesis and is a subject on its own right. For the practical application in device simulation, one has to resort to suitably parametrized effective transition rates, that can be included phenomenologically in the coupled system (5.37).

Recombination

In low Q resonators, the spontaneous decay rate of the bright multi-particle states of the quantum system (see Fig. 6.3) can be modeled by the Weisskopf–Wigner rate [317]

$$\gamma_{i \rightarrow f}^0 = F_{i,f}^P \frac{d_{c,v}^2 n_r}{6\pi \hbar \epsilon_0 c_0^3} \left(\frac{\epsilon_i - \epsilon_f}{\hbar} \right)^3 \left(1 + n_{\text{pt}} \left(\frac{\epsilon_i - \epsilon_f}{\hbar} \right) \right), \quad (6.5)$$

where (i, f) are allowed index pairs giving $A_{i,f}^0 = 1$. Here, $n_{\text{pt}}(\omega) = (e^{\beta \hbar \omega} - 1)^{-1}$ is the thermal photon number at the transition energy $\hbar \omega$, n_r is the refractive index of the material (at the respective wavelength), $d_{c,v}$ denotes the interband dipole matrix element and c_0 is the vacuum speed of light. Due to cavity effects, the decay rate can be slightly modified with respect to the free space decay rate, which is reflected by the Purcell factors $F_{i,f}^P$ [240]. Using the parameters $n_r = 3.55$, $F_{i,f}^P = 1.8$ (for all optical transitions) and $d_{c,v} = q \times 0.6$ nm, all radiative decay rates are found to be approximately $\gamma_{i \rightarrow f}^0 \approx 1$ ns⁻¹. At low temperatures the enhancement of the decay rate due to the thermal photon number n_{pt} is negligible. A microscopic derivation of the Weisskopf–Wigner decay rate in the framework of Lindblad master equations can be found, e.g., in Ref. [39].

Capture and escape

For semiconductor QDs, the phonon-assisted carrier scattering mediated by the Fröhlich coupling and Auger scattering processes constitute the dominant mechanisms for carrier capture. As a rule of thumb, at low continuum carrier densities, the capture via the emission of LO phonons is dominant, whereas at elevated carrier densities Auger processes

become increasingly efficient [48, 54, 73]. The relevant processes have been briefly reviewed in Sec. 5.3.6, details can be found in the literature cited there.

In the following, phenomenological laws are used for the *effective capture rates*, that describe the typical time scale of the scattering processes as a function of the continuum charge carrier density.¹ The functional form of the phenomenological effective capture rates is motivated from the microscopically calculated results given in Refs. [73, 322]. Since the corresponding escape rates are “hard-wired” in Eq. (6.3), it is sufficient to model the capture rates only. In the following, the effective electron capture rates entering Eq. (6.3a) are modeled by the phenomenological law

$$\begin{aligned} \gamma_{i \rightarrow f}^e (\langle \mu_c \rangle_w, \langle \mu_v \rangle_w, \langle \phi \rangle_w) &= \frac{1}{\tau_{\text{LO}}^e} (1 + n_{\text{LO}}) \frac{1}{e^{\beta(E_c - q\langle \phi \rangle_w - \langle \mu_c \rangle_w + a_{\text{LO}}^e + C_{i,f}^e)} + 1} + \\ &+ \frac{1}{\tau_{\text{Au}}^{e,e}} \frac{\bar{n}_w^2}{1 + \bar{n}_w^{2 - \gamma_{\text{Au}}^{e,e}}} + \frac{1}{\tau_{\text{Au}}^{e,h}} \frac{\bar{n}_w \bar{p}_w}{1 + (\bar{n}_w \bar{p}_w)^{1 - \gamma_{\text{Au}}^{e,h}/2}}, \end{aligned} \quad (6.6a)$$

for the admitted index pairs (i, f) giving $\mathbb{A}_{i,f}^e = 1$. Analogously, the effective hole capture rates in Eq. (6.3b) are assumed as

$$\begin{aligned} \gamma_{i \rightarrow f}^h (\langle \mu_c \rangle_w, \langle \mu_v \rangle_w, \langle \phi \rangle_w) &= \frac{1}{\tau_{\text{LO}}^h} (1 + n_{\text{LO}}) \frac{1}{e^{-\beta(E_v - q\langle \phi \rangle_w - \langle \mu_v \rangle_w - a_{\text{LO}}^h - C_{i,f}^h)} + 1} + \\ &+ \frac{1}{\tau_{\text{Au}}^{h,h}} \frac{\bar{p}_w^2}{1 + \bar{p}_w^{2 - \gamma_{\text{Au}}^{h,h}}} + \frac{1}{\tau_{\text{Au}}^{h,e}} \frac{\bar{n}_w \bar{p}_w}{1 + (\bar{n}_w \bar{p}_w)^{1 - \gamma_{\text{Au}}^{h,e}/2}}, \end{aligned} \quad (6.6b)$$

for the admitted index pairs (i, f) yielding $\mathbb{A}_{i,f}^h = 1$. The first lines in Eqs. (6.6a)–(6.6b) describe the LO-phonon assisted relaxation of continuum carriers to the QD states and the second lines are each attributed to Auger capture processes.

The phonon-assisted processes depend on the number of thermally excited LO-phonons $n_{\text{LO}} = (e^{\beta \hbar \omega_{\text{LO}}} - 1)^{-1}$, where $\hbar \omega_{\text{LO}} = 36.5$ meV is the LO-phonon energy in bulk GaAs [188]. The parameters τ_{LO}^λ and a_{LO}^λ for $\lambda \in \{e, h\}$ are considered as fitting parameters that can be adjusted to microscopically calculated capture rates or experimental data. Here, the values are assumed as $\tau_{\text{LO}}^e = \tau_{\text{LO}}^h = 10$ ps, $a_{\text{LO}}^e = 25$ meV and $a_{\text{LO}}^h = 7$ meV. Due to the relatively large Coulomb matrix elements in semiconductor QDs [11], the scattering rates into charged states differ significantly from those into neutral states. This effect is known as *Coulomb enhancement* or *Coulomb suppression*, respectively (see Sec. 5.5). In the phonon-assisted contribution to the capture rates in Eq. (6.6), this is reflected by the Coulomb enhancement/suppression factors

$$\begin{aligned} C_{i,f}^e &= \varepsilon_f - \varepsilon_i - \varepsilon_c, \\ C_{i,f}^h &= \varepsilon_f - \varepsilon_i + \varepsilon_v, \end{aligned}$$

which describe the additional attractive or repulsive Coulomb shifts that enter the energy balance of the scattering process. Hence, the capture rate is either enhanced (if $C_{i,f}^\lambda < 0$, $\lambda \in \{e, h\}$) or reduced (if $C_{i,f}^\lambda > 0$, $\lambda \in \{e, h\}$). For example, the secondary electron capture process $|e^\uparrow\rangle \rightarrow |ee\rangle$ is suppressed in comparison to the primary process $|0\rangle \rightarrow |e^\uparrow\rangle$, since the additional Coulomb repulsion energy $C_{e^\uparrow, ee}^e = V_{c,c}$ (cf. energies in Tab. 6.1) requires the presence of a higher energetic continuum electron that is thermally suppressed in

¹ More precisely, the capture rate models need to be expressed as functions of the spatially averaged potentials of the macroscopic environment, see Secs. 5.3.5 and 5.3.6.

comparison to the lower energetic one for the primary electron capture process ($C_{0,e\uparrow}^e = 0$). At cryogenic temperatures the effect of Coulomb enhancement/suppression becomes increasingly important. On a microscopic level, the impact of Coulomb effects on the scattering process is very complex and can also lead to *Coulomb inhibition* [73], which is not considered here.

The Auger-related contributions to the capture rates (second lines of Eqs. (6.6a)–(6.6b)) become important at high continuum carrier densities, where the impact of Coulomb shifts is assumed to be small because of screening effects. The functional form of Eq. (6.6) takes the saturation of the capture rate at high carrier densities into account (cf. Refs. [73, 322]). The abbreviations $\bar{n}_w = n_w/n_{\text{Au}}^{\text{crit}}$ and $\bar{p}_w = p_w/p_{\text{Au}}^{\text{crit}}$ describe the dependency on the continuum carrier densities $n_w = N_c F_{1/2}(\beta[\langle\mu_c\rangle_w + q\langle\phi\rangle_w - E_c])$ and $p_w = N_v F_{1/2}(\beta[E_v - q\langle\phi\rangle_w - \langle\mu_v\rangle_w])$, which are functions of the averaged macroscopic potentials. Note that also interband scattering processes are taken into account via the last terms of Eqs. (6.6a)–(6.6b). The parameters $n_{\text{Au}}^{\text{crit}}$, $p_{\text{Au}}^{\text{crit}}$ and $\gamma_{\text{Au}}^{\lambda,\lambda'}$, $\lambda, \lambda' \in \{e, h\}$ are fitting factors. Here the values are set to $n_{\text{Au}}^{\text{crit}} = 10^{19} \text{ cm}^{-3}$, $p_{\text{Au}}^{\text{crit}} = 5 \times 10^{18} \text{ cm}^{-3}$, $\tau_{\text{Au}}^{\lambda,\lambda'} = 1 \text{ ps}$ and $\gamma_{\text{Au}}^{\lambda,\lambda'} = 0.7$ for all $\lambda, \lambda' \in \{e, h\}$.

In the low density limit ($E_c - q\langle\phi\rangle_w \gg \langle\mu_c\rangle_w$ and $\langle\mu_v\rangle_w \gg E_v - q\langle\phi\rangle_w$) the capture rate models (6.6) asymptotically take the form

$$\begin{aligned}\gamma_{i \rightarrow f}^e &\approx \frac{(n_{\text{LO}} + 1) e^{-\beta a_{\text{LO}}^e}}{\tau_{\text{LO}}^e N_c} e^{-\beta C_{i,f}^e} n_w^{\text{MB}} + \frac{(\bar{n}_w^{\text{MB}})^2}{\tau_{\text{Au}}^{e,e}} + \frac{\bar{n}_w^{\text{MB}} \bar{p}_w^{\text{MB}}}{\tau_{\text{Au}}^{e,h}}, \\ \gamma_{i \rightarrow f}^h &\approx \frac{(n_{\text{LO}} + 1) e^{-\beta a_{\text{LO}}^h}}{\tau_{\text{LO}}^h N_v} e^{-\beta C_{i,f}^h} p_w^{\text{MB}} + \frac{(\bar{p}_w^{\text{MB}})^2}{\tau_{\text{Au}}^{h,h}} + \frac{\bar{n}_w^{\text{MB}} \bar{p}_w^{\text{MB}}}{\tau_{\text{Au}}^{h,e}}.\end{aligned}$$

Here, the dependency on the continuum carrier density is linear for the phonon-assisted contributions and quadratic for the Auger-like capture processes. The low-density (Maxwell–Boltzmann) approximations of the average continuum carrier densities n_w^{MB} , p_w^{MB} are obtained by replacing $F_{1/2}(\cdot) \rightarrow \exp(\cdot)$ in the above definitions. The Coulomb enhancement and suppression effect in the phonon-assisted contributions is apparent in this form.

Finally, it shall be noted that the hybrid system (5.37) describes only bulk and QD carriers. For the sake of simplicity, the wetting layer (WL), which is a 2D-like carrier reservoir that is always present in self-assembled QD systems (Stranski–Krastanov growth mode), is excluded from the model (5.37). Following Refs. [111, 157, 175, 289], the system (5.37) could be extended by additional equations of motion for the wetting layer carrier population, which increases the model complexity but does not change the basic structure of the coupling mechanism. As the focus here is on a simple but non-trivial proof-of-principle application of the hybrid modeling approach, the transition rates presented above need to be understood as *effective* scattering rates that describe the entire sequence of microscopic relaxation processes (bulk \rightarrow WL \rightarrow QD, see Fig. 6.4).

6.3 Numerical method

The discretized hybrid system is solved by a full Newton iteration using the electrostatic potential ϕ , the quasi-Fermi energies μ_c , μ_v and the density matrix elements $\langle k | \rho_S | l \rangle$ as independent variables. In order to obtain a system of ordinary differential equations (ODEs), the quantum master equation (5.37d) is projected on the Hilbert space basis spanned by the eigenstates of H_S . The numerical method for the solution of the van

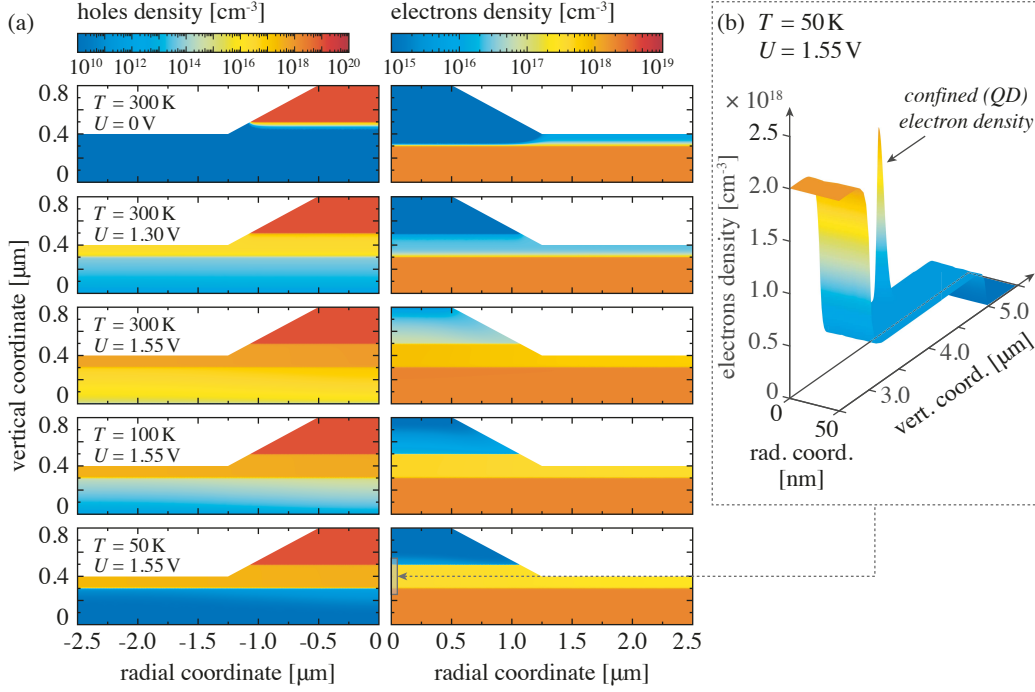


Fig. 6.5 (a) Snapshots of the annealing procedure described in Sec. 3.6 to perform the transport simulation at $T = 50$ K. First, at $T = 300$ K the bias is increased from 0 V to 1.55 V. Subsequently, the temperature is lowered to $T = 50$ K. The plot shows how the minority carrier densities freeze out in the respective regions. (b) Zoom on the electron density in the vicinity of the QD at $(r, z) = (0 \mu\text{m}, 0.4 \mu\text{m})$. At $U = 1.55$ V the occupation probability of the biexciton state is close to unity $\langle B \rangle \approx 1.0$, which leads to a very high density of confined QD electrons (similarly for holes).

Roosbroeck system with degenerate carrier statistics at cryogenic temperatures is described in Chap. 3. The application of the annealing procedure described in Sec. 3.6 on the device under investigation is shown in Fig. 6.5. Here the method must be extended to account for the new coupling terms $Q(\rho_S)$ and $S_{n/p}(u_w, \rho_S)$ given by Eqs. (5.43) and (5.58). The coupling terms induce a non-local interaction of the van Roosbroeck system with the open quantum system via the spatial profile function $w(\mathbf{r})$. The additional terms in the discretization (3.4a)–(3.4c) read

$$\begin{aligned}
 F_{\phi_K^{(i)}} &\sim - \sum_r \int_{\Omega_K \cap \Omega_r} d^3r q Q(\rho_S) = +q |\Omega_K| w_K \text{tr}_S(N_S \rho_S), \\
 F_{\phi_{n,K}^{(i)}} &\sim +\Delta t^{(i)} \sum_r \int_{\Omega_K \cap \Omega_r} d^3r S_n(u_w, \rho_S) = +\Delta t^{(i)} |\Omega_K| w_K \text{tr}_S(N_S \mathcal{D}_e(u_w^{(i)}) \rho_S), \\
 F_{\phi_{p,K}^{(i)}} &\sim +\Delta t^{(i)} \sum_r \int_{\Omega_K \cap \Omega_r} d^3r S_p(u_w, \rho_S) = +\Delta t^{(i)} |\Omega_K| w_K \text{tr}_S(N_S \mathcal{D}_h(u_w^{(i)}) \rho_S),
 \end{aligned}$$

where $w_K = |\Omega_K|^{-1} \int_{\Omega_K} d^3r w(\mathbf{r})$ is the discretized spatial profile function on the K -th Voronoï cell, cf. Sec. 3.1.1. The discrete analogue of Eq. (5.44) is given as $\sum_K |\Omega_K| w_K = 1$. The non-local coupling impacts the sparsity pattern of the Jacobian of the discrete system, since the open quantum system interacts in general with all control volumes of the

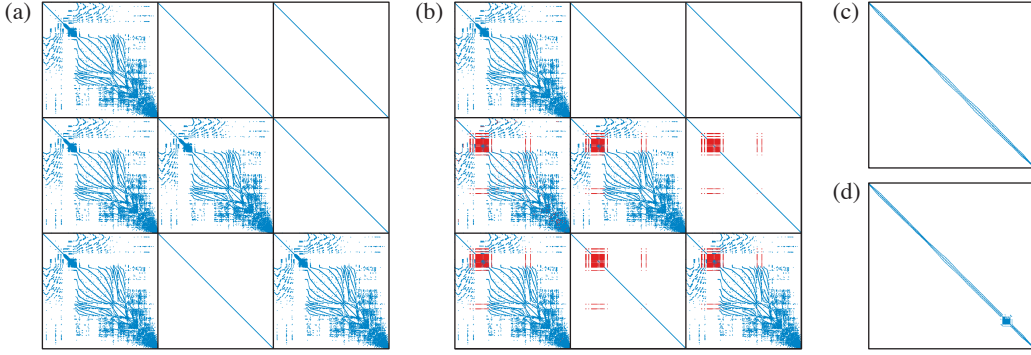


Fig. 6.6 Comparison of the Jacobian matrix of the discrete problem with and without QD. (a) Jacobian without QD (number of non-zero elements $\text{nnz} = 566141$) on a mesh with 14984 nodes. The block structure corresponds to the structure given in Eq. (3.22). (b) Jacobian of the same problem with QD (number of non-zero elements $\text{nnz} = 3407219$) on the same mesh. The block matrix contains an additional 16×16 block matrix on the diagonal and non-square off-diagonal blocks, which are not visible in the plot. The additional non-zero terms due to the continuum-QD coupling are shown in red. Coupling elements below 10^{-12} have been truncated to keep an acceptable level of sparsity (see text). (c) Re-ordered matrix of the problem without QD using the sparse reverse Cuthill-McKee algorithm [97]. The small bandwidth of the matrix is important for the LU factorization. (d) Re-ordered matrix of the problem with QD using the same algorithm. The larger bandwidth leads to a higher effort in solving the linear problem.

macroscopic environment where w_K is non-zero. However, sufficiently far away from the QD location the spatial profile function, that mimics the squared ground state wave function, decays very quickly (typically exponentially). For the Jacobian blocks corresponding to the continuity equations (this is where the non-local coupling yields additional matrix elements), the decay is even faster as the contributions are of quadratic order in w_K , e.g.,

$$\frac{\partial F_{\phi_{n,K}^{(i)}}}{\partial \phi_L^{(i)}} \sim \Delta t^{(i)} |\Omega_K| |\Omega_L| w_L w_K \text{tr}_S \left(N_S \frac{\partial \mathcal{D}_e(u_w)}{\partial \langle \phi \rangle_w} \rho_S \right).$$

Hence, by discarding small matrix elements below a chosen threshold, the quadratic convergence of the Newton iteration can be preserved (due to an accurate approximation of the exact Jacobian), while the numerical effort for the LU-factorization is reduced. The modification of the Jacobian's sparsity pattern is illustrated in Fig. 6.6.

Finally, as the Liouvillian of the Lindblad equation is trace-free, the Jacobian corresponding to the ODE system (i.e., the quantum master equation) has zero rank. In order to solve the hybrid system by a full Newton iteration, a single ODE must be replaced by the trace condition $\text{tr}(\rho_S) = \sum_k \langle k | \rho_S | k \rangle = 1$ to obtain an invertible Jacobian matrix.

6.4 Stationary operation

The occupation probability of the QD states $\langle k \rangle = \langle k | \rho_S | k \rangle$ is controlled by the externally applied voltage as shown in Fig. 6.7 (a). Since the QD is located within the intrinsic zone of the device, it is most probably unoccupied in the thermodynamic equilibrium and the low bias regime, cf. Fig. 6.2. When the applied bias approaches the diode's threshold voltage (around $U \approx 1.52$ V), the QD population changes towards a clear non-equilibrium

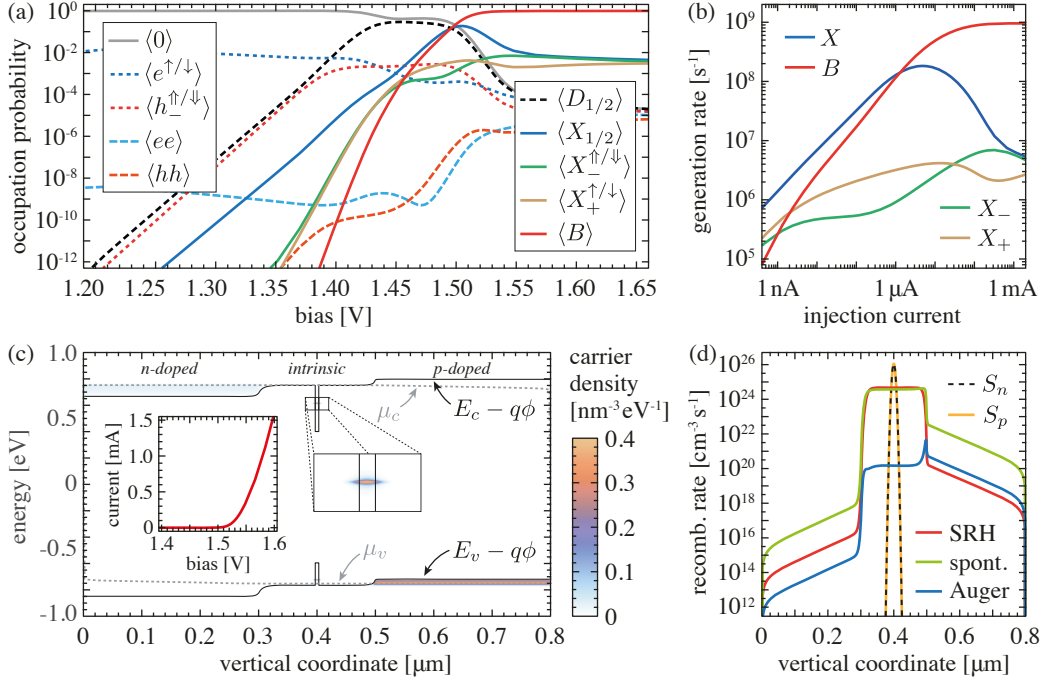


Fig. 6.7 Simulation results at stationary injection. (a) Occupation probability of the QD states vs. applied bias. The short notation of many-body QD states is given in Tab. 6.1. (b) Single-photon generation rates on the different emission lines vs. injection current. (c) Energy band diagram, chemical potentials and energy-resolved carrier density along the symmetry axis (see Fig. 6.1) of the device at $U = 1.5$ V. The inset shows the current-voltage curve of the diode. (d) Comparison of the (net-)recombination rates R of the continuum carriers and the macroscopic (net-)capture rates $S_{n/p}$ along the symmetry axis of the device at $U = 1.5$ V. Reprinted with permission from Ref. [160]. © 2017 American Physical Society.

distribution: First, due to the increased continuum carrier density in the vicinity of the QD, the single-particle and excitonic states become populated. In particular, due to the lack of a radiative decay channel, the dark excitons $\langle D_{1/2} \rangle$ have a high occupation probability in this regime. By further increasing the bias beyond the threshold voltage, the QD is driven into saturation and the population is dominated by the biexciton state $\langle B \rangle$. Due to the Coulomb enhancement and suppression of the carrier capture rates, the population of neutral states is favored over the whole bias range. In particular, Fig. 6.7 (a) shows that the population of the doubly charged states $\langle ee \rangle$ and $\langle hh \rangle$ is strongly suppressed.

The single-photon generation rates of the different emission lines are given by

$$\Gamma_k = \sum_l \mathbb{A}_{k,l}^0 \gamma_{k \rightarrow l}^0 \langle k | \rho_S | k \rangle \quad (6.7)$$

with Eqs. (6.4c) and (6.5). As the decay rates of all radiative channels are roughly equal, the single-photon generation rates shown in Fig. 6.7 (b) are directly proportional to the occupation probabilities depicted in Fig. 6.7 (a). At low injection currents, the emission is dominated by photons generated from the decay of bright excitons. Close to the threshold voltage, the bright exciton emission reaches a maximum ($\Gamma_X^{\max} \approx 0.2 \text{ ns}^{-1}$). At higher injection currents the exciton emission intensity quickly decreases whereas the intensity of

the biexciton emission grows until it saturates at around $\Gamma_B^{\text{sat}} \approx 1 \text{ ns}^{-1}$. In this regime, the capture rates exceed the radiative decay rates by several orders of magnitude. This simulation result agrees well with the experimental observations presented in Ref. [330].

Fig. 6.7(c) shows the calculated energy band structure, chemical potentials and energy resolved carrier densities along the symmetry axis of the device at $U = 1.5 \text{ V}$. Due to the cryogenic operation temperature ($T = 50 \text{ K}$) the majority Fermi energy levels in the doped domains are pinned close to the band edges. Therefore the diode's threshold voltage approximately equals the energy band gap of the material (around $U \approx 1.52 \text{ V}$), which is reflected in the current-voltage curve shown in the inset of Fig. 6.7(c). Finally, in Fig. 6.7(d) the recombination rate R of the continuum carriers and the capture rates $S_{n/p}$ are plotted along the symmetry axis of the diode. In the vicinity of the QD, the scattering of continuum carriers into the QD exceeds the recombination rate by almost two orders of magnitude and therefore constitutes the dominant loss mechanism of continuum carriers.

The (stationary) power spectrum of the QD can be computed from the Fourier transform of the first-order autocorrelation function of the photon operators [313]

$$P(\omega) = 2 \text{Re} \int_0^\infty d\tau e^{i\omega\tau} \langle a^\dagger(\tau) a(0) \rangle. \quad (6.8)$$

As the system (6.1) is purely electronic, the photon operators must be expressed in terms of electronic transition operators [75]. For the power spectrum calculation the operator $a = |X_1\rangle\langle 0| + |X_2\rangle\langle 0| + |X_-^\uparrow\rangle\langle e^\uparrow| + |X_-^\downarrow\rangle\langle e^\downarrow| + |X_+^\uparrow\rangle\langle h^\uparrow| + |X_+^\downarrow\rangle\langle h^\downarrow| + |B\rangle\langle X_1| + |B\rangle\langle X_2|$ is used. The two-time expectation value in Eq. (6.8) is evaluated using the *quantum regression theorem*, see Appx. A.4. The resulting emission spectrum at $U = 1.5 \text{ V}$ is shown in Fig. 6.8(a), that exhibits four different emission lines corresponding to the decay of the bright exciton, the positively and negatively charged trions and the biexciton. Here, close to the threshold voltage, the exciton and the biexciton lines are most dominant and of similar intensity (cf. Fig. 6.7(a, b)). The evaluation of Eq. (6.8) involves the time evolution of non-diagonal matrix elements (polarizations), that experience a damping according to the scattering processes changing their initial or final configurations (cf. Ref. [252]). This excitation-induced dephasing mechanism is inherently included in the Lindblad master equation, even though the evolution of the diagonal and non-diagonal matrix elements is decoupled in the present example. Hence, as a consequence of the carrier capture and escape processes, the emission lines in Fig. 6.8(a) are homogeneously broadened. The unbroadened spectrum, where only the natural line width of the transitions is taken into account, is shown for comparison as a dotted grey line. The line broadening is strongest for the charged trions, which results from the Coulomb enhancement of the capture rates from charged to neutral states.

Finally, an essential figure of merit for quantum light sources is the second-order autocorrelation function of the generated photons [276]

$$g^{(2)}(\tau) = \frac{\langle a^\dagger(0) a^\dagger(\tau) a(\tau) a(0) \rangle}{\langle a^\dagger(0) a(0) \rangle^2}, \quad (6.9)$$

which quantifies the photon anti-bunching effect and thereby distinguishes quantum light sources from emitters of thermal and coherent radiation (see Sec. 1.2). A value of $g^{(2)}(0) < 0.5$ indicates the presence of a single-photon Fock state in the radiation field [209]. Here, Eq. (6.9) is evaluated for the exciton line by substituting the photon annihilation operator in Eq. (6.9) with $a = |X_1\rangle\langle 0|$. The computation of the two-time expectation value is again based on the quantum regression theorem, that requires a transient simulation

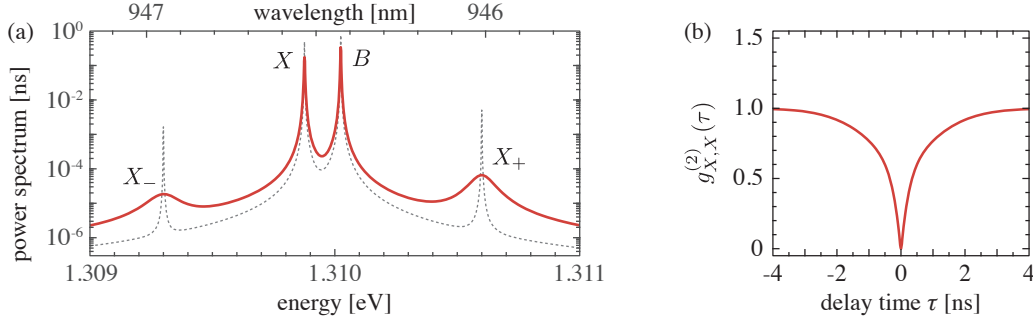


Fig. 6.8 (a) Power spectrum according to Eq. (6.8) at $U = 1.5$ V. The spectrum shows 4 different lines corresponding to the admitted radiative transitions shown in Fig. 6.3 (a), where the biexciton and the exciton lines are most dominant. The carrier capture and escape processes lead to an additional homogeneous broadening of the emission lines. For comparison, also the unbroadered spectrum is shown (dotted grey line), where only the natural line width of the transitions is taken into account. Due to Coulomb enhancement of the capture processes, the line broadening is strongest for the charged trions. (b) Second-order autocorrelation function of the exciton line at $U = 1.5$ V. The curve shows a dip at $\tau = 0$ ns, which is characteristic for quantum light sources, and approaches one after approximately 4 ns. In the idealized model discussed in this section, the photons are instantaneously emitted from the cavity, which leads to the ideal value $g^{(2)}(0) = 0$. Reprinted with permission from Ref. [160]. ©2017 American Physical Society.

of the full system (5.37), cf. Appx. A.4. The result is shown in Fig. 6.8 (b) and features the characteristic dip for high-quality single-photon sources around $\tau = 0$. Current state-of-the-art QD-based solid state single-photon sources indeed show $g^{(2)}(0)$ values practically indistinguishable from zero (after deconvolution of the detector noise) [274], the result $g^{(2)}(0) \equiv 0$ obtained here however must be regarded as an artifact of the model assumptions. The model discussed in this chapter describes the limit of a perfectly open cavity such that the generated photons are instantaneously extracted. In this limit, the value of $g^{(2)}(0)$ is always exactly zero (this follows easily from $a(0)^2 \equiv 0$ with a defined above). For an improved description featuring finite values of $g^{(2)}(0)$, the cavity photons and a coherent light-matter interaction must be included in the Hamiltonian H_S . Moreover, the dissipation superoperator \mathcal{D}_0 must be extended by a photon out-coupling mechanism (cf. Refs. [48, 96]).

6.5 Pulsed electrical excitation

For many applications, the generation of single photons on demand at certain instances of time is required. Therefore, the operation under pulsed excitation is of particular importance. Electrically driven QD-based single-photon sources offer an easy off-resonant excitation scheme, where the QD is pumped by short voltage pulses and subsequently relaxes to its initial state by radiative emission [75, 210]. This process shall be simulated in the following, where a rectangular voltage pulse with a fixed duration of 100 ps is applied to the single-photon diode. The pulse is superimposed on a DC bias of 1.35 V, as shown in Fig. 6.9 (a). In the following, the role of the pulse repetition time and the peak bias, which are the key external control parameters, is investigated. The results of the numerical carrier transport simulation for a single pulse with a peak bias of 1.6 V are shown in Fig. 6.9 (b) and (c). Due to the high carrier mobilities and the long non-radiative life times at low temperatures, the carriers quickly spread out within the intrinsic zone of the diode, which

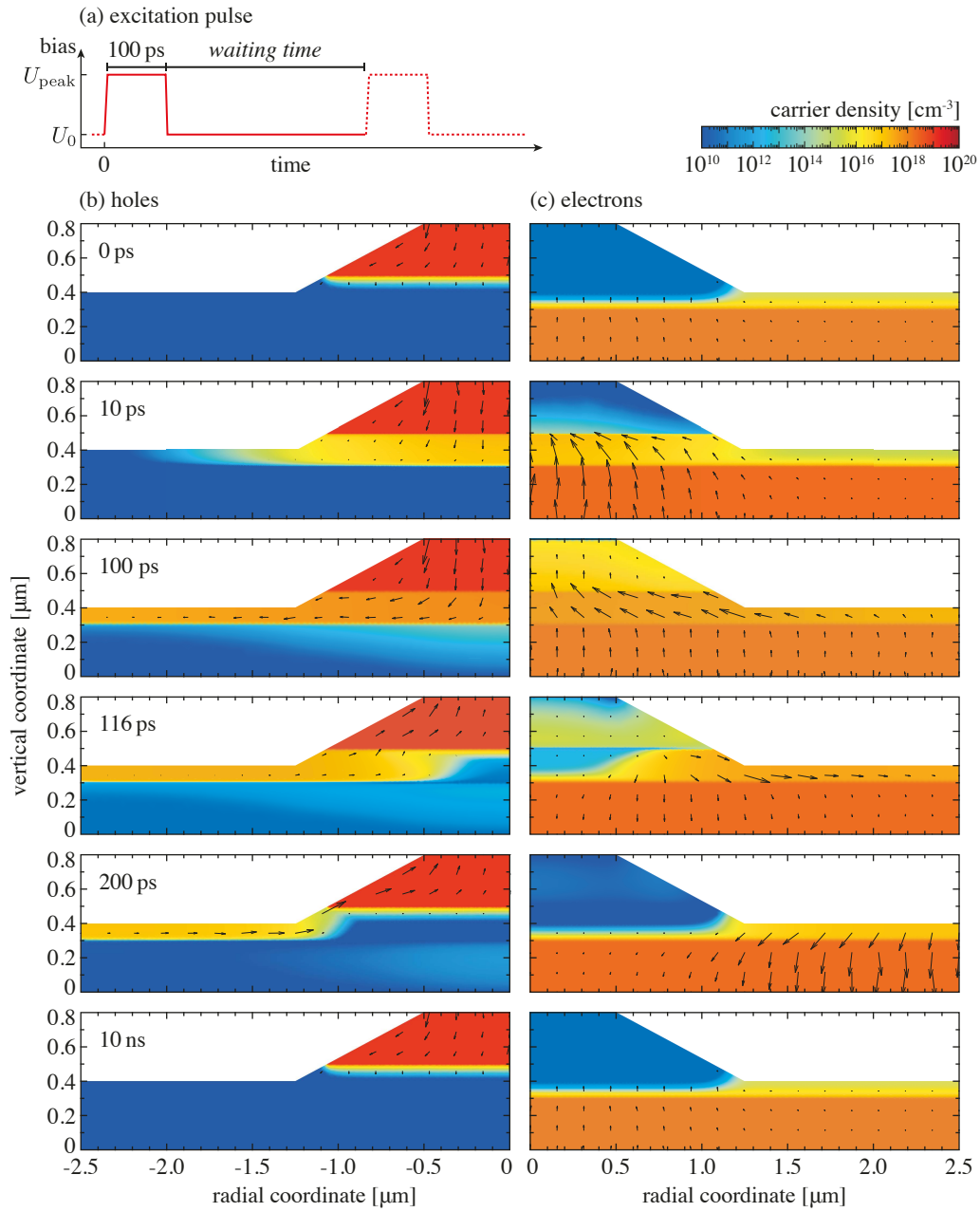


Fig. 6.9 Numerical simulation of the carrier transport at pulsed excitation. (a) Illustration of the bias pulse used in the simulations. The excitation time is fixed to 100 ps and the DC offset bias is taken as $U_0 = 1.35$ V. (b, c) Snapshots of the hole and electron density distribution on a 2D cross-section at several instances of time. The carrier density is color-coded, the arrows indicate the current density vector field (arrows point into the direction of particle motion). The peak voltage in the simulation was set to $U_{\text{peak}} = 1.6$ V. Reprinted with permission from Ref. [160]. © 2017 American Physical Society.

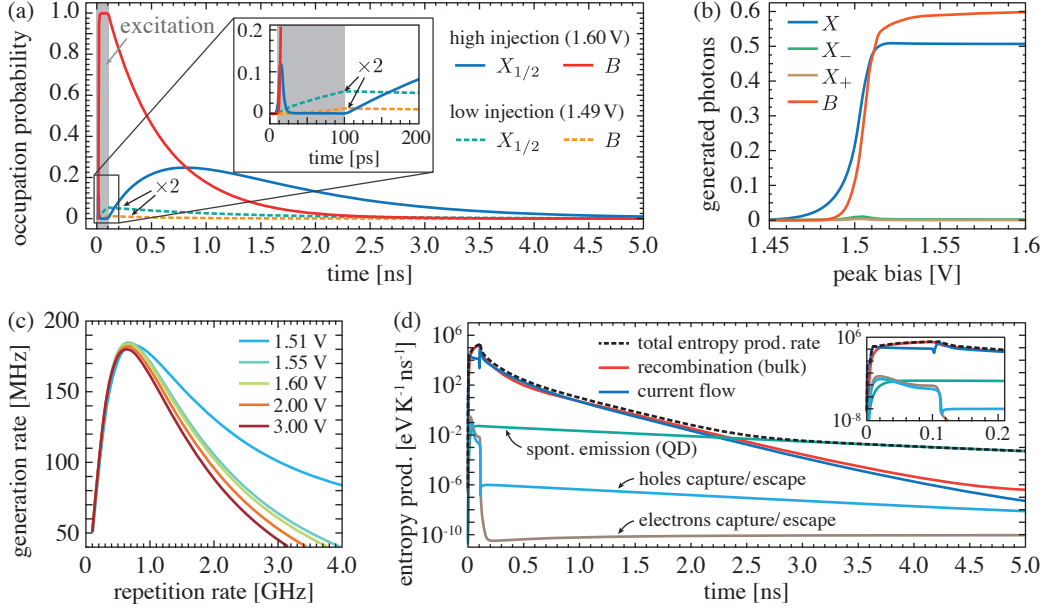


Fig. 6.10 (a) Time-resolved exciton and biexciton occupation probabilities in the case of low and high injection (peak bias $U = 1.49$ V and $U = 1.60$ V). In the low-injection case the occupation probabilities have been multiplied by a factor 2 for better visibility. (b) Number of generated photons per pulse vs. peak bias on the different emission lines. (c) Single-photon generation rate on the bright exciton line as a function of the repetition frequency of the time-periodic excitation pulse (for different values of the peak bias). (d) Time-resolved entropy production rate under pulsed excitation with a peak bias $U = 1.60$ V. The plot shows the five contributions (colored solid lines) arising from the individual terms in Eq. (5.61) and the total entropy production rate (dashed black line). The inset is a zoom on the first 200 ps. Reprinted with permission from Ref. [160]. ©2017 American Physical Society.

is strongly populated at the end of the excitation pulse ($t = 100$ ps). Subsequently the applied voltage is restored to the resting DC bias value, such that the carriers quickly leave the intrinsic zone (cf. Fig. 6.9 (b, c) at $t = 116$ ps and $t = 200$ ps). In particular the vicinity of the QD (which is located at the center of the symmetry axis at ($r = 0$ μm , $z = 0.4$ μm)) is depleted within a few picoseconds. Moreover, a highly conductive channel of holes is formed underneath the insulator layer at the sides of the mesa. The plot at $t = 10$ ns shows the stationary state reached after a long time.

The impact of the excitation pulse on the occupation of the QD is shown in Fig. 6.10 (a). In the case of a strong excitation pulse with a peak voltage of 1.6 V (“high injection”), one observes a very fast occupation of the biexciton state which decays radiatively after the end of the excitation pulse. Via the so-called *biexciton-cascade* [210], this leads to the population of a bright exciton state that subsequently emits a second photon. Comparing the time scales of the carrier transport simulation with the life times of the bright QD states, see Fig. 6.9 (b, c) and Fig. 6.10 (a), one observes that the decay of the bright exciton happens a long time after the continuum carriers have already left the vicinity of the QD. This separation of time scales can be of particular importance for the generation of indistinguishable photons, which crucially depends on the absence of fluctuating continuum charge carriers in the vicinity of the QD [26].

The impact of the peak bias value is shown in Fig. 6.10 (b), where the number of

generated photons (cumulated after 10 ns) on different lines is plotted as a function of the peak bias. The number of generated photons on line k until time t is obtained from

$$N_k(t) = \int_0^t dt' \Gamma_k(t'),$$

where the single-photon generation rate Γ_k is given in Eq. (6.7). The plot indicates that there are two regimes: A sub-threshold (low-injection) regime, where the peak voltage is not sufficient for the excitation of the QD (cf. Fig. 6.10 (a), “low injection”), and a high-injection regime where practically each excitation pulse triggers the biexciton-cascade. For the exciton-photons this implies a generation efficiency of around 50 % for each polarization, while the generation efficiency of the two differently polarized photons on the biexciton line is a little higher than 50 %, due to additional recombination during the excitation phase (first 100 ps), see Fig. 6.10 (a, b).

The efficiency of the single-photon source under pulsed operation can be controlled by adjusting the repetition frequency, such that the number of single-photons generated per time is maximized. For a fixed duration of the excitation pulse (100 ps), this corresponds to an optimization of the waiting time before the next pulse is applied (see Fig. 6.9 (a)). If the waiting time is too short, the next excitation pulse re-populates the QD before the exciton-photon has been emitted and, if the waiting time is too long, the generation efficiency of exciton-photons is decreased as too much time is spent waiting in the long time tail with low photon generation probability (cf. Fig. 6.10 (a)). The optimal repetition frequency $f_{\text{opt}} = \tau_{\text{opt}}^{-1}$ for the generation of single exciton-photons is obtained from maximizing

$$\bar{\Gamma}_X(\tau) = \frac{1}{\tau} N_X(\tau) = \frac{1}{\tau} \int_0^\tau dt \Gamma_X(t) \rightarrow \max$$

such that $\bar{\Gamma}_X(\tau_{\text{opt}}) = \max_\tau \bar{\Gamma}_X(\tau)$. Fig. 6.10 (c) shows $\bar{\Gamma}_X(\tau)$ as a function of the repetition rate $f = \tau^{-1}$ and reveals a clear maximum at $f_{\text{opt}} \approx 650$ MHz ($\tau_{\text{opt}} \approx 1.5$ ns). This corresponds to an optimal single-photon generation rate of $\bar{\Gamma}_X(\tau_{\text{opt}}) \approx 185$ MHz. Even though the photon generation efficiency per pulse shrinks to 28 % in this optimal case, the high repetition frequency leads to an enhanced overall performance. Moreover, Fig. 6.10 (c) shows that this result is practically independent of the peak voltage, as long as the system is excited in the high-injection regime. In order to obtain the actual single-photon emission rate, the generation rate must be multiplied with the photon extraction efficiency [112]. For current state-of-the-art microlens devices, photon extraction efficiencies around 40 % have been reported [74].

Finally, this section shall be concluded with a consideration of the entropy production rate (5.61) during an excitation cycle which is plotted in Fig. 6.10 (d). The plot shows that the entropy production rate during the first 2 ns is clearly governed by the contributions from the macroscopic system (recombination and current flow), whereas at later times $t > 2$ ns the slow decay of the QD-exciton constitutes the dominant contribution. The numerical result is in agreement with the theory presented in Sec. 5.3.7, which predicts a non-negative entropy production rate at all times.

6.6 Discussion and outlook

The numerical results presented in Secs. 6.4 and 6.5 represent a *proof-of-principle* demonstration of the hybrid quantum-classical modeling approach suggested in Chap. 5. An

electrically driven single-photon emitting diode has been simulated under stationary and pulsed excitation conditions. The model system (5.37) allowed for a comprehensive analysis of the device on multiple scales: The spatio-temporally resolved current flow has been calculated self-consistently along with the dynamics of a (simple) open quantum system (which gives access to the quantum optical characterization) in a realistic, multi-dimensional device geometry *out of one box*. The simulation results were found in good qualitative and quantitative agreement with experimental results reported in the literature for similar devices. The results indicate the computational tractability of the approach and its potential usefulness in realistic numerical semiconductor device simulation. In the following, possible simplifications and extensions of the approach shall be discussed.

If the feedback of the quantum system on its macroscopic environment is weak, i.e., if the capture rates $S_{n/p}$ are small in comparison to the recombination rate R , the coupling between both subsystems becomes effectively uni-directional such that the approach can be simplified. In this case, the evolution of the quantum system is *slaved* by the dynamics of its macroscopic environment, which can be exploited to reduce the computational effort in a two-step method: First, the carrier transport simulation is carried out whilst omitting the coupling terms to the quantum system as carried out, e.g., in Chap. 4. In a second step, the solution of the carrier transport simulation is used to parametrize the time-dependent transition rates in the dissipation superoperators (6.3a)–(6.3b) that drive the dynamics of the open quantum system. Finally, the quantum optical figures of merit are obtained by solving the quantum master equation in a “post-processing” step. With the explicit dependency of the microscopic transition rates on the state of the macroscopic environment, the hybrid model provides a consistent link between the two steps of the unidirectionally coupled simulation approach. Moreover, the accuracy of the simplified approach and approximation errors can be assessed by checking the validity of the decoupling condition $R \gg S_{n/p}$. If necessary, the hybrid model shows how the respective corrections can be perturbatively incorporated in the unidirectional approach (cf. also Sec. 4.4.2).

The application considered in this chapter is an example for a quantum system with a weak feedback on its macroscopic environment that, in principle, would allow for the one-way method described above. The reason for this is the slow radiative decay time in comparison to the fast electronic scattering processes, which keeps the capture rates $S_{n/p}$ small once the QD is occupied. However, this is not always the case. For example, in electrically driven QD nanolasers, where a single or a few QDs are placed inside a resonant cavity, the Purcell-enhanced light-matter interaction strongly decreases the radiative carrier life times [295]. As a consequence, the capture rates $S_{n/p}$ are expected to increase by some orders of magnitude such that the quantum system significantly couples back to its environment by spatial hole burning, which contributes to current guiding. In this case the predictions of the hybrid model are expected to differ clearly from the decoupled approach.

The model can be expanded in multiple directions to increase the accuracy and the level of detail. The *modular* structure of the system (5.37) is well-suited for extensions on the micro- and the macroscopic level. Moreover, the approach leaves a great freedom in dividing the full system into quantum mechanical and classical parts. Some possible directions are sketched in the following:

- An accurate description of the QD-photon interaction in single-photon sources of QD nanolasers requires the consideration of a reversible (Jaynes–Cummings-like) light-matter interaction in the Hamiltonian of the open quantum system (cf. Eq. (5.39)). This gives rise to the formation of dressed states and correlation effects that yield a refined description of the photon statistics, see Refs. [94, 95]. Note that this extension

is generally covered by the theory in Chap. 5, but was omitted in the example studied here. Regarding the inclusion of reversible light-matter interaction one has to keep in mind that this limits the approach to small electronic systems and very few (most likely one) optical modes as the dimensionality of the associated Hilbert space grows exponentially. A factorization approach that reduces the complexity in the case of an ensemble of identical emitters is given in Ref. [88].

- The example considered in this chapter neglects – for the sake of simplicity – the fine structure splitting of the exciton [19, 304], which yields different emission energies in polarization resolved spectroscopy. Just as in the previous point, the fine structure splitting can be included by an extension of the electronic Hamiltonian. The hybrid quantum-classical modeling approach can be applied to a broad range of physical situations by customizing the Hamiltonian and the dissipative system-environment interactions to the specific requirements of the particular problem at hand.
- At the interface between the macroscopic and the quantum system, the phenomenological approach building on the spatial profile function (see Sec. 5.3.2) can be refined by using realistic wave functions. The wave functions can be calculated dynamically by extending the system (5.37) towards a self-consistent Schrödinger–Poisson problem [17, 223]. This will violate the local charge balance (which is not severe, see Appx. A.5), but allows for an improved description of the radiative recombination rate and energy shifts by including a self-consistent description of the quantum confined Stark effect [130]. Together with the trap model explained in Appx. A.2, this gives also access to the description of spectral diffusion (and indistinguishability of generated photons) due to electrostatic interaction with carriers captured in nearby trap states. Moreover, the impact of noise effects can be studied using the approaches described in Ref. [36].
- The model system can be extended by additional continuity equations describing the population and carrier transport within the wetting layer (WL). This has been sketched in Ref. [157] following approaches from quantum well laser simulation [111, 175, 289]. The possible inclusion of a WL was already hinted in Sec. 6.2.3 and allows for a refined description of the carrier capture cascade.
- In the transient simulations in Chap. 4 and 6, the system reacts very fast on voltage pulses. A more realistic description should take external circuit elements into account, that slow down the dynamical response of the device due to additional capacity and resistivity. This can be included by coupling additional circuit equations to the model system and using current-controlled boundary conditions [83, 232].
- The van Roosbroeck systems can be extended towards a non-isothermal *energy-drift diffusion system* [4]. This allows for the description of temperature effects that could possibly affect the hybrid system on all levels: From self-heating on the macroscopic level and the Seebeck effect as an additional mechanism for macroscopic current flow down to temperature-induced energy level shifts and temperature-dependent decay and dephasing on the microscopic level. If the macroscopic system is furthermore extended by a Helmholtz equation for the optical modes [13, 14], also electro-thermo-optical phenomena like temperature and excitation induced changes of the refractive index profile [196] and shifts of the cavity resonance frequency can be studied in a self-consistent framework. This might be interesting for the investigation of strong light-matter coupling in electrically driven high Q resonators.

Finally it shall be noted that predictive simulations in the framework of macroscopic device modeling are always limited and require a precise tuning of parameters and the included

(often phenomenological) effective material laws. In the context of the hybrid system this requires in particular a precise tuning of the transition rate models for capture/escape of carriers. Once the model is calibrated to reproduce experimental findings, the simulation allows for a predictive investigation of design variations and the analysis of efficiency bottlenecks. An *ab initio* (fully quantum mechanical) simulation from first principles is not tractable and prohibitively expensive on the scale of macroscopic structures.

6.7 Conclusions

The hybrid quantum-classical model system introduced in Chap. 5 has been applied to the simulation of an electrically driven single-photon emitting diode in a *proof-of-principle* calculation. The model allows for the self-consistent simulation of the spatially resolved current flow in a realistic device geometry along with the calculation of the decisive quantum optical figures of merit (in particular the single-photon generation rate, the second-order correlation function and spectral properties of the emitted light). The approach has been demonstrated under stationary and pulsed excitation conditions. The simulation results were found in good qualitative and quantitative agreement with experimental observations reported for similar devices.

Chapter 7

Summary and outlook

Semiconductor quantum optics is on the leap from the lab to real world applications. To advance the development of novel devices such as non-classical light sources and nanolasers based on semiconductor quantum dots, device engineers will need simulation tools that combine classical device physics with cavity quantum electrodynamics. This thesis is focused on the device scale modeling and numerical simulation of electrically driven quantum light sources based on semiconductor quantum dots. Therefore a broad range of different topics is treated and connected to methodically advance the state-of-the-art — from semi-classical device physics and elements of non-equilibrium thermodynamics to the theory of open quantum systems.

The main result of this thesis is the introduction of a new *hybrid quantum-classical* modeling approach, that self-consistently describes the macroscopic current flow in semiconductors along with the dynamics of open quantum systems. This is achieved by coupling the van Roosbroeck system with a Markovian quantum master equation in Lindblad form. The approach allows for a comprehensive description of quantum dot based devices for quantum optical applications on multiple scales: It enables the characterization of the microscopic, quantum optical features together with the simulation of the spatially resolved current flow in realistic, multi-dimensional semiconductor device geometries in an unified way. The approach goes beyond existing multi-scale approaches in semiconductor device simulation and closes a gap between microscopic and macroscopic simulation tools, that could be useful to support the development and design of future devices. As the consistency with thermodynamics is of high importance in semiconductor device simulation, the thermodynamic properties of the hybrid model are investigated in detail: A thorough discussion of the model equations shows that the hybrid model guarantees the conservation of charge, the consistency with the thermodynamic equilibrium and the second law of thermodynamics. For this, the consideration of extremal principles in thermodynamics is applied to *hybrid* functionals with mixed classical and quantum mechanical contributions. Moreover, the model equations are shown to be interconnected and consistent with the GENERIC approach to non-equilibrium thermodynamics. The appealing thermodynamic properties provide a starting point for the extension of the hybrid model towards more complex systems taking, e.g., electro-thermal and electro-optical effects into account. Finally, the hybrid modeling approach is showcased by *proof-of-principle* simulations of a single-photon emitting diode both in the stationary and in the transient operation regime.

Single-photon sources based on InGaAs-QDs are typically operated at extremely low temperatures. For the numerical simulation of the current flow in such devices, this imposes a considerable challenge as the standard numerical methods break down due to severe convergence issues. The extreme freeze out of minority carriers at cryogenic temperatures leads to numerical underflow in finite precision arithmetics and inhibits the usage of the usual continuation method. The analysis of the condition number of the discrete system indicates that the problem is ill-conditioned and numerically intractable at low bias values. In this thesis a revised continuation procedure is introduced, that features an additional artificial annealing step. Thereby, the problem can be circumvented, such that the carrier transport simulation can be carried out at extremely low temperatures in the vicinity of flat band conditions. The annealing method is easy to implement and has already been adopted in the numerical simulation of nanowire LEDs [167, 168] and reaches out to the simulation of SiGe heterojunction bipolar transistors [258] and CMOS circuit elements for quantum computing systems [21]. With the advent of compact and cost-efficient cryocoolers, the interest in (practical) devices operated at cryogenic temperatures is expected to increase – also beyond opto-electronics and basic research.

A second challenge regarding the device simulation at cryogenic operation conditions emerges from the strong degeneration of the electron-hole plasma in semiconductors at extremely low temperatures. The consideration of degeneration effects, such as a nonlinear enhancement of the diffusion current, requires a revision of the standard discretization method – in particular the classical Scharfetter–Gummel scheme must be extended towards Fermi–Dirac statistics. In this work, several recently proposed generalizations of the Scharfetter–Gummel method are reviewed and assessed with respect to their structure preserving properties and accuracy. The review presented here goes beyond the literature on the topic.

The numerical methods are employed to investigate the current injection into electrically driven single-photon emitting diodes. This is carried out in a theory-experiment collaboration on the experimentally observed electroluminescence in an oxide-confined pin-diode structure featuring several quantum dots. The oxide-confined aperture is intended to serve two purposes: First, it enables the strain-driven site-controlled nucleation of a single quantum dot above the aperture, which is essential for deterministic device fabrication. Second, the insulating nature of the oxide is intended to funnel the injection current into a narrowly confined region. The experimentally observed optical activity of parasitic quantum dots in the outer regions of the mesa, however, contradicts the naive assumption on the current confining property and indicates a rapid lateral current spreading above the oxide layer. The phenomenon is reproduced and thoroughly investigated by numerical simulations. Based on the analysis, a revision of the doping profile is suggested, that shows a significantly improved confinement of the injection current under stationary and pulsed operation. The new design enables the highly selective electrical excitation of single quantum dots, which is of high importance for electrically driven single-photon sources.

In this thesis, the foundations on a new hybrid quantum-classical modeling approach for quantum dot devices have been laid. So far, the approach was employed only to prototypical structures, such that in the next step, the method should be applied to the simulation and optimization of real devices, e.g., electrically driven micropillars [132] or microlenses [112] for single-photon emission. Beyond that, the hybrid quantum-classical modeling approach provides a versatile modeling platform that can be applied to the simulation of a variety of different devices by adapting the equations to the particular problem at hand. Next to quantum light sources, a promising direction for future application of the approach are single and few quantum dot nanolasers that feature pronounced cavity-QED

effects [48, 49, 94, 295]. Such devices show a very interesting threshold behavior and emission characteristics that require a fully quantum optical modeling approach to properly describe the influence of spontaneous emission and strong light-matter coupling effects [49, 95]. The development of quantum dot nanolasers is driven by the on-going progress in miniaturization to reach ultimately downsized lasers which are expected to have a reduced power consumption, that is required for optical interconnects in optical communication and information processing tasks [49, 113]. For practical applications, it will be desirable to develop electrically driven nanolasers to overcome the need for expensive and bulky excitation lasers. Here, novel effects might come into play, that can not be explained by the consideration of the microscopic emitter-photon system alone, but require a fully coupled hybrid quantum-classical treatment. This may include, e.g., excitation-induced dephasing due to the freely roaming continuum carriers, spatial hole burning and heating effects. As pointed out in the discussion in Sec. 6.6, the hybrid modeling approach can be extended to meet these requirements by merging the quantum optical description with classical approaches to device scale laser simulation [13, 14, 111]. This way, the hybrid modeling approach may support the development of electrically driven quantum dot nanolasers.

Appendix

A.1 Dopant ionization at cryogenic temperatures

The van Roosbroeck system is still applicable at cryogenic temperatures [53, 116, 248, 258, 279], however, some modeling aspects need to be carefully considered. As a rule of thumb, the conductivity of doped semiconductors typically decreases at very low temperatures due to a *freeze-out* of the ionized dopant concentration [2, 116].

At low doping concentrations, the wave functions of the carriers can be considered as decoupled, such that charge transfer between different dopant states is only possible via hopping transport due to tunneling or thermionic emission [110]. Therefore, the semiconductor becomes an insulator at low temperatures. With increasing dopant concentration, the distance between the impurity atoms decreases such that the wave functions of the electronic states start to overlap. This leads to the formation of an impurity band as shown in Fig. A.1, where the tail states result from the random distribution of the dopants in the lattice [110]. At very high doping concentrations (see Fig. A.1 (c)), the impurity band overlaps with the continuum states. In this heavy doping regime, which marks the transition of the semiconductor to a metal, the conduction can take place within the impurity band – even at extremely low temperatures [110]. This metal-insulator transition is also known as *Mott transition* [221], which has to be taken into account in temperature-dependent models for the incomplete doping ionization [2]. Here the metal-insulator transition is treated only in a phenomenological fashion to describe the dopant activation in the van Roosbroeck system. A microscopic modeling approach, which is typically based on the Hubbard model [87, 140], is beyond the scope of this thesis.

The density of ionized dopants is given by [51, 110, 302]

$$N_D^+ = \frac{N_D}{1 + g_D e^{\beta(\mu_c - E_D + q\phi)}}, \quad N_A^- = \frac{N_A}{1 + g_A e^{\beta(E_A - q\phi - \mu_v)}},$$

where N_D and N_A are the built-in donor and acceptor concentrations and N_D^+ and N_A^- denote the singly ionized donor and acceptor densities, respectively. The degeneracy factor of the donor state is $g_D = 2$ in GaAs (spin-degeneracy), whereas the acceptor state is fourfold degenerate $g_A = 4$ (spin-degeneracy and twofold degenerate valence band) [51]. The donor and acceptor energy levels are taken as $E_D = E_c - E_D^{\text{act}}$ and $E_A = E_v + E_A^{\text{act}}$, where E_D^{act} and E_A^{act} are the activation energies of the dopants. In the *shallow dopant*

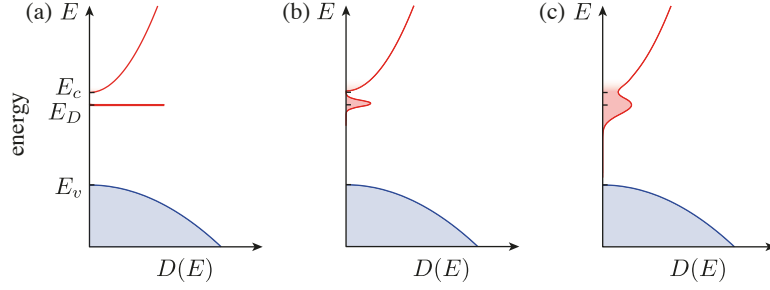


Fig. A.1 Formation of an impurity band in the case of heavy doping. (a) At low doping concentration the donor state at E_D is sharply defined. (b) Increasing doping concentration leads to the formation of an impurity band by broadening of the donor state, (c) which finally overlaps with the conduction band continuum at heavy doping. The picture is drawn after [110].

model, the dopants are modeled as a hydrogen-like impurity on a constant background material [110, 302], yielding the binding energies

$$E_{D,0}^{\text{act}} = \text{Ry} \frac{m_e^*}{m_0 \varepsilon_r^2}, \quad E_{A,0}^{\text{act}} = \text{Ry} \frac{m_h^*}{m_0 \varepsilon_r^2}, \quad (\text{A.1})$$

where $\text{Ry} = \frac{1}{2} q^4 m_0 / (4\pi \varepsilon_0 \hbar)^2 \approx 13.61 \text{ eV}$ is the Rydberg energy and m_0 is the free electron mass. The (static) dielectric constant ε_r and the effective electron or hole mass $m_{e/h}^*$ correspond to the host material. By the formation of the impurity band at high doping concentrations (see Fig. A.1), the activation energy is effectively decreased as [57, 110]

$$E_D^{\text{act}} = E_{D,0}^{\text{act}} \left(1 - \left(\frac{N_D^+}{N_D^{\text{crit}}} \right)^{1/3} \right), \quad E_A^{\text{act}} = E_{A,0}^{\text{act}} \left(1 - \left(\frac{N_A^-}{N_A^{\text{crit}}} \right)^{1/3} \right). \quad (\text{A.2})$$

Hence, the dopant activation depends on the density of the ionized dopants itself. The critical impurity densities for the metal-insulator transition $N_{D/A}^{\text{crit}}$ can be estimated from the Mott criterion [221] (a_0 is the hydrogen Bohr radius)

$$N_D^{\text{crit}} \approx \left(\frac{3}{4\pi \varepsilon_r a_0} \frac{m_e^*}{m_0} \right)^3, \quad N_A^{\text{crit}} \approx \left(\frac{3}{4\pi \varepsilon_r a_0} \frac{m_h^*}{m_0} \right)^3.$$

The activation energy model (A.2) describes a metal-insulator transition at low temperatures and heavy doping. The numerically calculated ionization acceptor density for GaAs data [232] under equilibrium conditions, i.e., the solution (N_A^-, μ_{eq}) of the system

$$N_A^- = N_A \left[1 + g_A e^{\beta(E_v + E_{A,0}^{\text{act}}(1 - (N_A^-/N_A^{\text{crit}})^{1/3}) - \mu_{\text{eq}})} \right]^{-1}, \quad (\text{A.3a})$$

$$0 = N_v F_{1/2} \left(\frac{E_v - \mu_{\text{eq}}}{k_B T} \right) - N_c F_{1/2} \left(\frac{\mu_{\text{eq}} - E_c}{k_B T} \right) - N_A^-, \quad (\text{A.3b})$$

is shown in Fig. A.2. The critical acceptor doping density is taken as $N_A^{\text{crit}} = 1 \times 10^{18} \text{ cm}^{-3}$ [70]. For built-in acceptor densities above the critical acceptor density (see $N_A = 10^{19} \text{ cm}^{-3}$ and 10^{20} cm^{-3} in Fig. A.2 (a-c)) and temperatures below around 65 K, the system (A.3) yields three coexisting solutions for the ionized acceptor concentration. Via Eq. (A.2) this

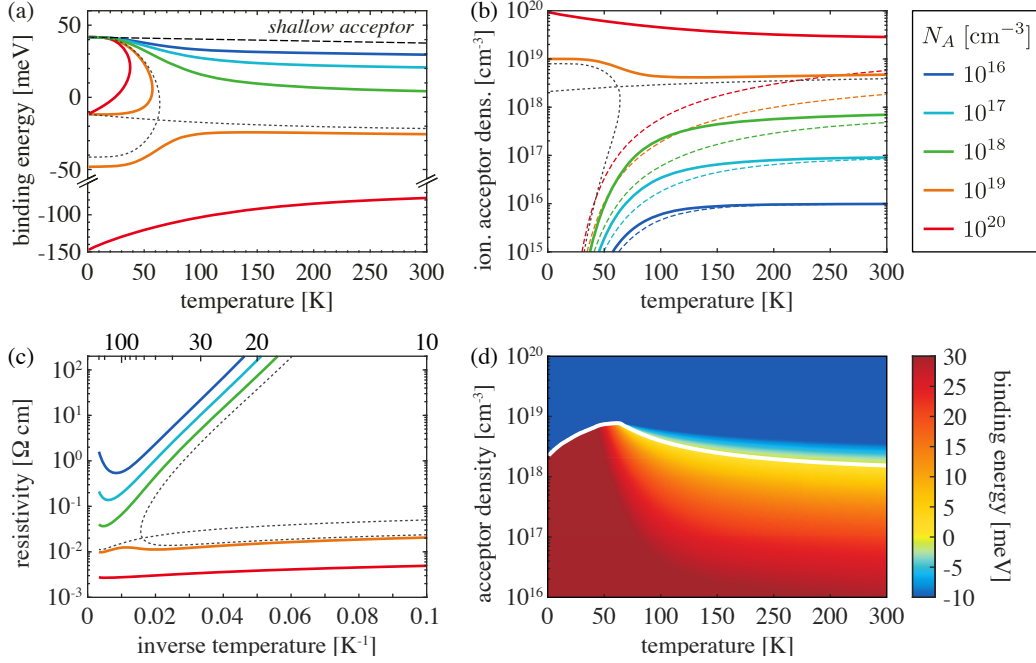


Fig. A.2 (a) Acceptor activation energy vs. temperature for different built-in acceptor densities. Beyond the metal-insulator transition, the model yields multiple coexisting solutions for the activation energy, where the lowest ones correspond to the fully activated acceptor doping. The dashed black line shows the activation energy according to the shallow doping model (A.1). The separatrix (degenerate configuration that has two coexisting solutions) is shown as a dotted grey line. (b) Calculated ionized acceptor density vs. temperature using the activation energy dependence (A.2) (solid lines) in comparison to the shallow dopant model (A.1) (dashed lines) for different built-in acceptor densities. For heavy doping, the model (A.2) exhibits a metal-insulator transition at low temperatures, which is not included in the simple model (A.1). (c) Numerically calculated resistivity σ_p^{-1} using the hole mobility model reported in Ref. [217] and $p \approx N_A^-$. Beyond the metal-insulator transition the resistivity of heavy doped samples remains small even at cryogenic temperatures. (d) Calculated (minimal) acceptor activation energy using the model (A.2) vs. temperature and the built-in acceptor density. The activation energy is color-coded. The white line marks the $E_A = 0$ eV level that corresponds to the Mott transition.

corresponds to three coexisting acceptor activation energies shown in Fig. A.2(a). The lowest value for activation energy yields the highest degree of ionization, which is plotted in Fig. A.2(b). The plot shows a completely different temperature-dependence of the ionized acceptor density for built-in acceptor densities below and above the metal-insulator transition. For comparison, also the ionized acceptor density calculated using the shallow dopant model (A.1) (i.e., with a constant acceptor activation energy) is shown, which does not exhibit the metal-insulator transition. Together with a temperature and ionized dopant density dependent mobility model, the system (A.3) allows to calculate the electrical resistivity $\sigma_p^{-1} \approx (qM_p(T, N_A^-) N_A^-)^{-1}$ of a p-doped sample with $p \approx N_A^-$. Fig. A.2(c) shows the calculated resistivity using the hole mobility model for GaAs presented in Ref. [217]. The result is in a good agreement with the experimentally measured resistivity of carbon-doped GaAs:C reported in Ref. [70]. A two-dimensional map of the calculated acceptor activation energy depending on the density of built-in acceptors and temperature is shown in Fig. A.2(d), where the Mott transition is indicated by a white line.

A.2 Recombination rate models

This section provides some details on the derivation of the recombination rate models of the van Roosbroeck system introduced in Sec. 2.1.4. In particular, it is shown how the structural form of the net-recombination rate (2.15) arises from the interband collision integral (2.28) and simple classical kinetics in a natural way by assuming quasi-equilibrium distribution functions. In the following, the even part of the distribution functions is written as

$$f_{\lambda,k} = \frac{1}{e^{\beta(\varepsilon_{\lambda,k} - q\phi - \mu_{\lambda})} + 1},$$

where $\lambda \in \{c, v\}$ labels the conduction and valence band electrons and μ_{λ} is the quasi-Fermi energy level of the electron ensemble in the corresponding band. The most simple case of direct band-to-band recombination is considered first, followed by the more complex Auger and Shockley–Read–Hall recombination processes.

Direct band-to-band recombination

In a semi-classical picture, the direct band-to-band recombination can be described by a master equation system for the population of conduction and valence band electrons as

$$\partial_t f_{c,k}|_{\text{dir}} = \sum_{k'} (G_{v,k' \rightarrow c,k}^{\text{dir}} - R_{c,k \rightarrow v,k'}^{\text{dir}}), \quad \partial_t f_{v,k}|_{\text{dir}} = \sum_{k'} (R_{c,k' \rightarrow v,k}^{\text{dir}} - G_{v,k \rightarrow c,k'}^{\text{dir}}),$$

with the generation and recombination rates

$$G_{v,k' \rightarrow c,k}^{\text{dir}} = g_{v,k' \rightarrow c,k}^{\text{dir}} f_{v,k'} (1 - f_{c,k}), \quad R_{c,k \rightarrow v,k'}^{\text{dir}} = r_{c,k \rightarrow v,k'}^{\text{dir}} f_{c,k} (1 - f_{v,k'}),$$

where $k = (\mathbf{k}, \sigma)$ is a multi-index labeling the wave vector and spin state. The scattering rates $r_{c,k \rightarrow v,k'}^{\text{dir}}$ and $g_{v,k' \rightarrow c,k}^{\text{dir}}$ describe the characteristic time scale of the corresponding transitions (including also the selection rules) and can be determined from quantum mechanical calculations. In the thermodynamic equilibrium, the chemical potentials of both carrier species equilibrate to μ_{eq} and all net-processes must vanish due to the principle of detailed balance (microscopic reversibility). This implies the relation

$$g_{v,k' \rightarrow c,k}^{\text{dir}} = r_{c,k \rightarrow v,k'}^{\text{dir}} \frac{f_{c,k}^{\text{eq}}}{1 - f_{c,k}^{\text{eq}}} \frac{1 - f_{v,k'}^{\text{eq}}}{f_{v,k'}^{\text{eq}}} = r_{c,k \rightarrow v,k'}^{\text{dir}} e^{-\beta(\varepsilon_{c,k} - \varepsilon_{v,k'})},$$

where $f_{c,k}^{\text{eq}} = (e^{\beta(\varepsilon_{c,k} - \mu_{\text{eq}})} + 1)^{-1}$ and $f_{v,k}^{\text{eq}} = (e^{\beta(\varepsilon_{v,k} - \mu_{\text{eq}})} + 1)^{-1}$ are the thermodynamic equilibrium distribution functions. This gives rise to the form

$$\begin{aligned} \partial_t f_{c,k}|_{\text{dir}} &= - \sum_{k'} r_{c,k \rightarrow v,k'}^{\text{dir}} f_{c,k} (1 - f_{v,k'}) \left(1 - e^{-\beta(\varepsilon_{c,k} - \varepsilon_{v,k'})} \frac{f_{v,k'}}{1 - f_{v,k'}} \frac{1 - f_{c,k}}{f_{c,k}} \right) \\ &= - (1 - e^{-\beta(\mu_c - \mu_v)}) \sum_{k'} r_{c,k \rightarrow v,k'}^{\text{dir}} f_{c,k} (1 - f_{v,k'}), \end{aligned}$$

where the “driving term” of the net-recombination process, which is independent of the summation index, has been taken out of the sum in the last line. By summing over \mathbf{k} and σ , one arrives at the form (2.15) with $\partial_t n|_{\text{dir}} = -R_{\text{dir}}$, $\partial_t p|_{\text{dir}} = -R_{\text{dir}}$ and

$$R_{\text{dir}} = (1 - e^{-\beta(\mu_c - \mu_v)}) \frac{V}{(2\pi)^6} \sum_{\sigma, \sigma'} \int_{\mathbb{R}^3} d^3 k \int_{\mathbb{R}^3} d^3 k' r_{c,\mathbf{k},\sigma \rightarrow v,\mathbf{k}',\sigma'}^{\text{dir}} f_{c,\mathbf{k},\sigma} f_{h,\mathbf{k}',\sigma'}.$$

Here, the hole distribution function was introduced as $f_{h,k} = 1 - f_{v,k}$. The electron density (cf. Sec. 2.2) involves only the even part of the distribution function (approximated by the quasi-equilibrium function above) and is taken as

$$n = \frac{1}{(2\pi)^3} \sum_{\sigma} \int_{\mathbb{R}^3} d^3k f_{c,k}$$

(holes analogously). As a result, the structural property $R \propto (1 - e^{-\beta(\mu_c - \mu_v)})$ of Eq. (2.15) is a general feature that merely requires a description of the carrier ensembles in terms of the quasi-equilibrium distribution functions. In particular, the form (2.15) is independent of the density of states, the transition rate matrix and selection rules. The structural form guarantees the detailed balance principle in the thermodynamic equilibrium and the non-negativity of the entropy production rate (cf. Sec. 2.3.2.3).

Finally, the expression (2.18) is obtained by neglecting the k -independency of the transition rates $r_{c,k \rightarrow v,k'}^{\text{dir}} \approx r_{c \rightarrow v}^{\text{dir}}$, such that the above integral factorizes and the recombination rate can be written in terms of carrier densities

$$R_{\text{dir}} \approx (1 - e^{-\beta(\mu_c - \mu_v)}) Bnp.$$

Auger recombination

Analogous to the case of direct band-to-band recombination, the Auger recombination rate model (2.19) follows from the master equation system

$$\partial_t f_{c,k}|_{\text{Au}} = \sum_{k'} (G_{v,k' \rightarrow c,k}^{\text{Au}} - R_{c,k \rightarrow v,k'}^{\text{Au}}), \quad \partial_t f_{v,k}|_{\text{Au}} = \sum_{k'} (R_{c,k' \rightarrow v,k}^{\text{Au}} - G_{v,k \rightarrow c,k'}^{\text{Au}})$$

with

$$\begin{aligned} R_{c,k \rightarrow v,k'}^{\text{Au}} &= \sum_{\lambda=c,v} \sum_{k_1, k_2} r_{c,k; \lambda, k_1 \rightarrow \lambda, k_2; v, k'}^{\text{Au}} f_{c,k} f_{\lambda, k_1} (1 - f_{\lambda, k_2}) (1 - f_{v, k'}), \\ G_{v,k' \rightarrow c,k}^{\text{Au}} &= \sum_{\lambda=c,v} \sum_{k_1, k_2} g_{v, k'; \lambda, k_2 \rightarrow \lambda, k_1; c, k}^{\text{Au}} f_{v, k'} f_{\lambda, k_2} (1 - f_{\lambda, k_1}) (1 - f_{c, k}). \end{aligned}$$

In contrast to the direct band-to-band transition, which is a two-particle scattering process, Auger recombination is a four-particle scattering process where the interband transition is assisted by an additional intraband energy transfer process in either the valence or the conduction band (labeled by $\lambda = \{c, v\}$). This is shown in Fig. 2.4 (c, d). Following the steps carried out above, one obtains the detailed balance condition

$$g_{v, k'; \lambda, k_2 \rightarrow \lambda, k_1; c, k}^{\text{Au}} = r_{c, k; \lambda, k_1 \rightarrow \lambda, k_2; v, k'}^{\text{Au}} e^{\beta(\varepsilon_{\lambda, k_2} - \varepsilon_{\lambda, k_1})} e^{-\beta(\varepsilon_{c, k} - \varepsilon_{v, k'})}$$

and the net-recombination rate using quasi-equilibrium distributions

$$\begin{aligned} R_{\text{Au}} &= (1 - e^{-\beta(\mu_c - \mu_v)}) \frac{V^3}{(2\pi)^{12}} \sum_{\lambda=c,v} \sum_{\sigma, \sigma', \sigma_1, \sigma_2} \int_{\mathbb{R}^3} d^3k \int_{\mathbb{R}^3} d^3k_1 \int_{\mathbb{R}^3} d^3k_2 \int_{\mathbb{R}^3} d^3k' \times \\ &\quad \times r_{c, \mathbf{k}, \sigma; \lambda, \mathbf{k}_1, \sigma_1 \rightarrow \lambda, \mathbf{k}_2, \sigma_2; v, \mathbf{k}', \sigma'}^{\text{Au}} f_{c, \mathbf{k}, \sigma} f_{\lambda, \mathbf{k}_1, \sigma_1} (1 - f_{\lambda, \mathbf{k}_2, \sigma_2}) (1 - f_{v, \mathbf{k}', \sigma'}), \end{aligned}$$

which is again of the form (2.15). As above, the approximation of k -independent scattering rates yields a factorization of the integral, which finally leads to the expression (2.19).

Shockley–Read–Hall recombination

Shockley–Read–Hall recombination is a non-radiative recombination process which involves an additional trap state within the band gap due to impurities and structural defects. The corresponding master equation system reads

$$\begin{aligned}\partial_t f_{c,k}|_{\text{SRH}} &= \sum_{k'} (G_{T,k' \rightarrow c,k}^{\text{SRH}} - R_{c,k \rightarrow T,k'}^{\text{SRH}}), \\ \partial_t f_{T,k}|_{\text{SRH}} &= \sum_{k'} (R_{c,k' \rightarrow T,k}^{\text{SRH}} - G_{T,k \rightarrow c,k'}^{\text{SRH}}) + \sum_{k'} (G_{v,k' \rightarrow T,k}^{\text{SRH}} - R_{T,k \rightarrow v,k'}^{\text{SRH}}), \\ \partial_t f_{v,k}|_{\text{SRH}} &= \sum_{k'} (R_{T,k' \rightarrow v,k}^{\text{SRH}} - G_{v,k \rightarrow T,k'}^{\text{SRH}})\end{aligned}$$

with

$$\begin{aligned}R_{\lambda,k \rightarrow \lambda',k'}^{\text{SRH}} &= r_{\lambda,k \rightarrow \lambda',k'}^{\text{SRH}} f_{\lambda,k} (1 - f_{\lambda',k'}), & (\lambda, \lambda') \in \{(c, T), (T, v)\}, \\ G_{\lambda,k \rightarrow \lambda',k'}^{\text{SRH}} &= g_{\lambda,k \rightarrow \lambda',k'}^{\text{SRH}} f_{\lambda,k} (1 - f_{\lambda',k'}), & (\lambda, \lambda') \in \{(v, T), (T, c)\}\end{aligned}$$

and

$$g_{\lambda',k' \rightarrow \lambda,k}^{\text{SRH}} = r_{\lambda,k \rightarrow \lambda',k'}^{\text{SRH}} e^{-\beta(\varepsilon_{\lambda,k} - \varepsilon_{\lambda',k'})}.$$

Here, $f_{T,k}$ describes the electron occupation of the k -th trap band state. Following the steps carried out above, one obtains the transient model for the population dynamics of the conduction, valence and trap band carriers [232].

The recombination rate model (2.17) is obtained either in the steady state or by adiabatic elimination of the trap state occupation function $f_{T,k}$, which is valid for fast recombination life times in comparison to the internal time scales of the van Roosbroeck system. From $\partial_t f_{T,k}^{\text{stat}}|_{\text{SRH}} = 0$ one obtains the stationary trap level occupation probability as

$$f_{T,k}^{\text{stat}} = \frac{\sum_{k_1} r_{c,k_1 \rightarrow T,k}^{\text{SRH}} f_{c,k_1} + \sum_{k_2} g_{v,k_2 \rightarrow T,k}^{\text{SRH}} (1 - f_{h,k_2})}{(1 + e^{\beta(\tilde{\varepsilon}_{T,k} - \mu_c)}) \sum_{k_1} r_{c,k_1 \rightarrow T,k}^{\text{SRH}} f_{c,k_1} + (1 + e^{-\beta(\tilde{\varepsilon}_{T,k} - \mu_v)}) \sum_{k_2} r_{T,k \rightarrow v,k_2}^{\text{SRH}} f_{h,k_2}}$$

with the abbreviation $\tilde{\varepsilon}_{T,k} = \varepsilon_{T,k} - q\phi$. Using this, one obtains the Shockley–Read–Hall recombination rate from the master equation for the conduction or valence band population (after integration over k) as

$$\begin{aligned}R_{\text{SRH}} &= (1 - e^{-\beta(\mu_c - \mu_v)}) \times \\ &\times \sum_{k'} \frac{\frac{1}{(2\pi)^3} \sum_{\sigma} \int_{\mathbb{R}^3} d^3k f_{c,\mathbf{k},\sigma} r_{c,\mathbf{k},\sigma \rightarrow T,k'}^{\text{SRH}} \sum_{k_2} r_{T,k' \rightarrow v,k_2}^{\text{SRH}} f_{h,k_2}}{(1 + e^{\beta(\tilde{\varepsilon}_{T,k'} - \mu_c)}) \sum_{k_1} r_{c,k_1 \rightarrow T,k'}^{\text{SRH}} f_{c,k_1} + (1 + e^{-\beta(\tilde{\varepsilon}_{T,k'} - \mu_v)}) \sum_{k_2} r_{T,k' \rightarrow v,k_2}^{\text{SRH}} f_{h,k_2}},\end{aligned}$$

which has again the structure of Eq. (2.15).

The Shockley–Read–Hall recombination rate model (2.17) is obtained, again, by assuming k -independent scattering rates $r_{c,k \rightarrow T,k'}^{\text{SRH}} \approx \tau_n^{-1}$, $r_{T,k \rightarrow v,k'}^{\text{SRH}} \approx \tau_p^{-1}$ and a δ -like density of states of the trap mini band at $\varepsilon_{T,k'} \equiv E_T$ such that one arrives at

$$R_{\text{SRH}} = \frac{np}{\tau_p (n + n_d) + \tau_n (p + p_d)} (1 - e^{-\beta(\mu_c - \mu_v)}),$$

where $n_d = ne^{\beta(E_T - q\phi - \mu_c)}$, $p_d = pe^{\beta(\mu_v - E_T + q\phi)}$ depend weakly on the chemical potentials.

A.3 Numerical evaluation of Fermi–Dirac integrals

The assembly of the discrete van Roosbroeck system (3.4) (Jacobian matrix, right hand side) requires fast and accurate routines for the numerical evaluation of the Fermi–Dirac integral $F_{1/2}$ and its derivative $F_{-1/2}$ (see Eq. (2.8)). As there is no closed form solution of Eq. (2.8), numerical approximation needs to be employed. The decision for a routine is usually a trade-off between accuracy and efficiency.

Numerical methods with high accuracy (IEEE double precision) were given by Goano [100] and MacLeod [200] for several Fermi–Dirac integrals of half order. Another method for half order Fermi–Dirac integrals based on analytic continuation and trapezoidal rule with pole correction using the residual theorem was presented by Mohankumar & Natarajan [219]. Two famous approximations of $F_{1/2}$ that employ only a single closed form expression with an acceptable accuracy on the whole range $-\infty < \eta < \infty$ were obtained by Bednarczyk & Bednarczyk [22] (maximum relative error 0.4%) and Aymerich-Humet et al. [10] (maximum relative error 0.53%). Other fast and simple to implement routines based on Chebyshev expansions are due to Werner & Raymann [318], Cody & Thatcher [52] and van Halen & Pulfrey [120]. A comprehensive review on approximations of Fermi–Dirac integrals was given by (among others) Blakemore [32] and Wong et al. [326]. Some of the approximations are compared in Fig. A.3 with respect to accuracy and speed.

An important advantage of, e.g., the formulas by Bednarczyk & Bednarczyk [22] and Halen & Pulfrey [120] is that they can be easily differentiated yielding a cheap and consistent approximation of $F_{-1/2}$, which are required for the Newton iteration (see Sec. 3.5).

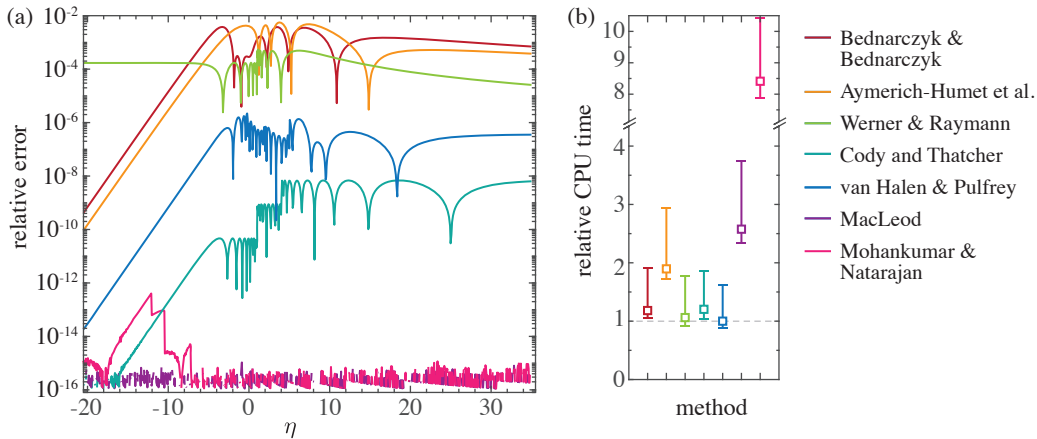


Fig. A.3 (a) Comparison of the relative errors of some of the routines mentioned in the text. The numerically exact reference value was obtained by Gauss–Kronrod quadrature. The closed form expressions by Bednarczyk & Bednarczyk [22] and Aymerich-Humet et al. [10] provide a rather coarse approximation and are clearly below the accuracy provided by the Chebyshev expansions based routines by Cody & Thatcher [52] and van Halen & Pulfrey [120]. The methods by MacLeod [200] and Mohankumar and Natarajan [219] are accurate to machine precision over the entire range. (b) Comparison of the relative CPU times for the evaluation of $F_{1/2}$ at $\eta = 10$ for 1 million runs. The evaluation times are normalized with respect to the runtime of the van Halen & Pulfrey method. The error bars range from the minimal time needed for evaluation to the mean time plus standard deviation. The mean time is indicated by a square box.

A.4 Two-time correlation functions and the quantum regression theorem

For the calculation of optical spectra and higher order intensity correlation functions, cf. Sec. 6.4, it is necessary to compute two- and multi-time expectation values. This can be achieved by the *quantum regression theorem* [39, 44]. Consider two (Schrödinger picture) operators $A, B \in \mathcal{H}_S$ and the two-time correlation function

$$g_{A,B}(t + \tau, t) = \langle A(t + \tau) B(t) \rangle = \text{tr}(A_{\text{H}}(t + \tau) B_{\text{H}}(t) \rho(0)), \quad (\text{A.4})$$

which is defined using the Heisenberg picture operator representation

$$A_{\text{H}}(t) = U^\dagger(t) A U(t).$$

The unitary time evolution operator U obeys Schrödinger's equation $\partial_t U(t) = -\frac{i}{\hbar} H U(t)$, $U(0) = I$, where H is the Hamiltonian (5.1) of the composite system. The time evolution operator satisfies the semigroup property $U(t_1 + t_2) = U(t_1) U(t_2)$ and $U(t) = U^\dagger(-t)$. Note that the trace in Eq. (A.4) is taken over the composite system $\mathcal{H}_S \otimes \mathcal{H}_R$. Using cyclic permutations under the trace operation, the two-time correlation function can be written in terms of Schrödinger picture operators

$$\begin{aligned} g_{A,B}(t + \tau, t) &= \text{tr}(U^\dagger(t + \tau) A U(t + \tau) U^\dagger(t) B U(t) \rho(0)) = \text{tr}(A U(\tau) B \rho(t) U^\dagger(\tau)) \\ &= \text{tr}_S(\text{Atr}_R(U(\tau) (B \rho_S(t) \otimes \rho_R(t)) U^\dagger(\tau))), \end{aligned}$$

where the Born approximation (5.9) was employed in the last line. By comparison with Eq. (5.3) this is

$$g_{A,B}(t + \tau, t) = \text{tr}_S(A R_B(t + \tau)),$$

with

$$R_B(t + \tau) = V(t + \tau, t) R_B(t) = \text{tr}_R(U(\tau) (B \rho_S(t) \otimes \rho_R(t)) U^\dagger(\tau)).$$

Hence, the practical calculation of $g_{A,B}(t + \tau, t)$ requires the following steps: First, the open system S is propagated from the initial time $\rho_S(t=0)$ to $\rho_S(t) = V(t, 0) \rho_S(0)$ by solving the initial value problem (5.23)

$$\partial_t \rho_S(t) = \mathcal{L}(t) \rho_S(t).$$

Then, B is applied from the left on $\rho_S(t)$ yielding the “new density matrix” $R_B(t) = B \rho_S(t) = B V(t, 0) \rho_S(0)$. Subsequently, $R_B(t)$ is propagated by the dynamical map V for an additional time τ according to the same evolution equation as before

$$\partial_\tau R_B(t + \tau) = \partial_\tau V(t + \tau, t) R_B(t) = \mathcal{L}(t + \tau) R_B(t + \tau).$$

Then the Schrödinger picture operator A is applied from the left on the resulting $R_B(t + \tau)$. Subsequently one takes the trace over \mathcal{H}_S , which finally yields the two-time correlation function $g_{A,B}(t + \tau, t) = \text{tr}_S(A V(t + \tau, t) B V(t, 0) \rho_S(0))$. In the case of a time-dependent Liouvillian $\mathcal{L}(t)$, also the temporal evolution of the environment (which gives the time-dependence of \mathcal{L} in Sec. 5.2.2) from t to $t + \tau$ must be taken into account in the second step. The method is readily generalized to multi-time correlation functions [39].

A.5 Alternative approach for the macroscopic scattering rates

This section provides a different formulation of the macroscopic scattering rates S_n and S_p considered in Sec. 5.3.5. Here, the transition rates are evaluated locally everywhere in the environment of the QD and weighted by $w(\mathbf{r})$ instead of employing the spatial-average approximation (5.57) on the level of the arguments of the transition rates.

First, the *local* (indicated by a hat) dissipation superoperators are introduced as

$$\begin{aligned}\hat{\mathcal{D}}_e(u(\mathbf{r}))\rho_S &= \sum_{\alpha \in \mathcal{I}_e} \sum_{\omega < 0} \gamma_\alpha(\omega, u(\mathbf{r})) (L_{A_\alpha(\omega, -1)}\rho_S + e^{-\beta\Delta_\alpha(u(\mathbf{r}))}L_{A_\alpha^\dagger(\omega, -1)}\rho_S), \\ \hat{\mathcal{D}}_h(u(\mathbf{r}))\rho_S &= \sum_{\alpha \in \mathcal{I}_h} \sum_{\omega > 0} \gamma_\alpha(\omega, u(\mathbf{r})) (L_{A_\alpha(\omega, +1)}\rho_S + e^{-\beta\Delta_\alpha(u(\mathbf{r}))}L_{A_\alpha^\dagger(\omega, +1)}\rho_S), \\ \hat{\mathcal{D}}_0(u(\mathbf{r}))\rho_S &= \sum_{\alpha \in \mathcal{I}_0} \sum_{\omega > 0} \gamma_\alpha(\omega, u(\mathbf{r})) (L_{A_\alpha(\omega, 0)}\rho_S + e^{-\beta\Delta_\alpha(u(\mathbf{r}))}L_{A_\alpha^\dagger(\omega, 0)}\rho_S),\end{aligned}$$

which resemble the definitions in Eq. (5.60). The form of $\Delta_\alpha(u(\mathbf{r}))$ is discussed below. The local terms enter the Lindblad Eq. (5.37d) as a spatially accumulated integral average

$$\partial_t \rho_S|_{\text{diss}} = \mathcal{D}(u)\rho_S = \int_{\Omega} d^3r w(\mathbf{r}) \hat{\mathcal{D}}(u(\mathbf{r}))\rho_S = \langle \hat{\mathcal{D}}(u)\rho_S \rangle_w$$

with the sum of the local dissipators $\hat{\mathcal{D}}(u(\mathbf{r})) = \hat{\mathcal{D}}_e(u(\mathbf{r})) + \hat{\mathcal{D}}_h(u(\mathbf{r})) + \hat{\mathcal{D}}_0(u(\mathbf{r}))$ (cf. Eq. (5.55)) and the notation $\langle \hat{\mathcal{D}}(u)\rho_S \rangle_w = \int_{\Omega} d^3r w(\mathbf{r}) \hat{\mathcal{D}}(u(\mathbf{r}))\rho_S$. The analogue of the charge preserving property (5.56) is reflected in the (now local) relation

$$\text{tr}_S(N_S \hat{\mathcal{D}}_0(u(\mathbf{r}))\rho_S) = 0$$

(use Eq. (5.15b) and cyclic permutations). In the modified setting, the macroscopic scattering rates are introduced as

$$S_n(u(\mathbf{r}), \mathbf{r}, \rho_S) = +w(\mathbf{r}) \text{tr}_S(N_S \hat{\mathcal{D}}_e(u(\mathbf{r}))\rho_S), \quad (\text{A.5a})$$

$$S_p(u(\mathbf{r}), \mathbf{r}, \rho_S) = -w(\mathbf{r}) \text{tr}_S(N_S \hat{\mathcal{D}}_h(u(\mathbf{r}))\rho_S). \quad (\text{A.5b})$$

The definition (5.43) for the bound charge density confined to the quantum system is kept unchanged.

With Eq. (A.5), the derivative of Poisson's Eq. (5.37a) yields

$$\begin{aligned}\frac{1}{q} \nabla \cdot \mathbf{j}_{\text{tot}} &= w(\mathbf{r}) \text{tr}_S(N_S [\hat{\mathcal{D}}_e(u(\mathbf{r}))\rho_S - \langle \hat{\mathcal{D}}_e(u)\rho_S \rangle_w + \hat{\mathcal{D}}_h(u(\mathbf{r}))\rho_S - \langle \hat{\mathcal{D}}_h(u)\rho_S \rangle_w]) \\ &\neq 0,\end{aligned}$$

which contradicts the principle of local charge balance (5.46). Instead, the non-local condition (5.47) is satisfied, which is reflected in

$$\frac{1}{q} \int_{\Omega} d^3r \nabla \cdot \mathbf{j}_{\text{tot}} = 0.$$

This property is sufficient to satisfy Kirchhoff's current law and the constraints (5.6).

Regarding the consistency with the thermodynamic equilibrium, there are two consid-

erations that need to be made. First, the equilibrium state ρ_S^{eq} obtained in Eq. (5.53) results merely from the minimization of the hybrid grand potential. The equilibrium state therefore remains unchanged and the property $\mathcal{D}(u_{\text{eq}})\rho_S^{\text{eq}} \equiv 0$ must be obeyed by any reasonably constructed dissipation superoperator. Second, in the setting considered here, the right hand sides of the continuity Eqs. (5.37b)–(5.37c) involve the modified macroscopic scattering rates defined above. As the right hand sides must vanish in the thermodynamic equilibrium, the relation $\hat{\mathcal{D}}_\alpha(u_{\text{eq}}(\mathbf{r}))\rho_S^{\text{eq}} \equiv 0$ (for any α) must be satisfied *locally*. Analysis of the action of the local dissipation superoperator

$$\begin{aligned} 0 &\stackrel{!}{=} \hat{\mathcal{D}}(u_{\text{eq}}(\mathbf{r}))\rho_S^{\text{eq}} = \\ &= \sum_\alpha \sum_\ell \sum_{\omega>0} (\gamma_\alpha(\omega, \ell, u_{\text{eq}}(\mathbf{r})) - \gamma_\alpha(-\omega, -\ell, u_{\text{eq}}(\mathbf{r}))e^{\beta(\hbar\omega - [q\langle\phi_{\text{eq}}\rangle_w + \mu_{\text{eq}}]\ell)}) \times \\ &\quad \times (A_\alpha(\omega, \ell)\rho_S^{\text{eq}}A_\alpha^\dagger(\omega, \ell) - e^{-\beta(\hbar\omega - [q\langle\phi_{\text{eq}}\rangle_w + \mu_{\text{eq}}]\ell)}A_\alpha^\dagger(\omega, \ell)\rho_S^{\text{eq}}A_\alpha(\omega, \ell)) \end{aligned}$$

shows that the equilibrium transition rate $\gamma_\alpha(\omega, \ell, u_{\text{eq}}(\mathbf{r})) = \gamma_\alpha(\omega, \ell, \mu_{\text{eq}}, \mu_{\text{eq}}, \langle\phi_{\text{eq}}\rangle_w)$ must be a spatially independent function (recall the quantum detailed balance relation (5.29)). More precisely, the rate must depend on the average $\langle\phi_{\text{eq}}\rangle_w$ (instead of a local value) in order to yield a consistent equilibrium state while still obeying the quantum detailed balance relation. An admissible relation for non-equilibrium transition rates is

$$\gamma_\alpha(-\omega, -\ell, u(\mathbf{r})) = e^{-\beta(\hbar\omega - [q\langle\phi\rangle_w + \mu_\alpha(\mathbf{r})]\ell)}\gamma_\alpha(\omega, \ell, u(\mathbf{r})), \quad (\text{A.6})$$

where $u(\mathbf{r}) = (\mu_c(\mathbf{r}), \mu_v(\mathbf{r}), \langle\phi\rangle_w)$. Note that the different consideration of chemical potentials (local) and the electrostatic potential (spatial average) in the presentation here originates from the QD charge density expression (5.43) that was kept unchanged.¹

Finally, by introducing the auxiliary density matrix

$$\rho_\alpha^*(u(\mathbf{r})) = e^{-\beta(H_S - [\langle\phi\rangle_w + \mu_\alpha(\mathbf{r})]N_S)} / \text{tr}_S(e^{-\beta(H_S - [\langle\phi\rangle_w + \mu_\alpha(\mathbf{r})]N_S)})$$

which is a stationary state of the local dissipation superoperator $\hat{\mathcal{D}}_\alpha(u(\mathbf{r}))\rho_\alpha^*(u(\mathbf{r})) \equiv 0$, it is possible to give a “local version” of Spohn’s inequality:

$$\text{tr}_S([\log(\rho_\alpha^*(u(\mathbf{r}))) - \log(\rho_S)]\hat{\mathcal{D}}_\alpha(u(\mathbf{r}))\rho_S) \geq 0.$$

As a result, the non-negativity of the entropy production rate of the hybrid system with the modifications introduced in this section follows from

$$\begin{aligned} 0 \leq \dot{\mathcal{S}}_{\text{tot}} &= \frac{1}{T} \int_\Omega d^3r (\mu_c - \mu_v) R + \frac{1}{qT} \int_\Omega d^3r (\mathbf{j}_n \cdot \nabla \mu_c + \mathbf{j}_p \cdot \nabla \mu_v) \\ &\quad + k_B \sum_{\alpha \in \{0, e, h\}} \int_\Omega d^3r w(\mathbf{r}) \text{tr}_S([\log(\rho_\alpha^*(u(\mathbf{r}))) - \log(\rho_S)]\hat{\mathcal{D}}_\alpha(u(\mathbf{r}))\rho_S). \end{aligned}$$

¹ If the entirely local relation $\gamma_\alpha(-\omega, -\ell, u(\mathbf{r})) = e^{-\beta(\hbar\omega - [q\phi(\mathbf{r}) + \mu_\alpha(\mathbf{r})]\ell)}\gamma_\alpha(\omega, \ell, u(\mathbf{r}))$ with $u(\mathbf{r}) = (\mu_c(\mathbf{r}), \mu_v(\mathbf{r}), \phi(\mathbf{r}))$ was used, the consistency with the thermod. equilibrium is violated. One obtains

$$\begin{aligned} \int_\Omega d^3r w(\mathbf{r}) \hat{\mathcal{D}}(u_{\text{eq}}(\mathbf{r}))\rho_S^{\text{eq}} &\approx \frac{1}{2}\beta^2 q^2 \sum_\alpha \sum_\ell \sum_{\omega>0} \gamma_\alpha(\omega, \ell, \langle u_{\text{eq}} \rangle_w) \ell^2 \underbrace{(\langle\phi_{\text{eq}}\rangle_w^2 - \langle\phi_{\text{eq}}^2\rangle_w)}_{\neq 0} \times \\ &\quad \times (A_\alpha(\omega, \ell)\rho_S^{\text{eq}}A_\alpha^\dagger(\omega, \ell) - e^{-\beta(\hbar\omega - [q\langle\phi_{\text{eq}}\rangle_w + \mu_{\text{eq}}]\ell)}A_\alpha^\dagger(\omega, \ell)\rho_S^{\text{eq}}A_\alpha(\omega, \ell)). \end{aligned}$$

A.6 Wave functions and energy levels of lens shape InGaAs quantum dots

The one-particle wave functions and energy levels of carriers confined to lens shape InAs QDs are well approximated by a two-dimensional harmonic oscillator potential for the in-plane confinement combined with a finite well potential in growth direction [325]. This approximation allows for an analytical solution of the single-particle problem and enables a low-cost approximation of the Coulomb matrix elements. The single particle energy levels and Coulomb matrix elements are used in Chap. 5 to describe the many-body energy spectrum of the QD. The harmonic/step-like confinement potential is frequently used for the computation of scattering rates [54, 203, 226, 322], which is however beyond the scope of this work.

Single-particle states

The Schrödinger equation for the confined electrons and holes reads

$$\left[-\frac{\hbar^2}{2} \nabla \cdot \frac{1}{m_\lambda^*(z)} \nabla + U_\lambda(\mathbf{r}) \right] \psi_{\lambda, n_x, n_y}(\mathbf{r}) = E_{\lambda, n_x, n_y} \psi_{\lambda, n_x, n_y}(\mathbf{r}),$$

where $\lambda \in \{c, v\}$ is the band index, $m_c^* > 0$, $m_v^* = -m_h^* < 0$ are the effective masses and

$$U_\lambda(\mathbf{r}) = E_\lambda + \frac{1}{2} m_{\lambda, \text{QD}}^* \omega_\lambda^2 (x^2 + y^2) + z_\lambda U_\lambda^0 \Theta\left(\frac{L}{2} - |z|\right)$$

is the single-particle confinement potential with the harmonic oscillator frequency ω_λ , the continuum band edge E_λ and the potential steps $U_c^0, U_v^0 > 0$, the height L of the QD and the signs $z_c = -1$, $z_v = +1$. The Heaviside step function is denoted by Θ . The effective masses have a discontinuity in z -direction $m_\lambda^*(z) = m_{\lambda, \text{QD}}^* \Theta\left(\frac{L}{2} - |z|\right) + m_{\lambda, \text{bulk}}^* \Theta\left(|z| - \frac{L}{2}\right)$. Even though the problem has a axisymmetric potential, it is easier to solve it in cartesian coordinates². Using the separation ansatz

$$\psi_{\lambda, n_x, n_y}(x, y, z) = \varphi_{\lambda, n_x}(x) \varphi_{\lambda, n_y}(y) \chi_\lambda(z)$$

and $E_{\lambda, n, l} = E_{\lambda, n_x}^{(x)} + E_{\lambda, n_y}^{(y)} + E_\lambda^{(z)}$, the problem can be cast in the form

$$\begin{aligned} \left[-\frac{\hbar^2}{2m_\lambda^*} \frac{\partial^2}{\partial x^2} + \frac{1}{2} m_{\lambda, \text{QD}}^* \omega_\lambda^2 x^2 \right] \varphi_{\lambda, n_x}(x) &= E_{\lambda, n_x}^{(x)} \varphi_{\lambda, n_x}(x), \\ \left[-\frac{\hbar^2}{2m_\lambda^*} \frac{\partial^2}{\partial y^2} + \frac{1}{2} m_{\lambda, \text{QD}}^* \omega_\lambda^2 y^2 \right] \varphi_{\lambda, n_y}(y) &= E_{\lambda, n_y}^{(y)} \varphi_{\lambda, n_y}(y), \\ \left[-\frac{\hbar^2}{2} \frac{\partial}{\partial z} \frac{1}{m_\lambda^*(z)} \frac{\partial}{\partial z} + E_\lambda + z_\lambda U_\lambda^0 \Theta\left(\frac{L}{2} - |z|\right) \right] \chi_\lambda(z) &= E_\lambda^{(z)} \chi_\lambda(z). \end{aligned}$$

² In cartesian coordinates the solution involves Hermite polynomials, which are easier to handle than the Laguerre polynomials arising in the formulation employing polar coordinates.

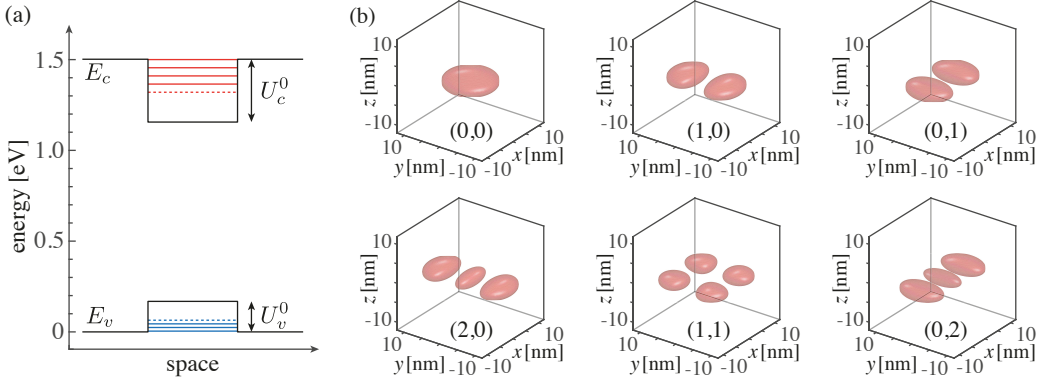


Fig. A.4 (a) Energy eigenvalues for $U_c^0 = 350$ meV, $U_v^0 = 170$ meV, $L = 3$ nm, $\hbar\omega_c = 45.5$ meV, $\hbar\omega_v = 20.3$ meV, $m_{c,\text{QD}}^* = 0.067$ meV and $m_{v,\text{QD}}^* = -0.15$ meV. (b) Iso-surfaces of the energetically lowest QD electron orbitals with $(n_x, n_y) = \{(0, 0), (1, 0), (0, 1), (2, 0), (1, 1), (0, 2)\}$.

The problem is solved by the wave functions

$$\varphi_{\lambda,n}(x) = \sqrt{\frac{\alpha_\lambda}{\pi^{1/2} 2^n n!}} H_n(\alpha_\lambda x) e^{-\frac{1}{2}\alpha_\lambda^2 x^2},$$

$$\chi_\lambda(z) = \begin{cases} \Xi_\lambda \cos\left(\frac{k_\lambda L}{2}\right) e^{\kappa_\lambda(\frac{1}{2}L - |z|)} & \text{for } |z| > \frac{L}{2}, \\ \Xi_\lambda \cos(k_\lambda z) & \text{for } |z| \leq \frac{L}{2} \end{cases}$$

where $\alpha_\lambda = \sqrt{|m_{\lambda,\text{QD}}^*|\omega_\lambda/\hbar}$, $H_n(x)$ is the n -th Hermite polynomial, the wave number k_λ is connected with the decay constant κ_λ via the transcendental equation $\kappa_\lambda = k_\lambda \tan\left(\frac{k_\lambda L}{2}\right)$ and $\Xi_\lambda = \left(\frac{1}{\kappa_\lambda} \cos^2\left(\frac{k_\lambda L}{2}\right) + \frac{L}{2} \left(1 + \frac{\sin(k_\lambda L)}{k_\lambda L}\right)\right)^{-1/2}$ serves for normalization. Here, only the energetically lowest state of the problem in z -direction is taken into account. The single-particle energy reads

$$E_{\lambda,n_x,n_y} = E_\lambda + z_\lambda U_\lambda^0 + \frac{\hbar^2 k_\lambda^2}{2m_{\lambda,\text{QD}}^*} - z_\lambda \hbar\omega_\lambda (n_x + n_y + 1).$$

Coulomb matrix elements

The (unscreened) Coulomb matrix elements are given as [130]

$$V_{i,j,k,l}^{\lambda,\lambda'} = \frac{q^2}{4\pi\epsilon_0\epsilon_b} \int_{\mathbb{R}^3} d^3r \int_{\mathbb{R}^3} d^3r' \frac{\psi_{\lambda,i}^*(\mathbf{r}) \psi_{\lambda',j}^*(\mathbf{r}') \psi_{\lambda',k}(\mathbf{r}') \psi_{\lambda,l}(\mathbf{r})}{\|\mathbf{r} - \mathbf{r}'\|} \quad (\text{A.7})$$

where $i = (n_x^{(i)}, n_y^{(i)})$ is a multi-index and ϵ_b is a background dielectric constant [226]. With the Fourier representation

$$\frac{1}{\|\mathbf{r} - \mathbf{r}'\|} = 4\pi \int_{\mathbb{R}^3} \frac{d^3Q}{(2\pi)^3} \frac{e^{-i\mathbf{Q}\cdot(\mathbf{r}-\mathbf{r}')}}{\|\mathbf{Q}\|^2}$$

and the Schwinger parametrization $\|\mathbf{Q}\|^{-2} = \int_0^\infty du e^{-\|\mathbf{Q}\|^2 u}$, the integral takes the form

$$V_{i,j,k,l}^{\lambda,\lambda'} = \frac{q^2}{\varepsilon_0 \varepsilon_b} \int_0^\infty du \int_{\mathbb{R}^3} \frac{d^3 Q}{(2\pi)^3} e^{-\|\mathbf{Q}\|^2 u} W_{i,l}^\lambda(-\mathbf{Q}) W_{j,k}^{\lambda'}(\mathbf{Q})$$

where

$$W_{i,j}^\lambda(\mathbf{Q}) = \int_{\mathbb{R}^3} d^3 r e^{i\mathbf{Q}\cdot\mathbf{r}} \psi_{\lambda,i}^*(\mathbf{r}) \psi_{\lambda,j}(\mathbf{r}) = w_{n_x^{(i)}, n_x^{(j)}}^\lambda(Q_x) w_{n_y^{(i)}, n_y^{(j)}}^\lambda(Q_y) \bar{w}^\lambda(Q_z)$$

and

$$w_{n_i, n_j}^\lambda(Q) = \frac{\alpha_\lambda}{\sqrt{2^{n_i+n_j} \pi n_i! n_j!}} \int_{\mathbb{R}} d\xi e^{iQ\xi - \alpha_\lambda^2 \xi^2} H_{n_i}(\alpha_\lambda \xi) H_{n_j}(\alpha_\lambda \xi),$$

$$\bar{w}^\lambda(Q_z) = \int_{\mathbb{R}} dz e^{iQ_z z} |\chi_\lambda(z)|^2.$$

Introducing

$$I_{n_i, n_j, n_k, n_l}^{\lambda, \lambda'}(u) = \int_{\mathbb{R}} \frac{dQ}{2\pi} e^{-Q^2 u} w_{n_i, n_l}^\lambda(-Q) w_{n_j, n_k}^\lambda(Q),$$

$$\bar{I}^{\lambda, \lambda'}(u) = \int_{\mathbb{R}} \frac{dQ_z}{2\pi} e^{-Q_z^2 u} \bar{w}^\lambda(-Q_z) \bar{w}^{\lambda'}(Q_z),$$

one arrives at the one-dimensional integral

$$V_{i,j,k,l}^{\lambda,\lambda'} = \frac{q^2}{\varepsilon_0 \varepsilon_b} \int_0^\infty du I_{n_x^{(i)}, n_x^{(j)}, n_x^{(k)}, n_x^{(l)}}^{\lambda, \lambda'}(u) I_{n_y^{(i)}, n_y^{(j)}, n_y^{(k)}, n_y^{(l)}}^{\lambda, \lambda'}(u) \bar{I}^{\lambda, \lambda'}(u). \quad (\text{A.8})$$

With the orthonormality of Hermite polynomials $\int_{\mathbb{R}} dt e^{-t^2} H_k(t) H_l(t) = \delta_{k,l} \sqrt{\pi} 2^k k!$, their binomial type identity [1] and an integral representation of the confluent hypergeometric function [1], one obtains the lowest order integrands as

$$I_{0,0,0,0}^{\lambda, \lambda'}(u) = \frac{1}{\sqrt{\pi}} \frac{1}{\sqrt{4u + \alpha_\lambda^{-2} + \alpha_{\lambda'}^{-2}}},$$

$$I_{1,0,0,0}^{\lambda, \lambda'}(u) = I_{0,1,0,0}^{\lambda, \lambda'}(u) = I_{0,0,1,0}^{\lambda, \lambda'}(u) = I_{0,0,0,1}^{\lambda, \lambda'}(u) = 0,$$

$$I_{1,1,0,0}^{\lambda, \lambda'}(u) = I_{1,0,1,0}^{\lambda, \lambda'}(u) = I_{0,1,0,1}^{\lambda, \lambda'}(u) = I_{0,0,1,1}^{\lambda, \lambda'}(u) = \frac{1}{\sqrt{\pi}} \frac{1}{\alpha_\lambda \alpha_{\lambda'}} \frac{1}{(4u + \alpha_\lambda^{-2} + \alpha_{\lambda'}^{-2})^{3/2}},$$

$$I_{1,0,0,1}^{\lambda, \lambda'}(u) = \frac{1}{\sqrt{\pi}} \frac{4u + \alpha_{\lambda'}^{-2}}{(4u + \alpha_\lambda^{-2} + \alpha_{\lambda'}^{-2})^{3/2}},$$

$$I_{0,1,1,0}^{\lambda, \lambda'}(u) = \frac{1}{\sqrt{\pi}} \frac{4u + \alpha_\lambda^{-2}}{(4u + \alpha_\lambda^{-2} + \alpha_{\lambda'}^{-2})^{3/2}},$$

$$I_{1,1,1,0}^{\lambda, \lambda'}(u) = I_{1,1,0,1}^{\lambda, \lambda'}(u) = I_{1,0,1,1}^{\lambda, \lambda'}(u) = I_{0,1,1,1}^{\lambda, \lambda'}(u) = 0,$$

$$I_{1,1,1,1}^{\lambda, \lambda'}(u) = \frac{1}{\sqrt{\pi}} \frac{3\alpha_\lambda^{-2} \alpha_{\lambda'}^{-2} + 4u(4u + \alpha_\lambda^{-2} + \alpha_{\lambda'}^{-2})}{(4u + \alpha_\lambda^{-2} + \alpha_{\lambda'}^{-2})^{5/2}}.$$

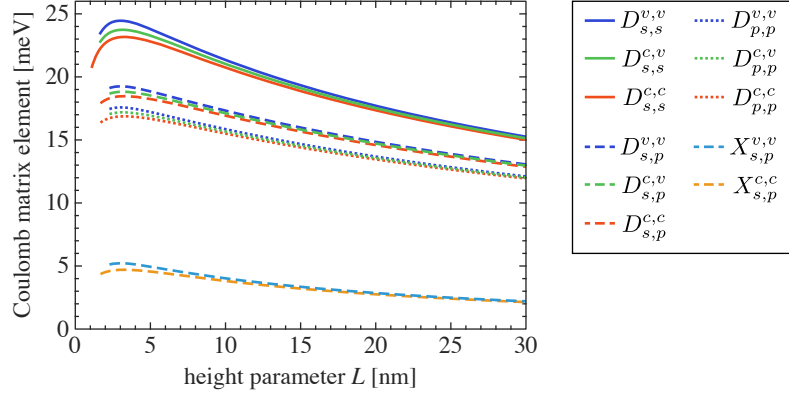


Fig. A.5 Plot of the dominant Coulomb matrix elements vs. the height parameter L of the QD. The direct (Hartree) matrix elements are $D_{i,j}^{\lambda,\lambda'} = V_{i,j,j,i}^{\lambda,\lambda'}$ and exchange (Fock) matrix elements are denoted as $X_{i,j \neq i}^{\lambda,\lambda} = V_{i,j,i,j}^{\lambda,\lambda}$. Here, short notations $s = (n_x = 0, n_y = 0)$, $p = (n_x = 1, n_y = 0)$ and symmetry properties of the integral (A.7) are used. For large QDs the Coulomb interaction strength generally decreases. For very small QDs some of the matrix elements do not exist since the corresponding bound states are not existent. The background dielectric constant is set to $\varepsilon_b = 12.5$, the remaining parameters are given in the caption of Fig. A.4.

The integrand corresponding to the confinement in growth direction can be approximated by a saddle-point method as

$$\bar{I}^{\lambda,\lambda'}(u) = \int_{\mathbb{R}} \frac{dQ_z}{2\pi} e^{-Q_z^2 u + \log(f_{\lambda,\lambda'}(Q_z))} \approx \frac{f_{\lambda,\lambda'}(0)}{\sqrt{2\pi(2u - a_{\lambda,\lambda'})}} \sqrt{\frac{2}{\pi}} X_{\lambda,\lambda'} e^{X_{\lambda,\lambda'}} K_{-\frac{1}{4}}(X_{\lambda,\lambda'}),$$

where $f_{\lambda,\lambda'}(Q_z) = \bar{w}^\lambda(-Q_z) \bar{w}^{\lambda'}(Q_z)$, $a_{\lambda,\lambda'} = f_{\lambda,\lambda'}''(0) / f_{\lambda,\lambda'}(0)$, $b_{\lambda,\lambda'} = f_{\lambda,\lambda'}^{(4)}(0) / f_{\lambda,\lambda'}(0)$, $X_{\lambda,\lambda'} = \frac{3}{4}(2u - a_{\lambda,\lambda'})^2 / (3a_{\lambda,\lambda'}^2 + b_{\lambda,\lambda'})$ and K_ν is the modified Bessel function of second kind [1]. For numerical evaluation, it is beneficial to transform the integral (A.8) on a finite interval by, e.g., the substitution $u = u_0 \cot^2(\frac{\theta}{2})$ (the parameter u_0 is free and can be used for improved conditioning of the integral). The leading order Coulomb matrix elements are shown in Fig. A.5.

Bibliography

- [1] M. Abramowitz and I. A. Stegun, *Handbook of mathematical functions with formulas, graphs, and mathematical tables* (Dover Publications, New York, 1964).
- [2] A. Akturk, J. Allnutt, Z. Dilli, N. Goldsman, and M. Peckerar, “Device modeling at cryogenic temperatures: Effects of incomplete ionization,” *IEEE Trans. Electron Devices* **54**, 2984–2990 (2007).
- [3] G. Albinus, “Thermodynamics of energy models of semiconductor devices,” *J. Appl. Math. Mech. (ICIAM/GAMM 95)* **76**, 289–292 (1996).
- [4] G. Albinus, H. Gajewski, and R. Hünlich, “Thermodynamic design of energy models of semiconductor devices,” *Nonlinearity* **15**, 367–383 (2002).
- [5] R. Alicki, “On the detailed balance condition for non-Hamiltonian systems,” *Rep. Math. Phys.* **10**, 249–258 (1976).
- [6] R. Alicki, “The Markov master equations and the Fermi golden rule,” *Int. J. Theor. Phys.* **16**, 351–355 (1977).
- [7] A. Aspuru-Guzik and P. Walther, “Photonic quantum simulators,” *Nat. Phys.* **8**, 285 (2012).
- [8] M. Auf der Maur, M. Povolotskiy, F. Sacconi, A. Pecchia, G. Romano, G. Penazzi, and A. Di Carlo, “TiberCAD: Towards multiscale simulation of optoelectronic devices,” *Proc. Int. Conf. Numerical Simulation of Optoelectronic Devices*, 43–44 (2008).
- [9] M. Auf der Maur, T. Albes, and A. Gagliardi, “Thin-film solar cells,” in *Handbook of Optoelectronic Device Modeling and Simulation: Lasers, Modulators, Photodetectors, Solar Cells, and Numerical Methods*, Vol. 2, edited by J. Piprek (CRC Press, Taylor & Francis Group, Boca Raton, 2017) Chap. 43, pp. 497–538.
- [10] X. Aymerich-Humet, F. Serra-Mestres, and J. Millan, “An analytical approximation for the Fermi–Dirac integral $F_{3/2}(\eta)$,” *Solid-State Electron.* **24**, 981–982 (1981).
- [11] N. Baer, P. Gartner, and F. Jahnke, “Coulomb effects in semiconductor quantum dots,” *Eur. Phys. J. B* **42**, 231–237 (2004).
- [12] N. Baer, C. Gies, J. Wiersig, and F. Jahnke, “Luminescence of a semiconductor quantum dot system,” *Eur. Phys. J. B* **50**, 411–418 (2006).
- [13] U. Bandelow, H. Gajewski, and R. Hünlich, “Fabry–Perot lasers: Thermodynamics-based modeling,” in *Optoelectronic devices*, edited by J. Piprek (Springer, New York, 2005) Chap. 3, pp. 63–85.
- [14] U. Bandelow, R. Hünlich, and T. Koprucki, “Simulation of static and dynamic properties of edge-emitting multiple-quantum-well lasers,” *IEEE J. Sel. Top. Quant.* **9**, 798–806 (2003).
- [15] R. E. Bank, W. M. Coughran Jr., and L. C. Cowsar, “The finite volume Scharfetter–Gummel method for steady convection diffusion equations,” *Comput. Visual. Sci.* **1**, 123–136 (1998).
- [16] W. L. Barnes, G. Björk, J. M. Gérard, P. Jonsson, J. A. E. Wasey, P. T. Worthing, and V. Zwiller, “Solid-state single photon sources: Light collection strategies,” *Eur. Phys. J. D* **18**, 197–210 (2002).
- [17] M. Baro, H. Neidhardt, and J. Rehberg, “Current coupling of drift-diffusion models and Schrödinger–Poisson systems: Dissipative hybrid models,” *SIAM J. Math. Anal.* **37**, 941–981 (2005).

- [18] T. Basché, W. E. Moerner, M. Orrit, and H. Talon, “Photon antibunching in the fluorescence of a single dye molecule trapped in a solid,” *Phys. Rev. Lett.* **69**, 1516 (1992).
- [19] M. Bayer, G. Ortner, O. Stern, A. Kuther, A. A. Gorbunov, A. Forchel, P. Hawrylak, S. Fafard, K. Hinzer, T. L. Reinecke, S. N. Walck, J. P. Reithmaier, F. Klopff, and F. Schäfer, “Fine structure of neutral and charged excitons in self-assembled In(Ga)As/(Al)GaAs quantum dots,” *Phys. Rev. B* **65**, 195315 (2002).
- [20] A. R. Beattie and P. T. Landsberg, “Auger effect in semiconductors,” *P. Roy. Soc. Lond. A. Mat.* **249**, 16–29 (1959).
- [21] A. Beckers, F. Jazaeri, and C. Enz, “Characterization and modeling of 28 nm bulk CMOS technology down to 4.2 K,” *IEEE J. Electron Devices Soc.*, (Early access), 1–1 (2018).
- [22] D. Bednarczyk and J. Bednarczyk, “The approximation of the Fermi–Dirac integral $F_{1/2}(\eta)$,” *Phys. Lett. A* **64**, 409–410 (1978).
- [23] H. Benisty, “Reduced electron-phonon relaxation rates in quantum-box systems: Theoretical analysis,” *Phys. Rev. B* **51**, 13281 (1995).
- [24] H. Benisty, C. M. Sotomayor-Torres, and C. Weisbuch, “Intrinsic mechanism for the poor luminescence properties of quantum-box systems,” *Phys. Rev. B* **44**, 10945 (1991).
- [25] A. J. Bennett, P. Atkinson, P. See, M. B. Ward, R. M. Stevenson, Z. L. Yuan, D. C. Unitt, D. J. P. Ellis, K. Cooper, D. A. Ritchie, and A. J. Shields, “Single-photon-emitting diodes: A review,” *Phys. Status Solidi B* **243**, 3730–3740 (2006).
- [26] A. J. Bennett, R. B. Patel, A. J. Shields, K. Cooper, P. Atkinson, C. A. Nicoll, and D. A. Ritchie, “Indistinguishable photons from a diode,” *Appl. Phys. Lett.* **92**, 193503 (2008).
- [27] M. Bessemoulin-Chatard, “A finite volume scheme for convection-diffusion equations with nonlinear diffusion derived from the Scharfetter–Gummel scheme,” *Numer. Math.* **121**, 637–670 (2012).
- [28] P. Bhattacharya and Z. Mi, “Quantum-dot optoelectronic devices,” *Proc. IEEE* **95**, 1723–1740 (2007).
- [29] D. Bimberg, M. Grundmann, and N. N. Ledentsov, *Quantum dot heterostructures* (John Wiley & Sons, Chichester, 1999).
- [30] D. Bimberg and U. W. Pohl, “Quantum dots: Promises and accomplishments,” *Mater. Today* **14**, 388–397 (2011).
- [31] D. Bimberg, E. Stock, A. Lochmann, A. Schliwa, J. A. Toffinger, W. Unrau, M. Munnix, S. Rodt, V. A. Haisler, A. I. Toropov, A. Bakarov, and A. K. Kalagin, “Quantum dots for single- and entangled-photon emitters,” *IEEE Photon. J.* **1**, 58–68 (2009).
- [32] J. S. Blakemore, “Approximations for Fermi–Dirac integrals, especially the function $F_{1/2}(\eta)$ used to describe electron density in a semiconductor,” *Solid-State Electron.* **25**, 1067–1076 (1982).
- [33] U. Bockelmann and G. Bastard, “Phonon scattering and energy relaxation in two-, one-, and zero-dimensional electron gases,” *Phys. Rev. B* **42**, 8947 (1990).
- [34] U. Bockelmann and T. Egeler, “Electron relaxation in quantum dots by means of Auger processes,” *Phys. Rev. B* **46**, 15574 (1992).
- [35] C. Böckler, S. Reitzenstein, C. Kistner, R. Debusmann, A. Löffler, T. Kida, S. Höfling, A. Forchel, L. Grenouillet, J. Claudon, and J.-M. Gérard, “Electrically driven high-Q quantum dot-micropillar cavities,” *Appl. Phys. Lett.* **92**, 091107 (2008).

-
- [36] F. Bonani and G. Ghione, *Noise in semiconductor devices – Modeling and simulation*, Advanced Microelectronics 7 (Springer, Berlin, Heidelberg, 2001).
- [37] A. Boretti, L. Rosa, A. Mackie, and S. Castelletto, “Electrically driven quantum light sources,” *Adv. Opt. Mat.* **3**, 1012–1033 (2015).
- [38] M. Brasken, M. Lindberg, M. Sopanen, H. Lipsanen, and J. Tulkki, “Temperature dependence of carrier relaxation in strain-induced quantum dots,” *Phys. Rev. B* **58**, R15993 (1998).
- [39] H.-P. Breuer and F. Petruccione, *The theory of open quantum systems* (Oxford University Press, Oxford, 2002).
- [40] F. Brezzi, L. D. Marini, and P. Pietra, “Numerical simulation of semiconductor devices,” *Comput. Methods Appl. Mech. Eng.* **75**, 493–514 (1989).
- [41] S. Buckley, K. Rivoire, and J. Vučković, “Engineered quantum dot single-photon sources,” *Rep. Prog. Phys.* **75**, 126503 (2012).
- [42] G. Bulnes Cuetara, M. Esposito, and G. Schaller, “Quantum thermodynamics with degenerate eigenstate coherences,” *Entropy* **18**, 447 (2016).
- [43] A. Carmele, F. Milde, M.-R. Dachner, M. B. Harouni, R. Roknizadeh, M. Richter, and A. Knorr, “Formation dynamics of an entangled photon pair: A temperature-dependent analysis,” *Phys. Rev. B* **81**, 195319 (2010).
- [44] H. J. Carmichael, *An open systems approach to quantum optics*, Vol. 18, Lecture Notes in Physics (Springer, Berlin, Heidelberg, 1993).
- [45] H. J. Carmichael, *Statistical methods in quantum optics 1 – Master equations and Fokker–Planck equations* (Springer, Berlin, Heidelberg, 1999).
- [46] T. Y. Chang and A. Izabelle, “Full range analytic approximations for Fermi energy and Fermi–Dirac integral $F_{-1/2}$ in terms of $F_{1/2}$,” *J. Appl. Phys.* **65**, 2162–2164 (1989).
- [47] J. R. Chelikowsky and M. L. Cohen, “Nonlocal pseudopotential calculations for the electronic structure of eleven diamond and zinc-blende semiconductors,” *Phys. Rev. B* **14**, 556–582 (1976).
- [48] W. W. Chow and F. Jahnke, “On the physics of semiconductor quantum dots for applications in lasers and quantum optics,” *Prog. Quantum Electron.* **37**, 109–184 (2013).
- [49] W. W. Chow, F. Jahnke, and C. Gies, “Emission properties of nanolasers during the transition to lasing,” *Light-Sci. Appl.* **3**, e201 (2014).
- [50] W. W. Chow, S. W. Koch, and M. Sargent III, *Semiconductor-laser physics* (Springer, Berlin, Heidelberg, 1994).
- [51] S. L. Chuang, *Physics of photonic devices*, 2nd ed. (Wiley, Hoboken, 2009).
- [52] W. J. Cody and H. C. Thacher Jr., “Rational Chebyshev approximations for Fermi–Dirac integrals of orders $-1/2$, $1/2$ and $3/2$,” *Math. Comput.* **21**, 30–40 (1967).
- [53] J. D. Cressler and H. A. Mantooth, eds., *Extreme environment electronics* (CRC Press, Taylor & Francis Group, Boca Raton, 2012).
- [54] M.-R. Dachner, E. Malić, M. Richter, A. Carmele, J. Kabuss, A. Wilms, J.-E. Kim, G. Hartmann, J. Wolters, U. Bandelow, and A. Knorr, “Theory of carrier and photon dynamics in quantum dot light emitters,” *Phys. Status Solidi B* **247**, 809–828 (2010).
- [55] T. A. Davis, “Algorithm 832: UMFPACK v4.3 – An unsymmetric-pattern multifrontal method,” *ACM T. Math. Software* **30**, 196–199 (2004).
- [56] P. Dawson, O. Rubel, S. D. Baranovskii, K. Pierz, P. Thomas, and E. O. Göbel, “Temperature dependent optical properties of InAs/GaAs quantum dots: Independent carrier versus exciton relaxation,” *Phys. Rev. B* **72**, 235301 (2005).

- [57] P. P. Debye and E. M. Conwell, “Electrical properties of n-type germanium,” *Phys. Rev.* **93**, 693 (1954).
- [58] P. Deuffhard, *Newton methods for nonlinear problems: Affine invariance and adaptive algorithms*, Vol. 35, Springer Series in Computational Mathematics (Springer, Berlin, Heidelberg, 2004).
- [59] D. H. Doan, P. Farrell, J. Fuhrmann, M. Kantner, T. Koprucki, and N. Rotundo, *ddf Fermi – A drift-diffusion simulation tool*, 2016.
- [60] J. P. Dowling and G. J. Milburn, “Quantum technology: The second quantum revolution,” *Philos. T. Roy. Soc. A.* **361**, 1655–1674 (2003).
- [61] R. Dümcke and H. Spohn, “The proper form of the generator in the weak coupling limit,” *Z. Phys. B. Con. Mat.* **34**, 419–422 (1979).
- [62] A. P. Engelhardt, J. S. Kolb, F. Roemer, U. Weichmann, H. Moench, and B. Witzigmann, “Temperature-dependent investigation of carrier transport, injection, and densities in AlGaAs-based multi-quantum-well active layers for vertical-cavity surface-emitting lasers,” *Opt. Eng.* **54**, 016107–016107 (2015).
- [63] W. L. Engl, H. K. Dirks, and B. Meinerzhagen, “Device modeling,” *Proc. IEEE* **71**, 10–33 (1983).
- [64] D. Englund, D. Fattal, E. Waks, G. Solomon, B. Zhang, T. Nakaoka, Y. Arakawa, Y. Yamamoto, and J. Vučković, “Controlling the spontaneous emission rate of single quantum dots in a two-dimensional photonic crystal,” *Phys. Rev. Lett.* **95**, 013904 (2005).
- [65] R. Eymard, J. Fuhrmann, and K. Gärtner, “A finite volume scheme for nonlinear parabolic equations derived from one-dimensional local Dirichlet problems,” *Numer. Math.* **102**, 463–495 (2006).
- [66] R. Eymard, T. Gallouët, and R. Herbin, “Finite volume methods,” in *Handbook of numerical analysis*, Vol. 7, edited by P. Ciarlet and J. Lions, Handbook of Numerical Analysis (Elsevier, 2000), pp. 713–1018.
- [67] P. Farrell, T. Koprucki, and J. Fuhrmann, “Computational and analytical comparison of flux discretizations for the semiconductor device equations beyond Boltzmann statistics,” *J. Comput. Phys.* **346**, 497–513 (2017).
- [68] P. Farrell, M. Patriarca, J. Fuhrmann, and T. Koprucki, “Comparison of thermodynamically consistent charge carrier flux discretizations for Fermi–Dirac and Gauss–Fermi statistics,” *Opt. Quant. Electron.* **50**, 101 (2018).
- [69] P. Farrell, N. Rotundo, D. H. Doan, M. Kantner, J. Fuhrmann, and T. Koprucki, “Drift-diffusion models,” in *Handbook of Optoelectronic Device Modeling and Simulation: Lasers, Modulators, Photodetectors, Solar Cells, and Numerical Methods*, Vol. 2, edited by J. Piprek (CRC Press, Taylor & Francis Group, Boca Raton, 2017) Chap. 50, pp. 733–771.
- [70] A. Ferreira da Silva, I. Pepe, B. E. Sernelius, C. Persson, R. Ahuja, J. de Souza, Y. Suzuki, and Y. Yang, “Electrical resistivity of acceptor carbon in GaAs,” *J. Appl. Phys.* **95**, 2532–2535 (2004).
- [71] R. Ferreira and G. Bastard, “Phonon-assisted capture and intradot Auger relaxation in quantum dots,” *Appl. Phys. Lett.* **74**, 2818 (1999).
- [72] R. Ferreira and G. Bastard, “Carrier capture and intra-dot Auger relaxation in quantum dots,” *Physica E* **7**, 342–345 (2000).
- [73] R. Ferreira and G. Bastard, *Capture and relaxation in self-assembled semiconductor quantum dots*, 2053–2571 (Morgan & Claypool Publishers, San Rafael, CA, 2015).
- [74] S. Fischbach, A. Schlehahn, A. Thoma, N. Srocka, T. Gissibl, S. Ristok, S. Thiele, A. Kaganskiy, A. Strittmatter, T. Heindel, S. Rodt, A. Herkommer, H. Giessen, and

-
- S. Reitzenstein, “Single quantum dot with microlens and 3d-printed micro-objective as integrated bright single-photon source,” *ACS Photonics* **4**, 1327–1332 (2017).
- [75] M. Florian, C. Gies, P. Gartner, and F. Jahnke, “Improved antibunching by using high-excitation pulses from a single semiconductor quantum dot – A theoretical study,” *J. Opt. Soc. Am. B* **29**, A31 (2012).
- [76] M. Fox, *Quantum optics – An introduction*, Vol. 15, Oxford Master Series in Physics (Oxford University Press, Oxford, 2006).
- [77] J. Fuhrmann, “Comparison and numerical treatment of generalised Nernst–Planck models,” *Comput. Phys. Commun.* **196**, 166–178 (2015).
- [78] H. Gajewski, “On existence, uniqueness and asymptotic behavior of solutions of the basic equations for carrier transport in semiconductors,” *J. Appl. Math. Mech.* **65**, 101–108 (1985).
- [79] H. Gajewski and K. Gärtner, “On the iterative solution of van Roosbroeck’s equations,” *J. Appl. Math. Mech.* **72**, 19–28 (1992).
- [80] H. Gajewski, “Analysis und Numerik von Ladungstransport in Halbleitern,” WIAS Rep. No. 6 (1993).
- [81] H. Gajewski and K. Gärtner, “On the discretization of van Roosbroeck’s equations with magnetic field,” *J. Appl. Math. Mech.* **76**, 247–264 (1996).
- [82] H. Gajewski and K. Gröger, “On the basic equations for carrier transport in semiconductors,” *J. Math. Anal. Appl.* **113**, 12–35 (1986).
- [83] H. Gajewski, M. Liero, R. Nürnberg, and H. Stephan, “WIAS-TeSCA – Two-dimensional semi-conductor analysis package,” WIAS Tech. Rep. No. 14 (2016).
- [84] K. Gärtner, “Existence of bounded discrete steady state solutions of the van Roosbroeck system with monotone Fermi–Dirac statistic functions,” *J. Comput. Electron.* **14**, 773–787 (2015).
- [85] K. Gärtner, “DEPFET sensors, a test case to study 3D effects,” *J. Comput. Electron.* **6**, 275–278 (2007).
- [86] K. Gärtner, “Existence of bounded discrete steady-state solutions of the van Roosbroeck system on boundary conforming Delaunay grids,” *SIAM J. Sci. Comput.* **31**, 1347–1362 (2009).
- [87] F. Gebhard, *The Mott metal-insulator transition*, Vol. 137, Springer Tracts in Modern Physics (Springer, Berlin, Heidelberg, 1997).
- [88] M. Gegg and M. Richter, “Efficient and exact numerical approach for many multi-level systems in open system CQED,” *New J. Phys.* **18**, 043037 (2016).
- [89] J. Gemmer, M. Michel, and G. Mahler, *Quantum thermodynamics*, Vol. 657, Lecture Notes in Physics (Springer, Berlin, Heidelberg, 2004).
- [90] *Genius semiconductor device simulator: Reference manual*, Version 1.9.0, Cogenda Pte Ltd. (2017).
- [91] S. Gerhardt, J. Iles-Smith, D. P. S. McCutcheon, Y.-M. He, S. Unsleber, S. Betzold, N. Gregersen, J. Mørk, S. Höfling, and C. Schneider, “Intrinsic and environmental effects on the interference properties of a high-performance quantum dot single-photon source,” *Phys. Rev. B* **97**, 195432, 195432 (2018).
- [92] C. Gies, M. Florian, F. Jahnke, and P. Gartner, “Modeling single quantum dots in microcavities,” in *Quantum optics with semiconductor nanostructures*, Vol. 28, edited by F. Jahnke, Series in Electronic and Optical Materials (Woodhead Publishing, Oxford, 2012) Chap. 3, pp. 78–114.
- [93] C. Gies, M. Florian, P. Gartner, and F. Jahnke, “The single quantum dot-laser: Lasing and strong coupling in the high-excitation regime,” *Opt. Express* **19**, 14370–14388 (2011).

- [94] C. Gies, M. Florian, A. Steinhoff, and F. Jahnke, “Theory of quantum light sources and cavity-QED emitters based on semiconductor quantum dots,” in *Quantum dots for quantum information technologies*, edited by P. Michler, Springer Series in Nano-Optics and Nanophotonics (Springer, Cham, 2017) Chap. 1, pp. 3–40.
- [95] C. Gies, F. Gericke, P. Gartner, S. Holzinger, C. Hopfmann, T. Heindel, J. Wolters, C. Schneider, M. Florian, F. Jahnke, S. Höfling, M. Kamp, and S. Reitzenstein, “Strong light-matter coupling in the presence of lasing,” *Phys. Rev. A* **96**, 023806 (2017).
- [96] C. Gies, J. Wiersig, M. Lorke, and F. Jahnke, “Semiconductor model for quantum-dot-based microcavity lasers,” *Phys. Rev. A* **75**, 013803 (2007).
- [97] J. R. Gilbert, C. Moler, and R. Schreiber, “Sparse matrices in MATLAB: Design and implementation,” *SIAM J. Matrix Anal. Appl.* **13**, 333–356 (1992).
- [98] M. Gioannini, A. P. Cedola, N. D. Santo, F. Bertazzi, and F. Cappelluti, “Simulation of quantum dot solar cells including carrier intersubband dynamics and transport,” *IEEE J. Photovolt.* **3**, 1271–1278 (2013).
- [99] N. Gisin, G. Ribordy, W. Tittel, and H. Zbinden, “Quantum cryptography,” *Rev. Mod. Phys.* **74**, 145 (2002).
- [100] M. Goano, “Algorithm 745: Computation of the complete and incomplete Fermi–Dirac integral,” *ACM T. Math. Software* **21**, 221–232 (1995).
- [101] J. Gomis-Bresco, S. Dommers, V. V. Temnov, U. Woggon, M. Lämmlin, D. Bimberg, E. Malić, M. Richter, E. Schöll, and A. Knorr, “Impact of Coulomb scattering on the ultrafast gain recovery in InGaAs quantum dots,” *Phys. Rev. Lett.* **101**, 256803 (2008).
- [102] V. Gorini, A. Kossakowski, and E. C. G. Sudarshan, “Completely positive dynamical semigroups of N-level systems,” *J. Math. Phys.* **17**, 821–825 (1976).
- [103] T. Goudon, V. Miljanović, and C. Schmeiser, “On the Shockley–Read–Hall model: Generation-recombination in semiconductors,” *SIAM J. Appl. Math.* **67**, 1183–1201 (2007).
- [104] T. Grasser, T.-W. Tang, H. Kosina, and S. Selberherr, “A review of hydrodynamic and energy-transport models for semiconductor device simulation,” *Proc. IEEE* **91**, 251–274 (2003).
- [105] D. Gready and G. Eisenstein, “Carrier dynamics and modulation capabilities of 1.55- μm quantum-dot lasers,” *IEEE J. Sel. Top. Quant.* **19**, 1900307–1900307 (2013).
- [106] N. Gregersen, D. P. S. McCutcheon, and J. Mørk, “Single-photon sources,” in *Handbook of Optoelectronic Device Modeling and Simulation: Lasers, Modulators, Photodetectors, Solar Cells, and Numerical Methods*, Vol. 2, edited by J. Piprek (CRC Press, Taylor & Francis Group, Boca Raton, 2017) Chap. 46, pp. 585–607.
- [107] M. Grmela and H. C. Öttinger, “Dynamics and thermodynamics of complex fluids. I. Development of a general formalism,” *Phys. Rev. E* **56**, 6620–6632 (1997).
- [108] S. R. de Groot and P. Mazur, *Non-equilibrium thermodynamics* (Dover Publications, New York, 1984).
- [109] M. Grundmann, R. Heitz, D. Bimberg, J. H. H. Sandmann, and J. Feldmann, “Carrier dynamics in quantum dots: Modeling with master equations for the transitions between micro-states,” *Phys. Status Solidi B* **203**, 121–132 (1997).
- [110] M. Grundmann, *Physics of semiconductors – An introduction including nanophysics and applications* (Springer, Berlin, Heidelberg, 2006).
- [111] M. Grupen and K. Hess, “Simulation of carrier transport and nonlinearities in quantum-well laser diodes,” *IEEE J. Quantum Electron.* **34**, 120–140 (1998).

-
- [112] M. Gschrey, A. Thoma, P. Schnauber, M. Seifried, R. Schmidt, B. Wohlfeil, L. Krüger, J.-H. Schulze, T. Heindel, S. Burger, F. Schmidt, A. Strittmatter, S. Rodt, and S. Reitzenstein, “Highly indistinguishable photons from deterministic quantum-dot microlenses utilizing three-dimensional in situ electron-beam lithography,” *Nat. Commun.* **6**, 7662 (2015).
- [113] Q. Gu and Y. Fainman, *Semiconductor nanolasers* (Cambridge University Press, Cambridge, 2017).
- [114] L. J. Guibas, D. E. Knuth, and M. Sharir, “Randomized incremental construction of Delaunay and Voronoi diagrams,” *Algorithmica* **7**, 381–413 (1992).
- [115] H. K. Gummel, “A self-consistent iterative scheme for one-dimensional steady state transistor calculations,” *IEEE Trans. Electron Devices* **11**, 455–465 (1964).
- [116] E. A. Gutiérrez-D., M. J. Deen, and C. L. Claeys, *Low temperature electronics – Physics, devices, circuits, and applications* (Academic Press, San Diego, 2000).
- [117] R. Haag, N. M. Hugenholtz, and M. Winnink, “On the equilibrium states in quantum statistical mechanics,” *Commun. Math. Phys.* **5**, 215–236 (1967).
- [118] W. W. Hager, “Condition estimates,” *SIAM J. Sci. Stat. Comp.* **5**, 311–316 (1984).
- [119] H. Haken, *Quantenfeldtheorie des Festkörpers* (Springer, Wiesbaden, 1993).
- [120] P. van Halen and D. L. Pulfrey, “Accurate, short series approximations to Fermi-Dirac integrals of order- $1/2$, $1/2$, 1 , $3/2$, 2 , $5/2$, 3 , and $7/2$,” *J. Appl. Phys.* **57**, 5271–5274 (1985).
- [121] R. N. Hall, “Germanium rectifier characteristics,” *Phys. Rev.* **83**, 228 (1951).
- [122] R. N. Hall, “Recombination processes in semiconductors,” *Proceedings of the IEE-Part B: Electronic and Communication Engineering* **106**, 923–931 (1959).
- [123] S. Hameau, Y. Guldner, O. Verzelen, R. Ferreira, G. Bastard, J. Zeman, A. Lemaitre, and J. Gérard, “Strong electron-phonon coupling regime in quantum dots: Evidence for everlasting resonant polarons,” *Phys. Rev. Lett.* **83**, 4152 (1999).
- [124] R. Hanbury Brown and R. Q. Twiss, “A test of a new type of stellar interferometer on Sirius,” *Nature* **178**, 1046–1048 (1956).
- [125] W. Hänsch, *The drift diffusion equation and its applications in MOSFET modeling*, Series in Computational Microelectronics (Springer, Vienna, 1991).
- [126] F. Hargart, C. A. Kessler, T. Schwarzbäck, E. Koroknay, S. Weidenfeld, M. Jetter, and P. Michler, “Electrically driven quantum dot single-photon source at 2 GHz excitation repetition rate with ultra-low emission time jitter,” *Appl. Phys. Lett.* **102**, 011126 (2013).
- [127] J. W. Harris and H. Stöcker, *Handbook of mathematics and computational science* (Springer, New York, 1998).
- [128] A. Haug, “Temperature dependence of Auger recombination in gallium antimonide,” *J. Phys. C: Solid State Phys.* **17**, 6191 (1984).
- [129] H. Haug and A.-P. Jauho, *Quantum kinetics in transport and optics of semiconductors*, 2nd ed., Vol. 123, Springer Series in Solid-State Sciences (Springer, Berlin, Heidelberg, 2008).
- [130] H. Haug and S. W. Koch, *Quantum theory of the optical and electronic properties of semiconductors*, 4th ed. (World Scientific, Singapore, 2004).
- [131] P. Hawrylak and M. Korkusiński, “Electronic properties of self-assembled quantum dots,” in *Single quantum dots*, Vol. 90, edited by P. Michler, Topics in Applied Physics (Springer, Berlin, Heidelberg, 2003) Chap. 2, pp. 25–91.
- [132] T. Heindel, C. Schneider, M. Lerner, S. H. Kwon, T. Braun, S. Reitzenstein, S. Höfling, M. Kamp, and A. Forchel, “Electrically driven quantum dot-micropillar single photon source with 34% overall efficiency,” *Appl. Phys. Lett.* **96**, 011107 (2010).

- [133] T. Heindel, C. A. Kessler, M. Rau, C. Schneider, M. Fürst, F. Hargart, W.-M. Schulz, M. Eichfelder, R. Roßbach, S. Nauerth, M. Lermer, H. Weier, M. Jetter, M. Kamp, S. Reitzenstein, S. Höfling, P. Michler, H. Weinfurter, and A. Forchel, “Quantum key distribution using quantum dot single-photon emitting diodes in the red and near infrared spectral range,” *New J. Phys.* **14**, 083001 (2012).
- [134] F. Heinrichsdorff, “MOCVD growth and laser applications of In(Ga)As/GaAs quantum dots,” PhD thesis (Technical University Berlin, 1998).
- [135] K. Hess, *Advanced theory of semiconductor devices*, 2nd ed. (Wiley-IEEE Press, New York, 2000).
- [136] N. J. Higham and F. Tisseur, “A block algorithm for matrix 1-norm estimation, with an application to 1-norm pseudospectra,” *SIAM J. Matrix Anal. Appl.* **21**, 1185–1201 (2000).
- [137] C. Hopfmann, A. Carmele, A. Musiał, C. Schneider, M. Kamp, S. Höfling, A. Knorr, and S. Reitzenstein, “Transition from Jaynes–Cummings to Autler–Townes ladder in a quantum dot–microcavity system,” *Phys. Rev. B* **95**, 035302 (2017).
- [138] W. Hu, “P-n junction photodiodes,” in *Handbook of Optoelectronic Device Modeling and Simulation: Lasers, Modulators, Photodetectors, Solar Cells, and Numerical Methods*, Vol. 2, edited by J. Piprek (CRC Press, Taylor & Francis Group, Boca Raton, 2017) Chap. 36, pp. 307–336.
- [139] G. A. M. Hurkx, D. B. M. Klaassen, and M. P. G. Knuvers, “A new recombination model for device simulation including tunneling,” *IEEE Trans. Electron Devices* **39**, 331–338 (1992).
- [140] M. Imada, A. Fujimori, and Y. Tokura, “Metal-insulator transitions,” *Rev. Mod. Phys.* **70**, 1039 (1998).
- [141] T. Inoshita and H. Sakaki, “Electron-phonon interaction and the so-called phonon bottleneck effect in semiconductor quantum dots,” *Physica B* **227**, 373–377 (1996).
- [142] J. D. Jackson, *Classical electrodynamics* (John Wiley & Sons, New York, 1962).
- [143] C. Jacoboni, *Theory of electron transport in semiconductors* (Springer, Berlin, Heidelberg, 2010).
- [144] F. Jahnke, ed., *Quantum optics with semiconductor nanostructures*, Vol. 28, Series in Electronic and Optical Materials (Woodhead Publishing, Oxford, 2012).
- [145] J. W. Jerome, *Analysis of charge transport: A mathematical study of semiconductor devices* (Springer, Berlin, Heidelberg, 2012).
- [146] R. Jordan, D. Kinderlehrer, and F. Otto, “Free energy and the Fokker–Planck equation,” *Physica D* **107**, 265–271 (1997).
- [147] R. Jordan, D. Kinderlehrer, and F. Otto, “The variational formulation of the Fokker–Planck equation,” *SIAM J. Math. Anal.* **29**, 1–17 (1998).
- [148] W. B. Joyce and R. W. Dixon, “Analytic approximations for the Fermi energy of an ideal Fermi gas,” *Appl. Phys. Lett.* **31**, 354–356 (1977).
- [149] A. Jüngel, “Numerical approximation of a drift-diffusion model for semiconductors with nonlinear diffusion,” *J. Appl. Math. Mech.* **75**, 783–799 (1995).
- [150] A. Jüngel, “On the existence and uniqueness of transient solutions of a degenerate nonlinear drift-diffusion model for semiconductors,” *Math. Models Methods Appl. Sci.* **4**, 677–703 (1994).
- [151] A. Jüngel, “Qualitative behaviour of solutions of a degenerate nonlinear drift-diffusion model for semiconductors,” *Math. Models Methods Appl. Sci.* **5**, 497–518 (1995).
- [152] A. Jüngel, *Transport equations for semiconductors*, Vol. 773, Lecture Notes in Physics (Springer, Berlin, Heidelberg, 2009).

-
- [153] P. Kaer, N. Gregersen, and J. Mørk, “The role of phonon scattering in the indistinguishability of photons emitted from semiconductor cavity QED systems,” *New J. Phys.* **15**, 035027 (2013).
- [154] P. Kaer, T. R. Nielsen, P. Lodahl, A.-P. Jauho, and J. Mørk, “Microscopic theory of phonon-induced effects on semiconductor quantum dot decay dynamics in cavity QED,” *Phys. Rev. B* **86**, 085302 (2012).
- [155] A. Kaganskiy, S. Fischbach, A. Strittmatter, S. Rodt, T. Heindel, and S. Reitzenstein, “Enhancing the photon-extraction efficiency of site-controlled quantum dots by deterministically fabricated microlenses,” *Opt. Commun.* **413**, 162–166 (2018).
- [156] M. Kantner, U. Bandelow, T. Koprucki, J.-H. Schulze, A. Strittmatter, and H.-J. Wünsche, “Efficient current injection into single quantum dots through oxide-confined p-n-diodes,” *IEEE Trans. Electron Devices* **63**, 2036–2042 (2016).
- [157] M. Kantner, U. Bandelow, T. Koprucki, and H.-J. Wünsche, “Modeling and simulation of injection dynamics for quantum dot based single-photon sources,” *Proc. Int. Conf. Numerical Simulation of Optoelectronic Devices*, edited by J. Piprek, 219–220 (2016).
- [158] M. Kantner and T. Koprucki, “Numerical simulation of carrier transport in semiconductor devices at cryogenic temperatures,” *Opt. Quantum. Electron.* **48**, 543 (2016).
- [159] M. Kantner, A. Mielke, M. Mittnenzweig, and N. Rotundo, “Mathematical modeling of semiconductors: From quantum mechanics to devices,” submitted (2018).
- [160] M. Kantner, M. Mittnenzweig, and T. Koprucki, “Hybrid quantum-classical modeling of quantum dot devices,” *Phys. Rev. B* **96**, 205301 (2017).
- [161] S. Y. Karpov, “Light-emitting diode fundamentals,” in *Handbook of Optoelectronic Device Modeling and Simulation: Fundamentals, Materials, Nanostructures, LEDs, and Amplifiers*, Vol. 1, edited by J. Piprek (CRC Press, Taylor & Francis Group, Boca Raton, 2017) Chap. 14, pp. 451–472.
- [162] K. V. Kavokin, “Fine structure of the quantum-dot trion,” *Phys. Status Solidi A* **195**, 592–595 (2003).
- [163] H. J. Kimble, “The quantum internet,” *Nature* **453**, 1023–1030 (2008).
- [164] H. J. Kimble, M. Dagenais, and L. Mandel, “Photon antibunching in resonance fluorescence,” *Phys. Rev. Lett.* **39**, 691 (1977).
- [165] A. Kiraz, C. Reese, B. Gayral, L. Zhang, W. V. Schoenfeld, B. D. Gerardot, P. M. Petroff, E. L. Hu, and A. İmamoğlu, “Cavity-quantum electrodynamics with quantum dots,” *J. Opt. B: Quantum Semiclassical Opt.* **5**, 129 (2003).
- [166] C. Kittel, *Introduction to solid state physics*, 8th ed. (John Wiley & Sons, Hoboken, New Jersey, 2005).
- [167] P. Kivisaari, Y. Chen, M. E. Pistol, and N. Anttu, “Full optoelectronic simulation of nanowire LEDs: Effects of temperature,” *Proc. Int. Conf. Numerical Simulation of Optoelectronic Devices*, edited by J. Piprek, 109–110 (2017).
- [168] P. Kivisaari, Y. Chen, and N. Anttu, “Emission enhancement, light extraction and carrier dynamics in InGaAs/GaAs nanowire arrays,” *Nano Futures* **2**, 015001 (2018).
- [169] E. Knapp, R. Häusermann, H. U. Schwarzenbach, and B. Ruhstaller, “Numerical simulation of charge transport in disordered organic semiconductor devices,” *J. Appl. Phys.* **108**, 054504 (2010).
- [170] E. Knill, R. Laflamme, and G. J. Milburn, “A scheme for efficient quantum computation with linear optics,” *Nature* **409**, 46–52 (2001).
- [171] M. Kolarczik, N. Owschimikow, B. Herzog, F. Buchholz, Y. I. Kaptan, and U. Woggon, “Exciton dynamics probe the energy structure of a quantum dot-in-a-well

- system: The role of Coulomb attraction and dimensionality,” *Phys. Rev. B* **91**, 235310 (2015).
- [172] T. Koprucki and K. Gärtner, “Discretization scheme for drift-diffusion equations with strong diffusion enhancement,” *Opt. Quantum. Electron.* **45**, 791–796 (2013).
- [173] T. Koprucki, M. Kantner, J. Fuhrmann, and K. Gärtner, “On modifications of the Scharfetter–Gummel scheme for drift-diffusion equations with Fermi-like statistical distribution functions,” *Proc. Int. Conf. Numerical Simulation of Optoelectronic Devices*, 155–156 (2014).
- [174] T. Koprucki, N. Rotundo, P. Farrell, D. H. Doan, and J. Fuhrmann, “On thermodynamic consistency of a Scharfetter–Gummel scheme based on a modified thermal voltage for drift-diffusion equations with diffusion enhancement,” *Opt. Quantum. Electron.* **47**, 1327–1332 (2015).
- [175] T. Koprucki, A. Wilms, A. Knorr, and U. Bandelow, “Modeling of quantum dot lasers with microscopic treatment of Coulomb effects,” *Opt. Quantum. Electron.* **42**, 777–783 (2011).
- [176] R. Kosloff, “Quantum thermodynamics: A dynamical viewpoint,” *Entropy* **15**, 2100–2128 (2013).
- [177] A. Kossakowski, A. Frigerio, V. Gorini, and M. Verri, “Quantum detailed balance and KMS condition,” *Commun. Math. Phys.* **57**, 97–110 (1977).
- [178] D. Kosumi, T. Kusumoto, R. Fujii, M. Sugisaki, Y. Iinuma, N. Oka, Y. Takaesu, T. Taira, M. Iha, H. A. Frank, and H. Hashimoto, “One- and two-photon pump-probe optical spectroscopic measurements reveal the S_1 and intramolecular charge transfer states are distinct in fucoxanthin,” *Chem. Phys. Lett.* **483**, 95–100 (2009).
- [179] S. Kreinberg, W. W. Chow, J. Wolters, C. Schneider, C. Gies, F. Jahnke, S. Höfling, M. Kamp, and S. Reitzenstein, “Emission from quantum-dot high- β microcavities: Transition from spontaneous emission to lasing and the effects of superradiant emitter coupling,” *Light-Sci. Appl.* **6**, e17030 (2017).
- [180] R. Kubo, “The fluctuation-dissipation theorem,” *Rep. Prog. Phys.* **29**, 255–284 (1966).
- [181] S. C. Kuhn, A. Knorr, S. Reitzenstein, and M. Richter, “Cavity assisted emission of single, paired and heralded photons from a single quantum dot device,” *Opt. Express* **24**, 25446–25461 (2016).
- [182] C. Kurtsiefer, S. Mayer, P. Zarda, and H. Weinfurter, “Stable solid-state source of single photons,” *Phys. Rev. Lett.* **85**, 290 (2000).
- [183] H. Kurtze, J. Seebeck, P. Gartner, D. R. Yakovlev, D. Reuter, A. D. Wieck, M. Bayer, and F. Jahnke, “Carrier relaxation dynamics in self-assembled semiconductor quantum dots,” *Phys. Rev. B* **80**, 235319 (2009).
- [184] T. D. Ladd, F. Jelezko, R. Laflamme, Y. Nakamura, C. Monroe, and J. L. O’Brien, “Quantum computers,” *Nature* **464**, 45 (2010).
- [185] P. T. Landsberg, “On the diffusion theory of rectification,” *Proc. R. Soc. Lond. A* **213**, 226–237 (1952).
- [186] P. Lax and B. Wendroff, “Systems of conservation laws,” *Commun. Pure Appl. Math.* **13**, 217–237 (1960).
- [187] K. S. Lee, G. Oh, E. K. Kim, and J. D. Song, “Temperature dependent photoluminescence from InAs/GaAs quantum dots grown by molecular beam epitaxy,” *Appl. Sci. Converg. Technol.* **26**, 86–90 (2017).
- [188] M. Levinstein, S. Rumyantsev, and M. Shur, eds., *Handbook series on semiconductor parameters – Ternary and quaternary III-V compounds*, Vol. 2 (World Scientific, Singapore, 1996).

-
- [189] E. M. Lifshitz and L. P. Pitaevskii, *Physical kinetics*, Vol. 10, Course of Theoretical Physics (Pergamon Press, Oxford, 1981).
- [190] A. C. Limache and S. R. Idelsohn, “On the development of finite volume methods for computational solid mechanics,” *Mecánica Computacional* **26**, 827–843 (2007).
- [191] G. Lindblad, “On the generators of quantum dynamical semigroups,” *Commun. Math. Phys.* **48**, 119–130 (1976).
- [192] G. Lindblad, “Completely positive maps and entropy inequalities,” *Commun. Math. Phys.* **40**, 147–151 (1975).
- [193] U. Lindefelt, “Heat generation in semiconductor devices,” *J. Appl. Phys.* **75**, 942–957 (1994).
- [194] P. Lodahl, S. Mahmoodian, and S. Stobbe, “Interfacing single photons and single quantum dots with photonic nanostructures,” *Rev. Mod. Phys.* **87**, 347–400 (2015).
- [195] P. Lodahl, A. F. Van Driel, I. S. Nikolaev, A. Irman, K. Overgaag, D. Vanmaekelbergh, and W. L. Vos, “Controlling the dynamics of spontaneous emission from quantum dots by photonic crystals,” *Nature* **430**, 654 (2004).
- [196] M. Lorke, F. Jahnke, and W. W. Chow, “Excitation dependences of gain and carrier-induced refractive index change in quantum-dot lasers,” *Appl. Phys. Lett.* **90**, 051112 (2007).
- [197] M. Lorke, T. R. Nielsen, J. Seebeck, P. Gartner, and F. Jahnke, “Influence of carrier-carrier and carrier-phonon correlations on optical absorption and gain in quantum-dot systems,” *Phys. Rev. B* **73**, 085324 (2006).
- [198] K. Lüdge, M. J. P. Bormann, E. Malić, P. Hövel, M. Kuntz, D. Bimberg, A. Knorr, and E. Schöll, “Turn-on dynamics and modulation response in semiconductor quantum dot lasers,” *Phys. Rev. B* **78**, 035316 (2008).
- [199] K. Lüdge and E. Schöll, “Quantum-dot lasers—desynchronized nonlinear dynamics of electrons and holes,” *IEEE J. Quantum Electron.* **45**, 1396–1403 (2009).
- [200] A. J. MacLeod, “Algorithm 779: Fermi–Dirac functions of order $-1/2$, $1/2$, $3/2$, $5/2$,” *ACM T. Math. Software* **24**, 1–12 (1998).
- [201] I. Magnúsdóttir, A. V. Uskov, S. Bischoff, B. Tromborg, and J. Mørk, “One- and two-phonon capture processes in quantum dots,” *J. Appl. Phys.* **92**, 5982 (2002).
- [202] I. Magnúsdóttir, S. Bischoff, A. V. Uskov, and J. Mørk, “Geometry dependence of Auger carrier capture rates into cone-shaped self-assembled quantum dots,” *Phys. Rev. B* **67**, 205326 (2003).
- [203] E. Malić, M. J. P. Bormann, P. Hövel, M. Kuntz, D. Bimberg, A. Knorr, and E. Schöll, “Coulomb damped relaxation oscillations in semiconductor quantum dot lasers,” *IEEE J. Sel. Top. Quant.* **13**, 1242–1248 (2007).
- [204] P. A. Markowich, *The stationary semiconductor device equations*, Series in Computational Microelectronics (Springer, Vienna, 1986).
- [205] J. Márquez, L. Geelhaar, and K. Jacobi, “Atomically resolved structure of InAs quantum dots,” *Appl. Phys. Lett.* **78**, 2309–2311 (2001).
- [206] S. L. M. van Mensfoort and R. Coehoorn, “Effect of gaussian disorder on the voltage dependence of the current density in sandwich-type devices based on organic semiconductors,” *Phys. Rev. B* **78**, 085207 (2008).
- [207] R. Michalzik, “VCSEL fundamentals,” in *VCSELs – Fundamentals, technology and applications of vertical-cavity surface-emitting lasers*, Vol. 166, edited by R. Michalzik, Springer Series in Optical Sciences (Springer, Berlin, Heidelberg, 2013) Chap. 2, pp. 19–75.
- [208] P. Michler, ed., *Single quantum dots*, Vol. 90, Topics in Applied Physics (Springer, Berlin, Heidelberg, 2003).

- [209] P. Michler, A. Kiraz, C. Becher, W. V. Schoenfeld, P. M. Petroff, L. Zhang, E. Hu, and A. İmamoğlu, “A quantum dot single-photon turnstile device,” *Science* **290**, 2282–2285 (2000).
- [210] P. Michler, “Quantum dot single-photon sources,” in *Single semiconductor quantum dots*, edited by P. Michler, NanoScience and Technology (Springer, Berlin, Heidelberg, 2009) Chap. 6, pp. 185–225.
- [211] P. Michler, ed., *Single semiconductor quantum dots*, NanoScience and Technology (Springer, Berlin, Heidelberg, 2009).
- [212] P. Michler, ed., *Quantum dots for quantum information technologies*, Springer Series in Nano-Optics and Nanophotonics (Springer, Cham, 2017).
- [213] A. Mielke, “A gradient structure for reaction-diffusion systems and for energy-drift-diffusion systems,” *Nonlinearity* **24**, 1329–1346 (2011).
- [214] A. Mielke, “Dissipative quantum mechanics using GENERIC,” in *Recent trends in dynamical systems*, edited by A. Johann, H.-P. Kruse, F. Rupp, and S. Schmitz, Springer Proceedings in Mathematics & Statistics 35 (Springer, Basel, 2013) Chap. 21, pp. 555–585.
- [215] A. Mielke, “On thermodynamical couplings of quantum mechanics and macroscopic systems,” in *Mathematical results in quantum mechanics*, edited by P. Exner, W. König, and H. Neidhardt (2015), pp. 331–348.
- [216] M. Mittnenzweig and A. Mielke, “An entropic gradient structure for lindblad equations and couplings of quantum systems to macroscopic models,” *J. Stat. Phys.* **167**, 205–233 (2017).
- [217] T. T. Mnatsakanov, M. E. Levinshstein, L. I. Pomortseva, and S. N. Yurkov, “Universal analytical approximation of the carrier mobility in semiconductors for a wide range of temperatures and doping densities,” *Electronic and Optical Properties of Semiconductors* **38**, 56–60 (2004).
- [218] M. S. Mock, *Analysis of mathematical models of semiconductor devices* (Boole Press, Dublin, 1983).
- [219] N. Mohankumar and A. Natarajan, “The accurate numerical evaluation of half-order Fermi–Dirac integrals,” *Phys. Status Solidi B* **188**, 635–644 (1995).
- [220] T. Monz, D. Nigg, E. A. Martinez, M. F. Brandl, P. Schindler, R. Rines, S. X. Wang, I. L. Chuang, and R. Blatt, “Realization of a scalable Shor algorithm,” *Science* **351**, 1068–1070 (2016).
- [221] N. F. Mott, “Metal-insulator transition,” *Rev. Mod. Phys.* **40**, 677–683 (1968).
- [222] M. Müller, “Solar cell fundamentals,” in *Handbook of Optoelectronic Device Modeling and Simulation: Lasers, Modulators, Photodetectors, Solar Cells, and Numerical Methods*, Vol. 2, edited by J. Piprek (CRC Press, Taylor & Francis Group, Boca Raton, 2017) Chap. 39, pp. 383–413.
- [223] D. Munteanu and J.-L. Autran, “A 2-D/3-D Schrödinger–Poisson drift-diffusion numerical simulation of radially-symmetric nanowire MOSFETs,” in *Nanowires*, edited by X. Peng (IntechOpen, London, 2012) Chap. 15, pp. 341–370.
- [224] G. Nanz, “A critical study of boundary conditions in device simulation,” in *Simulation of semiconductor devices and processes*, Vol. 4, edited by W. Fichtner and D. Aemmer (1991), pp. 321–328.
- [225] G. A. Narvaez, G. Bester, and A. Zunger, “Excitons, biexcitons, and trions in self-assembled (In,Ga)As/ GaAs quantum dots: Recombination energies, polarization, and radiative lifetimes versus dot height,” *Phys. Rev. B* **72**, 245318 (2005).
- [226] T. R. Nielsen, P. Gartner, and F. Jahnke, “Many-body theory of carrier capture and relaxation in semiconductor quantum-dot lasers,” *Phys. Rev. B* **69**, 235314 (2004).

-
- [227] N. G. Nilsson, “An accurate approximation of the generalized Einstein relation for degenerate semiconductors,” *Phys. Status Solidi A* **19**, 75–78 (1973).
- [228] L. Onsager, “Reciprocal relations in irreversible processes. I.” *Phys. Rev.* **37**, 405 (1931).
- [229] H. C. Öttinger, “Nonlinear thermodynamic quantum master equation: Properties and examples,” *Phys. Rev. A* **82**, 052119 (2010).
- [230] H. C. Öttinger, “The geometry and thermodynamics of dissipative quantum systems,” *Europhys. Lett.* **94**, 10006 (2011).
- [231] H. C. Öttinger and M. Grmela, “Dynamics and thermodynamics of complex fluids. II. Illustrations of a general formalism,” *Phys. Rev. E* **56**, 6633–6655 (1997).
- [232] V. Palankovski and R. Quay, *Analysis and simulation of heterostructure devices*, Series in Computational Microelectronics (Springer, Vienna, 2004).
- [233] J. E. Parrott, “Thermodynamic theory of transport processes in semiconductors,” *IEEE Trans. Electron Devices* **43**, 809–826 (1996).
- [234] H. Paul, *Photonen: Eine Einführung in die Quantenoptik* (Vieweg+Teubner Verlag, Stuttgart, Leipzig, 1995).
- [235] C. G. Petra, O. Schenk, M. Lubin, and K. Gärtner, “An augmented incomplete factorization approach for computing the Schur complement in stochastic optimization,” *SIAM J. Sci. Comput.* **36**, C139–C162 (2014).
- [236] J. Piprek, ed., *Optoelectronic devices - Advanced simulation and analysis* (Springer, New York, 2005).
- [237] J. Piprek, ed., *Handbook of Optoelectronic Device Modeling and Simulation: Fundamentals, Materials, Nanostructures, LEDs and Amplifiers* (CRC Press, Taylor & Francis Group, Boca Raton, 2017).
- [238] J. Piprek, ed., *Handbook of Optoelectronic Device Modeling and Simulation: Lasers, Modulators, Photodetectors, Solar Cells, and Numerical Methods* (CRC Press, Taylor & Francis Group, Boca Raton, 2017).
- [239] O. W. Purbo, D. T. Cassidy, and S. H. Chisholm, “Numerical model for degenerate and heterostructure semiconductor devices,” *J. Appl. Phys.* **66**, 5078–5082 (1989).
- [240] E. M. Purcell, H. C. Torrey, and R. V. Pound, “Resonance absorption by nuclear magnetic moments in a solid,” *Phys. Rev.* **69**, 37–38 (1946).
- [241] A. Rahmani and G. W. Bryant, “Modification of spontaneous emission of quantum dots: Purcell effect in semiconductor microcavities,” *Phys. Status Solidi B* **224**, 807–810 (2001).
- [242] M. Reischle, C. Kessler, W.-M. Schulz, M. Eichfelder, R. Roßbach, M. Jetter, and P. Michler, “Triggered single-photon emission from electrically excited quantum dots in the red spectral range,” *Appl. Phys. Lett.* **97**, 143513 (2010).
- [243] J. P. Reithmaier, G. Şek, A. Löffler, C. Hofmann, S. Kuhn, S. Reitzenstein, L. V. Keldysh, V. D. Kulakovskii, T. L. Reinecke, and A. Forchel, “Strong coupling in a single quantum dot–semiconductor microcavity system,” *Nature* **432**, 197–200 (2004).
- [244] S. Reitzenstein, T. Heindel, C. Kistner, A. Rahimi-Iman, C. Schneider, S. Höfing, and A. Forchel, “Low threshold electrically pumped quantum dot-micropillar lasers,” *Appl. Phys. Lett.* **93**, 061104 (2008).
- [245] S. Reitzenstein, “Semiconductor quantum dot–microcavities for quantum optics in solid state,” *IEEE J. Sel. Top. Quant.* **18**, 1733–1746 (2012).
- [246] S. Reitzenstein, T. Heindel, C. Kistner, F. Albert, T. Braun, C. Hopfmann, P. Mrowinski, M. Lermer, C. Schneider, S. Höfing, M. Kamp, and A. Forchel, “Electrically driven quantum dot micropillar light sources,” *IEEE J. Sel. Top. Quant.* **17**, 1670–1680 (2011).

- [247] Y. L. A. Rezus, S. G. Walt, R. Lettow, A. Renn, G. Zumofen, S. Götzinger, and V. Sandoghdar, “Single-photon spectroscopy of a single molecule,” *Phys. Rev. Lett.* **108**, 093601 (2012).
- [248] D. M. Richey, J. D. Cressler, and R. C. Jaeger, “Numerical simulation of SiGe HBT’s at cryogenic temperatures,” *J. Phys. IV France* **04**, C6–127–C6–32 (1994).
- [249] M. Richter, A. Carmele, A. Sitek, and A. Knorr, “Few-photon model of the optical emission of semiconductor quantum dots,” *Phys. Rev. Lett.* **103**, 087407 (2009).
- [250] B. K. Ridley, *Quantum processes in semiconductors*, 4th ed. (Oxford University Press, Oxford, 2013).
- [251] M. F. Riedel, D. Binosi, R. Thew, and T. Calarco, “The european quantum technologies flagship programme,” *Quantum Sci. Technol.* **2**, 030501 (2017).
- [252] S. Ritter, P. Gartner, C. Gies, and F. Jahnke, “Emission properties and photon statistics of a single quantum dot laser,” *Opt. Express* **18**, 9909–9921 (2010).
- [253] A. Rivas and S. F. Huelga, *Open quantum systems – An introduction*, SpringerBriefs in Physics (Springer, Berlin, Heidelberg, 2012).
- [254] A. Rogach, ed., *Semiconductor nanocrystal quantum dots – synthesis, assembly, spectroscopy and applications* (Springer, Vienna, 2008).
- [255] W. W. van Roosbroeck, “Theory of the flow of electrons and holes in germanium and other semiconductors,” *Bell Syst. Tech. J.* **29**, 560–607 (1950).
- [256] W. W. van Roosbroeck and W. Shockley, “Photon-radiative recombination of electrons and holes in germanium,” *Phys. Rev.* **94**, 1558 (1954).
- [257] K. Roy-Choudhury and S. Hughes, “Theory of phonon dressed light-matter interactions and resonance fluorescence in quantum dot cavity systems,” in *Quantum dots for quantum information technologies*, edited by P. Michler, Springer Series in Nano-Optics and Nanophotonics (Springer, Cham, 2017) Chap. 2, pp. 41–74.
- [258] H. Rucker, J. Korn, and J. Schmidt, “Operation of SiGe HBTs at cryogenic temperatures,” in Bipolar/BiCMOS circuits and technology meeting (BCTM) (IEEE, 2017), pp. 17–20.
- [259] M. Rudan, *Physics of semiconductor devices* (Springer, New York, 2015).
- [260] Y. Saad, *Iterative methods for sparse linear systems* (SIAM, 2003).
- [261] S. Sant and A. Schenk, “The effect of density-of-state tails on band-to-band tunneling: Theory and application to tunnel field effect transistors,” *J. Appl. Phys.* **122**, 135702 (2017).
- [262] C. Santori, D. Fattal, J. Vučković, G. S. Solomon, and Y. Yamamoto, “Indistinguishable photons from a single-photon device,” *Nature* **419**, 594–597 (2002).
- [263] C. Santori, D. Fattal, and Y. Yamamoto, *Single-photon devices and applications* (Wiley, Weinheim, 2010).
- [264] W. Schäfer and M. Wegener, *Semiconductor optics and transport phenomena* (Springer, Berlin, Heidelberg, 2002).
- [265] G. Schaller, “Quantum equilibration under constraints and transport balance,” *Phys. Rev. E* **83**, 031111 (2011).
- [266] G. Schaller, *Open quantum systems far from equilibrium*, Vol. 881, Lecture Notes in Physics (Springer, Cham, 2014).
- [267] G. Schaller, G. Kießlich, and T. Brandes, “Transport statistics of interacting double dot systems: coherent and non-markovian effects,” *Phys. Rev. B* **80**, 245107 (2009).
- [268] D. L. Scharfetter and H. K. Gummel, “Large-signal analysis of a silicon Read diode oscillator,” *IEEE Trans. Electron Devices* **16**, 64–77 (1969).
- [269] A. Schenk, “A model for the field and temperature dependence of Shockley–Read–Hall lifetimes in silicon,” *Solid-State Electron.* **35**, 1585–1596 (1992).

-
- [270] A. Schenk, M. Stahl, and H.-J. Wünsche, “Calculation of interband tunneling in inhomogeneous fields,” *Phys. Status Solidi B* **154**, 815–826 (1989).
- [271] A. Schlehahn, L. Krüger, M. Gschrey, J.-H. Schulze, S. Rodt, A. Strittmatter, T. Heindel, and S. Reitzenstein, “Operating single quantum emitters with a compact Stirling cryocooler,” *Rev. Sci. Instrum.* **86**, 013113 (2015).
- [272] A. Schlehahn, A. Thoma, P. Munnely, M. Kamp, S. Höfling, T. Heindel, C. Schneider, and S. Reitzenstein, “An electrically driven cavity-enhanced source of indistinguishable photons with 61% overall efficiency,” *APL Photonics* **1**, 011301 (2016).
- [273] A. Schliwa, G. Hönl, and D. Bimberg, “Electronic properties of III-V quantum dots,” in M. Ehrhardt and T. Koprucki, *Multi-band effective mass approximations – Advanced mathematical models and numerical techniques*, Vol. 94, edited by M. Ehrhardt and T. Koprucki, Lecture Notes in Computational Science and Engineering (Springer, Cham, 2014) Chap. 2, pp. 57–85.
- [274] P. Schnauber, J. Schall, S. Bounouar, T. Höhne, S.-I. Park, G.-H. Ryu, T. Heindel, S. Burger, J.-D. Song, S. Rodt, and S. Reitzenstein, “Deterministic integration of quantum dots into on-chip multimode interference beamsplitters using in situ electron beam lithography,” *Nano Lett.* **18**, 2336–2342 (2018).
- [275] D. Schröder, *Modelling of interface carrier transport for device simulation*, Series in Computational Microelectronics (Springer, Vienna, 1994).
- [276] M. O. Scully and M. S. Zubairy, *Quantum optics* (Cambridge University Press, Cambridge, 1997).
- [277] J. Seebeck, T. R. Nielsen, P. Gartner, and F. Jahnke, “Polarons in semiconductor quantum dots and their role in the quantum kinetics of carrier relaxation,” *Phys. Rev. B* **71**, 125327 (2005).
- [278] S. Selberherr, *Analysis and simulation of semiconductor devices* (Springer, Vienna, 1984).
- [279] S. Selberherr, “MOS device modeling at 77 K,” *IEEE Trans. Electron Devices* **36**, 1464–1474 (1989).
- [280] P. Shah, V. Mitin, M. Grupen, G. H. Song, and K. Hess, “Numerical simulation of wide band-gap AlGaIn/InGaIn light-emitting diodes for output power characteristics and emission spectra,” *J. Appl. Phys.* **79**, 2755 (1996).
- [281] J. R. Shewchuk, “Triangle: Engineering a 2D quality mesh generator and Delaunay triangulator,” in *Applied computational geometry: Towards geometric engineering*, Vol. 1148, edited by M. C. Lin and D. Manocha, Lecture Notes in Computer Science (Springer, Berlin, Heidelberg, 1996), pp. 203–222.
- [282] A. J. Shields, R. M. Stevenson, R. M. Thompson, Z. Yuan, and B. E. Kardynal, “Generation of single photons using semiconductor quantum dots,” in *Nano-physics & bio-electronics: A new odyssey*, edited by T. Chakraborty, F. Peeters, and U. Sivan (Elsevier Science, Amsterdam, 2002) Chap. 4, pp. 111–146.
- [283] A. J. Shields, “Semiconductor quantum light sources,” *Nat. Photonics* **1**, 215–223 (2007).
- [284] W. Shockley and W. Read Jr., “Statistics of the recombinations of holes and electrons,” *Phys. Rev.* **87**, 835–842 (1952).
- [285] H. Si, K. Gärtner, and J. Fuhrmann, “Boundary conforming delaunay mesh generation,” *Comput. Math. Math. Phys.* **50**, 38–53 (2010).
- [286] Silvaco International, *Atlas user’s manual* (Santa Clara, CA, 2016).
- [287] H. Spohn, “Entropy production for quantum dynamical semigroups,” *J. Math. Phys.* **19**, 1227–1230 (1978).

- [288] H. Spohn and J. L. Lebowitz, “Irreversible thermodynamics for quantum systems weakly coupled to thermal reservoirs,” in *Advances in chemical physics*, Vol. 38, edited by S. A. Rice (John Wiley & Sons, 1978) Chap. 2, pp. 109–142.
- [289] S. Steiger, R. G. Veprek, and B. Witzigmann, “Unified simulation of transport and luminescence in optoelectronic nanostructures,” *J. Comput. Electron.* **7**, 509–520 (2008).
- [290] A. Steinhoff, H. Kurtze, P. Gartner, M. Florian, D. Reuter, A. D. Wieck, M. Bayer, and F. Jahnke, “Combined influence of Coulomb interaction and polarons on the carrier dynamics in InGaAs quantum dots,” *Phys. Rev. B* **88**, 205309 (2013).
- [291] A. Steinhoff, P. Gartner, M. Florian, and F. Jahnke, “Treatment of carrier scattering in quantum dots beyond the boltzmann equation,” *Phys. Rev. B* **85**, 205144 (2012).
- [292] O. Stier, M. Grundmann, and D. Bimberg, “Electronic and optical properties of strained quantum dots modeled by 8-band k-p theory,” *Phys. Rev. B* **59**, 5688–5701 (1999).
- [293] S. Stodtmann, R. M. Lee, C. K. F. Weiler, and A. Badinski, “Numerical simulation of organic semiconductor devices with high carrier densities,” *J. Appl. Phys.* **112**, 114909 (2012).
- [294] R. Stratton, “Diffusion of hot and cold electrons in semiconductor barriers,” *Phys. Rev.* **126**, 2002 (1962).
- [295] S. Strauf and F. Jahnke, “Single quantum dot nanolaser,” *Laser Photonics Rev.* **5**, 607–633 (2011).
- [296] A. Strittmatter, A. Schliwa, J.-H. Schulze, T. D. Germann, A. Dreismann, O. Hitzemann, E. Stock, I. A. Ostapenko, S. Rodt, W. Unrau, U. W. Pohl, A. Hoffmann, D. Bimberg, and V. A. Haisler, “Lateral positioning of InGaAs quantum dots using a buried stressor,” *Appl. Phys. Lett.* **100**, 093111 (2012).
- [297] A. Strittmatter, A. Holzbecher, A. Schliwa, J.-H. Schulze, D. Quandt, T. D. Germann, A. Dreismann, O. Hitzemann, E. Stock, I. A. Ostapenko, S. Rodt, W. Unrau, U. W. Pohl, A. Hoffmann, D. Bimberg, and V. A. Haisler, “Site-controlled quantum dot growth on buried oxide stressor layers,” *Phys. Status Solidi A* **209**, 2411–2420 (2012).
- [298] J. Stuhler, “Quantum optics route to market,” *Nat. Phys.* **11**, 293–295 (2015).
- [299] V. Sverdlov, E. Ungersboeck, H. Kosina, and S. Selberherr, “Current transport models for nanoscale semiconductor devices,” *Mater. Sci. Eng. R* **58**, 228–270 (2008).
- [300] T. Switaiski, U. Woggon, D. E. Alden Angeles, A. Hoffmann, J.-H. Schulze, T. D. Germann, A. Strittmatter, and U. W. Pohl, “Carrier dynamics in InAs/GaAs submonolayer stacks coupled to Stranski–Krastanov quantum dots,” *Phys. Rev. B* **88**, 035314 (2013).
- [301] Synopsys, Inc., *Sentaurus device userguide* (Mountain View, CA, 2010).
- [302] S. M. Sze, *Physics of semiconductor devices*, 2nd ed. (John Wiley & Sons, New York, 1981).
- [303] A. Thoma, P. Schnauber, M. Gschrey, M. Seifried, J. Wolters, J.-H. Schulze, A. Strittmatter, S. Rodt, A. Carmele, A. Knorr, T. Heindel, and S. Reitzenstein, “Exploring dephasing of a solid-state quantum emitter via time- and temperature-dependent Hong–Ou–Mandel experiments,” *Phys. Rev. Lett.* **116**, 033601 (2016).
- [304] J. G. Tischler, A. S. Bracker, D. Gammon, and D. Park, “Fine structure of trions and excitons in single GaAs quantum dots,” *Phys. Rev. B* **66**, 081310 (2002).
- [305] W. Unrau, D. Quandt, J.-H. Schulze, T. Heindel, T. D. Germann, O. Hitzemann, A. Strittmatter, S. Reitzenstein, U. W. Pohl, and D. Bimberg, “Electrically driven

-
- single photon source based on a site-controlled quantum dot with self-aligned current injection,” *Appl. Phys. Lett.* **101**, 211119 (2012).
- [306] W. Unrau, “Realisierung einer elektrisch betriebenen Einzelphotonenquelle mit verspannungsinduziert platzierten Quantenpunkten,” PhD thesis (Technical University Berlin, 2015).
- [307] A. V. Uskov, F. Adler, H. Schweizer, and M. H. Pilkuhn, “Auger carrier relaxation in self-assembled quantum dots by collisions with two-dimensional carriers,” *J. Appl. Phys.* **81**, 7895–7899 (1997).
- [308] A. V. Uskov, J. McInerney, F. Adler, H. Schweizer, and M. H. Pilkuhn, “Auger carrier capture kinetics in self-assembled quantum dot structures,” *Appl. Phys. Lett.* **72**, 58 (1998).
- [309] A. V. Uskov, I. Magnúsdóttir, B. Tromborg, J. Mørk, and R. Lang, “Line broadening caused by Coulomb carrier–carrier correlations and dynamics of carrier capture and emission in quantum dots,” *Appl. Phys. Lett.* **79**, 1679–1681 (2001).
- [310] H. Van Cong and G. Debiasis, “A simple accurate expression of the reduced Fermi energy for any reduced carrier density,” *J. Appl. Phys.* **73**, 1545–1546 (1993).
- [311] D. Vasileska, S. M. Goodnick, and G. Klimeck, *Computational electronics – Semiclassical and quantum device modeling and simulation* (CRC Press, Taylor & Francis Group, Boca Raton, 2010).
- [312] C. Villani, *Optimal transport: Old and new*, Vol. 338, Grundlehren der mathematischen Wissenschaften (Springer, Berlin, Heidelberg, 2009).
- [313] W. Vogel and D.-G. Welsch, *Quantum optics*, 3rd ed. (Wiley, Weinheim, 2006).
- [314] G. K. Wachutka, “Rigorous thermodynamic treatment of heat generation and conduction in semiconductor device modeling,” *IEEE Trans. Comput.-Aided Design Integr. Circuits Syst.* **9**, 1141–1149 (1990).
- [315] D. F. Walls, “Evidence for the quantum nature of light,” *Nature* **280**, 451–454 (1979).
- [316] M. B. Ward, T. Farrow, P. See, Z. L. Yuan, O. Z. Karimov, A. J. Bennett, A. J. Shields, P. Atkinson, K. Cooper, and D. A. Ritchie, “Electrically driven telecommunication wavelength single-photon source,” *Appl. Phys. Lett.* **90**, 063512 (2007).
- [317] V. Weisskopf and E. Wigner, “Berechnung der natürlichen Linienbreite auf Grund der Diracschen Lichttheorie,” *Z. Phys.* **63**, 54–73 (1930).
- [318] H. Werner and G. Raymann, “An approximation to the Fermi integral $F_{1/2}(x)$,” *Math. Comput.* **17**, 193–194 (1963).
- [319] R. Wetzler, A. Wacker, and E. Schöll, “Coulomb scattering with remote continuum states in quantum dot devices,” *J. Appl. Phys.* **95**, 7966–7970 (2004).
- [320] Wikimedia Commons, *A diagram of the first Brillouin zone of a face-centred cubic (FCC) lattice*, (2008) [https://commons.wikimedia.org/wiki/File:Brillouin_Zone_\(1st,_FCC\).svg](https://commons.wikimedia.org/wiki/File:Brillouin_Zone_(1st,_FCC).svg).
- [321] R. M. Wilcox, “Exponential operators and parameter differentiation in quantum physics,” *J. Math. Phys.* **8**, 962–982 (1967).
- [322] A. Wilms, P. Mathé, F. Schulze, T. Koprucki, A. Knorr, and U. Bandelow, “Influence of the carrier reservoir dimensionality on electron-electron scattering in quantum dot materials,” *Phys. Rev. B* **88**, 235421 (2013).
- [323] T. Windbacher, V. Sverdlov, and S. Selberherr, “Classical device modeling,” in *Nano-electronic devices – semiclassical and quantum transport modeling*, edited by D. Vasileska and S. Goodnick (Springer, New York, 2011) Chap. 2, pp. 1–96.
- [324] H. M. Wiseman and G. J. Milburn, *Quantum measurement and control* (Cambridge University Press, Cambridge, 2009).

- [325] A. Wojs, P. Hawrylak, S. Fafard, and L. Jacak, “Electronic structure and magneto-optics of self-assembled quantum dots,” *Phys. Rev. B* **54**, 5604–5608 (1996).
- [326] S. A. Wong, S. P. McAlister, and Z.-M. Li, “A comparison of some approximations for the Fermi–Dirac integral of order $1/2$,” *Solid State Electron.* **37**, 61–64 (1994).
- [327] J. Wu, S. Chen, A. Seeds, and H. Liu, “Quantum dot optoelectronic devices: Lasers, photodetectors and solar cells,” *J. Phys. D: Appl. Phys.* **48**, 363001 (2015).
- [328] Y. Wu, G. Zhang, L. Guo, X. Li, and G. Qi, “Theoretical simulation of carrier capture and relaxation rates in quantum-dot semiconductor optical amplifiers,” *J. Appl. Phys.* **115**, 224502 (2014).
- [329] Z. Yu, D. Chen, L. So, and R. W. Dutton, *PISCES-2ET 2D device simulator*, tech. rep. (Integrated Circuits Laboratory, Stanford University, Stanford, 1994).
- [330] Z. Yuan, B. E. Kardynal, R. M. Stevenson, A. J. Shields, C. J. Lobo, K. Cooper, N. S. Beattie, D. A. Ritchie, and M. Pepper, “Electrically driven single-photon source,” *Science* **295**, 102–105 (2002).
- [331] D. Zuras and M. Cowlishaw, *IEEE standard for floating-point arithmetic*, tech. rep. (IEEE Computer Society, New York, 2008), pp. 1–70.
- [332] V. Zwiller, T. Aichele, and O. Benson, “Quantum optics with single quantum dot devices,” *New J. Phys.* **6**, 96 (2004).